Brain and cervical cord myelin water imaging in neuromyelitis optica spectrum disorder

Combes, Anna Julie Elise

Awarding institution:
King's College London

Brain and cervical cord myelin water imaging in neuromyelitis optica spectrum disorder

Anna Combes

A thesis submitted in fulfilment of the requirements
for the degree of Doctor of Philosophy

Institute of Psychiatry, Psychology & Neuroscience

King's College London

Supervised by Prof. Gareth Barker & Prof. Shannon Kolind

August 2017

Abstract

Neuromyelitis optica spectrum disorder (NMOSD) is a chronic disease of the central nervous system that primarily affects the optic nerves and spinal cord. Despite similarities with relapsing-remitting multiple sclerosis (MS), NMOSD was recently recognized as a separate disease entity with different pathophysiological mechanisms and prognosis, and its clinical and imaging features are still being described. This project aims to explore brain and cervical spinal cord pathology in NMOSD by employing myelin water imaging, a magnetic resonance imaging method that has seen several applications in MS research. mcDESPOT is a novel technique based on multicomponent relaxometry that yields several quantitative tissue parameters, including the myelin water fraction, an index of myelin content, and T_1 and T_2 relaxation times, as well as structural volumetric measures. In this work, a mcDESPOT brain protocol was first acquired across three time points in healthy older adults on a single 3 Tesla scanner. Data on the test-retest reliability of mcDESPOT-derived indices are reported. Brain and cord mcDESPOT datasets were used to characterise focal and diffuse pathology in NMOSD in contrast with healthy controls. Results revealed abnormal parameters in several white matter regions, raising questions about the nature of non-lesional damage in the brain. Investigation of the thalamus showed normal volume, preserved microstructural integrity, and a link with a measure of information processing speed. Finally, cross-sectional and longitudinal measures of myelin content and atrophy in the cervical cord showed differences between NMOSD, MS and control groups. This work brings further evidence to address outstanding questions in NMOSD research regarding the nature and extent of brain involvement, the correlates of cognitive impairment, and the existence of subclinical disease progression between clinical relapses, and supports the use of mcDESPOT as an informative technique in the study of this rare disease in particular, and neurological disorders involving white matter in general.

Acknowledgements

An incredible amount of gratitude goes to my supervisors Shannon Kolind and Gareth Barker for their endless patience and kindness, never running out of encouragements, and allowing me to cross over the ocean – several times! I have been *extremely* lucky.

Special thanks to Vincent Giampietro, David Li, Alex MacKay, Tony Traboulsee, Irene Vavasour and Steve Williams, for their support, expertise, and the many, many amazing opportunities; to Katrina McMullen, Stephen Wastling and Toby Wood for help and guidance; and to Lucy Matthews and Jacqueline Palace for sharing their data and valuable advice.

Many thanks to the staff and radiographers/technologists at the Centre for Neuroimaging Sciences and the UBC MRI Centre, and everyone involved with recruitment and data collection. I am grateful to everyone who went in the scanner and especially the volunteers who gave up their time for research.

Thanks to everyone who welcomed me in London and Vancouver, and to officemates and coworkers past, present and honorary for enduring the stressful times and making the rest a lot of fun.

Et par-dessus tout, merci à tout le monde à la maison.

Table of contents

Brain and cervical cord myelin water imaging in neuromyelitis optica spectrum disorder **1**

Abstract **2**

Acknowledgements **3**

Table of contents **4**

Statement of contributions **10**

List of associated publications **11**

List of abbreviations **12**

List of tables **15**

List of figures **16**

Chapter I. Introduction **18**

Chapter II. Theoretical background **20**

Part 1: Quantitative magnetic resonance imaging of the central nervous system **20**

II.1. White matter imaging *in vivo* **22**

II.1.1. Myelin in the central nervous system 22

II.1.1.1. Basic neuroanatomy 22

II.1.1.2. Myelin role and biology 23

II.1.1.3. Functional relevance of myelin in health and disease 24

II.1.2. Quantitative MRI and relaxometry 26

II.1.2.1. Magnetic resonance and the relaxation properties of tissue 26

II.1.2.2. Beyond traditional MR contrast 28

II.1.2.3. T_1 mapping 28

II.1.2.4. T_2 mapping 29

II.1.2.5. Relaxation does not follow a single-exponential behaviour in tissue 30

II.1.3. Myelin water imaging 30

II.1.3.1. Overview and general principle 30

II.1.3.2. The three-pool model of tissue 31

II.1.3.3. Myelin water imaging using multi-echo T_2 relaxometry 32

II.1.3.4. Available methods for MWI 33

II.1.3.5. Specificity and potential confounds 34
II.1.3.6. Validation studies 35
II.1.3.7. Other methods for *in vivo* myelin imaging 36
II.2. mcDESPOT 37
II.2.1. Overview 37
II.2.2. Acquisition protocol 39
II.2.2.1. Steady-state sequences 39
II.2.2.2. SPGR 39
II.2.2.3. IR-SPGR 40
II.2.2.4. bSSFP 40
II.2.3. T_1 and T_2 mapping with single-component DESPOT 41
II.2.3.1. DESPOT1&2 41
II.2.3.2. DESPOT1-HIFI 42
II.2.3.3. DESPOT2-FM 43
II.2.4. Myelin water imaging with mcDESPOT 43
II.2.4.1. Overview 43
II.2.4.2. Stochastic Region Contraction 44
II.2.4.3. The three-pool model in mcDESPOT 46
II.2.4.4. Effect of water exchange 48
II.2.4.5. Algorithm stability 49
II.2.4.6. Advantages and critiques 50
II.2.4.7. Preclinical and clinical applications 50
Part 2: Multiple sclerosis and neuromyelitis optica spectrum disorder 52
II.3. Multiple sclerosis 53
II.3.1. Clinical and epidemiological features 53
II.3.2. Diagnosis 53
II.3.3. Disease course and subtypes 54
II.3.4. Pathophysiology 56
II.3.5. Conventional MRI findings in MS 59
II.3.6. Role of advanced MRI in MS 61
II.4. Neuromyelitis optica spectrum disorder 63
II.4.1. Clinical and epidemiological features 63
II.4.2. The NMO spectrum 63
II.4.3. Differential diagnosis 65
II.4.4. Disease course and progression 65
II.4.5. Pathophysiology 67
II.4.6. Conventional MRI findings in NMOSD 68

Chapter III. Intra-scanner reliability of mcDESPOT in healthy older adults 74
III.1. Introduction 75
III.2. Background 76
III.2.1. Concept of reliability 76
III.2.2. Previous work 78
III.2.3. Choice of sample 81
III.3. Methods 81
III.3.1. Acquisition 81
III.3.2. Analysis 83
III.3.2.1. Preprocessing 83
III.3.2.2. Creating maps 84
III.3.2.3. Post-processing 84
III.3.3. Reliability assessment 86
III.4. Results 88
III.4.1. Example data 88
III.4.2. Absolute measurements 91
III.4.3. Voxelwise reliability 91
III.4.4. ROI-specific reliability 92
III.5. Discussion 99
III.5.1. Reliability of T_1 99
III.5.2. Reliability of T_2 99
III.5.3. Applications of T_1 and T_2 mapping 100
III.5.4. Reliability of f_M 101
III.5.5. Generalizability to other populations 101
III.6. Conclusion 102
III.7. Additional information 102
Chapter IV. Subcortical pathology and relationship with cognitive performance in neuromyelitis optica spectrum disorder 106
IV.1. Introduction 107
IV.2. Background 108
IV.2.1. Cortical pathology 109
IV.2.2. White matter pathology 110
IV.2.3. Thalamus pathology 112
IV.2.3.1. Neuroanatomy and function 112
IV.2.3.2. Thalamic pathology in NMOSD 113

IV.2.3.3. Functional abnormalities of thalamic networks 114
IV.2.3.4. Differentiating between MS and NMOSD with thalamic volume 115
IV.2.4. Brain substrates of cognitive impairment in NMOSD 115
IV.2.5. Study aims 117
IV.2.5.1. Summary of current evidence 117
IV.2.5.2. Research questions and hypotheses 118
IV.3. Methods 119
IV.3.1. Population characteristics 119
IV.3.2. Data acquisition 120
IV.3.2.1. MRI acquisition 120
IV.3.2.2. Cognitive testing 121
IV.3.3. Image processing 122
IV.3.3.1. Lesion identification 122
IV.3.3.2. Tissue-class volume estimation using SIENAX 123
IV.3.3.3. mcDESPOT analysis 123
IV.3.3.4. Segmentation of white matter regions 124
IV.3.3.5. Thalamic segmentation 124
IV.3.4. Statistical analysis 125
IV.4. Results 126
IV.4.1.1. Sample description 126
IV.4.1.2. Volumes 126
IV.4.1.3. WM regions 127
IV.4.1.4. Thalamus metrics 129
IV.4.1.5. Relationships with SDMT score 131
IV.5. Discussion 132
IV.5.1. Summary of findings 132
IV.5.2. Volumetric measures 132
IV.5.3. NAWM pathology 132
IV.5.3.1. Possible aetiology 132
IV.5.3.2. Corpus callosum 134
IV.5.4. Thalamus findings 134
IV.5.4.1. Structural damage 134
IV.5.4.2. Influence of demographic factors 135
IV.5.4.3. Thalamic segmentation 135
IV.5.4.4. Relationship of thalamic metrics with cognitive performance 136
IV.5.5. General limitations 137
IV.5.5.1. Population 137
IV.5.5.2. Defining cognitive performance 138
IV.5.5.3. Lesion segmentation 139

IV.6. Conclusion 140

Chapter V. Longitudinal cervical cord myelin water imaging in multiple sclerosis and neuromyelitis optica spectrum disorder 141

V.1. Introduction 142

V.2. Background 143

V.2.1. Disease progression in MS and NMOSD 143

V.2.2. Imaging the cervical cord 144

V.2.3. Cervical cord pathology in MS and NMOSD 146

V.2.4. Rationale for this study 147

V.2.4.1. Previous work 147

V.2.4.2. Study aims 147

V.3. Methods 148

V.3.1. Study design and population characteristics 148

V.3.2. MRI acquisition 148

V.3.3. Image analysis 149

V.3.3.1. Cord segmentation 149

V.3.3.2. Lesion identification 150

V.3.3.3. Volume measurements 151

V.3.3.4. Myelin water fraction measurements 151

V.3.4. Statistical analysis 152

V.4. Results 153

V.4.1. Cross-sectional 153

V.4.1.1. Lesion identification 153

V.4.1.2. Cord volume 154

V.4.1.3. Myelin measurements 155

V.4.2. Longitudinal 158

V.4.2.1. Changes in EDSS 158

V.4.2.2. Lesions 158

V.4.2.3. Volume changes 158

V.4.2.4. Changes in myelin water fraction 159

V.5. Discussion 159

V.5.1. Summary of findings 159

V.5.2. Volume differences and atrophy 160

V.5.3. Myelin water fraction measurements 161

V.5.3.1. f_M is reduced in lesioned areas in MS and NMOSD 161

V.5.3.2. f_M is reduced in NASCT in MS and NMOSD 161

V.5.3.3. f_M decreases over time in MS NASCT only 162

V.5.4. Methodological considerations 164

V.5.4.1. Influence of motion 164
V.5.4.2. Methods for cord volume measurement 164
V.5.4.3. Segmentation of lesions 166
V.5.4.4. Variations in myelin content along the cord 166
V.5.4.5. Treatment effects 167
V.5.4.6. Sample size 167
V.6. Conclusion 167
V.7. Additional information 169
Chapter VI. Conclusion 171
References 178

Statement of contributions

The data presented in **Chapter III ("reliability study")** were acquired as part of a study sponsored by Janssen at the Centre for Neuroimaging Sciences, King's College London. The project was overseen by Prof. Steve Williams and Prof. Gareth Barker. I helped set up the study including obtaining ethics approval and organising scanner access, and was in charge of the recruitment and data collection. I analysed these data with help from Dr Tobias Wood for use of his code (based on work by Prof. Sean Deoni).

The data presented in **Chapter IV ("brain study")** were acquired at the University of British Columbia MRI Research Centre. Alice Li, Emma Eberts, Julia Schubert and Dr Katrina McMullen collected clinical data. Ludmila Litvin and I performed the lesion segmentation, using software by Dr Christian Kames. Lesion masks were reviewed by Dr Emmanuelle Lapointe. Emil Ljungberg provided the beautiful colour map. Some of the data in this study were acquired with support from the Milan & Maureen Ilich Foundation and the Diamond Family Foundation.

The data presented in **Chapter V ("spinal cord study")** were acquired at FMRIB in Oxford as part of a project previously designed and set up by Dr Jacqueline Palace, Dr Lucy Matthews and my supervisor Prof. Shannon Kolind. Data collection for the original study was supported by the NHS Highly Specialised Service for NMO and the NIHR Oxford Biomedical Research Centre, as well as staff from the John Radcliffe Hospital and Nuffield Department of Clinical Neurosciences, University of Oxford. I analysed the data and interpreted the results, with advice and input from them as well as insight from David Li, Roger Tam and Cornelia Laule who have experience with spinal cord data analysis. Jimmy Lee performed the lesion identification. Janet Lam and Eric Fu advised on statistical analysis.

List of associated publications

Below is a list of peer-reviewed publications and conference proceedings related to the work presented in this thesis.

Journal articles

Combes AJE, Matthews L, Lee JS, Li DK, Carruthers R, Traboulsee AL, Barker GJ, Palace J, Kolind S. (2017). Cervical cord myelin water imaging shows degenerative changes over one year in multiple sclerosis but not neuromyelitis optica spectrum disorder. *Neuroimage Clin (16), 17-22,* doi:10.1016/j.nicl.2017.06.019

Conference proceedings

Combes A, Vavasour IM, Lapointe E, McMullen K, Carruthers R, Li DKB, Barker GJ, Traboulsee A, Kolind S. (2017). Thalamic involvement in neuromyelitis optica spectrum disorder: multicomponent relaxometry parameters and relationship with cognition [Poster]. *ISMRM 25th Meeting, Honolulu, USA*

Combes A, McMullen K, Carruthers R, Kolind S, Traboulsee A. (2016). Processing speed, cognitive flexibility and mood disturbances in neuromyelitis optica Spectrum Disorder [Poster & oral pitch]. *PACTRIMS 9th Meeting, Bangkok, Thailand*

Combes A, Manogaran P, Vavasour IM, McMullen K, Carruthers R, Li DKB, Barker GJ, Traboulsee T, Kolind S. (2016). Detection of diffuse myelin changes in MS and NMOSD with atlas-based myelin water imaging [E-poster]. *ECTRIMS 32nd Meeting, London, UK*

Combes A, Matthews L, Barker GJ, Williams SCR, McMullen K, Lam J, Traboulsee A, Li DKB, Palace J & Kolind S. (2016). Longitudinal mcDESPOT shows contrasting patterns of change in multiple sclerosis and neuromyelitis optica cervical cord [E-poster]. *ISMRM 24th Meeting, Singapore*

Combes A, Matthews L, Li DKB, McMullen K, Barker GJ, Williams SCR, Traboulsee A, Palace J & Kolind S. (2016). MRI measures of cervical cord atrophy and water content in neuromyelitis optica [Poster]. *AAN 68th Meeting, Vancouver, Canada*

List of abbreviations

α – flip angle (or alpha)

τ_m – myelin water residence time

2/3D – two/three-dimensional

B_1 – transmit field

BET – Brain Extraction Tool

bSSFP – balanced steady state free precession

CC – corpus callosum

CNS – central nervous system

CPMG - Carr-Purcell-Meiboom-Gill

CSF – cerebrospinal fluid

CST – corticospinal tract

CV – coefficient of variation

DESPOT – Driven Equilibrium Single Pulse Observation of T_1 and T_2

DESPOT1-HIFI – DESPOT1 with High-Speed Incorporation of RF Field Inhomogeneities

DESPOT2-FM - DESPOT2 with Full Modelling

DGM – deep grey matter

DOF – degrees of freedom

DTI – diffusion tensor imaging

DWI – diffusion-weighted imaging

EDSS – Expanded Disability Status Scale

FA – fractional anisotropy

FLAIR – fluid-attenuated inversion recovery

f_0 – off-resonance

f_{CSF} – CSF 'free water' fraction

f_{IE} – intra/extracellular water fraction

f_M – myelin water fraction (mcDESPOT-derived)

FSL – FMRIB's Software Library

GM – grey matter

ICC – intraclass correlation coefficient

IE – intra/extra-cellular

IPS – information processing speed

IQR – inter-quartile range

IR – inversion recovery

LETM – longitudinally extensive transverse myelitis

mcDESPOT – multicomponent DESPOT

MD – mean diffusivity

MET_2 – multi-echo T_2

MRI – magnetic resonance imaging

MS – multiple sclerosis

MWF – myelin water fraction (general denomination)

MWI – myelin water imaging

NAA – n-acetylaspartate

NAGM – normal-appearing grey matter

NASCT – normal-appearing spinal cord tissue

NAWM – normal-appearing white matter

NMO(SD) – neuromyelitis optica (spectrum disorder)

NMR – nuclear magnetic resonance

NNLS – nonlinear non-negative least squares

PNS – peripheral nervous system

PD – proton density

ON – optic neuritis

OR – optic radiation

PASAT – Paced Auditory Serial Addition Test

SC – spinal cord

SD – standard deviation

SDMT – Symbol Digit Modalities Test

SIENA(X) – (Cross-Sectional) Structural Image Evaluation, using Normalization, of Atrophy

SPGR – spoiled gradient recalled

T – Tesla

TBSS – tract-based spatial statistics

TE – echo time

TI – inversion time

TR – repetition time

VBM – voxel-based morphometry

vCSF: ventricular cerebrospinal fluid

WM – white matter

List of tables

Table II.1. Summary of DESPOT techniques. 38
Table III.1. Studies addressing the intra- and/or inter-scanner reproducibility of DESPOT or mcDESPOT-derived parameters. 79
Table III.2. mcDESPOT values for each parameter averaged across subjects and sessions. 91
Table III.3. Voxelwise reliability for all three parameters. 92
Table III.4. Reliability metrics for T_1, T_2, and myelin water fraction across three time points. 95
Table IV.1. Population characteristics for healthy controls and NMOSD subjects. 120
Table IV.2. Tissue compartment volumes. 126
Table IV.3. f_M and T_1 values for white matter regions of interest. 129
Table IV.4. Thalamic quantitative metrics. 130
Table V.1. Population characteristics for the cross-sectional sample. 153
Table V.2. Baseline and longitudinal spinal cord MRI measures. 156
Table V.3. Population characteristics and MRI metrics at baseline for the longitudinal sub-sample. 170

List of figures

Figure II.1. Illustration of a neuron and its myelin sheath in the central nervous system 23
Figure II.2. Different mechanisms of neuronal damage and demyelination 25
Figure II.3. Schema of the relative time scales of T_1 and T_2 relaxation times in human tissue 27
Figure II.4. Spectrum of T_2 distributions from human white matter 32
Figure II.5. Schema of the three-pool model of compartmental relaxation in human brain. 47
Figure II.6. Schema of the course of disease progression in MS and NMO 57
Figure II.7. Conventional MRI scans used in the radiological assessment of MS 59
Figure II.8. Examples of brain lesions in neuromyelitis optica spectrum disorder 70
Figure III.1. Three examples of test-retest data with varying degrees of reliability, and how they relate to commonly used statistical measures 77
Figure III.2. Example regions of interest, overlaid on an SPGR image 86
Figure III.3. Example of a mcDESPOT acquired protocol 89
Figure III.4. Representative maps for one subject at baseline, 1 and 4 weeks 90
Figure III.5. Example parameter histograms for two subjects 93
Figure III.6. Example coefficient of variation maps, across the three time points, for two subjects 94
Figure III.7. Coefficients of variation for T_1 across three sessions 96
Figure III.8. Coefficients of variation for T_2 across three sessions 97
Figure III.9. Coefficients of variation for f_M across three sessions 98
Figure III.10. T_1 values by region of interest across the three sessions 103
Figure III.11. T_2 values by region of interest across the three sessions 104
Figure III.12. Myelin water fraction values by region of interest across the three sessions 105
Figure IV.1. Example task sheet for the Symbol Digit Modalities Test 121
Figure IV.2. Example of FLAIR^2 image for lesion segmentation for a subject with periventricular lesions 122
Figure IV.3. Example thalamic masks and quantitative maps with overlaid regions of interest 125
Figure IV.4. Group comparison between SIENAX-derived normalized volumes 127
Figure IV.5. Myelin water fraction and T_1 across white matter regions of interest 128
Figure IV.6. Group differences in normalized thalamic volume, thalamic f_M and T_1 ... 130
Figure IV.7. Scatter plots between white matter lesion volume 130
Figure IV.8. Scatter plots between SDMT score and thalamic metrics 131
Figure V.1. mcDESPOT protocol in the cervical spinal cord 145

Figure V.2. Cord segmentation and vertebral level identification using the Spinal Cord Toolbox **150**
Figure V.3. Procedure for segmentation of lesioned areas **151**
Figure V.4. Cervical cord volumes at baseline and over time **154**
Figure V.5. Example myelin water fraction (f_M) maps for three subjects **155**
Figure V.6. Myelin water fraction for the cross-sectional sample, by group and tissue type **157**
Figure V.7. Percent changes in median myelin water fraction by group and tissue type over one year **157**
Figure V.8. Repartition of lesions by cervical segment for the cross-sectional and longitudinal sub-samples **169**

Chapter I. Introduction

This thesis is an investigation into brain and cervical spinal cord pathology in neuromyelitis optica spectrum disorder (NMOSD) using myelin water imaging (MWI).

NMOSD is a relapsing disease of the central nervous system (CNS) that causes inflammation of the optic nerves and spinal cord. Despite similarities with relapsing-remitting multiple sclerosis (MS), NMOSD was recently recognized as a separate disease entity, and is now known to be an immune-mediated astrocytopathy, with secondary demyelination occurring in the brain as well as in the cord and optic nerves. Magnetic resonance imaging (MRI) plays a central role in the diagnosis and evaluation of both diseases, and MRI investigations into brain and cord pathology have shown great promise in helping differential diagnosis and disease management. While advanced, quantitative, MRI techniques - and in particular MWI - have greatly informed understanding of the extent, temporal dynamics, and clinical correlates of demyelination in MS, the imaging features of NMOSD have only recently started to be described. Thus, there is interest in using biologically specific MRI methods to probe tissue pathology in this condition.

Histopathological and imaging studies in both MS and NMOSD have endeavoured to describe CNS injury beyond focal pathology. In NMOSD, the number of these studies is limited, and these vary greatly in their conclusion regarding the existence or extent of widespread abnormalities. Discrepancies in those findings may be influenced by the choice of MRI technique and analysis methods, as well as small sample sizes due to the rarity of this condition. In addition to the relatively consistent findings of abnormalities in the optic and spinal pathways, there is some evidence for the presence of subtle normal-appearing tissue damage that may become evident with the use of more sensitive imaging techniques.

This project aims to explore brain and cervical spinal cord pathology in NMOSD by employing multicomponent Driven Equilibrium Single Pulse Observation of T_1 and T_2 (mcDESPOT), a novel MWI method. mcDESPOT yields estimates of several quantitative tissue parameters, including the T_1 and T_2 relaxation times, and the myelin water fraction, an index of myelin content. Due to its three-dimensional acquisition and high spatial resolution compared to other similar methods, individual scans from the protocol can also be used to derive structural volumetric measures.

mcDESPOT protocols have been developed for the brain and cervical spinal cord,

and have seen previous applications in MS research. The overall aim of this work is to contribute to establishing mcDESPOT as a valuable technique in this setting, firstly by demonstrating the test-retest reliability of one implementation of the protocol, and then by employ it to advance current knowledge of NMOSD pathology *in vivo*.

Following the current introductory chapter, this thesis includes a chapter on the theoretical background behind the work presented, three separate studies, and concluding remarks in the form of a sixth chapter.

In **Chapter II**, I review the main principles behind quantitative relaxometry and myelin water imaging, with a focus on the mcDESPOT technique. The main clinical and imaging features of MS and NMOSD are introduced.

In **Chapter III**, I report an investigation on the scan-rescan reliability of mcDESPOT-derived measures in the brain in healthy adults, at three time points, on a single 3 Tesla scanner. The aim of this study is to inform on the repeatability of the technique, thus providing evidence to support its use in single-site, longitudinal studies. Data on the test-retest reliability of mcDESPOT-derived indices are reported. I then present two applications of the method in the brain and cervical spinal cord in NMOSD.

In **Chapter IV**, I aim to characterise subcortical brain pathology in NMOSD using mcDESPOT, focusing on the thalamus and normal-appearing white matter. The study investigates abnormalities of myelin content and T_1 in various regions of interest, including regions typically vulnerable to secondary demyelination, as well as others that are not. It investigates thalamic volume and microstructural integrity and assess their relationship with a measure of information processing speed, a cognitive domain known to be subject to impairment in demyelinating diseases, seeking evidence for the potential role of the thalamus in cognition in NMOSD.

In **Chapter V** I present a longitudinal study of cervical cord pathology in NMOSD and MS subjects. I report cross-sectional and longitudinal measures of cord volume and myelin water fraction at baseline and after one year, in the absence of clinical relapses. The study aims to determine whether myelin content is abnormal in seemingly preserved areas of the cord, differentiating between lesional and normal-appearing areas. Given the known lack of clinical disease progression between attacks in NMOSD, we aim to compare the evolution of these parameters over time between the MS and NMOSD groups.

Concluding remarks are found in **Chapter VI**.

Chapter II. Theoretical background

This chapter is organized in two sections. In **Part 1**, we discuss quantitative magnetic resonance imaging and specifically the technique of interest in this thesis. In **Part 2**, we provide an introduction to multiple sclerosis and neuromyelitis optica spectrum disorder.

Part 1: Quantitative magnetic resonance imaging of the central nervous system

In this section we present a basic introduction to nuclear magnetic resonance imaging (MRI), focusing on quantitative MRI and especially relaxation time measurement. We describe the principles behind myelin water imaging and in particular the mcDESPOT technique, describe current evidence for the validation of this method and show its applications in the study of demyelination in neurological disease.

II.1. White matter imaging *in vivo* 22

II.1.1. Myelin in the central nervous system 22

II.1.1.1. Basic neuroanatomy 22

II.1.1.2. Myelin role and biology 23

II.1.1.3. Functional relevance of myelin in health and disease 24

II.1.2. Quantitative MRI and relaxometry 26

II.1.2.1. Magnetic resonance and the relaxation properties of tissue 26

II.1.2.2. Beyond traditional MR contrast 28

II.1.2.3. T_1 mapping 28

II.1.2.4. T_2 mapping 29

II.1.2.5. Relaxation does not follow a single-exponential behaviour in tissue 30

II.1.3. Myelin water imaging 30

II.1.3.1. Overview and general principle 30

II.1.3.2. The three-pool model of tissue 31

II.1.3.3. Myelin water imaging using multi-echo T_2 relaxometry 32

II.1.3.4. Available methods for MWI 33

II.1.3.5. Specificity and potential confounds 34
II.1.3.6. Validation studies 35
II.1.3.7. Other methods for *in vivo* myelin imaging 36
II.2. mcDESPOT 37
II.2.1. Overview 37
II.2.2. Acquisition protocol 39
II.2.2.1. Steady-state sequences 39
II.2.2.2. SPGR 39
II.2.2.3. IR-SPGR 40
II.2.2.4. bSSFP 40
II.2.3. T_1 and T_2 mapping with single-component DESPOT 41
II.2.3.1. DESPOT1&2 41
II.2.3.2. DESPOT1-HIFI 42
II.2.3.3. DESPOT2-FM 43
II.2.4. Myelin water imaging with mcDESPOT 43
II.2.4.1. Overview 43
II.2.4.2. Stochastic Region Contraction 44
II.2.4.3. The three-pool model in mcDESPOT 46
II.2.4.4. Effect of water exchange 48
II.2.4.5. Algorithm stability 49
II.2.4.6. Advantages and critiques 50
II.2.4.7. Preclinical and clinical applications 50

II.1. White matter imaging *in vivo*

II.1.1. Myelin in the central nervous system

II.1.1.1. Basic neuroanatomy

The human central nervous system (CNS) is comprised of the brain and spinal cord, within which are distinguished two tissue types. The grey matter (GM) is formed of neuronal cell bodies, and includes the cortex, forming the outer surface of the brain and organized in layers, and subcortical structures termed 'deep' GM nuclei (DGM). Within the brain, the white matter (WM), named for its clear appearance on dissection, is made up of myelinated axons, forms connections between the cortical and subcortical GM and links with the brainstem and spinal cord. WM makes up about half the volume of brain tissue in humans (Mancall and Brock, 2011). Cerebrospinal fluid (CSF) is found in interstitial and ventricular spaces within the brain, and a central canal within the cord.

The spinal cord connects the PNS to the brain, and is responsible for afferent and efferent nerve transmission, enabling movement, sensation and autonomic functions. Like the cerebrum is protected by the skull, the cord is located within the vertebral column, a skeletal structure formed of 33 vertebral bodies, organized in levels: cervical, thoracic, lumbar and sacral levels, and coccyx. The cord is situated in the CSF-filled spinal canal, dorsal to the vertebral bodies.

Unlike in the brain, the WM is situated on the outside of the spinal cord, with the GM within it having the characteristic shape of a butterfly. Without myelin, the cord would have to be the size of "a good-sized tree trunk" to achieve similar neuronal transmission speed (Morell and Quarles, 1999).

The spinal cord is a highly eloquent structure, meaning that due to its size and compact organization, its functional redundancy is limited, and therefore most insults to the tissue will manifest clinically. This is in contrast to the concept of 'brain reserve', according to which tissue injury may be clinically silent due to compensatory mechanisms or functional redundancy (i.e. the number and strength of existing connections exceeding that needed for effective functioning). Moreover, the cord has a limited capacity for repair (Cohen-Adad and Wheeler-Kingshott, 2014).

II.1.1.2. Myelin role and biology

In the CNS, electrical impulses are carried between neurons via axons forming synaptic connections, the basis of neuronal activity. Healthy axons are covered in myelin, an insulating membrane made up of lipids (~70-80%), proteins, and water (Mancall and Brock, 2011). Oligodendrocytes are the glial cells responsible for creating and maintaining myelin, by wrapping around axons in layers to form the myelin sheath (**Figure II.1**) in what has been described as "one of the most spectacular and intimate cell–cell interactions in the nervous system" (Nave, 2010). In the peripheral nervous system (PNS), this function is assumed by Schwann cells that myelinate a single axonal segment, while oligodendrocytes can be responsible for several axons. Glial cells protect as well as promote optimal functioning of the axon. Myelin allows electrical impulses to travel faster via the phenomenon of saltatory conduction, as well as lowering energy demands by limiting the surface of the axon producing action potentials and ion currents to less than 0.5% (Nave, 2010).

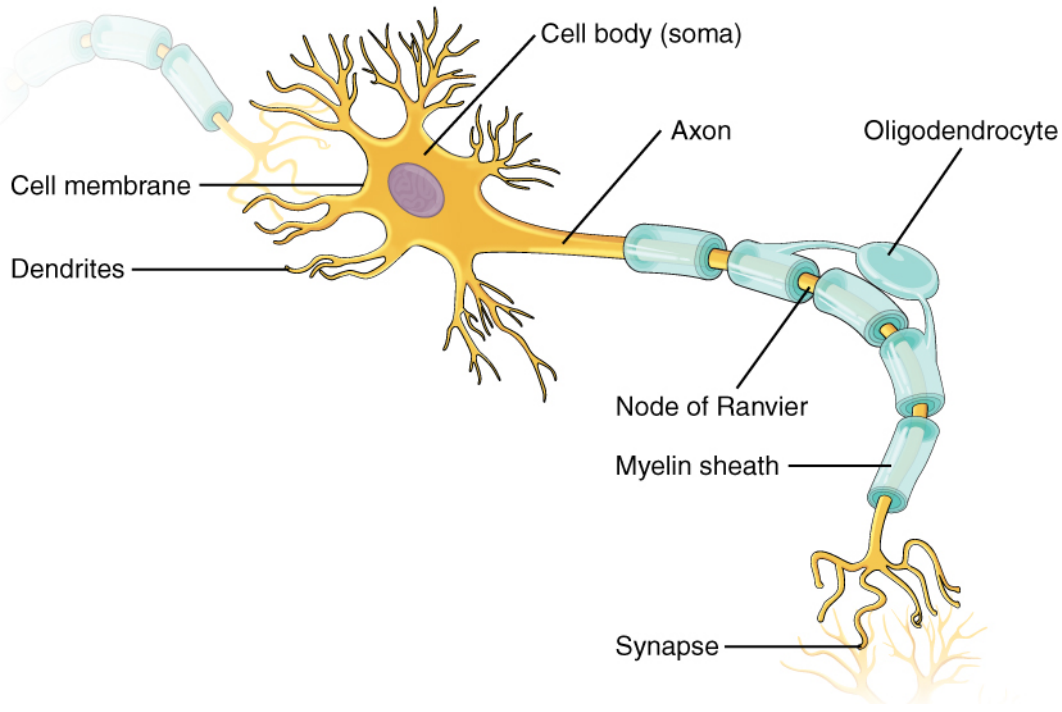

Figure II.1. Illustration of a neuron and its myelin sheath in the central nervous system. Source: OpenStax (Creative Commons license: CC-BY-4.0).

II.1.1.3. Functional relevance of myelin in health and disease

Myelin is necessary for efficient neuronal transmission, and therefore serves a crucial role in motor, sensory and higher order functions underlying behaviour and cognition. Myelination evolves through the lifespan and in response to stimuli; relationships between WM integrity, demographic factors (e.g. gender, age, handedness, and education), and neuropsychological performance have been observed (Fields, 2008). The role of WM in functional plasticity has been observed on a time scale of months following learning, training, or behavioural interventions. Such dynamics can be observed with myelin-sensitive MRI (Filley and Fields, 2016), as will be seen in later sections of this chapter. Myelin health is also subject to ageing-related decline and mediates the relationship between age and neuropsychological performance across several domains, highlighting the importance of WM in supporting cognitive function (Gunning-Dixon et al., 2009). WM changes are also observed in a range of psychiatric conditions (Filley, 2010).

Abnormalities of myelin can be idiopathic (dysmyelination), or occur as a result of pathology or injury (demyelination). Animal models of transiently induced demyelination (e.g. cuprizone-fed mice), as well as genetically determined models (e.g. canine model of congenital hypomyelination, or 'shaking pup' syndrome) are available (Duncan and Radcliff, 2016). Primary demyelination refers to a disease or injury process that will result in damage to the myelin sheath itself and/or to the oligodendrocytes via inflammation, autoimmune reaction, toxicity, etc. Secondary demyelination refers to myelin degradation following axonal injury, as is the case in Wallerian degeneration (the degeneration of an axon and its sheath distal to a site of focal injury) (Kandel et al., 2000). Different scenarios of secondary neuronal degeneration and demyelination mechanisms are illustrated in **Figure II.2**.

Multiple sclerosis (MS) and neuromyelitis optica spectrum disorder (NMOSD) are generally considered primary demyelinating disorders, although these mechanisms may also play a role in damage to the CNS in both diseases; these are discussed **Part 2: Multiple sclerosis and neuromyelitis optica spectrum disorder**.

MRI in the clinical and research setting has brought considerable advances in the study of white matter diseases. In the next section, we go over the basic principles behind MRI and in particular myelin water imaging.

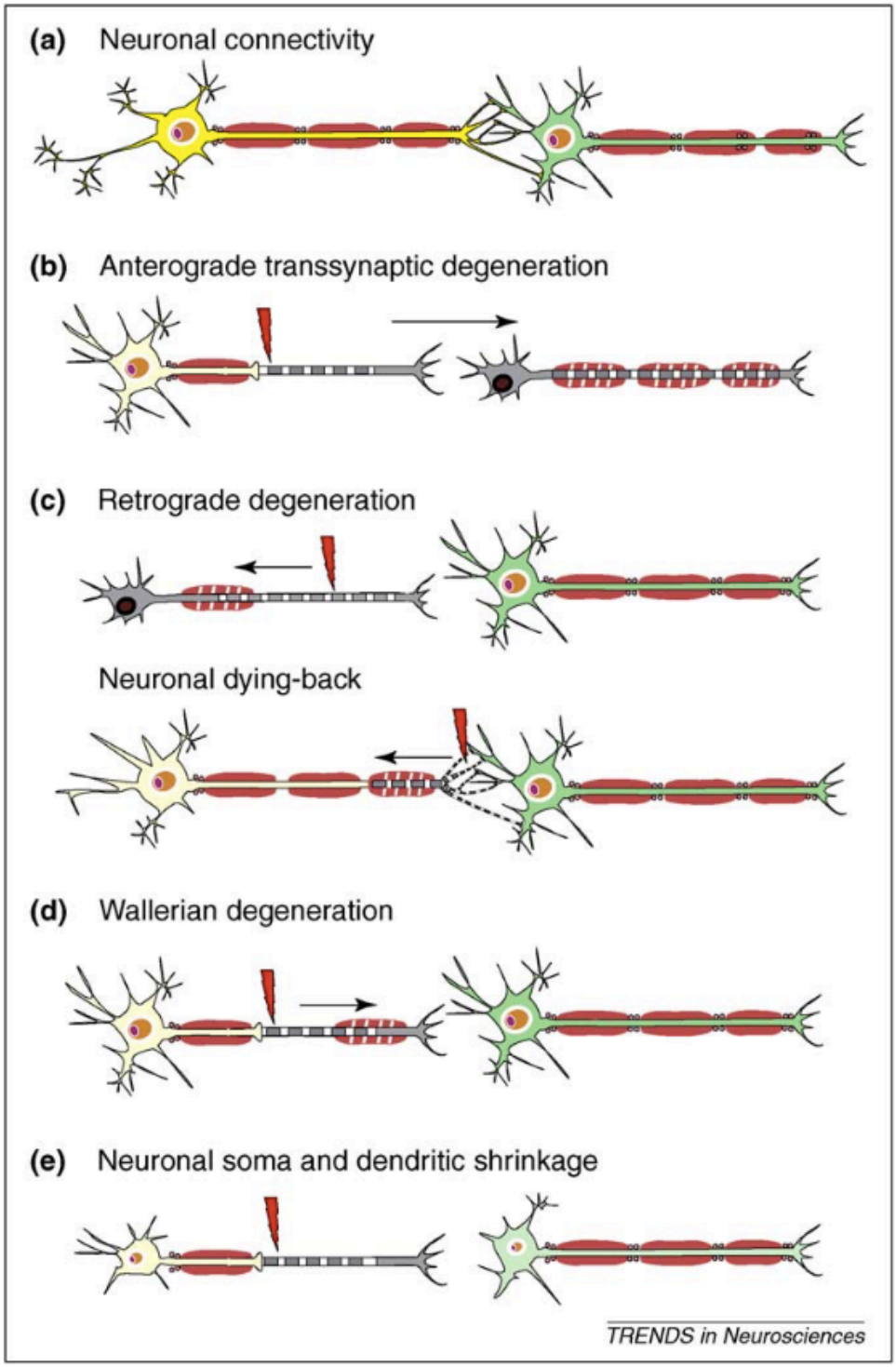

Figure II.2. Different mechanisms of neuronal damage and demyelination. **a)** Healthy neurons (yellow, green) with myelinated axons (red) forming a synaptic connection. **b)** Anterograde transsynaptic degeneration following injury to the axon, causing damage to the axon downstream (grey). **c)** Retrograde degeneration, causing death of the affected axon's parent neuron. **d)** Wallerian (anterograde) degeneration, causing degeneration to the part of the axon distal to injury. **e)** Case of both retrograde and anterograde damage. Source: (Siffrin et al., 2010).

II.1.2. Quantitative MRI and relaxometry

II.1.2.1. Magnetic resonance and the relaxation properties of tissue

An MRI system is, simplistically, an extremely powerful magnet, within which magnetic field gradients and radiofrequency (RF) pulses are used to manipulate the nuclear magnetic resonance properties of imaged objects. The principle behind MRI is that protons will react to these external magnetic forces, and will emit a signal that can be spatially and temporally encoded to allow reconstruction into a two- or three-dimensional image. Most human applications in research and medicine are conducted on scanners ranging in strength from 0.5 to 7 Tesla (T), with the greatest number of machines operating at 1.5 or 3T.

The MRI scanner can be conceptualized using a three-dimensional frame of reference: a 'longitudinal' *z* axis parallel to the scanner bore, and a 'transverse' two-dimensional plane defined by *x* and *y* axes. When placed into the scanner's main magnetic field, termed B_0, the hydrogen protons of water in human tissue, or 'spins', align along *z* in either direction. Fortuitously, a small difference will exist between the number of spins pointing 'up' and 'down' along *z*, thereby creating the opportunity for MR imaging. The sum of aligned vectors corresponding to spins' orientation corresponds to the net magnetization *M*, which, when perturbed, will give rise to the measured signal in the *xy* plane.

A spin system within the scanner is governed by relaxation phenomena, i.e. the tendency of magnetization to revert to a state of natural equilibrium after being perturbed. These parameters are dependent on both magnetic field and tissue properties. With knowledge of these interactions, MRI sequences can be designed to probe specific tissue properties, and we gain the capacity to visualize tissue *in vivo*. The basic dynamics of relaxation in the longitudinal and transverse planes are illustrated in **Figure II.3**, and described below.

Protons can be 'excited' by the application of an RF pulse that tips *M* into the transverse plane to a degree determined by a chosen flip angle. In addition to their tendency to align along *z*, spins are also subject to precession, i.e. rotating about their axes at a speed that is determined by the total magnetic field they are subjected to, which includes the effects of their biological environment.

When an RF 'excitation' pulse is applied, the net magnetization *M* is tipped into the transverse plane by a second magnetic field known as B_1, giving rise to M_{xy}. In a

rotating frame of reference, the amplitude of M_{xy} is dependent on the individual spins precessing with the same phase. Within one tenth of a second, the spins will naturally tend to lose phase coherence, and the amplitude of M_{xy} gradually decays. This is due to two phenomena: interactions between the spins themselves (T_2 relaxation), and inhomogeneity in the main magnetic field (T_2* effect). Through manipulation of M_{xy} using gradient and/or RF pulses, this dephasing can be reversed and the signal in the *xy* plane measured; this is called a signal echo, and occurs at a determined moment called the echo time (TE). The duration between repeated cycles of excitation and signal readout is called the repetition time (TR).

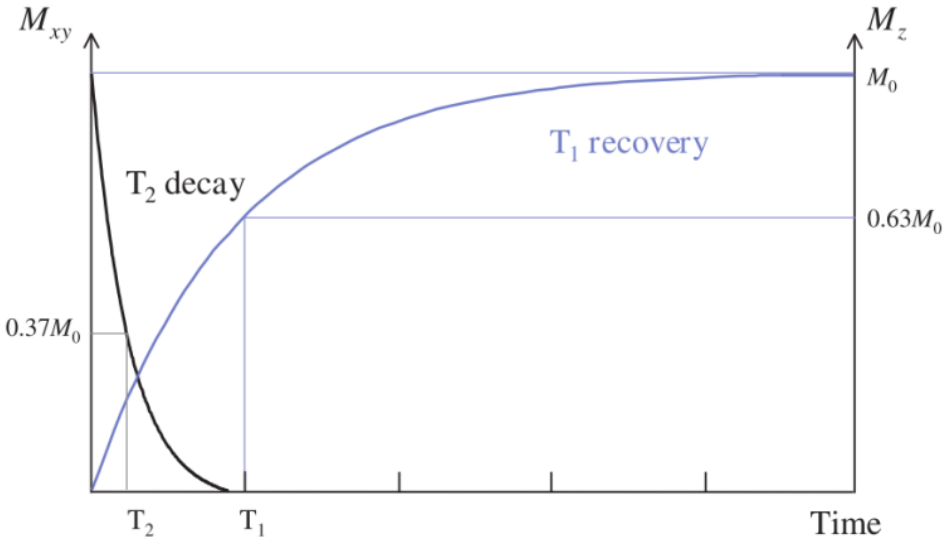

Figure II.3. Schema of the relative time scales of T_1 and T_2 relaxation times in human tissue. Source: (McRobbie et al., 2006).

T_2* is the time it takes for signal to drop from its maximum intensity, immediately after a 90° pulse, to ~37%, while T_2 is the time taken to drop to the same extent in a perfectly uniform magnetic field, or when the effects of inhomogeneity are refocussed using a spin-echo acquisition. T_2 is expressed in time units and on the order of 50-100 milliseconds (ms) in human tissue. Simultaneously and over a time scale of about a second, the protons interact with the surrounding biological environment (the tissue or 'lattice') and naturally realign along *z* to a state of equilibrium. This phenomenon of spin-lattice relaxation is characterized by the relaxation time T_1, defined as the time it takes for M_z to recover to ~63% of its maximum amplitude, M_0, along the longitudinal axis. In tissue, $T_1 > T_2 > T_2$*. With

increasing field strength, T_1 lengthens, and T_2 shortens, although T_1 is more field strength-dependent than T_2 (McRobbie et al., 2006).

II.1.2.2. Beyond traditional MR contrast

Because T_1 and T_2 relaxation occur simultaneously, the acquired signal depends on both T_1 and T_2 to different degrees depending on acquisition parameters, field strength, and the density of protons found in the imaged volume (three-dimensional pixel or 'voxel'). The resulting image is said to have varying degrees of T_1 or T_2-*weighting*. For instance, CSF appears dark on a T_1-weighted image due to having very long T_1, but bright on a T_2-weigthed image due to having longer T_2.

In addition to visualization of anatomy, a number of pathological characteristics of tissue give rise to different contrasts, making MRI a useful diagnostic tool. However, in conventional imaging, image intensities are a mixture of several parameters, and arbitrarily scaled. Weighted images lack biological specificity, and hold no quantitative information – limiting their use to radiological interpretation, or extraction of structural information, e.g. volumetric or morphometric measures that rely on contrast differences between tissue classes or areas (e.g. measurement of GM concentration via voxel-based morphometry (Ashburner and Friston, 2000)).

Moreover, the main and transmitted magnetic fields in an MR system are subject to hardware limitations and biophysical phenomena that can give rise to imperfections or inhomogeneities. These can cause signal loss or spatially distributed artefacts that increase in severity at higher field strength.

Quantitative MRI methods aim to decompose the MR signal into scalable parameters, so that voxel intensities become reliable, reproducible, and can be interpreted as potentially biologically meaningful metrics. Relaxation time mapping, or relaxometry, consists of measuring actual T_1 and T_2 values; this is usually achieved by sampling the recovery and decay curves at different time points. The gold standard approaches to T_1 and T_2 quantification are described below.

II.1.2.3. T_1 mapping

The most commonly used methods for T_1 quantification are inversion recovery (IR)-based sequences. These methods rely on 180° or 'inversion' pulses that flip M_z vertically, a manipulated inversion time (TI) delay during which M_z recovers,

followed by a 90° pulse that flips *M* into the transverse plane for signal measurement. IR-based methods are generally considered optimal in terms of accuracy. However, because T_1 in tissue is on the order of a second, and TR must be at least 5 times T_1 to allow for the complete restoration of M_0 along the longitudinal axis, each TR cycle contains a lot of 'dead time'. IR sequences are therefore often unpractically long for *in vivo* multi-slice experiments, although some marginally faster variants exist (saturation recovery, Look-Locker, MP-RAGE methods) (McRobbie et al., 2006).

With all of these techniques, T_1 can be measured by fitting the data to an exponential model of the longitudinal recovery curve (Cheng et al., 2012). T_1 mapping methods can be confounded by inaccurate flip angles, which is most commonly corrected for with separate acquisition of a B_1 field map.

For situations where speed is a main concern, variable flip angle (VFA)-based methods offer an alternative approach. In this framework, contrast in a series of T_1-weighted images with constant TR and TE is made dependent only on flip angle, proton density (PD) and T_1 (Stikov et al., 2015). Both TR and flip angles can be small, making this a fast acquisition. DESPOT1 is one such method, presented in **II.2.3**.

II.1.2.4. T_2 mapping

The gold standard for T_2 measurement is a Carr-Purcell-Meiboom-Gill (CPMG) sequence, relying on a 90° pulse followed by a series ('train') of regularly-spaced 180° pulses to sample the decay curve at different TEs. A typical sequence will employ 32 echoes with 10 ms spacing (Bydder et al., 2012). T_2 values are calculated voxelwise by fitting single-exponential curves to all available echoes; this is typically done offline using a least-squares minimization approach[1] (Tofts, 2003a).

[1] The least-squares approach to optimization works by finding the set of parameters – here, tissue biophysical parameters such as relaxation times – that best explain the available data. This is achieved by generating theoretical data for a range of possible parameters, and comparing how well these predicted data points match the acquired data. The differences between each pair of data point, i.e. the residuals, are calculated, squared and added up to provide a measure of discrepancy between predicted and acquired data. The optimal solution is the one with the smallest 'sum-of-squares'.

Characterization of the decay curve, and thus T_2 measurement precision, increases with the number of echoes acquired. This is generally considered a long sequence with poor spatial coverage, and thus often limited to single-slice or partial coverage acquisitions.

DESPOT2 offers an alternative approach based on a different principle – creating a steady state with both T_1 and T_2 contributions, and utilizing prior PD and T_1 information to calculate T_2 – described in **II.2.3**.

II.1.2.5. Relaxation does not follow a single-exponential behaviour in tissue

At the current spatial resolution of MRI, typically ~1 millimetre $(mm)^3$, several cellular environments or 'compartments' are known to exist within each voxel, and all are expected to have their own T_1 and T_2 relaxation properties.

Because water protons move very fast between environments relative to the scale of T_1 relaxation, it is harder to untangle the relative contributions of signal from each compartment to the T_1 recovery curve. Therefore, using conventional T_1 relaxation mapping methods, T_1 relaxation can generally be assumed to have a mono-exponential profile, with the corresponding single T_1 time being a weighted average of the T_1 values of the individual compartments.

On the other hand, sampling experiments of the T_2 decay curve have shown that several components can be reliably identified, related to the different water compartments in tissue. The single-exponential fitted T_2 value in a voxel is known to be different from the sum, or a weighted average, of its various components (Boulby and Rugg-Gunn, 2003); therefore, summing up these different components with a single T_2 value is not a trivial problem. Moreover, these different components have the potential to provide information about tissue microstructure. Exploitation of these properties has given rise to myelin water imaging, which is described in the next section.

II.1.3. Myelin water imaging

II.1.3.1. Overview and general principle

Imaging myelin *in vivo* has many clinical and research applications for the study of neurodevelopment, functional plasticity, and disease. However, even in highly

myelinated structures, myelin only represents a relatively small portion of the tissue. While traditional techniques are *sensitive* to myelin, most lack biological specificity. An area of research pioneered by MacKay et al. and expanded upon over the last 25 years has aimed to develop and apply an advanced MRI framework that exploits the T_2 properties of myelinated tissue to gain information about tissue microstructure (MacKay et al., 1994).

T_2 relaxometry assumes a mono-exponential decay curve – that is, that a single number is sufficient to characterize the properties of all tissue within the voxel. However, due to the architecture of tissue at the sub-millimetre scale, it stands to reason that within one imaging voxel – typically a volume of 1 mm^3 – several cellular environments are found, the relaxation characteristics of which differ. Multi-echo techniques allow the T_2 decay curve to be observed and decomposed into contributions from these different compartments. When applied to the CNS, where one of the distinguishable compartments corresponds to water within the myelin sheath, this technique is termed myelin water imaging (MWI).

II.1.3.2. The three-pool model of tissue

In healthy myelinated tissue, the sampled T_2 decay curve in human brain can be separated into the following components which, when displayed as a histogram (spectrum) of signal intensity versus T_2, appear as follows.

1) A short, fast-relaxing peak at ~40 ms (10-55 ms) attributed to water trapped within the myelin sheath, between the lipid bilayers. In this tightly packed environment, water protons are in close proximity with non-aqueous molecules, e.g. lipids and proteins, and therefore loss of phase coherence occurs faster. The width of this peak is thought to be due to measurement error rather than true biological variation.
2) A long, slow-relaxing component at ~80 ms (70-95 ms), corresponding to water in the cytoplasmic (intracellular) and extracellular spaces. Currently achievable signal-to-noise ratios (SNR) do not allow for distinction between these two biologically distinct environments in the CNS (MacKay et al., 2006).
3) A third component corresponding to CSF ('free water'), around ~2 seconds. This is especially relevant in voxels affected by partial volume effects with CSF. Earlier studies have used a two-pool model, fitting only the two

components above, but the inclusion of this third peak is recommended, as signal contamination by free water can occur in WM, but to a greater extent in DGM and even more so in cortical GM (Whittall et al., 1999).

II.1.3.3. Myelin water imaging using multi-echo T_2 relaxometry

Sampling the T_2 decay curve can be achieved with a CPMG sequence, described above in **II.1.2**. In a CPMG experiment, the acquired signal is characterized by the measured amplitude at each TE. Starting with a TE of 10 ms ensures that only aqueous protons contribute to the signal, since non-aqueous protons (e.g. in lipids) have an extremely fast decay rate (under 1 ms) (MacKay et al., 1994). The T_2 decay curve can be converted to a spectrum of T_2 signal amplitude by T_2 time via nonlinear non-negative least-squares (NNLS) fitting[2] (**Figure II.4**).

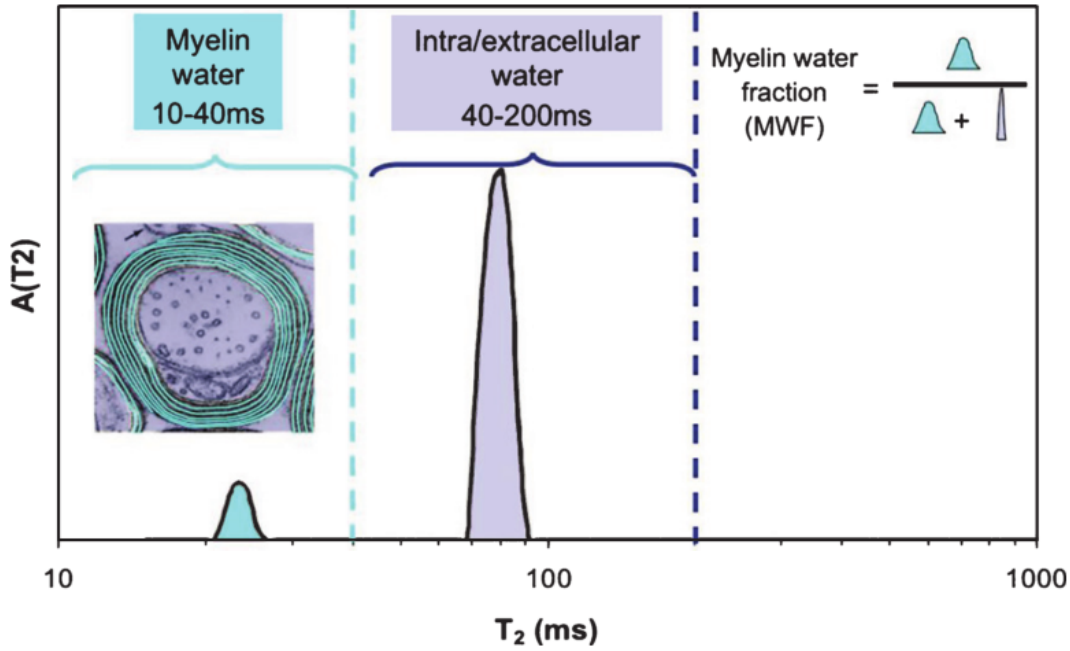

Figure II.4. Spectrum of T_2 distributions from human white matter: amplitude of T_2 signal ($A(T_2)$) by relaxation time (in milliseconds, on a logarithmic scale). The inset (left) shows a 135,000x magnified axonal transection in canine spinal cord for illustrative purposes. In blue are the myelin layers and corresponding 'short' myelin water T_2 component. In purple are the intra/extra-cellular water compartment and corresponding 'long' peak. Source: (MacKay and Laule, 2016).

[2] NNLS is used to find non-negative solutions only, since the parameters to determine are intrinsically null or positive (in this context, signal amplitudes).

This approach operates with the following specification (Whittall et al., 1997):

1) solutions are null or positive;
2) the number of exponential components to be fitted is unspecified;
3) a regularization feature is employed that favours broad peaks and a 'smooth' distribution, which is a better representation of tissue microstructure while being more robust in the presence of noise in the acquired data;
4) no initial guess at the solution is required.

The signal time (T_2 value) is an intrinsic characteristic of each water pool. The fitting procedure does not require peaks to be discrete, and thus defining the area for each component requires cut-off values to be assigned: typically below 50 ms for the short peak, and above 1 second for the long CSF peak (MacKay et al., 2006).

The signal amplitude is proportional to the quantity of water protons with a particular T_2. The sum of all components corresponds to the signal from all mobile protons, and is therefore proportional to the total water content. By normalizing the area of the short myelin-associated peak to the total area under the curve, we get a measure of the proportion of physical space taken by the associated water pool within the voxel. This is the myelin water fraction (MWF). Performing this analysis voxelwise, MWF maps can be obtained.

In healthy WM, the MWF was first estimated at 1.5T to be ~10-15%, an estimate corroborated by *in vitro* studies (MacKay et al., 1994), and 2-6% in GM (Whittall et al., 1997). Calculated MWF values increase with field strength; the reasons for this are not yet fully understood (Kolind et al., 2009a).

II.1.3.4. Available methods for MWI

The original MWI technique was based on a multi-echo spin-echo acquisition, as described above. This experiment was initially performed using a 32-echo CPMG sequence, which produced a single 5-mm thick slice image with in-plane voxel size of 0.86 x 1.7 mm in 25 minutes at 1.5T (Whittall et al., 1997). This technique, referred to as multi-echo T_2 (MET_2), remains the gold standard, although acquisition time is long and thus often limited to single-slice or 2D acquisitions. Prasloski et al. proposed a combined gradient and spin-echo sequence (GRASE) to shorten scan time to under 15 minutes and enable 3D acquisitions (Prasloski et al., 2012b). Moreover, improvements have been made to the original NNLS method, including

correction for imperfect RF pulses (Prasloski et al., 2012a), and spatial regularization to reduce noise and improve measurement consistency while preserving structure (Yoo and Tam, 2013).

More recent techniques have attempted to reduce acquisition times and improve coverage by implementing alternative T_2 curve sampling methods; these are described in a comprehensive comparative review by Alonso-Ortiz et al (Alonso-Ortiz et al., 2015). Some of these methods, such as multi-gradient echo (Hwang et al., 2010) and direct Visualization of Short Transverse relaxation time component (ViSTa) (Oh et al., 2013), are based on quantifying T_2* relaxation to calculate the MWF, which is advantageous in terms of acquisition time and coverage, but comes at the expense of increased vulnerability to additional sources of noise in the decay curve such as motion artefacts, reduced SNR, and inhomogeneity effects.

The MWI technique of interest to the present work is mcDESPOT, which will be described in section **II.2**.

II.1.3.5. Specificity and potential confounds

Here we discuss the specificity and limitations of the MWF as a measure of myelin.

First and foremost, MWI is a direct measurement of myelin *water*, which makes up ~40% of the myelin sheath space (Siegel and Agranoff, 1999) – a 'negative space' measure of the myelin sheath structure of sorts. Therefore, the tenet that probing myelin water is equivalent to measuring the myelin membrane itself is an assumption (Laule et al., 2007a). In addition, several parameters apart from myelin content may affect the MWF, and thus potentially confound interpretation; these are discussed below.

First, the MWF is scaled to total water content, which in the case of pathology may be affected by oedema. Laule et al. proposed a model of different scenarios of oedema, demyelination, and cellular infiltration, and compared these with observed measures of relative water content obtained from MET_2 relaxation data, MWF and volume in MS brain tissue, to determine which scenario was in each case most likely (Laule et al., 2004). This approach can be useful to differentiate between oedema and demyelination when tracking longitudinal changes in MS lesions (Vavasour et al., 2009).

Changes in water content are mainly thought to be a potential confound in pathology, as hydration status has been found not to have an effect on total water content in healthy controls (Meyers et al., 2016). When assessing myelin changes in MS lesions, it has been suggested that the MWF, as a measure affected by the combined influences of increased water content and decreased myelin, still reflects the degree of severity of an inflammatory event (Vargas et al., 2015). Alternatively, normalization using a water phantom, or concurrent absolute water content mapping, can help address this limitation (Meyers et al., 2017).

Looking at T_2 spectra in *ex vivo* animal models of inflammation and demyelination, Stanisz' group characterized the myelin- and IE-water associated peaks under different scenarios, and showed strong associations between MWF and demyelination, while observation of the full spectra (peak positions and widths) could help distinguishing between different biological scenarios (Odrobina et al., 2005; Stanisz et al., 2004). MET_2-derived MWF also proved insensitive to inflammatory-related changes in the NAWM in an animal model of MS (Gareau et al., 2000).

The short T_2 component may reflect signal from myelin debris, as well as intact myelin, indiscriminately. This has been shown in a model of Wallerian degeneration in the rat sciatic nerve (Webb et al., 2003), and using histological myelin staining in a longitudinal study of spinal cord injury in rat (Kozlowski et al., 2008).

II.1.3.6. Validation studies

Despite these limitations, the validity of the MWF as a measure of myelination has been supported by a number of *in* and *ex vivo* human and animal studies, which have shown good qualitative and quantitative correspondence between histological measures of myelin and MWF maps.

Good qualitative and quantitative agreement has been found between measures of myelin (staining, histomorphometry) and MWF in the guinea pig (Stewart et al., 1993) and rat spinal cord (Kozlowski et al., 2008), and in a rat model of PNS primary demyelination (Pun et al., 2005).

Post-mortem MRI validation is also possible in human specimens, as the tissue compartments do not undergo major change after death and fixation, with T_2 times becoming shorter but the decay curves remaining qualitatively similar (Laule et al., 2006). Moore et al. successfully compared a MWF map derived using the previously

described 32-echo CPMG method to myelin staining using Luxol Fast Blue in brain (Moore et al., 2000). This was reproduced by Laule et al. using quantitative comparisons between optical density measures of myelin staining and MWF maps in a series of post-mortem MS brain specimens, across several WM regions and areas of pathology (Laule et al., 2008, 2006).

Studying human neurodevelopment, Deoni et al. found good agreement between MWF maps stratified by age in the first few years of life, and known spatio-temporal patterns of myelination determined histologically (Deoni et al., 2012, 2011).

II.1.3.7. Other methods for *in vivo* myelin imaging

In this section we present a brief overview of other imaging methods for myelin measurement *in vivo*.

The use of diffusion-weighted (DWI) and DTI in research is extremely widespread. DWI offers fast, high-resolution acquisitions and flexible, informative options for visualization of WM tracts. However, despite an active field of research and constant improvements in reconstruction models, it suffers from relatively low biological specificity to WM content. DTI measures reflect myelination in a broad sense, but are affected by tissue architecture (e.g. crossing fibres, fibre orientation coherence), and come with their own lot of artefacts, theoretical problems and implementation issues (Jones et al., 2013). One of the advantages of MWI is not being susceptible to these same confounds (Groeschel et al., 2016; Mädler et al., 2008).

Creation of 'myelin-enhanced contrast' maps has been proposed via combination of T_1 and T_2-weighted conventional scans (Glasser and Van Essen, 2011). However, the specificity of this approach has been disputed, and this ratio was found not to be correlated with the MET_2-derived MWF in cerebral WM (Arshad et al., 2017).

Magnetization transfer ratio (MTR) imaging is based on the relationship and exchange characteristics between 'bound' and free protons, i.e. the ratio of protons bound to macromolecules (e.g. cell membranes, proteins). Although MTR dependence on myelin is strong in WM, the technique has very low specificity and is also influenced by other tissue parameters such as axonal density, inflammation, and oedema (Vavasour et al., 2011). MTR is considered a 'semi-quantitative' technique due to dependence on the choice of acquisition parameters (Mallik et al.,

2014). Quantitative MT measurements are possible, although suffer from the same limitations regarding specificity to myelin (Tozer et al., 2003).

Macromolecular tissue volume (MTV) imaging uses 1 minus PD (as an approximation of water content) to calculate the proportion of a voxel not occupied by water, assumed to be taken up by macromolecules. By combining T_1 measurement with PD mapping, measures of 'macromolecular composition' can be obtained (Mezer et al., 2013). However, the biological specificity of the MTV fraction remains to be determined, and further clinical application studies are warranted to ascertain its utility in representing healthy tissue characteristics and disease states.

Recent work with positron emission tomography (PET) aims at using myelin-binding tracers to quantify and track myelin dynamics *in vivo* with high specificity and precision (Bodini and Stankoff, 2016), although use of PET imaging is hampered by its very high costs and safety profile.

II.2. mcDESPOT

An alternative MWI technique is the multicomponent Driven Equilibrium Single Pulse Observation of T_1 and T_1 (mcDESPOT). In this section, we discuss the theory and implementation of the single- and multi-component DESPOT sequences, their advantages and pitfalls, and present some applications focusing on the study of white matter disease.

II.2.1. Overview

DESPOT1&2 refer to the acquisition and analysis techniques for T_1 and T_2 mapping from spoiled gradient recalled (SPGR) and balanced steady-state free precession (bSSFP) data, respectively. Both were initially developed at 1.5T. Extensions to these methods have been developed to compensate for the artefacts that arise at higher field strength. DESPOT1 with High-Speed Incorporation of RF Field Inhomogeneities (DESPOT1-HIFI) enables correction for imperfect transmit flip angles using an additional inversion recovery-prepared SPGR (IR-SPGR) scan. DESPOT2 with Full Modelling (DESPOT2-FM) makes use of additional bSSFP data collected with a different RF phase cycle to correct for off-resonance effects, using prior information from DESPOT1.

mcDESPOT is a MWI technique that extends these methods using additional data for multi-component analysis. By acquiring a series of spoiled T_1-weighted and T_2-weighted balanced steady-state images over a range of flip angles, the longitudinal and transverse relaxation times T_1 and T_2 can be measured, and the contributions from different water pools within each voxel modelled, including the proportion of signal attributable to myelin water. This allows for voxelwise mapping of T_1, T_2 and MWF.

The DESPOT techniques are summarized in **Table II.1**. A typical processing pipeline for multi-component analysis will involve: DESPOT1-HIFI to obtain T_1, PD and B_1 maps; DESPOT2-FM to obtain an off-resonance (f_0) map; multi-component analysis.

Table II.1. Summary of DESPOT techniques.

Technique	Purpose	Acquisition	Output	Original reference
DESPOT1	T_1 mapping	Dual-angle SPGR	T_1, PD maps	(Deoni et al., 2003)
DESPOT1-HIFI	B_1 correction	DESPOT1, IR-SPGR	B_1 map	(Deoni, 2007)
DESPOT2	T_2 mapping	DESPOT1, dual-angle bSSFP	T_2 map	(Deoni et al., 2003)
DESPOT2-FM	B_0 correction	DESPOT2, multi-angle bSSFP	f_0 map	(Deoni, 2009a)
mcDESPOT	Myelin water imaging	Multi-angle SPGR, multi-angle bSSFP, B_1 and f_0 maps	11 parameter maps; see **II.2.4**	(Deoni et al., 2008a)

B_0: main field. B_1: transmit field. bSSFP: balanced steady-state free precession. DESPOT: Driven Equilibrium Single Pulse Observation of T_1 and T_2. f_0: off-resonance. FM: full modelling. HIFI: high-speed incorporation of radiofrequency field inhomogeneities. mcDESPOT: multi-component DESPOT. PD: proton density.

Below we describe the mcDESPOT acquisition protocol in **II.2.2** and present the single- and multi-component analysis techniques in **II.2.3** and **II.2.4**. Example images of a full mcDESPOT protocol in brain can be seen in **Figure III.3**.

II.2.2. Acquisition protocol

II.2.2.1. Steady-state sequences

Steady-state sequences are gradient echo techniques that take advantage of the relative time scales for T_1 and T_2 relaxation to collect data at high SNR (maximising the magnitude of signal received) within very short TRs and using low flip angles.

'Steady state' refers to an equilibrium state where either transverse, or both transverse and longitudinal magnetization reach a constant magnitude from one TR cycle to the next. A spoiled steady-state sequence only achieves steady state for the longitudinal component, resulting in primarily T_1-weighted contrast, while in 'classic' sequences steady state is reached by both longitudinal and transverse magnetization (Chavhan et al., 2008). Steady-state sequences eliminate the necessity to wait for full longitudinal or transverse relaxation between TR cycles, which reduces acquisition times.

mcDESPOT acquisition in the brain is usually done at a resolution of 1.7 x 1.7 x 1.7 mm^3, for an acquisition time of ~15 minutes. It typically includes 8 SPGR scans at increasing flip angles up to 18°, one IR-SPGR scan for DESPOT1-HIFI, and 8 bSSFP scans across a range of flip angles (e.g. up to 70°) acquired twice with two different RF phase cycles.

The SPGR, IR-SPGR, and bSSFP sequences are described in the next sections.

II.2.2.2. SPGR

SPGR[3] images are a type of T_1-weighted gradient echo scan with short TR (TR < T_2*) in which longitudinal steady state is achieved; this mechanism is described below.

When TR > T_2*, the transverse magnetization M_{xy} will naturally decay between TR cycles. In order to achieve even shorter TR, and to eliminate the need to wait for transverse signal decay, M_{xy} can be spoiled, or eliminated at the end of each cycle. Excitatory RF pulses are used that will give M_{xy} random phases across successive

[3] SPGR scans on GE systems correspond to Fast Low-Angle Shot (FLASH) on Siemens, and Fast Field Echo (FFE) on Philips.

TRs, preventing the build-up of transverse magnetization from one cycle to the next (i.e. preventing transverse steady state) (Chavhan et al., 2009).

A longitudinal steady state occurs when the amount of longitudinal magnetization M_z recovered within a TR cycle is equal to the amount that is excited by the next RF pulse. Since residual M_{xy} is spoiled before the next TR, then the amount of M_z magnetization tipped into the transverse plane in the next cycle will only depend on a constant amount of T_1 recovery. Thus, after each excitation pulse, the measured signal is a function of T_1, TR, flip angle, and spin density M_0 (equivalent to PD) (Chang et al., 2008).

In DESPOT sequences, two or more SPGR images are acquired with short TR (< 10 ms) and TE, both parameters being kept constant, and varying flip angles.

II.2.2.3. IR-SPGR

An IR-SPGR scan with identical TR/TE as the SPGR can be acquired as part of the DESPOT1-HIFI method. A brief explanation of IR sequences has been given in **II.1.2,** and the DESPOT1-HIFI method for B_1 correction is described below in **II.2.3**.

A TI of 450 ms is currently used in most protocols. This value is optimized in terms of accuracy and precision for the T_1 of human tissue T_1 (on the order of 1 second),. Since the transmit field B_1+ should follow a smooth variation across the imaged volume, this scan can be collected at lower resolution than the SPGR and bSSFP to speed up acquisition (Deoni, 2007).

II.2.2.4. bSSFP

In SSFP sequences, both longitudinal and transverse magnetization reach dynamic equilibrium. Free precession refers to the state in which, when TR << T_2, the induced, naturally decaying signal and the echo signal overlap, i.e. the transverse signal never fully dephases.

A special case of SSFP sequence is balanced (or 'fully refocussed') SSFP[4]. A bSSFP sequence uses the same principle as an SPGR acquisition, i.e. using a train of RF pulses and with TR < T_2. Instead of spoiling the transverse magnetization, fully refocusing gradients are used for slice-encoding, phase-encoding, and readout. With all gradients remaining constant, effectively cancelling themselves out within one TR, M_z and M_{xy} hold constant magnitude across repeated cycles. Thus, both longitudinal and transverse magnetization can achieve steady state, and signal intensity is dependent on relaxation times and acquisition parameters.

At high field strength, acquisition of bSSFP images will be subject to off-resonance effects caused by inhomogeneities in the main field. In these areas, local B_0 inhomogeneity will cause the precession phase in the transverse plane to be slightly offset with regards to readout, resulting in decreased signal. These 'banding' artefacts tend to occur in areas near air/tissue interfaces: in the brain, above the sinuses and in temporal lobe areas.

To remedy this, two bSSFP acquisitions can be collected with different RF phase cycle patterns (often 0° and 180°), resulting in identical scans except for the areas of signal loss occurring in non-overlapping areas of the imaged structure (Deoni, 2009a). The off-resonance correction scheme using these data is described in **II.2.3**.

II.2.3. T_1 and T_2 mapping with single-component DESPOT

II.2.3.1. DESPOT1&2

DESPOT1 is a VFA-based T_1 mapping method (see **II.1.2**) that uses SPGR data as described in **II.2.2**. By keeping TR/TE constant and only varying the flip angle, the SPGR signal equation can be linearized so that only two data points are required to find PD and T_1 (Deoni et al., 2003; Homer and Beevers, 1985).

DESPOT2 relies on a similar principle. In the absence of off-resonance artefacts, the bSSFP signal equation can be transformed to a linear expression. By keeping flip angle and TR constant, creating longitudinal and transverse steady states thus creating signal dependence on both T_1 and T_2, and using PD and T_1 information

[4] bSSFP sequences are implemented as FIESTA on GE, TrueFISP on Siemens, and balanced Fast Field Echo (bFFE) on Philips systems.

acquired with DESPOT1, the signal equation can be resolved and T_2 estimated. DESPOT2 is possible from only two bSSFP flip angles, but additional scans allow nonlinear fitting and hence greater accuracy (Deoni et al., 2003).

The DESPOT algorithms were originally developed at 1.5T. At higher field strength, several problems arise with regards to image quality. Correction schemes have been proposed that involve additional acquisitions and offline analysis, which are described below. The only implementations of the technique at 7T so far have been preclinical (Hurley et al., 2010; Wood et al., 2013, 2016).

II.2.3.2. DESPOT1-HIFI

Imperfections in the transmitted RF field, as well as dielectric effects in tissue (interference of the body's composition on RF wavelengths) lead to discrepancies between the flip angle that is prescribed, and what it actually is across the imaged volume. Deviations of ± 10% will have a significant effect on MWF estimation (Deoni, 2011). A solution for this is transmit field (B_1+ or simply B_1) mapping: calculating the difference between nominal and actual flip angle, which can be used to provide the algorithm with the correct flip angles in post-processing.

B_1 mapping can be achieved via a separate, stand-alone sequence; some of these include actual flip angle (AFI) and Bloch-Siegert methods, that come at the expense of an additional sequence (McRobbie et al., 2006).

DESPOT1-HIFI was developed as an extension of the DESPOT1 method and only requires an additional IR-SPGR scan. The IR-SPGR inversion pulse is adiabatic, meaning that it is intrinsically insensitive to B_1 inhomogeneity. The IR-SPGR signal equation is determined by TR, the prescribed and actual flip angles, PD and T_1. Therefore, using both the SPGR and IR-SPGR data, a simultaneous fit for the three parameters PD, T_1, and B_1 can be achieved via least squares fitting (Deoni, 2007).

DESPOT1-HIFI yields a B_1 map that describes the actual transmitted flip angle as a fraction of the prescribed flip angle (e.g. from ~0.8 to ~1.2). Some degree of smoothing (e.g. Gaussian or median filtering) may be used, as the B_1 field is expected to show smooth variation across the acquired volume.

II.2.3.3. DESPOT2-FM

As seen in **II.2.2**, areas of decreased signal intensity (banding) can arise in bSSFP scans due to main field inhomogeneity. Using maximum intensity projection to correct the images themselves is possible, but not optimal, and leads to inaccurate T_2 values, with no increase in SNR. A correction scheme using alternating phase cycles across the chosen range of flip angles, in an interleaved fashion, was initially proposed but also proved insufficient at high field strength (Deoni et al., 2004).

The currently used method, DESPOT2-FM, requires the acquisition of two series of bSSFP scans, with at least two flip angles each, identical parameters but different phase-cycling schemes (see **II.2.2**). With prior calculation of T_1 and B_1 with DESPOT1-HIFI, it enables T_2 and off-resonance (f_0, in Hertz) fitting. The bSSFP scans can be normalized voxelwise to their mean across flip angles and phase-cycling patterns, which eliminates the need for PD to be included as an additional parameter. A region contraction approach was initially proposed (Deoni, 2009a), but subsequent implementations have used nonlinear least-squares fitting.

II.2.4. Myelin water imaging with mcDESPOT

II.2.4.1. Overview

DESPOT1&2 perform single-component analysis, relying on the assumption that the relaxation times measured in a voxel arise from tissue with homogeneous properties (Deoni et al., 2008a). Here, we present the mcDESPOT approach to multi-component relaxometry.

The multi-compartment characteristics of tissue in the CNS, and the principles behind MWI have been described in **II.1.3**. As seen therein, resolving the T_2 signal into contributions from different compartments requires plotting the T_2 decay curve. This cannot be achieved with bSSFP data only, since signal also includes T_1-weighting. Moreover, T_1 recovery is known to be multi-exponential, albeit at a time scale that is hard to probe due to fast exchange. Therefore, untangling the contributions of T_1 and inter-compartment exchange on the T_2 curve also requires multi-angle SPGR data. A B_1 map can be used to calibrate acquired flip angles, and a f_0 map computed from phase-cycled bSSFP data can be included as an additional parameter (Deoni, 2011).

Multi-angle SPGR and bSSFP acquisitions, the single-component methods for relaxation time mapping, and the accompanying correction schemes for high-field implementation have been described in **II.2.2** and **II.2.3**. In this section we describe the unique algorithm and the three-pool biophysical model of tissue used in mcDESPOT analysis, the advantages and drawbacks of this approach for MWI, and provide some example applications.

II.2.4.2. Stochastic Region Contraction

Least-squares methods belong to the category of local optimization curve-fitting strategies. In the context of mcDESPOT analysis, for the multiple-parameter estimation problem at hand, we run the risk of having the algorithm converge at a local optimum: one set of solutions that satisfies the algorithm's requirements for stopping the search, that may be the best set within close range of the starting point, but not necessarily the 'true' solution.

On the other hand, global optimization methods look for solutions within a predefined search-space[5], and converge to find the best of all possible solutions – the global optimum. In the present case, some parameters have a wide range of possible values – especially the slow and fast-relaxing species' respective residence times, since less is known about the possible values these parameters can take in human tissue. This would make the use of a global optimization method prohibitively computationally expensive (Deoni et al., 2008a).

A first proposed approach for mcDESPOT analysis was based on a genetic algorithm (Deoni et al., 2008a). In this framework, pairs of possible solutions were chosen based on their residuals, combined to create new solutions, and tested against the data. Local optimization was then used to refine the 'surviving' solutions before the next step. However, this approach came with extremely taxing computing demands (Deoni, 2011).

After the above as well as traditional fitting approaches proved inappropriate to resolve the complex combination of parameters in multi-angle SPGR and bSSFP data, Deoni et al. proposed an innovative solution that is a hybrid of the above

[5] The search-space refers to the ensemble of possible solutions for each parameter, delimited by user-defined limits or 'bounds'.

optimization methods (Deoni et al., 2008a). They used an iterative stochastic region contraction (SRC) algorithm that tests sets of solutions, which converge from random priors within constrained, biologically plausible ranges, to the optimal solution for each parameter. The use of this algorithm is a first in neuroimaging research since its original implementation in acoustic signal processing (Berger and Silverman, 1991).

It was designed to maintain the speed of local search methods, while retaining the power of global optimization methods to deal with large starting ranges for parameter estimates, and to operate regardless of initial guesses. The initial bounds for each parameter can be adjusted depending on considerations of time, computational power, and expectations regarding the underlying biology, informed by the literature as well as known relationships between parameters[6].

The algorithm follows the following steps (Deoni, 2011).

1) 5000 random combinations are picked from a uniform distribution within the chosen starting bounds.
2) Theoretical SPGR and bSSFP data are created and compared against real data using least-squares fitting. The sum-of-squares residuals are calculated cumulatively across all images.
3) The 50 solutions with the smallest residuals are kept. The search-space is narrowed by using the minimum and maximum value for each parameter within these top solutions.
4) Steps 2 and 3 are repeated, choosing 5000 new combinations within the contracted search-space and testing them against real data, ranking them, and contracting the search-space before a new iteration. The new 5000 selections were initially random, but the use of a Gaussian distribution from the top solutions (the minimum and maximum of which having defined the search-space) was subsequently proposed. Each contracted search-space is slightly expanded by a factor of 0.02 (one 50^{th}) to prevent discarding the true solution should it lie at the very 'edge' of a parameter search-space (Deoni and Kolind, 2015).

[6] These include: the three compartmental volume fractions adding up to one; f_{IE} comprising at least 5% of total volume; logical ordering of T_1 and T_2 compartmental values (myelin < IE < CSF).

5) The process repeats 6-8 times, or until each parameter converges to a unique solution on its own (convergence being defined as successive solutions lying within 0.5-1% of each other). The number of repetitions may be increased for enhanced precision, at the cost of longer computational time.

II.2.4.3. The three-pool model in mcDESPOT

The first version of the algorithm involved a two-pool model, only modelling the IE and myelin water components, resulting in a six-dimensional problem: T_1 and T_2 for each of the two compartments, residence time and volume fraction of the short myelin-associated component.

However, as seen in **II.1.3,** a long T_2 component is known to exist in voxels with partial volume (i.e. neighbouring meningeal or ventricular CSF), and has also been observed in abnormal WM in MS and phenylketonuria (Laule et al., 2007b). A three-pool model was therefore proposed that incorporated bulk 'free' water, comprising two exchanging pools, and a third non-exchanging one (see **Figure II.5**) which is therefore thought to be more appropriate in CSF-adjacent areas or in pathology (Deoni et al., 2013). Using a statistical model selection approach, performance of the three-pool model was found similar to that of the two-pool model in tissue and superior in PVE voxels as well as globally on a voxelwise basis (Deoni et al., 2013).

Thus, for each of the three compartments, the T_1, T_2, and volume fraction are estimated, as well as residence time, adding up to **nine free parameters** which are described below.

- The **T_1 and T_2 of each of the three compartments**. Of particular interest, an increase in the T_2 of the IE compartment (IET_2) has been linked with inflammation in animal peripheral nerve (Odrobina et al., 2005; Stanisz et al., 2004). Abnormalities in this parameter have been observed in both amyotrophic and progressive lateral sclerosis groups (Kolind et al., 2013). It has been suggested that intra- and extra-axonal water pools may have different characteristics, however these are not readily resolved using current acquisition and analysis strategies (Deoni and Kolind, 2015).

- The **myelin water fraction** (f_M[7]). Description, validation and potential confounds for this parameter are found in **II.1.3**. The **IE water fraction** (f_{IE}) is directly estimated in a three-pool model, otherwise it is simply defined as 1 – f_M.
- The **residence time of the fast-relaxing component** (τ_m), expressed in time units (or the inverse of the exchange rate). This parameter models the time spent by water in the myelin-associated pool before moving to the IE environment (see section on exchange below).

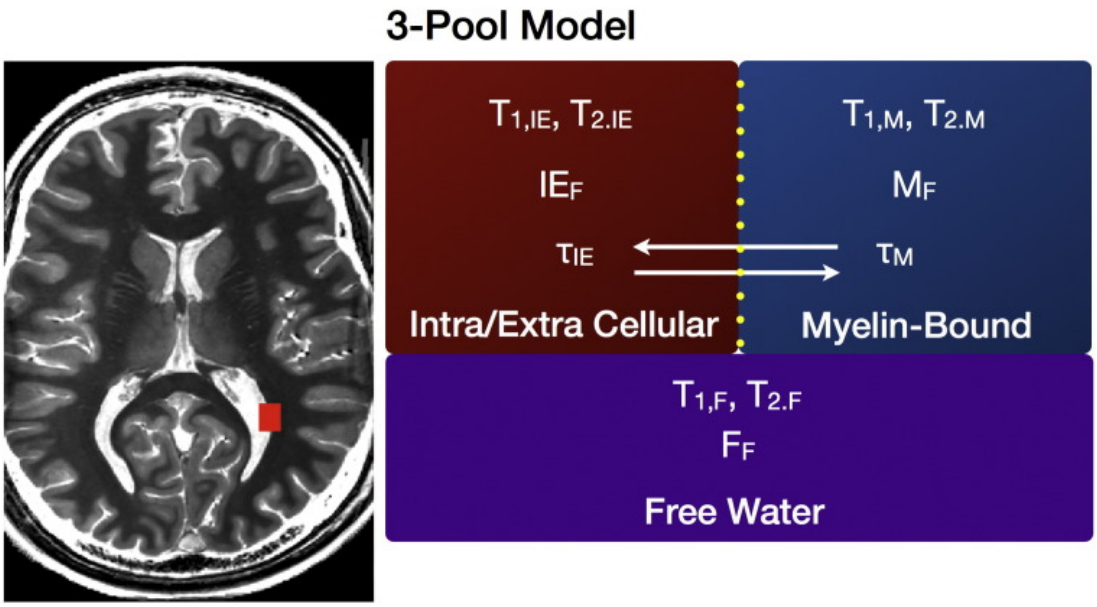

Figure II.5. Schema of the three-pool model of compartmental relaxation in human brain. In the case of tissue that includes 'free' water, as is the case in the ventricle-adjacent voxel depicted here (red box), three compartments are found each having different T_1, T_2, and volume fraction. The vertical yellow dotted line represents membrane permeability between the intra/extra-cellular (IE) and myelin (M) pools, with corresponding residence times (τ). Source: (Deoni et al., 2012).

[7] The myelin water fraction derived from various techniques is referred to in the literature as: MWF, MVF (myelin volume fraction), VF_m (volume fraction of myelin water), M_f or f_M (fraction of myelin water), etc. In an effort to differentiate between different methods, in this work we reserve the abbreviation MWF for MET_2-based methods, and refer to the mcDESPOT-derived myelin water fraction as f_M.

Parameters not directly estimated by the model are:

- The **CSF water fraction** (f_{CSF}) is the proportion of 'free' water in the voxel, computed as $1 – (f_{IE} + f_M)$.
- As in DESPOT2-FM, the need to fit for **PD** is eliminated by normalizing both the SPGR and bSSFP data to their means across flip angles.
- $\mathbf{B_1}$ is calculated a priori using DESPOT1**-**HIFI, and used to calibrate transmitted flip angles.
- $\mathbf{f_0}$ can be supplied a priori using the scheme described in **II.2.3**, or estimated within the model.

II.2.4.4. Effect of water exchange

Exchange refers to the motion of water molecules between compartments, exchange time being the inverse of the residence time.

Animal experiments have shown a potentially negligible role of exchange, but in human tissue and especially in pathological cases, it is likely to have an impact (Deoni et al., 2008a). Slow exchange will have a negligible effect on the relaxation of either compartment, and can thus be omitted (Deoni et al., 2008a). In human neural tissue, it is estimated between 100-500 ms, and may therefore be a confound on the timescale of MET_2 measurements. Fast exchange will lead to lower MWF, since water protons may move away from the myelin-associated environment and into another compartment before full transverse relaxation has taken place (Bydder et al., 2012).

Exchange is a heterogeneous, variable, poorly characterized parameter influenced by a number of factors including temperature (although this is only relevant *ex vivo*), cell biology, and pathology (Deoni and Kolind, 2015). Accounting for exchange is one of the strengths of the mcDESPOT approach: exchange between the IE and myelin water compartments is explicitly modelled, and its influence on f_M is minimized (Kolind and Deoni, 2011). Exchange between CSF and tissue water is prevented by the blood-brain barrier, although this may be untrue in cases of breakdown due to pathology; this is not accounted for in current models (Deoni et al., 2013).

Reductions in myelin residence time (τ_m) have been seen in preclinical studies, and a few preliminary observations exist in humans. A possible interpretation of short τ_m

is a thinning of the myelin sheath, which has been observed in the rat spinal cord using MET_2-based MWI (Dortch et al., 2013; Dula et al., 2010; Harkins et al., 2012). Average τ_m in WM was markedly reduced in a mildly disabled MS patient compared to four healthy controls in Deoni and Rutt's original mcDESPOT experiment, using a two-pool model (Deoni et al., 2008a). It was reduced in a small sample of MS patients with chronic neuropathic pain compared with matched pain-free patients (Kolind et al., 2009b), and may be increased in the corpus callosum of MS and NMOSD patients compared with healthy controls (Lee et al., 2017). The biological specificity of this parameter may warrant further investigation.

II.2.4.5. Algorithm stability

In the original two-pool model, estimate precision was found to increase with higher SNR, f_M, and longer residence time, possibly due to these characteristics making the signal curves more distinct from those that would characterize a single-exponential relaxation (Deoni et al., 2008a).

The precision of the two-pool model under unconstrained vs. constrained conditions (i.e. provision of initial boundaries for each parameter) has been questioned (Lankford and Does, 2013). However, these authors used a wholly or partially unconstrained approach, leaving all parameters (or all but the transverse relaxation times and τ_M) free to adopt any value regardless of biological plausibility, which is not usually done in practice.

The three-pool model was found to have high accuracy using simulations on a numerical phantom representing different realistic values of f_M and f_{CSF}, and under realistic noise conditions (less than 10% error, i.e. comparable or superior accuracy to the two-pool model). Iterated results tended to follow a Gaussian distribution around the 'true' solution, meaning that convergence operates consistently around the global optimum (Deoni and Kolind, 2015).

Using this model, good precision and accuracy were achieved in simulations under a range of priors (Deoni and Kolind, 2015). As with the two-pool model, accuracy increased with f_M values. When numerical phantom characteristics were manipulated to represent different biological environments, such as cases of axonal swelling or inflammation, bias in f_M estimation ranged from negligible (1% error) to moderate (11.5%). It was shown that f_M estimation depends most on accurate compartmental T_2 times measurement, a problem inherent to all MWI techniques.

Careful consideration is required to reach a compromise between constraining the search-space to increase precision, and choosing priors broad enough to encompass the true solution.

II.2.4.6. Advantages and critiques

f_M values derived from mcDESPOT have been found consistently higher than those from MET_2 experiments, even with a three-pool model. Inadequate B_1 and B_0 correction schemes will both result in f_M overestimation (Deoni, 2011), as will magnetization transfer (MT).

MT effects (i.e. the transfer of magnetization from macromolecule-bound to 'free' water protons, influencing MR signal) are known to occur with the use of short RF pulses, which are used to induce steady state in the bSSFP scans. These effects may influence the SPGR and bSSFP signal equations, and lead to a loss of accuracy and precision in T_1/T_2 measurement (Deoni et al., 2008a).

Zhang et al. (J. Zhang et al., 2015) showed the presence of MT effects in bSSFP, which manifested as loss of signal amplitude, especially in WM which has a higher macromolecular content than GM. However, the effect on two-pool-model-derived f_M values was minimal when compared to a modified mcDESPOT protocol that used longer RF pulses. Instead, MT effects manifested via other parameters (IET_1 and τ_M). This investigation however used very large starting bounds for f_M, as well as a two-pool model, and so results should be interpreted with caution.

Advantages of mcDESPOT over other techniques include its three-dimensional nature and complete coverage of the brain or cervical cord in feasible times (e.g. ~14 minutes for a whole-head acquisition). Another advantage is the simultaneous calculation of other parameters with potential biological relevance, as described above.

II.2.4.7. Preclinical and clinical applications

Applications of T_1 and T_2 mapping using single-component DESPOT are described in **III.5.3**.

Preliminary investigations in animal models have shown the feasibility of mcDESPOT at ultra-high field, and good qualitative agreement between histological

measures of myelin and f_M maps in a canine (Hurley et al., 2010) and a rat model of demyelination (Wood et al., 2016). These projects are so far the only published histological validation studies on mcDESPOT.

mcDESPOT has been used in large-scale cohort studies of neurodevelopment to study developmental patterns of myelination ((Croteau-Chonka et al., 2016; Deoni et al., 2016, 2012; O'Muircheartaigh et al., 2014); list not exhaustive), using a version that trades in longer scan time for lower noise and specific absorption rate levels (Deoni et al., 2011) as well as age-specific protocols customized for time, field of view, acquisition parameters in relation to expected relaxation values in each age group in the first 5 years of life (Deoni et al., 2012). Other applications of the protocol have been to characterize group differences in neurological diseases such as Parkinson's disease (Dean et al., 2016), amyotrophic and primary lateral sclerosis using f_M and IET_2 (Kolind et al., 2013), disorders involving dysmyelination such as schizophrenia (Flynn et al., 2003), and developmental conditions like autism (Deoni et al., 2015). It has also been suggested to hold promise in the study of traumatic brain injury (Jurick et al., 2016). In MS, mcDESPOT has been used to reveal abnormalities of myelin content using atlas-based approaches discriminating between MS subtypes and disability levels (Kitzler et al., 2012; Kolind et al., 2012), and related to functional indices in primary progressive MS (Kolind et al., 2015b). Applications in NMOSD are few, but will be mentioned in **Chapter IV**. The protocol has also been successfully implemented in the cervical spinal cord (Kolind and Deoni, 2011), which will be discussed in **Chapter V**.

Part 2: Multiple sclerosis and neuromyelitis optica spectrum disorder

Herein we provide a brief introduction to multiple sclerosis and neuromyelitis optica spectrum disorder, focusing on the concepts of disease progression and the contributions of advanced quantitative magnetic resonance imaging to the study of these conditions.

II.3. Multiple sclerosis 53

II.3.1. Clinical and epidemiological features 53

II.3.2. Diagnosis 53

II.3.3. Disease course and subtypes 54

II.3.4. Pathophysiology 56

II.3.5. Conventional MRI findings in MS 59

II.3.6. Role of advanced MRI in MS 61

II.4. Neuromyelitis optica spectrum disorder 63

II.4.1. Clinical and epidemiological features 63

II.4.2. The NMO spectrum 63

II.4.3. Differential diagnosis 65

II.4.4. Disease course and progression 65

II.4.5. Pathophysiology 67

II.4.6. Conventional MRI findings in NMOSD 68

II.3. Multiple sclerosis

II.3.1. Clinical and epidemiological features

Multiple sclerosis (MS) is a chronic demyelinating disease of the central nervous system (CNS). It is one of the most prevalent neurological disease in the Western world, and a leading cause of disability in young adults (Compston and Coles, 2008). The hallmark of MS is the presence of demyelinating lesions (or 'plaques') in the brain and spinal cord, that 'wax and wane' as new pathology appears, forming MRI-visible scars (sclerosis). MS most often presents with a highly variable clinical course, with periods of clinical quiescence interspersed with flare-ups or attacks that cause a wide range of motor, sensory, and cognitive symptoms. As a 'young adult' disease, with an average age at onset of 34 years and an often unpredictable evolution at the individual level (Compston et al., 2005), it has heavy impact at the individual, familial, and socio-economic level (Giovannoni et al., 2016).

MS affects women more frequently than men, at a ratio of 2:1 or higher. Onset occurs most frequently between 20 and 50 years, although paediatric and older-onset cases exist. A number of environmental factors have been linked with MS, although causal relationships have yet to be established. These factors include, but are not limited to: a family history of autoimmune disease, exposure to viral agents, smoking, vitamin D intake during childhood mediated by sun exposure (leading to an intriguing trend on the geographical distribution of disease prevalence by latitude). Epidemiological and genetic studies have revealed that gene-environment interactions may be at play, and that the aetiology of the disease is likely multifactorial and complex (Ramagopalan et al., 2010).

II.3.2. Diagnosis

A diagnosis of MS is made according to the revised McDonald criteria (McDonald et al., 2001; Polman et al., 2011), often on the basis of a clinical event "consistent with CNS demyelination" (Traboulsee et al., 2005).

These criteria can be summed up by the shorthand of 'dissemination in time and space', which refers to the evolving nature of MS pathology. **Dissemination in time** is the occurrence of at least two distinct episodes of CNS damage, suggestive of a relapsing course, which can be identified prospectively or retrospectively. In the latter case, this can be done via collection of clinical history, or from a single imaging exam: in some cases, the appearance of lesions at various stages. The

observation of enhancing and non-enhancing lesions simultaneously can point to the occurrence of previous episodes, and may constitute sufficient evidence to establish dissemination in time. **Dissemination in space** requires the identification of T_2-hyperintense lesions at two of four CNS locations typical of MS: periventricular, juxtacortical and infratentorial regions, and the spinal cord (Filippi et al., 2016). The exclusion of other conditions is required (Polman et al., 2011).

Diagnosis can be made on clinical grounds only, although a neurological assessment can be supplemented by imaging or laboratory exams, (Noseworthy et al., 2000). MRI is crucial to an easier, faster diagnosis (Rovira et al., 2015), and repeat exams are recommended (Polman et al., 2011).

II.3.3. Disease course and subtypes

The concepts of relapses and disease progression are central to MS diagnosis and management.

A **relapse** (or attack, flare-up, episode) is defined as a clinical episode of neurological dysfunction lasting at least 24 hours and not attributable to fever or infection (Polman et al., 2011).

Disease progression is defined clinically as a gradual increase in symptoms that do not recede during remission (Lublin and Reingold, 1996). In the context of clinical trials, disability progression is typically assessed via changes in score on a global measure of disability, such as the Expanded Disability Status Scale (EDSS) (Kurtzke, 1983).

MS is stratified into the following diagnostic categories (Compston et al., 2005; Lublin et al., 2014).

- **Radiologically isolated syndrome** (RIS) refers to the (often incidental) identification of an MRI profile suggestive of MS in the absence of overt symptoms, i.e. a clinically silent episode. **Clinically isolated syndrome** (CIS) refers to the occurrence of a single attack that does not fulfil all diagnostic criteria, namely evidence for the dissemination of symptoms in time. In a large-scale retrospective database study, Okuda et al. found that 34% of RIS patients presented with a clinical event within 5 years (Okuda et al., 2014). Progression of RIS into CIS as patients become symptomatic is

therefore frequent, as is subsequent conversion from CIS to a definite diagnosis of MS (Polman et al., 2011).

- **Relapsing-remitting MS** (RRMS) is the most frequent form of the disease, which 85% of patients are initially diagnosed with (Compston et al., 2005). The disease course is characterized by periods of remission interspersed with unpredictable relapses. MRI activity occurs even between attacks, but may be clinically silent (Noseworthy et al., 2000).
- **Secondary progressive MS** (SPMS) occurs when RRMS patients enter a progressive phase of the disease, with or without 'superimposed' relapses. In one prospective, single-centre, observational study, conversion occurred in 18.1% patients at a median disease duration of 16.8 years, translating to a risk of conversion of 6.4% 10 years after disease onset. Age at onset, male sex, and disease duration were found to increase risk of conversion from RRMS to SPMS. In this actively treated cohort, risk estimates were more favourable than previously assessed in natural history studies (Cree et al., 2016).
- Around 15% of patients have an initial diagnosis of **primary progressive MS** (PPMS), typically characterised by a progressive course from onset, and the steady accumulation of pathology and disability over time. A diagnosis of PPMS requires the observation of disease progression over a period of months. An estimated one-third of this patient group will also present with superimposed relapses (Wolinsky and the PROMiSe Study Group, 2003) – previously the 'progressive relapsing' phenotype, now described as 'active PPMS'. Between 12-16% present with Gadolinium-enhancing lesions on MRI at a given time (Wolinsky et al., 2007; Wolinsky and the PROMiSe Trial Study Group, 2004).

Of note, this classification system is continually being questioned. It has been hypothesized that these phenotypes only represent different configurations or stages of the same disease process. SPMS and PPMS would then be the same disease entity, on the basis of indistinguishable imaging and pathological characteristics other than clinical course and symptomatology. In the case of PPMS, successful functional compensation would effectively mask the relapsing stage, and disease progression would manifest only when these resources are exhausted, giving the illusion of a progressive course from onset (Absinta et al., 2016; Ransohoff et al., 2015). Whether PPMS is a pathologically distinct variant of MS, or should be considered as part of the spectrum of progressive MS disease is

therefore a matter of debate, although the latter is generally regarded as more likely (Antel et al., 2012).

Recent consensus guidelines have also proposed to characterize disease as active/inactive (occurrence of relapses), with/without worsening (confirmed incomplete recovery from relapse-related disability), and with/without progression (see above definition) in addition to classification into a subtype, to better represent the heterogeneity of clinical presentations even within each subtype (Lublin et al., 2014).

II.3.4. Pathophysiology

MS is thought to be an inflammatory, immune-mediated disease (Lassmann, 2014), although its pathophysiological mechanisms are complex, and its aetiology still considered uncertain.

The two main components of MS pathology are inflammation and neurodegeneration. In the typical course of the disease, inflammatory activity comes and goes, while neurodegeneration is ongoing. Over time, the inflammatory activity and accompanying relapses become less frequent, while neurodegeneration and clinical worsening become gradual and constant (**Figure II.6**).

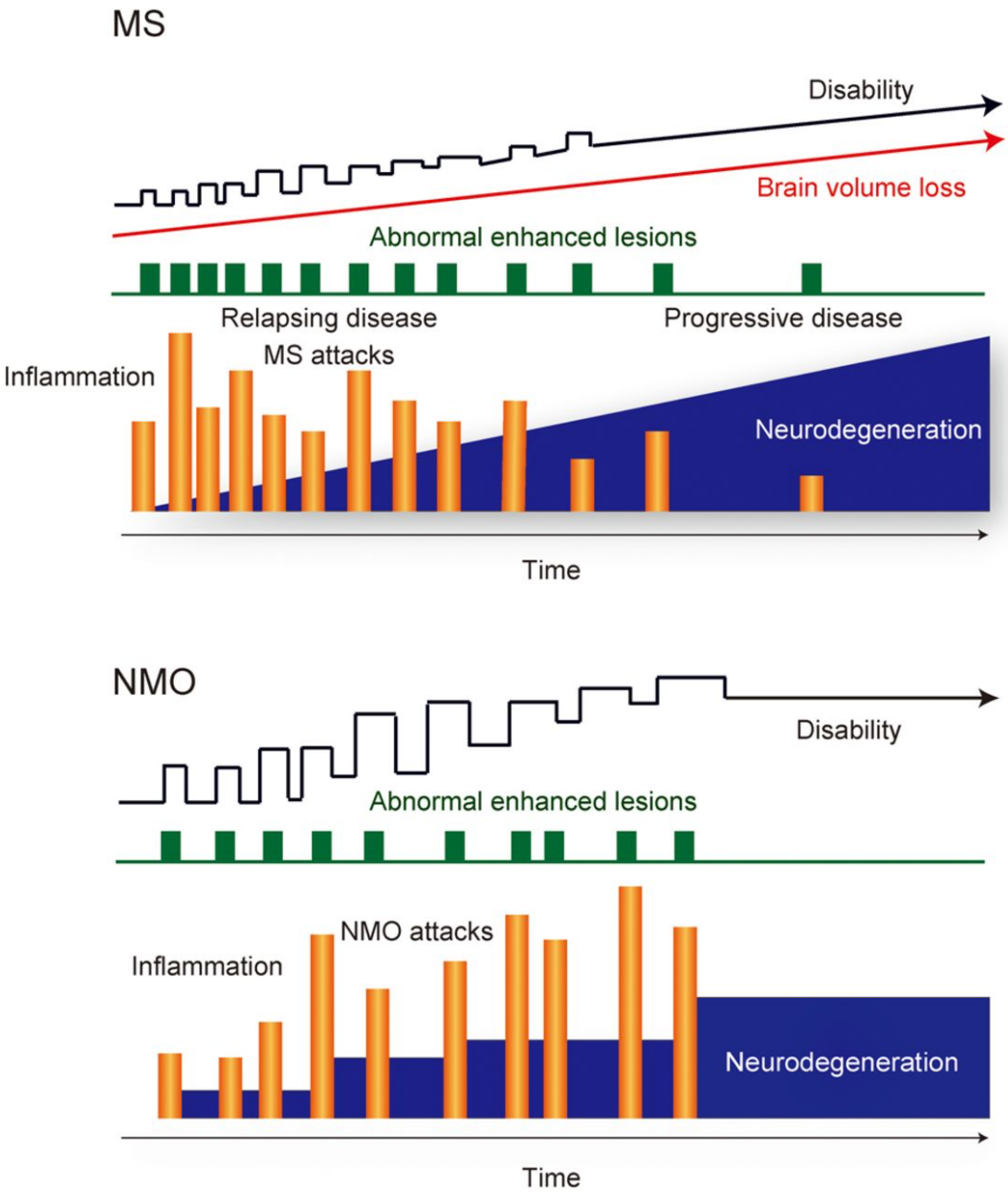

Figure II.6. Schema of the course of disease progression in MS and NMO. MS: multiple sclerosis. NMO: neuromyelitis optica. Source: (Kawachi and Lassmann, 2017).

During an MS attack, infiltration of inflammatory agents through a weakened blood-brain barrier causes oedema (influx of fluid in the extracellular space) and tissue damage. Different mechanisms of lesion formation via oligodendrocyte and/or myelin injury have been identified using post-mortem histology (Lucchinetti et al., 1996). These appeared consistent within subjects, suggesting the possibility of different immunological profiles culminating in a common manifestation (Lucchinetti et al., 2000).

In addition to demyelination, tissue injury in MS involves axonal loss within and outside lesions due to Wallerian degeneration, and neuronal loss causing brain and spinal cord atrophy. Oligodendrocyte depletion may contribute to demyelination through loss of support to the myelin sheath and impaired remyelination, while astrogliosis (reactive proliferation of astrocytes) and astrocytic scarring can prevent neuronal regrowth (Miller, 2002).

During remission, resolution of oedema, reorganization of sodium channels on axons, and remyelination may play a role in restoring function following an attack (Trapp and Nave, 2008), although cortical reorganisation is more likely to be a major factor in maintaining function (Frohman et al., 2005).

In the consensus theory of MS pathogenesis, repeated inflammation causes severe axonal damage, and eventually exhausts the compensation reserves of the CNS, at which point a neurodegenerative process starts occurring with or without continuing relapses – the progressive phase of the disease (Duncan and Radcliff, 2016).

An opposing view purports that recurring inflammation could be a consequence, and not the cause, of neurodegeneration (Nave, 2010). Progressive disease would be the ‘true’ disease process, and neurodegeneration the primary component of MS pathology, with a possible superimposed secondary component: an “aberrant” immune response causing relapses (Stys et al., 2012).

Genetic variants conferring increased risk for MS are consistent with an autoimmune aetiology, and neuropathological studies have found evidence for the presence of cortical inflammation predating signs of neurodegeneration early in the disease course – evidence for it occurring “on a background of inflammation” (Ransohoff et al., 2015). The observation that neurodegeneration dies down as inflammatory activity subsides in the progressive phase also supports inflammation as the driving factor (Frischer et al., 2009). MS as a primarily autoimmune disease, with a secondary neurodegenerative component, therefore remains the prevailing theory.

Knowing this and with the idea that preventing damage is easier than repairing it, recent education initiatives have stressed the importance of early treatment under the banner of “time is brain”, suggesting an aggressive approach to treatment (Giovannoni et al., 2016; Ransohoff et al., 2015).

II.3.5. Conventional MRI findings in MS

MRI is not required for MS diagnosis, but can serve to greatly increase confidence; allow for more criteria to be assessed using a single exam; and enable ruling out other pathology. It can serve to establish dissemination in space according to known criteria of location and, in some cases, dissemination in time by observing old in addition to acute lesions. Further along in the disease course, atrophy can also be assessed (Traboulsee et al., 2005).

The hallmark appearance of a brain affected by MS is multiple lesions in the WM. Typical sites of focal pathology include the temporal lobes, periventricular areas, brainstem, cerebellum, and juxtacortical areas (involving U-shaped association fibres) (Compston et al., 2005). Cortical and deep grey matter (GM) involvement (basal ganglia, thalamus) is less common (Fox, 2008); GM pathology in MS will be further discussed in **Chapter IV**.

The following sequences are part of a 'typical' brain MRI exam for MS; we describe the most often-seen features of the disease in this context. These different contrasts are shown in **Error! Reference source not found.**.

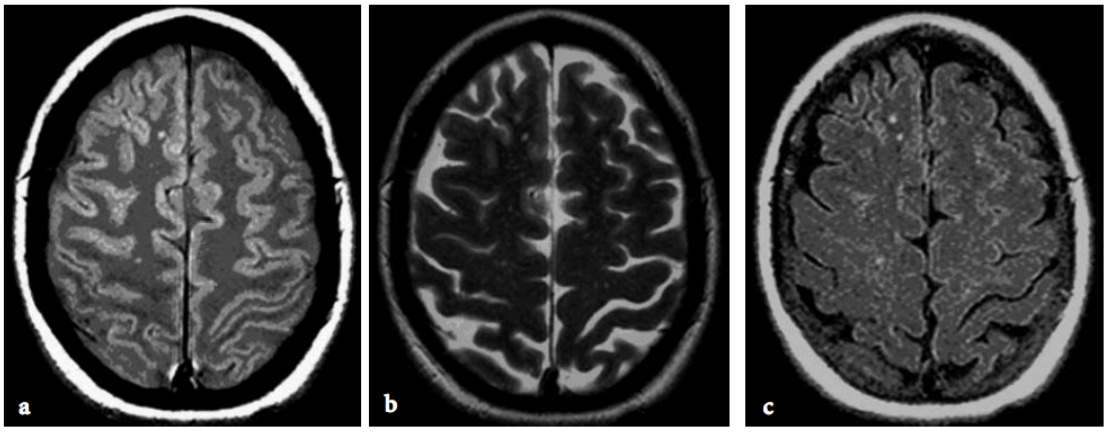

Figure II.7. Conventional MRI scans used in the radiological assessment of MS. a) Proton density, b) T_2-weighted, and c) FLAIR scans showing small hyperintense white matter lesions. Source: (Traboulsee et al., 2005).

Lesions may be seen on PD and T_2-weighted (fast) spin-echo scans. For improved visualization of periventricular, juxtacortical and cortical lesions, fluid-attenuated inversion recovery (FLAIR) scans are used to suppress signal from the adjacent CSF. The bright appearance of lesions on these scans is due to the increase in

water content typical of MS lesions, which leads to lengthened T_1 and T_2 relaxation times (Traboulsee et al., 2005). Typical 'T_2 lesions' have a round or ovoid shape, and vary in size; T_2 lesion load is highly heterogeneous across subjects, and non-normally distributed in a given sample (Traboulsee et al., 2005). Areas of predilection include periventricular regions, and especially the corpus callosum (CC). Callosal lesions tend to spread radially from the inner ventricular surface of the CC towards the surrounding WM, in a pattern known as Dawson's fingers that is best seen on sagittal scans (Fox, 2008).

Gadolinium (Gd)-enhancing lesions appear on T_1-weighted scans after injection of a contrast agent. Common enhancement patterns include an ovoid, homogeneous appearance with clearly-defined borders (nodular lesion), and a 'ring' shape with a hyperintense border and T_1-hypointense center. Although complete or partial ring enhancement is not exclusive to MS, 'open-ring' lesions are a specific sign of demyelination (Davis et al., 2010). Enhancement signifies blood-brain barrier disruption, and therefore areas of acute inflammation, and occurs on the time-scale of weeks. However, not all new lesions are enhancing, and old lesions can 'reactivate' (Martino et al., 2002). The detection of enhancing lesions can also be dependent on the technical details of contrast injection and image acquisition. After initial enhancement, lesions usually shrink and leave a T_2-visible scar (Traboulsee et al., 2005).

Diffuse, T_2-hyperintense pathology extending outside of focal lesions denotes diffusely-abnormal WM (formerly known as 'dirty-appearing WM'). These areas appear as large, periventricular lesions with poorly defined boundaries. They are underpinned by myelin pathology, mild axonal damage and gliosis, to an intermediate degree between healthy and lesioned tissue (Laule et al., 2011), which may be consistent with Wallerian degeneration (Seewann et al., 2009).

T_1-hypointense areas are suggestive of tissue destruction, and can underlie lesions that are currently enhancing (acute), resolving, or chronic. Concurrent T_1-hypointensity of a T_2 lesion is indicative of greater axonal loss (Traboulsee et al., 2005). T_1-hypointensity is more specific than T_2 contrast when differentiating lesions with different degrees of remyelination (Barkhof et al., 2003). T_1 'black holes', indicating severe tissue damage, are more often seen in the cerebrum than the posterior fossa and spinal cord (Fox, 2008).

Spinal cord pathology occurs in 80-90% of MS patients, with frequent involvement of the cervical cord. In RRMS, multiple T_2-hyperintense focal lesions are often seen.

Plaques most often appear in the cervical portion of the cord, often less than two segments in length, most often located in the dorsal and lateral WM and occupying under half of the cord area. Swelling and Gd-enhancement are commonly seen in the acute stage (Lycklama et al., 2003). Cord involvement in MS is further discussed in **Chapter V**.

II.3.6. Role of advanced MRI in MS

Biomarkers are, in general, measures that reflect a specific biological or pathological process, and can serve to improve diagnosis confidence, inform prognosis, study disease mechanisms or monitor treatment effects.

In MS specifically, MRI plays a crucial role in disease diagnosis, monitoring, and evaluation of treatment outcomes. The conventional MRI methods described in the previous section form part of a routine MRI exam in the clinical setting. The wide array of advanced MRI methods available have been applied to the study of MS; however, due to factors like cost and lack of standardisation in acquisition and analysis protocols, the use of these methods in the clinical setting is limited. At this stage, the benefits of advanced MRI for improving diagnosis of individual cases, guide treatment decisions, or inform prognosis is limited, and will require to be ascertained via prospective studies (Rovira et al., 2015), and these methods have yet to see widespread use in the clinic.

Validation of biomarkers requires establishing adequate sensitivity, specificity, and reliability, and superiority against existing measures (e.g. in terms of statistical power). Established biomarkers can be used as surrogate endpoints in clinical trials if indicative of, and correlated with clinical indices (Bielekova and Martin, 2004). In MS, evidence of disease activity using lesion-based measures can be detected 5 to 10 times more frequently than relapse rate (Filippi and Agosta, 2010), but lesion load correlates poorly with clinical symptoms and outcome. A reduction in whole-brain volume, or an increased atrophy rate, correlates more strongly with clinical outcomes, but is difficult to interpret; atrophy represents the end result of several processes, including axonal and myelin loss, tissue shrinkage due to gliosis (Traboulsee et al., 2005), and changes in water content (Miller, 2002).

Currently, lesion load (T_2-hyperintense and Gd-enhancing lesions) and cerebral atrophy can serve as primary endpoints in phase 2 clinical trials in MS, and are used as secondary outcome measures in phase 3 trials. In the latter, clinical

measures, i.e. EDSS and relapse rate measures, are used as the primary endpoints (Cohen et al., 2012; van Munster and Uitdehaag, 2017).

Development of MRI biomarkers for MS has been impeded by the fact that correlations between conventional MRI metrics and clinical status in MS are notoriously moderate at best. This discrepancy is termed the 'clinico-radiological paradox': the gap between MRI-visible disease activity and the burden of symptoms displayed by a patient at the individual level (Barkhof, 2002). Several reasons for this can be invoked.

First, standard MRI measures may lack the specificity required to isolate the pathological processes that affect clinical status (e.g. lesion load without consideration of lesion location; cerebral atrophy representing the end-point outcome of several long-term pathological processes). As many as 9 out of 10 cerebral lesions may be asymptomatic (Traboulsee et al., 2005); conversely, currently used clinical tools may not reflect all aspects of neurological dysfunction. Lesions in broadly functional regions may lead to more subtle manifestations than, for instance, impairment of autonomic or motor functions, or compensatory mechanisms may work to preserve function even in the presence of increasing pathology. Spinal cord measures are not always considered, despite most clinical tools being heavily geared towards locomotor dysfunction (van Munster and Uitdehaag, 2017).

This phenomenon highlights the importance of advanced MRI methods for understanding pathology *in vivo*, with greater biological specificity (Filippi and Agosta, 2010); increasing efficiency of clinical trials (i.e. assessing treatment effects over a shorter time period and/or with smaller sample sizes) (Traboulsee et al., 2005); and probing diffuse, MRI-occult changes in the normal-appearing tissue, a concept central to the pathology of MS (Filippi et al., 2012). Region-specific volume measurements, cervical spinal cord area, DTI and magnetization transfer ratio-based measures have been proposed as the main candidates for translation into the clinical setting (van Munster and Uitdehaag, 2017). From a research perspective, the wide array of available advanced MRI methods has been extensively applied in the study of MS, and has brought to light important features of the disease, including the role of axonal damage in disease progression, the nature and extent of cortical pathology, and the role of brain plasticity in compensating structural damage (Frohman et al., 2005). In particular, due to myelin pathology being central to the

disease, the development of *in vivo* myelin quantification methods has gone hand in hand with their application to MS research.

II.4. Neuromyelitis optica spectrum disorder

II.4.1. Clinical and epidemiological features

Neuromyelitis optica (NMO), previously called Devic's disease, is an inflammatory disorder of the CNS characterised by autoimmune attacks against the optic nerves and spinal cord, leading to severe disability. Previously considered a rare, severe variant of MS, emerging imaging and laboratory features have helped define it as a separate relapsing disease.

The prevalence of NMO is estimated at 1 to 3/100,000 (Etemadifar et al., 2015). It is especially prevalent in non-Caucasian populations (Wingerchuk et al., 2006), and has a female:male ratio of over 3:1, greater than in MS (Wingerchuk, 2009). The proportion of NMO to other demyelinating disorders cases is much higher in Japan than elsewhere, making it one of the most prevalent neuroimmunological disorders in Asia (Uzawa et al., 2014).

Disease onset is typically in the late 30's, slightly older than MS, although childhood, adolescence and later-onset cases also occur. While familial cases have been reported in Japanese populations, NMO is currently considered a sporadic disease (Wingerchuk, 2004). The coexistence of autoimmune disorders (e.g. type 1 diabetes, coeliac disease, etc.), or family history thereof among patients is very common, generally preceding disease onset (Wingerchuk et al., 2007a).

The main features of the disease are optic neuritis (ON), i.e. uni- or bilateral inflammation of the optic nerves, and longitudinally extensive transverse myelitis (LETM), i.e. inflammation of the spinal cord extending across 3 or more vertebral levels. A typical NMO case features episodic, severe bouts of LETM and/or ON. While brain involvement was previously thought to be minimal, standard and advanced MRI techniques have shown a distinct pattern of cerebral pathology that may aid differential diagnosis.

II.4.2. The NMO spectrum

According to its initial stringent definition as a monophasic disorder, NMO was diagnosed on the basis of simultaneous attacks of bilateral ON and acute myelitis

(Wingerchuk et al., 1999). The definition has now been broadened to encompass cases that present with index events of ON and myelitis that can occur weeks or years apart (Weinshenker, 2003). While exclusion of non-optic-spinal CNS symptoms used to be a requirement, significant brain involvement has now been demonstrated.

NMO immunoglobulin G (IgG) is a an autoantibody that targets aquaporin-4 (AQP4), a water channel protein found on astrocyte cell membranes; elevated levels in the blood serum are associated with NMO (Lennon et al., 2005, 2004). Its high specificity for NMO was brought to light in 2004 and 2005 by a Mayo Clinic group (ibid), and has greatly helped differentiate NMO from other conditions with similar clinical and imaging presentations.

Serological testing offers excellent specificity for clinically defined NMO (91%) – with few false positives, as 'classic' MS cases consistently test seronegative – while sensitivity varies depending on the method (48-77%) (Jarius et al., 2007; Waters et al., 2012; Wingerchuk et al., 2007a). Detection of NMO-IgG can predate fulfilment of all necessary clinical criteria, enabling earlier detection and treatment. NMO-IgG testing is especially useful in non-clinically-definite cases, such as presenting with bilateral or severe ON that may benefit from attentive follow-up or early intervention (Marignier et al., 2008).

Description of NMO as a disease entity fully distinct from MS has been a central theme of research over the last 15 years, albeit complicated by the heterogeneity in clinical presentations (Weinshenker and Wingerchuk, 2014). Around 70% of patients who fulfil NMOSD criteria test seropositive (Wingerchuk and Weinshenker, 2017). Following improvements in serological assays, and knowing that serostatus can change over time or be confounded by the effects of immunosuppressive treatment (Jarius et al., 2008a), it has been suggested that with careful re-testing, NMO-IgG can be detected in up to 88% of diagnosed cases (Jiao et al., 2013). However, the prevalence of seronegative cases remains confounding with regards to defining NMO as a homogeneous disease entity, with uniform presentation and consistent pathogenic mechanisms.

NMO has come to be considered as a spectrum of disorders not limited to the prototypical cases, with clinical presentation, imaging and serological tests coming together to aid diagnosis at the individual level (Wingerchuk et al., 2007a, 2006). Recent consensus guidelines proposed to merge the concepts of NMO and NMO spectrum disorders under the umbrella designation of NMOSD, and to redefine the

diagnostic guidelines accordingly, with different criteria incorporating the known heterogeneity in clinical presentation, seropositivity, and imaging findings (Wingerchuk et al., 2015). Serostatus is a central feature, and diagnosis is based on fulfilment of several clinical and MRI criteria that include ON and acute myelitis, as well as a characteristic brain MRI profile, including area postrema, brainstem or diencephalic syndromes (see **II.4.6**).

II.4.3. Differential diagnosis

Misdiagnosis of NMOSD as MS remains an issue, and was among the main focus points in the 2010 revisions to the McDonald diagnostic criteria (Polman et al., 2011). NMOSD is now recognised as following a relapsing course in most cases, and thus can 'mimic' the course of MS; anecdotal evidence reports patients having been misdiagnosed for upwards of 20 years (Braksick et al., 2014). Notwithstanding the obvious ethical and psychological considerations of an erroneous diagnosis (Mutch et al., 2014), early intervention is crucial in NMO, as clinical deterioration during attacks is faster than in MS (over the course of days or weeks), and intervention has been linked with improved prognosis (Pittock and Lucchinetti, 2016). Moreover, immunomodulatory treatments used in MS are ineffective in preventing NMO relapses, and can even be harmful; negative effects of MS disease-modifying therapies on NMO patients have been reported (Sato et al., 2012; Solomon et al., 2012), including in seronegative patients (Kitley et al., 2014a). In Asia, where the prevalence of MS is lower, the diagnosis of an opticospinal form of MS was frequent, and the question of whether these patient groups may overlap a matter of debate (Weinshenker, 2008). The current recommendation is that these are the same disease entity and that Asian 'opticospinal MS' belongs to the NMO spectrum (Wingerchuk et al., 2015).

II.4.4. Disease course and progression

A monophasic course is found in 10-20% of cases (Wingerchuk et al., 2007a), and defined as the quasi-simultaneous occurrence of the index events (i.e. ON and acute myelitis) over days or weeks, with moderate recovery but no subsequent attacks. However, relapses are possible even after a decade (Collongues et al., 2011), and thus cases of 'purely' monophasic NMOSD rare – a delay of at least 5 years has been recommended before this designation is made (Wingerchuk et al.,

2015). These patients present with an equal gender prevalence, are generally younger at onset than those with a relapsing course, and a lower percentage present with the AQP4 antibody (Ketelslegers et al., 2011; Waters and Vincent, 2008). Compared to the relapsing form, blindness and paraplegia following index events are more common, and recovery in motor scores and visual acuity is poorer; however, despite a poorer short-term prognosis, long-term recovery and survival rates are higher (Wingerchuk et al., 2007a).

The more common relapsing course (80-90% of cases (Wingerchuk et al., 2007a)) is associated with the female sex, an older age at onset compared to the monophasic form, a longer interval between index events and the presence of systemic autoimmunity, followed within a few years by clusters of severe relapses affecting the optic nerves and spinal cord. These patients often experience periods of quiescence; attacks, when they occur, may be grouped in bursts over months or years. According to one study, the first relapse after index events occurred within 1 year in 55% of patients, and within 5 years in 90% (Wingerchuk et al., 1999).

The following negative prognostic factors have been identified: older age at onset, high relapse rate in the first year after diagnosis, severity of the first attack and subsequent poor recovery, and high number of brain lesions (Kitley et al., 2012; Uzawa et al., 2014; Wingerchuk and Weinshenker, 2003). Non-white populations generally have a worse prognosis (Collongues et al., 2011; Kitley et al., 2012). In a predominantly non-white cohort from the French West Indies, clinical predictors of death included a higher relapse rate during the first year, blindness or sphincter symptoms at onset, and lack of recovery after the first attack (Collongues et al., 2011). In addition, the seasonal variation seen in the course of MS (with an increase in the risk of relapse in the summer) is not seen in NMOSD (Uzawa et al., 2014). Women undertaking pregnancy also face a higher relapse rate within the year after delivery, in contrast with the known protective effects of pregnancy in MS (Uzawa et al., 2014).

Around half of patients show severe visual defects or motor impairment within 5 years after onset (Uzawa et al., 2014); death from respiratory failure is a common occurrence (Wingerchuk et al., 1999). Although patients following a monophasic course suffer greater impairment following attacks, their long-term prognosis is overall better with regards to visual acuity, motor and sensory functions; relapsing patients generally experience permanent disability in these areas (Wingerchuk et al., 1999).

In MS, disease progression is defined as the gradual accumulation of neurological impairment, with or without the presence of relapses (Lublin and Reingold, 1996). Wingerchuk and colleagues define a secondary progressive course in NMOSD as “continuous, unremitting deterioration” in clinically-assessed visual, motor or sensory function over a 6-month period (Wingerchuk et al., 2007b). A secondary phase is extremely rare in NMOSD, and cases may even be absent from large population-based studies (Aboul-Enein et al., 2013; Cabre et al., 2009; Collongues et al., 2014, 2010), despite the fact that the rate and severity of attacks is more pronounced, and the median age of onset older, which are both predictive factors for conversion to the progressive phase in MS (Wingerchuk et al., 2007b).

Changes in NMO-IgG status may also inform the clinical course. It is known that initially seronegative patients may become positive upon retesting, although whether this is due to a genuine change in serostatus, limits in the detection thresholds of the assays used, or confounding factors at the time of testing is unknown (Jiao et al., 2013).

Fixed impairment in MS is mostly caused by the progressive phase, whereas in NMOSD, residual deficits from more frequent and severe relapses are responsible for the accruement of disability in a ‘stepwise’ manner (Collongues et al., 2011; Wingerchuk et al., 2007a). The EDSS is frequently used in NMOSD to assess disease progression. Its limitations in terms of instrument variability, clinical information content, and construct validity are well-document when applied to MS (van Munster and Uitdehaag, 2017). Its limitations in assessing the scope of clinical impairment in NMOSD have also been noted (Collongues et al., 2011; Wingerchuk et al., 2007b).

II.4.5. Pathophysiology

NMO is an immune-mediated astrocytopathy. The target of immune attacks is the AQP4 protein, found on astrocyte cell membranes, which regulates water exchange in the CNS (Lucchinetti et al., 2014). Regions of high AQP4 expression include the spinal cord, optic nerves especially in posterior regions, and cerebral periventricular areas, in line with the preferential and severe inflammation of these areas in NMOSD (Pittock et al., 2006b).

Current evidence suggests that NMO-IgG is produced peripherally, enters the CNS secondarily, and that other antibodies may be at the root of the observed BBB

disruption (Jacob et al., 2013). Peripheral administration of the antibody to mice fails to create an animal model of the disease, while intra-cerebral injection, or peripheral injection after induced BBB breakdown, does cause an ensemble of symptoms similar to the NMOSD phenotype (Bradl et al., 2009; Saadoun et al., 2010).

In NMOSD, autoimmune attacks on the AQP4 water channels lead to disruption of water homeostasis in the CNS, although the underlying mechanisms remain to be fully described (Jarius et al., 2008b; Ransohoff, 2012). Inflammation, water retention, oedema, necrosis and demyelination occur in areas where AQP4 expression is reduced or lost (Hinson et al., 2012). Demyelination in NMOSD is thought to be a secondary process, with astrocytes being the primary targets of autoimmune attacks (Takano et al., 2010). A possible pathway is that astrocyte dysfunction causes lack of support to oligodendrocytes, which in turn fail to support myelin (Marignier et al., 2010). Demyelination as a secondary phenomenon may also be due to retrograde or anterograde degeneration following neuronal loss (Rocca et al., 2004b).

Neuropathological examinations of NMOSD brains have shown extensive cortical neuronal loss and astrogliosis, but no evidence of cortical lesions, and normal AQP4 and myelin distributions in the cortex. This selective sparing may be due to structural and functional differences between WM and cortical GM characteristics regarding BBB permeability, or local differences in AQP4 expression that may lead to a different immune response in cortical regions (Popescu et al., 2010).

Immunosuppressive treatment is usually prescribed to prevent relapses (Mealy et al., 2014), and plasma exchange to modulate the humoral response associated with attacks, stunt lesion development and neurological damage (Bonnan and Cabre, 2011).

II.4.6. Conventional MRI findings in NMOSD

Neurological examination and structural brain and spine MRI are routine in the clinical assessment of NMOSD. The standard MRI sequences used in MS diagnosis have been described in **II.3.5**.

Although limited involvement or sparing of the brain is not uncommon in NMOSD, definition of a characteristic brain MRI profile has been made possible by advances in imaging techniques and the recognition of the NMO spectrum. Since a normal brain MRI is extremely rare in RRMS (around 1% of patients (Wingerchuk et al.,

1999)), a normal-seeming exam can help distinguish the two diseases. It is now accepted that around 50-60% of NMOSD patients show cerebral lesions, with 6-10% displaying an 'MS-like' profile on MRI (Bichuetti et al., 2008a; Blanc et al., 2008; Chan et al., 2011; Pittock et al., 2006a). Lesion load is typically greater in MS than in NMOSD (Matthews et al., 2013), although NMOSD patients may tend to have a more symmetric distribution pattern (Ito et al., 2009). In addition to qualitative assessment of lesion type and distribution (Juryńczyk et al., 2016), quantitative probability mapping has shown potential to inform differentiation between MS and NMOSD cases (Kister et al., 2013a; Matthews et al., 2013).

In NMOSD, cerebral lesions are often extensive, with a blurry appearance, of heterogeneous intensity, and frequently follow the distribution of AQP4 channels around the third and fourth ventricles and cerebral aqueduct, involving the thalamus and hypothalamus, corpus callosum, and brainstem, with a predilection for the dorsal surface adjoining the fourth ventricle (Barnett et al., 2014; Cabrera-Gomez and Kister, 2012; Chan et al., 2011). The absence of cortical lesions, confirmed at ultra-high field, is considered specific to NMOSD and also helps distinguish it from MS (Calabrese et al., 2012; Kister et al., 2013b; Popescu et al., 2010; Sinnecker et al., 2012). Deep GM involvement in NMOSD will be further discussed in **Chapter IV**.

Hemispheric WM lesions are only seen in 30-50% of patients. Large, confluent lesions with a 'spilled ink' appearance or a 'spindle-like' shape, following along WM tracts, are frequent (see **Figure II.8-B**) (Barnett et al., 2014). The temporary accumulation of water due to AQP4 channels disruption has been suggested as a possible cause for the large, diffuse and often 'vanishing' lesions observed (Cabrera-Gomez and Kister, 2012; Nakamura et al., 2009; Pittock et al., 2006a). In case of tumefactive, demyelinating lesions, the absence of Gd-enhancement may be more specific for seropositive NMOSD than MS (Ikeda et al., 2011).
Corticospinal tract lesions are another characteristic MRI finding; these can be uni- or bilateral, are often extensive and follow the pyramidal tracts, via the posterior limb of the internal capsule and the cerebral peduncle (Kim et al., 2010).

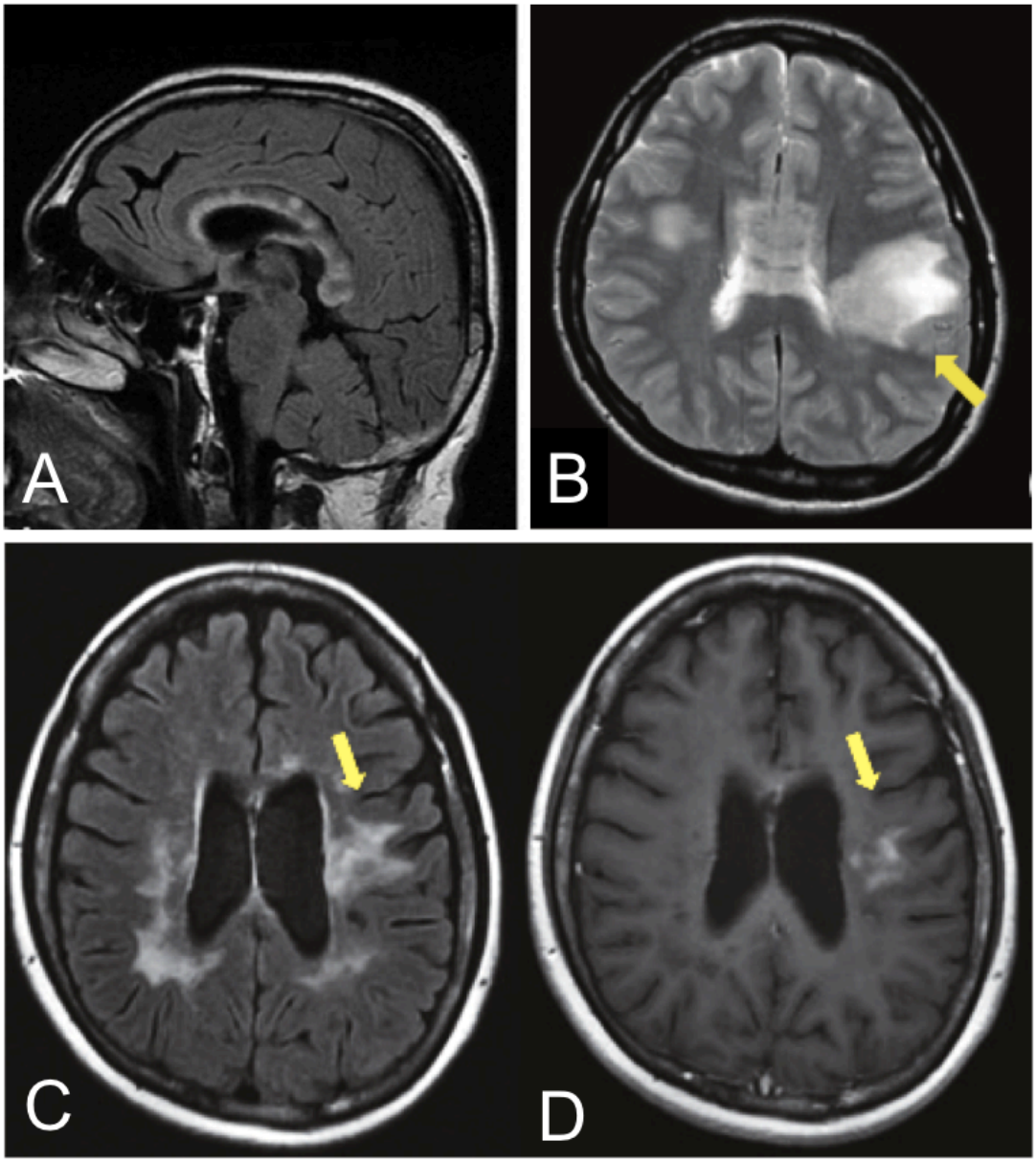

Figure II.8. Examples of brain lesions in neuromyelitis optica spectrum disorder. **A**: Acute, heterogeneous, "fluffy" lesions in the corpus callosum on a FLAIR scan. **B**: Lesions with a "spilled ink" appearance along the white matter tracts on a diffusion-weighted scan, suggestive of vasogenic oedema. **C, D**: FLAIR (left) and Gadolinium-enhanced T_1-weighted (right) scans showing large, extensive hemispheric lesions with typical patchy enhancement pattern and blurred margins. Sources: A: (Barnett et al., 2014); B, C, D: (Kim et al., 2012).

While callosal involvement is also frequently seen in MS, the appearance of lesions in this area differentiates the two conditions. A 'marbled pattern' in the corpus callosum is a typical feature of NMOSD, formed by a number of smaller lesions in close proximity and of varying intensities (see **Figure II.8-A**) (Nakamura et al., 2009; Pittock et al., 2006b). Another possible presentation consists in lesions lining the

lateral ventricles, and involving the entire thickness of the splenium in a typical ‘arch bridge’ pattern (Kim et al., 2012, 2010).

Non-specific T_2 lesions “in dots or patches” are frequent in the subcortical or deep WM, brainstem and cerebellum (Kim et al., 2015). Cystic lesions, or T_1-hypointense areas with the aforementioned ‘black hole’ appearance, are also seen (Ito et al., 2009). NMOSD lesions tend to be more destructive compared to MS plaques, with possible destruction of all cellular compartments, including axons, in addition to demyelination (Misu et al., 2013). At 7T, small, T_2-hyperintense WM lesions were observed to have different characteristics from typical MS lesions: not restricted to venules, and without a hypointense edge (Kister et al., 2013b; Sinnecker et al., 2012).

Gd-enhancing lesions may appear during the acute stage, and remain as areas of T_1-hypointensity or disappear entirely upon follow-up, suggesting heterogeneity in the underlying pathological processes (Cabrera-Gomez and Kister, 2012). Overall, Gd-enhancement is rare. The most prominent and specific feature is a ‘cloud-like’, patchy enhancement pattern, caused by multiple adjacent lesions with blurred margins (see **Figure II.8-C&D**). This pattern can be seen in 90% of patients with positive contrast enhancement, and it has been suggested it can differentiate between MS and NMOSD patients almost perfectly (Ito et al., 2009). Linear enhancement of the lining of the latera ventricles, in a ‘pencil-like’ shape, is also seen (Kim et al., 2015).

Lesions can be clinically silent (Kim et al., 2016a), or result only in ‘subtle’ symptoms that may resolve in periods of quiescence (Pittock et al., 2006a). New lesions do not seem to develop between relapses (Matthews et al., 2015), but asymptomatic lesions may appear during ON or myelitis attacks (Kim et al., 2016a). Brainstem lesions are common, associated with NMO-IgG seropositivity, and frequently result in multiple clinical symptoms (Barnett et al., 2014). Medullary lesions, mainly affecting the central GM and contiguous with upper cervical lesions, are associated with intractable hiccups and nausea (Cabrera-Gomez and Kister, 2012). Hypothalamic lesions are common to both NMOSD and MS (Ito et al., 2009), may be linked with narcolepsy-like hypersomnia and behavioural changes (Barnett et al., 2014; Pittock et al., 2006b; Viegas et al., 2009), and appear independently of other parenchymal lesions (Poppe et al., 2005). Lesions in the frontal, parietal and occipital lobes have been linked with cognitive impairment (Barnett et al., 2014). Other clinical symptoms linked with focal pathology may include trigeminal

neuralgia, vertigo, dysphagia, aphasia, hemiparesis, ataxia, facial weakness or sensory loss (Asgari et al., 2013b).

In the spinal cord, the main feature is the presence of LETM, defined as a transverse inflammatory lesion extending over at least 3 vertebral segments. Cord lesions in NMO can be located in the upper thoracic region or more frequently in the cervical cord, and may be contiguous with the brainstem (Asgari et al., 2013b; Cassinotto et al., 2009). Typical lesions have an irregular appearance, with bright, spotty T_2 hyperintensity and the same “patchy” enhancement pattern that occurs in the brain, and can stretch over 4-7 segments (Nakamura et al., 2008). As these are rarely seen in MS, and visible on conventional MRI, lesion type and length are useful in differentiating the two (Krampla et al., 2009).

The central GM is frequently involved in the acute stage (Nakamura et al., 2008), in contrast with preferential involvement of the dorsal and lateral WM in MS. Characteristic MRI findings include central T_2-hyperintensity of the cord, visible on axial scans. Ring enhancement is commonly seen in NMOSD cord lesions (in about a third of patients that present with cord involvement), although this can also occur in MS, albeit more rarely (Zalewski et al., 2016). T_1-hypointensity, necrosis and cavity formation are other features seen in NMOSD not typical of MS (Barnett et al., 2014; Cassinotto et al., 2009; Nakamura et al., 2008).

Despite LETM being the most specific MRI finding in adults with NMOSD, ‘short’ TM, defined as a T_2-hyperintense lesion extending less than 3 vertebral segments, can also arise. During a first episode of myelitis, 14-14.5% of NMOSD patients present with short TM as opposed to LETM, whether or not myelitis is the heralding manifestation of the disease (Flanagan et al., 2015; Huh et al., 2017). A first myelitis episode presenting with short TM is most commonly followed by the occurrence of LETM. Because this presentation is atypical in NMOSD, and more commonly seen in MS, it can lead to delays in diagnosis and treatment (Flanagan et al., 2015).

Moreover, lesion length is known to evolve over time, and thus appearance at the time of a single MRI may not suffice to classify the lesion as short or longitudinally extensive TM. Cord swelling can occur during the acute phase, and lesions can grow over a period of days (Asgari et al., 2013a). Lesions can subsequently be broken down following treatment with steroids, resolve into multiple shorter lesions during remission (Asgari et al., 2013b; Cassinotto et al., 2009), or disappear entirely on conventional imaging (Collongues et al., 2011). Cord atrophy is frequent and

severe, especially focally at sites of previous lesions; the patterns of atrophy particular to NMOSD will be discussed in **Chapter V**.

Chapter III. Intra-scanner reliability of mcDESPOT in healthy older adults

In this chapter we present a single-site study on the test-retest reliability of several quantitative metrics (myelin water fraction, and longitudinal and transverse relaxation times) derived from a mcDESPOT protocol, in healthy adults aged over 50 years old at three time points over one month.

Disclaimer: This study made use of the National Institute for Health Research (NIHR) Wellcome Trust King's Clinical Research Facility (CRF) MRI scanning facilities. The views expressed are those of the authors and not necessarily those of the UK National Health Service (NHS), the NIHR or the UK Department of Health.

III.1. Introduction 75

III.2. Background 76

III.2.1. Concept of reliability 76

III.2.2. Previous work 78

III.2.3. Choice of sample 81

III.3. Methods 81

III.3.1. Acquisition 81

Study design 81

MRI acquisition 82

III.3.2. Analysis 83

III.3.2.1. Preprocessing 83

III.3.2.2. Creating maps 84

III.3.2.3. Post-processing 84

III.3.3. Reliability assessment 86

Overview 86

Coefficient of variation 86

Intraclass correlation coefficient 87

III.4. Results 88

III.4.1. Example data 88

III.4.2. Absolute measurements 91

III.4.3. Voxelwise reliability 91

Histograms 91

Coefficient of variation maps 92
III.4.4. ROI-specific reliability 92
III.5. Discussion 99
III.5.1. Reliability of T_1 99
III.5.2. Reliability of T_2 99
III.5.3. Applications of T_1 and T_2 mapping 100
III.5.4. Reliability of f_M 101
III.5.5. Generalizability to other populations 101
III.6. Conclusion 102
III.7. Additional information 102

III.1. Introduction

Multicomponent Driven Equilibrium Single Pulse Observation of T_1 and T_2 (mcDESPOT) is a relaxometry-based technique that allows whole-brain, voxel-wise determination of several quantitative parameters related to tissue microstructure, including the longitudinal and transverse relaxation times T_1 and T_2, and the myelin water fraction (f_M). As a quantitative method yielding biologically stable and putatively platform-independent values, assessment of reproducibility is paramount. In this chapter we investigate the intra-scanner reliability of several parameters output by mcDESPOT[8] at 3 Tesla (T). We present results from a scan-rescan study in healthy adults between 50 and 75 years old at three time points on a single 3T scanner, using intraclass correlation coefficient (ICC) and coefficient of variation (CV) measures to assess within-subject reliability at the voxel and region of interest (ROI) level for T_1, T_2 and f_M.

[8] mcDESPOT technically refers to the multicomponent acquisition and processing technique. Here we use mcDESPOT to refer to the complete protocol from which both single-and multicomponent analyses can be carried out, using the appropriate corrections schemes for high-field acquisitions: High-Speed Incorporation of RF Field Inhomogeneities (HIFI) (Deoni, 2007) and the Full Modelling (FM) extension to DESPOT2 (Deoni, 2009a).

III.2. Background

III.2.1. Concept of reliability

In research concerned with quality assurance of magnetic resonance imaging (MRI) measurements, the following terms: *repeatability, reliability, reproducibility, accuracy, precision*, are often used interchangeably, or accompanied by conflicting definitions. The aim of the present study was to determine whether quantitative measurements from mcDESPOT on the same stable subjects, under the same conditions, are consistent, as a prerequisite for its use in cross-sectional and longitudinal investigations. Thus here, we are concerned with reliability and precision, which are related but distinct concepts.

For an intuitive understanding of the concepts of *accuracy* and *precision*, the 'bullseye metaphor' is often employed, with the following two illustrative examples: several marks centred around the middle of a target but with a large spread (high accuracy, low precision), and several marks close together but off-centre (high precision, low accuracy). Assessing the accuracy of a measurement necessitates comparing observations with its 'true' value, therefore requiring a gold standard measurement to be performed, or an objective truth to be known a priori, e.g. in phantoms or using histological validation. Since this is rare in human imaging, we are often more concerned with precision (Tofts, 2003b), i.e. how 'close together' repeated measurements are compared to the quantity measured. Precision can be measured with the CV, or ratio of the standard deviation of a measurement to the mean.

The psychometric definition of *reliability* is the ratio of subject variability, to subject variability plus measurement error (Streiner et al., 2015). With a perfect, highly precise instrument, repeated measurements of the same stable quantity would yield identical measures; any variation would be attributed to measurement error. However, in a real-world context, reliability is also related to the information value of a measurement as it enables discrimination between subjects or groups (Streiner and Norman, 2006). According to this definition, an instrument that yields the same measurement for a supposedly heterogeneous group of subjects, tested several times and yielding perfectly identical measures between trials, will have poor reliability, since inter-subject variability is low (even though the error may be low or null). Examples of the relationship between sample variance and reliability are shown in **Figure III.1**.

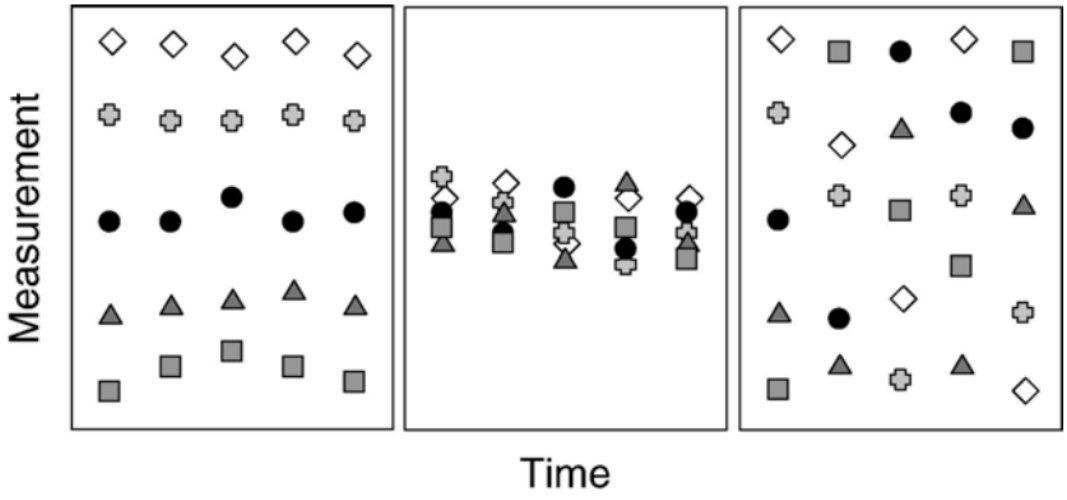

Figure III.1. Three examples of test-retest data with varying degrees of reliability, and how they relate to commonly used statistical measures: the coefficient of variation (CV) and intraclass correlation coefficient (ICC). Each symbol type represents a subject, with five repeat measurements across time on the x-axis. In all cases we assume the "true" value for each subject to be the average of all their repeat measurements (i.e. assuming perfect accuracy). **Case 1 (left):** high between-subjects variance, and low within-subject variance. The inter-subject variance is much greater than the intra-subject variance, hence would yield low CVs and very high ICC. **Case 2 (middle):** low within- and between-subjects variance. According to the 'classic' definition (Streiner et al., 2015), reliability is poor because information gained about subject differences is null. This scenario would result in good CVs, but a poor ICC, as this instrument applied to this particular population cannot be relied upon to discriminate between subjects. **Case 3 (right):** low between-subjects variance, high within-subject variance, yielding poor reliability overall. In this experimental situation the variance between repeat measurements is similar to, or greater than the variance between subjects, which would produce high CVs and a low ICC. From (Vavasour et al., 2006).

Reproducibility in imaging studies often refers to the agreement of measures taken at different sites, with the aim of assessing compatibility between identical scanners, different models from the same vendor, or different systems. In the present study, we are concerned with the test-retest reliability of a measurement, i.e. the consistency between scan-rescan acquisitions. Intuitively, this means how much we can trust that repeated measurements of the same subject will yield consistent measures, that error measurement is small, and that therefore any differences measured between subjects and/or time points are due to a true effect. Assessing the reliability of a measurement on a single platform is a first step towards establishing its cross-platform reproducibility; if different platforms are assumed to be reliable, then the presence of systematic bias across sites is easier to account for. Obtaining stable, precise measurements is necessary to draw information on

differences between groups, pool together datasets from different centres, or follow individuals across several time points. The latter may include longitudinal studies that follow the same subjects over time (e.g. developmental studies, clinical trials), or use several time points to compare different conditions (e.g. intervention studies).

III.2.2. Previous work

mcDESPOT is a quantitative technique that, in theory, yields measures that are platform-independent. As mcDESPOT is being increasingly used in developmental research in cohort studies necessitating several time points, and multi-centre studies are becoming commonplace, information on the reliability of the technique is required.

While no study to date has focused on assessing the protocol's reliability, several published methodological papers have included assessments of inter-scanner reproducibility and intra-subject reliability, which are summarized in **Table III.1**.

Overall, estimates for intra-site reliability (employing both voxelwise and ROI approaches) are good for T_1 and f_M, and slightly worse for T_2, although all studies bar one were performed at 1.5T, and all had very small sample sizes (1-9 subjects maximum for repeat measurements). We further these efforts in the current project, the first to directly address intra-scanner reliability in a larger sample and at several time points.

Of note, we only present here studies that address scanner and acquisition variation. Investigations into the stability and precision of the mcDESPOT algorithm itself are also an area of investigation (Lankford and Does, 2013). It has however been shown to be robust under the right conditions (mainly: adequate signal-to-noise ratio (SNR); choice of appropriate bounds; use of three-pool model and appropriate field corrections schemes) (Deoni and Kolind, 2015).

Table III.1. Studies addressing the intra- and/or inter-scanner reproducibility of DESPOT or mcDESPOT-derived parameters.

Study	Field strength	Sequence, parameters	Subjects	Intra-site	Inter-site
(Deoni et al., 2003)	1.5T	DESPOT1&2 T_1, T_2	1 WM phantom 4 scans	Scan-rescan CV for T_1: 6.4% For T_2: 5.5%	N/A
(Deoni et al., 2008b)	1.5T GE x 2 Siemens x 1	DESPOT1&2 T_1, T_2	7 HC (3 F, 22-34y) All scanned twice at each of 3 sites 4 scanned 3 times at site 1, 3 scanned 3 times at site 2	Mean whole-brain voxelwise CVs: T_1: 6.4 ± 0.52% T_2: 7.9 ± 0.71% Voxelwise paired t-tests for scan vs. rescan: no significant difference ($p > 0.1$). No differences in whole-brain histogram distributions overall (Kolmogorov-Smirnov test).	Mean voxelwise CV: T_1: 6.8 ± 0.67% T_2: 8.3 ± 0.92% No significant difference voxelwise ($p > 0.1$). No differences in histogram distributions.
(Deoni, 2009b)	1.5T GE x 2	mcDESPOT f_M (two-pool model)	9 HC (6 F, 23-41y) All scanned twice (5 at site 1, 4 at site 2) 7 subjects scanned at 2 sites All within 1 week	Voxelwise paired t-tests for scan vs. rescan (normalized, smoothed maps): no significant difference ($p > 0.1$). CVs across 3 GM ROIs (thalamus, putamen, globus pallidus): ~7-10% CVs across 4 WM ROIs (genu, body, splenium of corpus callosum, frontal WM): ~4-8%	No significant difference voxelwise for site 1 vs. 2 ($p > 0.1$). CVs across ROIs in GM: ~8-11% In WM: ~5-9%
(Kolind and Deoni, 2011)	1.5T	**Cervical cord** mcDESPOT f_M, other parameters (two-pool model)	5 HC (4 F, 23-35y) 2 scans within 3 months	Scan-rescan CV across the entire cervical spinal cord. T_1: mean 0.9% (range 0.4-1.7%) T_2: 6% (1.5-13.3%) f_M: 2.6% (0.6-5.7%)	N/A

(Kolind et al., 2012)	1.5T Siemens Avanto	mcDESPOT f_M (two-pool model with HIFI/FM corrections	7 HC, 9 PPMS 2 scans within 2 weeks	Scan-rescan CV for mean f_M within each tissue type: In HC – GM: 7.9%; WM: 3.8% In PPMS – NAGM: 14.3%; NAWM: 4.7% TBSS at each time point; voxelwise CV between each skeleton pair. Median CV (range) across skeleton for HC: 5% (3.5-6.5%) For PPMS: 5.8% (4.5-7.5%). Visual inspection of CVs on TBSS skeleton showed uniform spatial distributions, comparable between HC and PPMS.	N/A
(Deoni et al., 2013)	3T Siemens Tim Trio	mcDESPOT f_M (three-pool model with HIFI/FM corrections)	1 HC (M, 24y) 5 scans over 5 weeks	Mean voxelwise CV within 5 ROIs (frontal, occipital, cerebellar WM, thalamus): 5-6.5%	N/A

Studies are listed in chronological order. When exact values are not given in the original publication, estimated values derived from plots are reported here. CV: coefficient of variation. f_M: myelin water fraction. GE: General Electric. GM: grey matter. HC: healthy control. M/F: male/female. N/A: Not Applicable. NAGM: normal-appearing GM. NAWM: normal-appearing WM. PPMS: primary progressive multiple sclerosis. ROI: region of interest. TBSS: tract-based spatial statistics. T: Tesla. WM: white matter. y: years old.

III.2.3. Choice of sample

When testing reliability in human subjects, the chosen sample should be representative of the larger population that the instrument under investigation is to be applied to, especially when statistical techniques are used that make use of the group variance, as is the case with the ICC. The use of a heterogeneous sample is often recommended to obtain meaningful statistical estimates (Portney and Watkins, 2009), as reliability may be underestimated if the inter-subject variance is lower in the control group used for reliability assessment than in a future patient group (Tofts, 2003a).

For most applications in adult populations and, in the present case, with regards to application to demyelinating diseases, we posit that reliability measures collected among an older group are likely to be more representative of data acquired as part of clinical studies or trials, for several reasons. One, older subjects are more likely to exhibit motion during scanning, which leads to artefacts and decreased image quality. Two, the robustness of preprocessing pipelines is likely to diminish in ageing brains as ventricular and sulcal enlargement, demyelination and non-specific focal lesions are known to occur even in healthy subjects. Three, we expect a wider range of biological variation in people over 50 than in younger 'super-controls', while still being a more homogeneous population than a patient group, and thus representing a compromise between under- and over-estimation of reliability. By selecting participants nominally aged 50-75, we hoped to test the reliability of the protocol under conditions resembling those observed in clinical trials or studies of patient groups.

III.3. Methods

III.3.1. Acquisition

Study design

Sixteen healthy, right-handed participants (8 males, aged 51-72, mean age = 59 ± 7 years) were recruited via recruitment circulars at King's College London and a local Third Age University. Participants had no known neurological abnormalities or pre-existing conditions and were mentally and physically healthy, as determined by self-report. The study was approved by the King's College London Psychiatry, Nursing and Midwifery Research Ethics Sub-Committee (approval number: PNM/12/13-58) and written informed consent was obtained from all subjects.

Participants were scanned on a GE 3.0T Discovery MR750 at the NIHR Wellcome Trust King's Clinical Research Facility, King's College Hospital. Collection of mcDESPOT data was part of a larger study ('Serial Assessment of Good Ageing' – SAGA) that aimed to assess reproducibility of several structural and functional MRI sequences in healthy older adults. The mcDESPOT sequence was situated at around the one-hour mark into an hour-and-a-half scanning session. Participants were scanned three times on the same scanner at baseline, 1 week (range 2-10, median 7 days) and 4 weeks (range 20-38, median 28 days), as no significant global changes in relaxation times were expected to occur within this time frame.

MRI acquisition

The protocol consisted of nine spoiled gradient recalled (SPGR) images at different flip angles (α), one inversion recovery SPGR (IRSPGR) image, and eight balanced steady-state free precession (bSSFP) images with phase-cycling at 0° and 180° for correction of B_0 inhomogeneity, all acquired in sagittal orientation. The 12-channel head portion of a head/neck/spine coil was used for signal reception. Total acquisition time was under 15 minutes. Repetition (TR), echo (TE), and inversion times (TI) below are in milliseconds (ms).

SPGR: TR/TE = 8/3.6; α = [2, 3, 4, 5, 6, 7, 9, 13, 18]°; matrix size = 128 x 128 x 102; voxel size = 1.7 mm^3 isotropic.

IR-SPGR: TR/TE = 8/3.6; TI = 450; α = 5; matrix size = 220 x 110 x 88, reconstructed to 220 x 220 x 88; voxel size = 1 x 1 x 2 mm.

bSSFP: TR was dependent on the specific absorption rate, which is determined by the scanner based on subject weight and 'coil loading' (itself dependent on the participant's exact position within the scanner). This meant variability between participants and in a few cases sessions, ranging between 3.66-4.03 ms (mean 3.82). The actual TR for each subject, at each session, was collected from the image header and used for analysis. TE = TR/2; α = [12.4, 16.5, 21.62, 27.8, 34.0, 41.2, 52.5, 70.0]°; matrix size = 128 x 128 x 102; voxel size = 1.7 mm^3 isotropic.

III.3.2. Analysis

III.3.2.1. Preprocessing

Preprocessing steps were carried out using FMRIB's Software Library (FSL) (Smith et al., 2004).

In order to create mcDESPOT maps, the 26 images that compose the protocol need to be motion-corrected. Here we describe a combined motion correction and inter-session registration scheme that was found to perform well on the current dataset while only resampling each image once. All linear registrations were performed with FSL's Linear Image Registration Tool (FLIRT), using a mutual information cost function, 6 degrees of freedom (DOF) unless otherwise specified, and sinc interpolation.

1) Within each session, the SPGR 18° was chosen as a reference image as it possesses good grey/white matter contrast – an important feature for successful registration using FLIRT (Jenkinson and Smith, 2001).
2) For each subject, all three SPGR 18° images were co-registered to a mid-space by deriving the average transform from co-registration between the three time points. This procedure is similar to the one used in the FSL tool Structural Image Evaluation, using Normalization, of Atrophy (SIENA) for registering several time points for the same subject (Smith et al., 2002).
3) All remaining SPGR scans and the IR were registered to the SPGR 18° in this mid-space. Registration of the IR scan used 12 DOF, as this was found to perform better by accommodating the different acquisition resolution of this image.
4) The SSFP images represent a different problem; due to banding artefacts, failure of registration is more frequent. A two-step procedure was therefore implemented. Within each SSPF phase cycle (8 images), the lowest flip angle image (12.4° – the one with the least amount of banding appearing across the brain) was registered to the SPGR 18° in mid-space. Then, for each phase cycle, the remaining SSFP scans were registered to the corresponding SSFP in mid-space.

Following brain extraction using FSL's Brain Extraction Tool (BET) (Smith, 2002), the parameter maps, including T_1, T_2 and f_M, were created in each subject's mid-space.

III.3.2.2. Creating maps

The implementation of the mcDESPOT calculation algorithm that was used here is part of the Quantitative Imaging Tools (QUIT) suite[9]. The processing pipeline for single- and multi-component DESPOT analysis consists in the following four steps, which follow the procedure described in **II.2**, except where noted below.

1) Run DESPOT1-HIFI processing, to obtain B_1 map.
2) Run DESPOT1 processing, using the B_1 map from step 1, to obtain T_1 map. When only two SPGR flip angles are acquired, DESPOT1 and the HIFI extension default to linear least squares (LLS) fitting. Use of a nonlinear LLS algorithm is made possible by acquisition of more than two SPGR flip angles – here, nine. Theoretically, given the adequate SNR of SPGR scans at 3T, the nonlinear LLS algorithm affords higher precision and accuracy (Chang et al., 2008).
3) Run DESPOT2-FM processing, using the T_1 and B_1 maps from step 2, to obtain off-resonance (f_0) and T_2 map. A nonlinear optimization method is used.
4) Run mcDESPOT processing, with previously obtained B_1 and f_0 maps. This produces final estimates of all parameters, including f_M.

III.3.2.3. Post-processing

Tissue-type segmentation and ROIs were obtained for each subject. To achieve this, the mid-space image created above (by averaging each subject's three co-registered SPGR 18°) was used as a target image. Nonlinear transforms from each subject's target to the MNI152 structural template[10] (Evans et al., 1997) were derived with FSL's Nonlinear Image Registration Tool (FNIRT) (Andersson et al., 2007), using the default scheme optimized for normalization of a T_1-weighted scan. The following standard-space ROIs were selected:

- ROIs for the caudate, putamen and thalamus were extracted from the MNI structural atlas[10].

[9] Details and code can be found at: http://github.com/spinicist/QUIT.

[10] MNI152-2mm template, MNI-prob-2mm and HarvardOxford-sub-prob-2mm atlases: https://fsl.fmrib.ox.ac.uk/fsl/fslwiki/Atlases

- Bilateral spherical ROIs in the frontal white matter (WM) were hand-drawn on the MNI152 template.
- ROIs in the genu, body, and splenium or the corpus callosum were hand-drawn on the MNI152 brain, based on region identification from the John Hopkins University DTI-based WM atlas[11] (Hua et al., 2008).
- Corticospinal tract (CST) and optic radiation (OR) masks were obtained from the Jülich histological atlas[12] (Eickhoff et al., 2007).

The ROI masks were transformed from standard to mid-space using the inverse of each subject's nonlinear transform, and thresholded at visually determined levels before binarizing.

Tissue-type segmentation was performed on each subject's average mid-space SPGR 18^{o} image using FSL-FAST (Zhang et al., 2001), with partial volume estimation (PVE). Cerebrospinal fluid (CSF), grey matter (GM) and WM masks were created from the PVE maps, using conservative thresholds in order to exclude voxels with partial volume effects. The aforementioned CSF masks were used to exclude non-brain voxels where appropriate. Additionally, brainstem and cerebellum masks were obtained from the MNI and Harvard-Oxford subcortical atlases[10], respectively, and used to mask out infratentorial areas (e.g. for the CST and WM masks). Example ROIs are shown in **Figure III.2**.

[11] JHU-WhiteMatter-labels-2mm atlas: http://neuro.debian.net/pkgs/fsl-jhu-dti-whitematter-atlas.html

[12] Juelich-prob-2mm atlas: http://neuro.debian.net/pkgs/fsl-juelich-histological-atlas.html

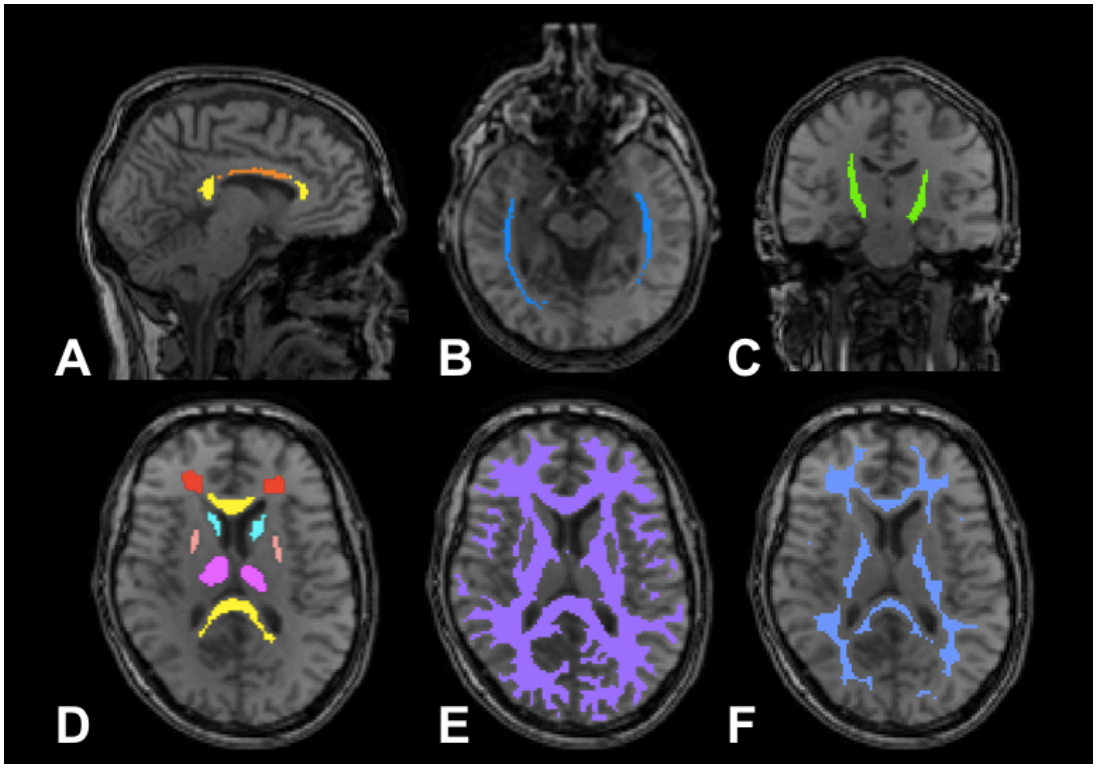

Figure III.2. Example regions of interest, overlaid on an SPGR image. A: corpus callosum genu, splenium (yellow), body (orange). B: optic radiations. C: corticospinal tracts. D: frontal white matter (red), putamen (blue), caudate (pink), thalamus (purple), corpus callosum genu and splenium (yellow). E: white matter mask. F: eroded, 'conservative' white matter mask.

III.3.3. Reliability assessment

Overview

Our aim was to assess test-retest reliability of parameter maps. In the following sections, example figures from representative participants are displayed, along with tables presenting group average metrics. We present voxelwise (histogram, CV maps) and ROI-specific results (CVs and ICC for mean parameter values). Bilateral ROIs were analysed separately in case asymmetrically distributed artefacts were present. Statistical analysis was conducted in R version 3.3.2 (R Core Team, 2017).

Coefficient of variation

The CV is a measure of variability that corresponds to the ratio of the standard deviation to the mean of a sample:

$$\mathrm{CV} = \frac{\text{standard deviation}}{\text{mean}} * 100$$

Some caution must be exercised in interpretation of the CV. It is sensitive to the quantity being measured, i.e. it will near infinity when the mean is close to zero, and cannot be computed for a variable with a negative mean.

CVs can be computed voxelwise, or on an ROI basis. CV maps enable visualization of spatial patterns of variability. An ROI-based approach, ubiquitous in research (e.g. tracking changes in segmented lesions over time) is likely to be more reliable, since the SNR will be higher when the measure is the average, or median, of many voxels.

CV maps were created for each subject by computing the CV voxelwise across sessions. We present CV maps for visual inspection, summary metrics of voxelwise reliability, and average CVs within the chosen ROIs.

Although interpretation of CV should be case-specific and based on the variable of interest, Duval et al. considered scan-rescan CVs < 10% to be good values for quantitative MRI metrics (Duval, 2016).

Intraclass correlation coefficient

The ICC is a measure of reliability that was originally used in the social sciences for determining agreement between raters or judges. Since every article that describes the ICC mentions the 'confusion' surrounding both its implementation and interpretation, in neuroimaging as in other fields, it must be used carefully when dealing with test-retest data, when the raters are, in fact, multiple scanning acquisitions. In its simplest form, it is summarized by Tofts (Tofts, 2003a) as:

$$\mathrm{ICC} = \frac{\text{variance between subjects}}{\text{variance between subjects} + \text{variance within subjects}}$$

It can therefore be described as the proportion of variance that can be attributed to the phenomenon of interest, once instrument variability (measurement error) is taken out (Fleiss, 1999).

The ICC is based on variance estimates, and thus a proper ANOVA model must first be defined. In the present case, a two-way mixed model was chosen, with subjects treated as random effects and sessions as fixed, measuring absolute

agreement between repeated measures. Moreover, we are interested in the reliability of a single measurement (i.e. reliability as it applies to a measurement made at a single time point, not the average of two or more scanning sessions). This design corresponds to an ICC(3,1) according to the nomenclature defined by Shrout and Fleiss (Shrout and Fleiss, 1979), the recommended metric for test-retest reliability assessment (Portney and Watkins, 2009). In order to measure absolute agreement, the error variance (representing the interaction between subjects and sessions, or measurement error for each data point (McGraw and Wong, 1996)) is added to the denominator representing the total variance in the equation above (Lewis-Beck et al., 2004).

Fleiss proposed the following interpretation of ICCs: poor below .40, “fair to good” between .40 and .75, and excellent above .75 (Fleiss, 1999).

ICC calculations were made using *ICC*, part of the *psych* package in R.

III.4. Results

III.4.1. Example data

Example of an acquired protocol is shown in **Figure III.3**. Representative slices from the T_1, T_2 and f_M maps for one subject are shown in **Figure III.4**.

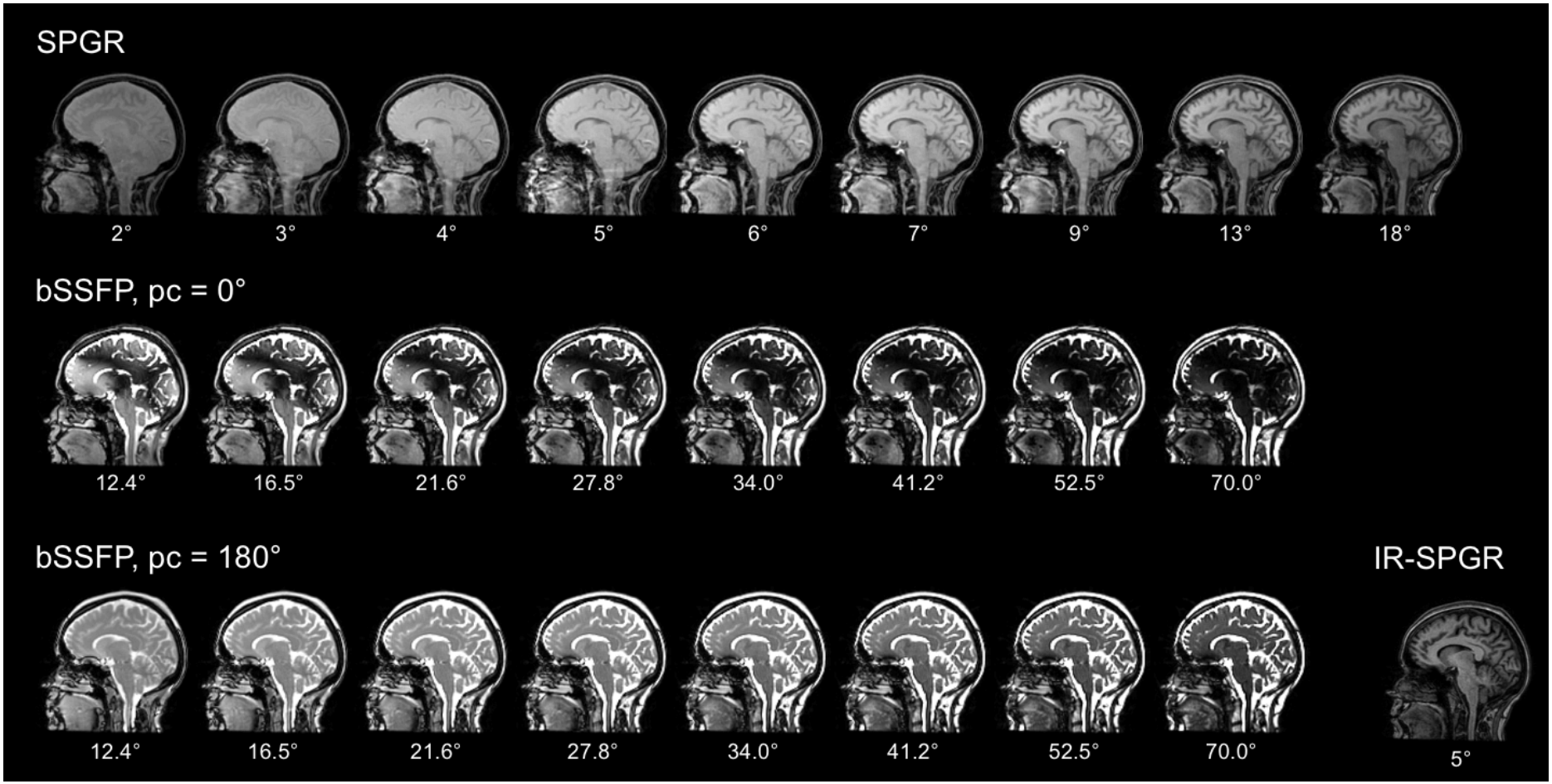

Figure III.3. Example of a mcDESPOT acquired protocol. Flip angles are indicated below each image; for full acquisition parameters, see **III.3.1**. IR-SPGR: inversion recovery SPGR. pc: phase cycle. SPGR: spoiled gradient recalled. bSSFP: balanced steady-state free precession.

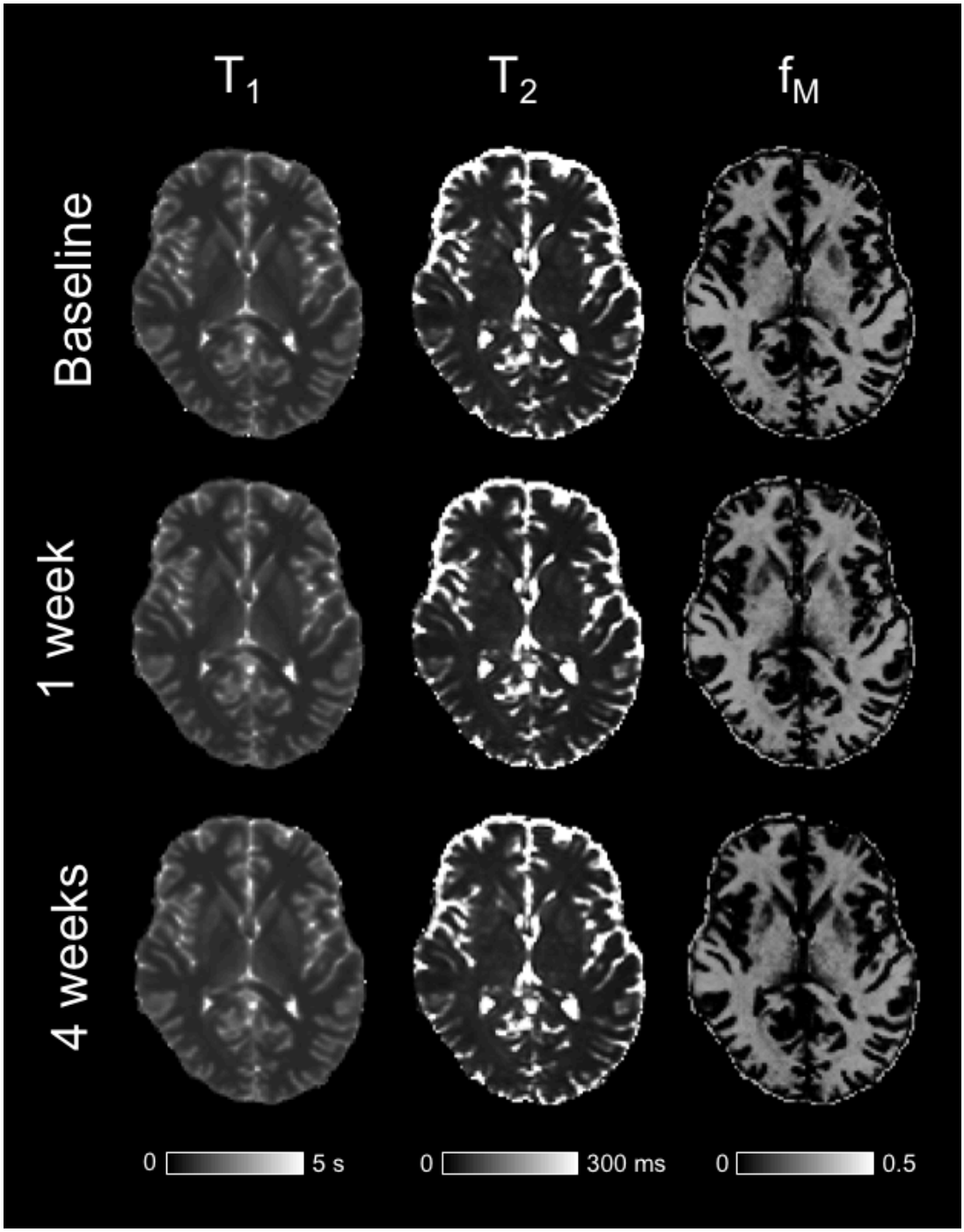

Figure III.4. Representative maps for one subject at baseline, 1 and 4 weeks. Subject shown is a 55-year-old male. f_M: myelin water fraction. (m)s: (milli)seconds.

III.4.2. Absolute measurements

Average values, across all three sessions and subjects, are presented in **Table III.2**. Data for each ROI, at each time point are shown in **Figure III.10**, **Figure III.11** and **Figure III.12** at the end of this chapter.

Table III.2. mcDESPOT values for each parameter averaged across subjects and sessions.

			T_1 (ms)	T_2 (ms)	f_M
Grey matter	**Caudate**	Left	1362.99 ± 54.97	60.23 ± 3.88	0.062 ± 0.02
		Right	1388.84 ± 44.41	63.12 ± 6.2	0.055 ± 0.015
	Putamen	Left	1297.28 ± 66.86	58.94 ± 5.04	0.091 ± 0.031
		Right	1339.18 ± 62.4	63.79 ± 6.32	0.07 ± 0.023
	Thalamus	Left	1229.85 ± 48.13	56.36 ± 3.59	0.119 ± 0.026
		Right	1190.75 ± 48.72	56.23 ± 3.5	0.139 ± 0.025
White matter	**Corpus callosum**	Genu	849.07 ± 37.04	34.44 ± 3.57	0.275 ± 0.012
		Body	897.67 ± 34.06	38.46 ± 2.79	0.273 ± 0.01
		Splenium	873.4 ± 36.91	43.81 ± 3.39	0.273 ± 0.01
	Frontal	Left	879.12 ± 41	40.37 ± 3.44	0.248 ± 0.016
		Right	893.86 ± 41.6	42.98 ± 3.59	0.243 ± 0.02
	Corticospinal tract	Left	920.36 ± 31.88	49.12 ± 3.06	0.247 ± 0.011
		Right	922.47 ± 32.82	50.72 ± 2.77	0.252 ± 0.009
	Optic radiation	Left	899.13 ± 40.04	41.14 ± 3.19	0.266 ± 0.013
		Right	922.81 ± 41.14	47.05 ± 3.5	0.254 ± 0.012

Average ± standard deviation across subjects. f_M: myelin water fraction. ms: milliseconds.

III.4.3. Voxelwise reliability

Histograms

To visualise the frequency distributions of intensity values within the calculated maps, whole-brain histograms were created with the following specifications.

- T_1: 30 bins between 0 and 3000 ms for T_1, whole-brain
- T_2: 20 bins between 0 and 200 ms for T_2, whole-brain
- f_M: : 35 bins between 0 and 0.35, within WM only

We present data from two representative subjects for each session, and a comparison between the two in **Figure III.5**.

Coefficient of variation maps

Example CV maps for two subjects are shown in **Figure III.6**.

Mean CVs were calculated across all voxels for T_1 and T_2, and within the WM for f_M. Due to the expected high variability in GM in f_M in cortical areas we only report voxelwise CVs for WM. Average ± standard deviation across the whole group are presented in **Table III.3**.

Table III.3. Voxelwise reliability for all three parameters.

	Voxelwise coefficient of variation (%)		
	T_1	T_2	f_M
Whole-brain	3.66 ± 0.59	13.17 ± 2.40	-
White matter	2.60 ± 0.61	10.37 ± 2.51	11.51 ± 4.38
'Core' white matter	2.04 ± 0.38	8.21 ± 2.16	9.02 ± 1.99

Average ± standard deviation across subjects. f_M: myelin water fraction.

III.4.4. ROI-specific reliability

CV and ICC results for selected ROIs are presented in **Table III**.4. The distribution of individual CVs are visualized in **Figure III.7**, **Figure III.8** and **Figure III.9**. Inspection of the ROIs-wise CVs plot showed no apparent bias towards better or worse reliability within left vs. right regions.

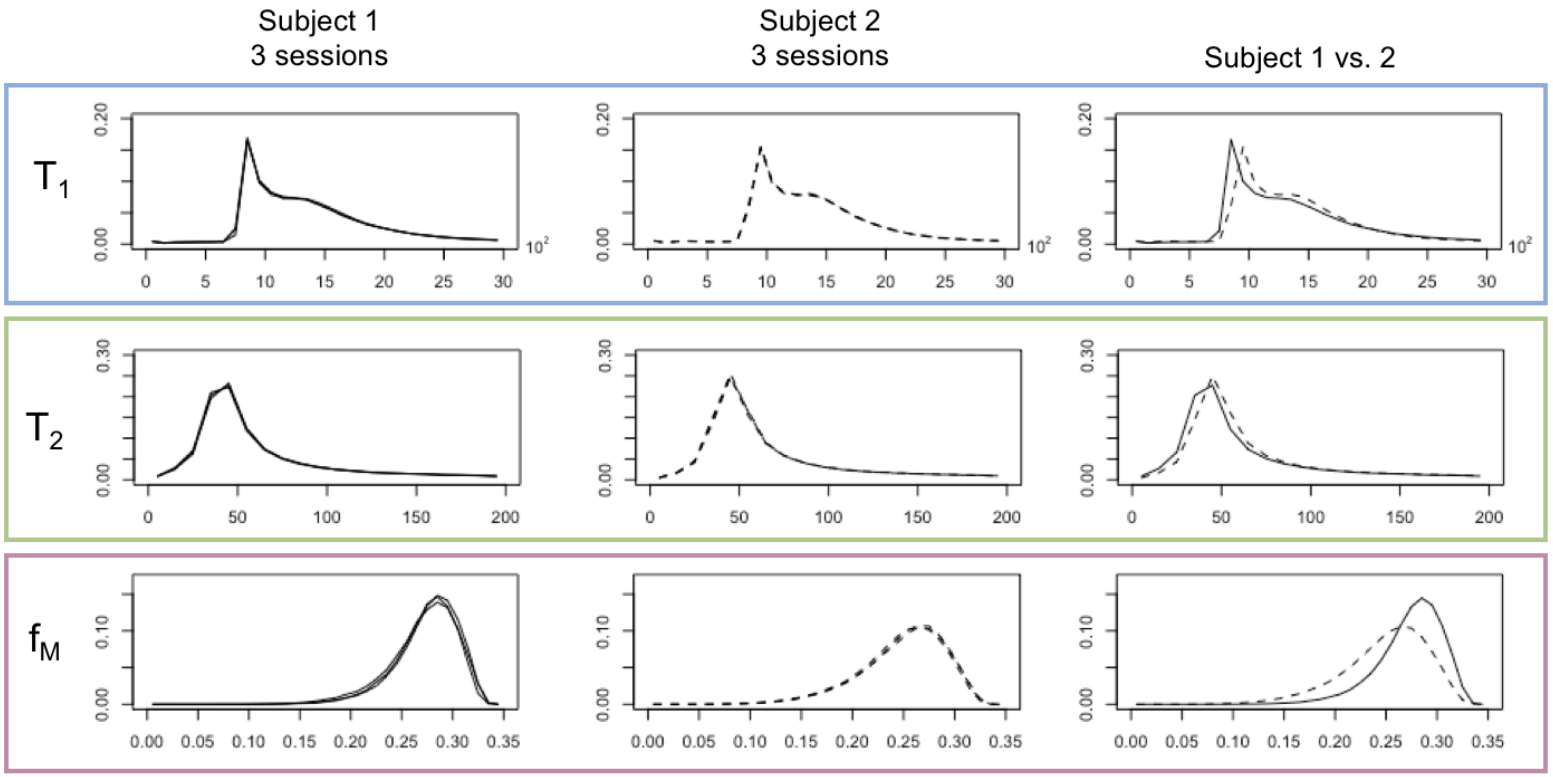

Figure III.5. Example parameter histograms for two subjects. In the first two columns, histograms for each of the three scans are overlaid, showing near-perfect agreement for all three parameters. In the last column, average across the three sessions for each subject are overlaid, showing visible differences in distributions. Histograms are normalized by the total number of voxels considered (therefore the y-axis on each plot is a fraction). Subject 1: female, 53 years old; subject 2: male, 69 years old. T_1 and T_2 histograms are over all brain tissue, myelin water fraction is within white matter only. f_M: myelin water fraction. ms: milliseconds.

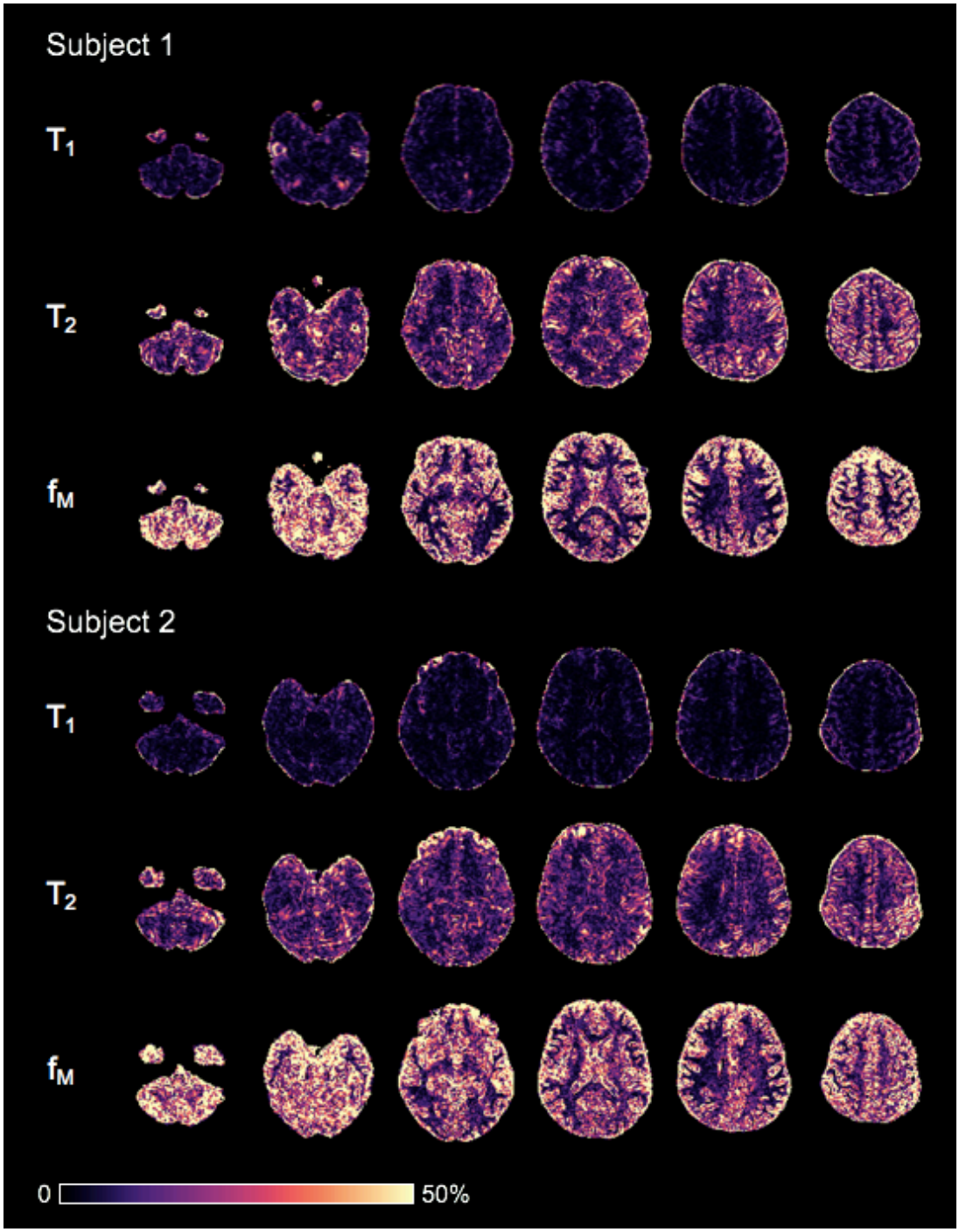

Figure III.6. Example coefficient of variation maps, across the three time points, for two subjects. **Subject 1**: female, 53 years old. **Subject 2**: male, 69 years old.

Table III.4. Reliability metrics for T_1, T_2, and myelin water fraction across three time points.

			T_1		T_2		f_M	
			CV (%)	**ICC**	**CV (%)**	**ICC**	**CV (%)**	**ICC**
Grey matter	**Caudate**	Left	1.08 ± 0.74	0.91	5.88 ± 4.96	0.26	14.83 ± 7.91	0.69
		Right	1.39 ± 1.16	0.75	6.22 ± 6.30	0.42	17.61 ± 8.55	0.59
	Putamen	Left	0.96 ± 0.47	0.96	3.64 ± 2.10	0.80	11.08 ± 5.37	0.87
		Right	1.28 ± 0.83	0.90	3.77 ± 1.62	0.85	15.00 ± 8.49	0.85
	Thalamus	Left	1.10 ± 0.63	0.90	3.57 ± 2.39	0.65	8.69 ± 4.85	0.81
		Right	1.07 ± 0.72	0.91	4.26 ± 2.67	0.56	6.98 ± 3.79	0.84
White matter	**Corpus callosum**	Genu	1.18 ± 0.91	0.90	5.63 ± 5.15	0.60	2.67 ± 2.06	0.58
		Body	1.00 ± 0.51	0.92	6.07 ± 2.97	0.45	2.28 ± 1.52	0.58
		Splenium	1.01 ± 0.45	0.94	3.53 ± 2.60	0.74	1.98 ± 0.93	0.74
	Frontal	Left	1.18 ± 0.70	0.92	4.39 ± 2.60	0.71	4.05 ± 2.17	0.66
		Right	1.30 ± 0.69	0.91	4.25 ± 2.09	0.75	4.06 ± 3.37	0.72
	Corticospinal tract	Left	1.03 ± 0.62	0.89	3.09 ± 1.40	0.76	2.40 ± 1.51	0.68
		Right	0.88 ± 0.35	0.93	3.31 ± 1.47	0.67	2.69 ± 1.64	0.50
	Optic radiation	Left	0.88 ± 0.63	0.94	2.99 ± 1.62	0.83	1.53 ± 1.17	0.88
		Right	0.85 ± 0.46	0.95	2.67 ± 1.51	0.85	2.80 ± 1.54	0.65

Average coefficients of variation across the three sessions are shown. CV: coefficient of variation. f_M: myelin water fraction. ICC: intraclass correlation coefficient.

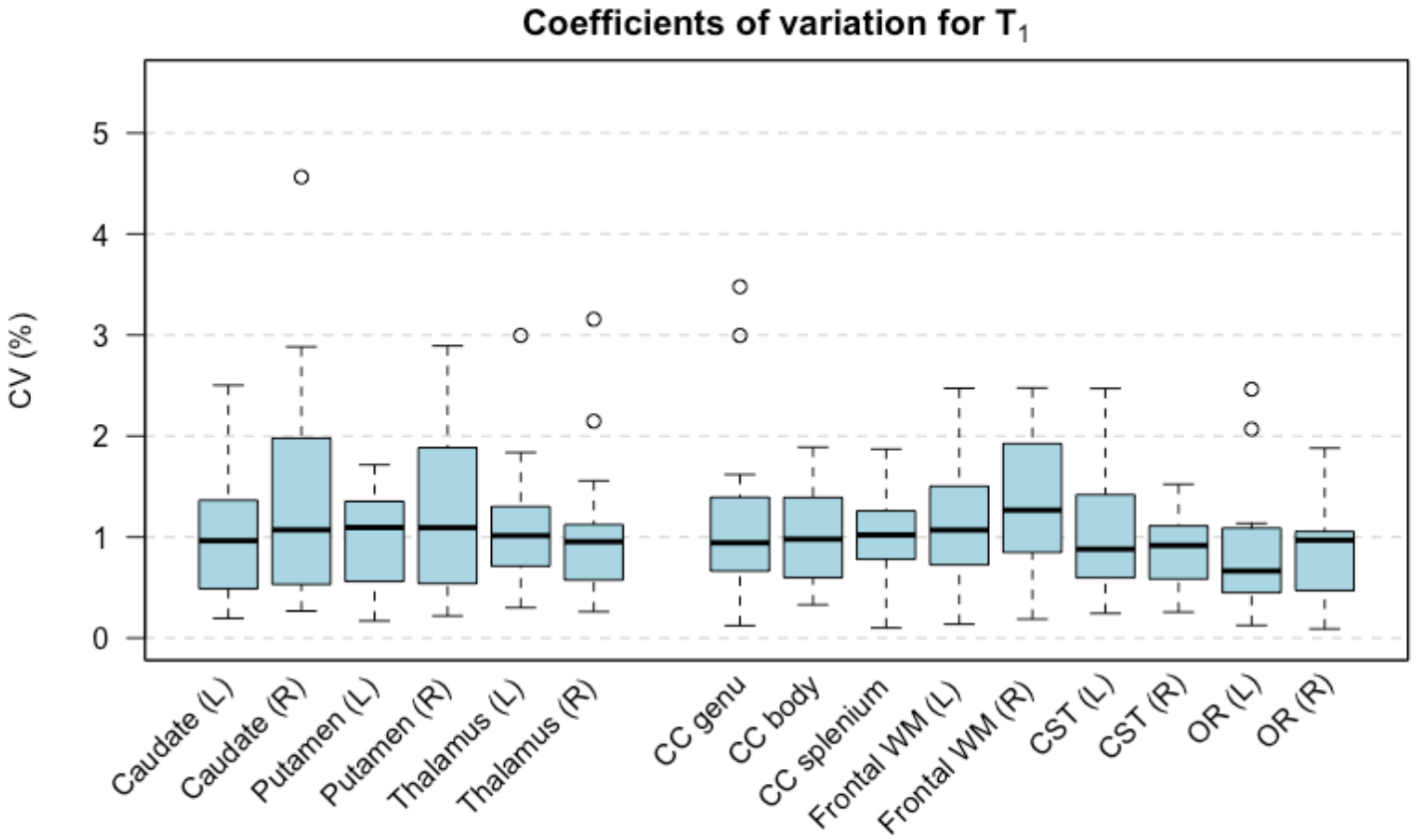

Figure III.7. Coefficients of variation for T_1 across three sessions. Data points outside of boxplot whiskers are outliers, defined as being beyond 1.5 interquartile range of each quartile. CC: corpus callosum. CST: corticospinal tract. L/R: left/right. OR: optic radiation.

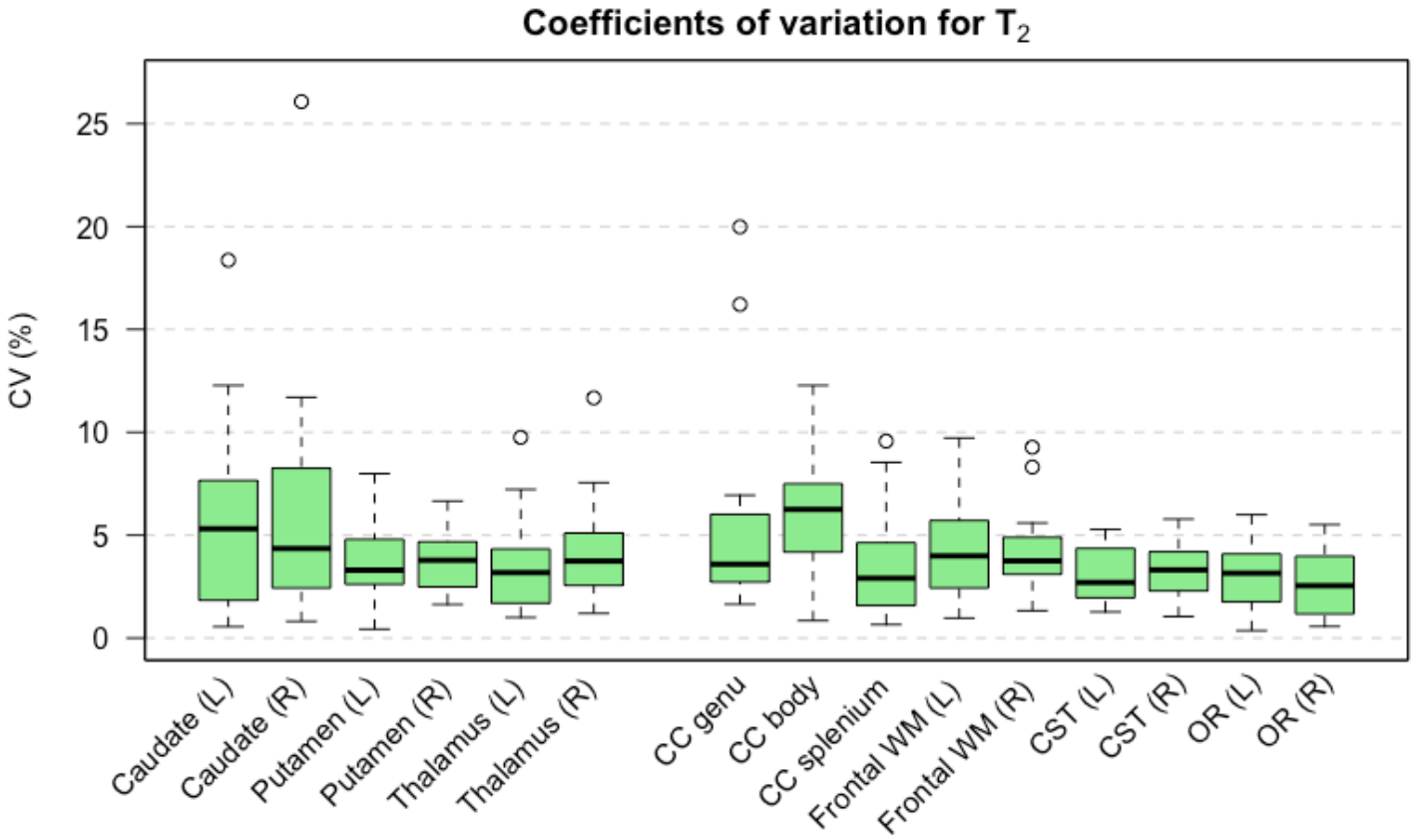

Figure III.8. Coefficients of variation for T_2 across three sessions. Data points outside of boxplot whiskers are outliers, defined as being beyond 1.5 interquartile range of each quartile. CC: corpus callosum. CST: corticospinal tract. L/R: left/right. OR: optic radiation.

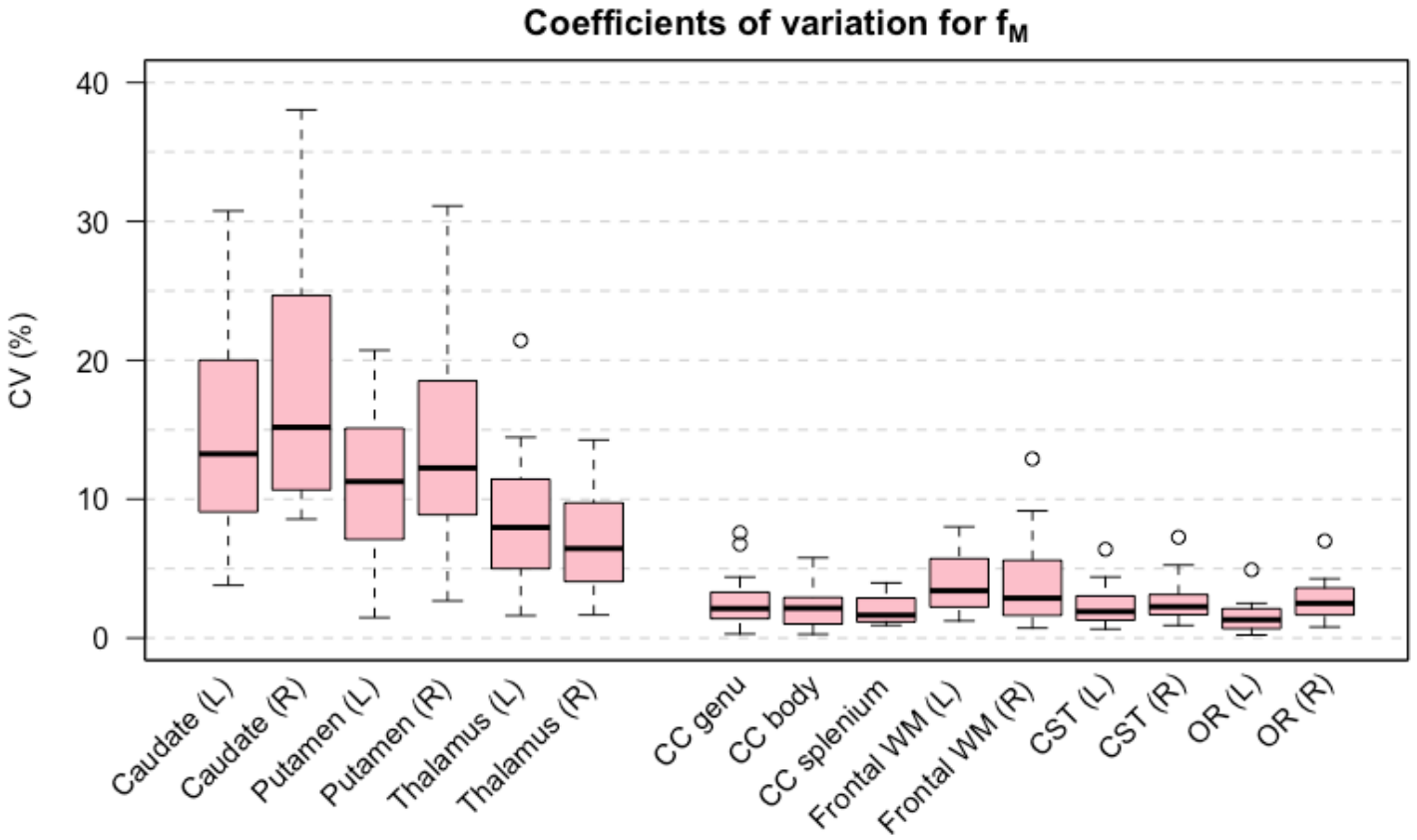

Figure III.9. Coefficients of variation for f_M across three sessions. Note the large range (0-40%) to accommodate the high CVs in grey matter, while CVs in white matter are mostly under 5%. Data points outside of boxplot whiskers are outliers, defined as being beyond 1.5 interquartile range of each quartile. CC: corpus callosum. CST: corticospinal tract. f_M: myelin water fraction. L/R: left/right. OR: optic radiation.

III.5. Discussion

III.5.1. Reliability of T_1

T_1 values were in the 1200-1350 ms range for GM, and 850-900 ms range across WM regions.

These values are overall lower than previous estimates using DESPOT1-HIFI, reported as ~1500-1600 ms in deep grey matter structures and ~1100 ms in WM (Deoni, 2007). In an experiment at 3T using saturation recovery, Wansapura et al. reported an average value of 1331 ms (range 1283-1392) in GM structures, and 832 ms (range 827-838) across WM ROIs (Wansapura et al., 1999).

Our results are reasonably in line with these values, although T_1 in both GM and WM appear slightly underestimated here. A possible explanation for this discrepancy is that inadequate B_1 correction will result in inaccurate calculated T_1 values, which may be the case since visual inspection of B_1 maps showed relatively high deviation between prescribed and transmitted flip angle.

Average CV within WM was very low for T_1 (< 3% on average across subjects), and CV maps show uniformly high reliability across the brain. Reliability was equally good in both GM and WM, with ROI-wise CVs around 1% and ICCs consistently > 0.90, denoting excellent reliability in the studied sample.

III.5.2. Reliability of T_2

We report mean T_2 values between 55-63 for GM, and 35-50 for WM structures. Using a multiple spin-echo approach, Wansapura et al. measured values around 98-132 (mean 110) for GM structures, and 74-84 (mean 80) in WM. Deoni (Deoni, 2009a) reported the following T_2 values using DESPOT2-FM (values given are range across four healthy volunteers): frontal WM: 48-53, thalamus: 70-76, putamen: 66-72, caudate: 78-86. The values in the present study, for the same ROIs as Deoni et al., are consistently lower (frontal WM: mean ~41, thalamus: ~56, putamen: ~61, caudate: ~61).

Overall, T_2 values here are lower in both GM and WM compared to previous studies using either DESPOT or other methods. DESPOT2 is known to provide lower T_2 estimates compared to traditional methods, due to magnetization transfer (MT) effects in tissue that arise due to short RF pulses used to achieve steady state in the bSSFP acquisition (Crooijmans et al., 2011).

CVs were low for T_2: between 3-6.5% for all structures, in line with previous reliability studies using DESPOT2 (see **Table III.1**). However, ICCs were overall only moderate, both for GM (range 0.26-0.85) and WM (range 0.45-0.76). ICCs showed great variability across ROIs, but also for the same structures between left and right hemispheres. Voxelwise estimates were moderately good, with a mean voxelwise CV of ~13% across the whole brain, ~10% in WM.

III.5.3. Applications of T_1 and T_2 mapping

DESPOT1&2 have high efficiency, defined as accuracy over scan time, rivalled only by that of MR fingerprinting (Deoni et al., 2003; Ma et al., 2013).

The excellent reliability of T_1 maps using DESPOT1-HIFI shown here, both voxelwise and using an ROI approach, supports the use of the technique for several research applications, examples of which are listed hereafter.

T_1 is strongly related to water content, and has been used in the study of multiple sclerosis (Neema et al., 2007) and epilepsy (Deoni, 2010). T_1 in the cerebral cortex has been suggested to reflect in large part myelin content (Lutti et al., 2014), although this interpretation has been criticized (MacKay and Laule, 2016). T_1 maps have also been used to improve segmentation estimates of particular structures (Deoni et al., 2007; Deoni and Catani, 2007) and to yield reliable tissue-type volume estimates (Deoni et al., 2008b). T_2 is influenced by iron content, and therefore also has applications in the study of neurological conditions, such as Parkinson's disease and Alzheimer's disease (Brass et al., 2006).

Relaxation time mapping is not limited to neuroimaging, and has applications in imaging of tissue throughout the body, i.e. heart, muscle, cartilage, breast and prostate tumours, etc. Another application is synthetic imaging, which refers to the creation of computer-generated structural images given chosen acquisition parameters and relaxometry data. Using this method, an effectively infinite range of images can be created at different T_1/T_2 weightings, the advantage being images free of artefacts, and the possibility of generating many different contrasts from a single acquisition (i.e. an economy of scanner time). An example is shown in Deoni et al. (Deoni et al., 2006), although preliminary research has shown limited advantages compares to conventional images in terms of diagnostic utility (Blystad et al., 2012).

III.5.4. Reliability of f_M

We observed, as expected, very low f_M values in the deep grey matter, slightly higher (~0.12-0.14) in the thalamus (of mixed GM/WM content), and the highest values in the callosal ROIs (~0.27) compared to other WM ROIs (0.24-0.25).

These values are higher than those usually observed with other methods (Alonso-Ortiz et al., 2015), a known phenomenon possibly also due in part to the influence of MT effects described above in **III.5.2**. While these would be expected to yield higher f_M values, an experiment showed minimal effect using a two-pool model (J. Zhang et al., 2015). However, these interactions have not been assessed with the three-pool model used here, and thus, their influence cannot be ruled out.

CV maps showed better voxelwise reliability within WM than GM. Reliability in GM was moderate, with CVs between 7-18%, and ICCs ranging between 0.59-0.87. In WM, CVs were low (all < 4.5%), and ICCs were moderate to good (0.50-0.74).

As noted above, CVs depend on the absolute quantity being measured; values will be higher for lower mean, and f_M in GM structures will therefore necessarily yield higher CVs compared to WM. Additionally, in simulations under a variety of conditions, accuracy and precision of f_M were better for higher values (Deoni and Kolind, 2015). Results are in line with those from previous studies, which showed ROI-based CVs of 7-10% in GM, 4-8% in WM as reported in **Table III.1**.

Investigations into other MWI methods have yielded comparable, or higher estimates of intra-site reliability (Arshad et al., 2017; Meyers et al., 2013; Nguyen et al., 2016), although the use of different methodologies (acquisition time and efficiency, statistical estimates of reliability) preclude direct comparisons. However, the mcDESPOT protocol presents other advantages in terms of spatial coverage and acquisition time.

III.5.5. Generalizability to other populations

Previous studies have reported consistency across subjects for values obtained in specific structures, which, in a homogeneous population, is suggestive of good precision. In the present sample however, we expect more heterogeneity, due to factors like age and education which are known to have an effect, but the trajectories of which have not yet been characterized in large-scale studies (MacKay and Laule, 2016). An index like the ICC is appropriate, when used in

conjunction with within-subject CVs, to inform on measurement error relative to the variance of the particular sample under investigation. However, because of this, the generalizability of the presented statistical results to other populations is limited. Given the recent applications of mcDESPOT in infants and children to study neurodevelopment, separate assessment of reliability in these populations would be useful, as additional problems may arise when scanning young populations, from data quality (potential for motion), to the biological (lower myelin content), to analysis challenges in post-processing non-adult brains (e.g. dearth of appropriate atlases), which would affect reliability.

III.6. Conclusion

As a well-supported marker of myelination (see **II.1.3**), f_M mapping has been used in studies of neurodevelopment and has the potential to be a clinically useful tool in MS research. We conducted a single-site 3T study of mcDESPOT at three short-term time points using healthy subjects aged 50 and over, in order to represent population variability in a patient population. Voxelwise reliability was excellent for T_1, and within acceptable range for T_2 and f_M. ROI-based results were excellent for T_1, and good for T_2 and f_M (ICCs within the 0.5-0.8 range).

We show here that reliable estimates of f_M, T_1 and T_2 can be obtained using mcDESPOT, and that it is therefore suitable for single-centre longitudinal assessments. Knowledge of the reliability of mcDESPOT overall, and in specific ROIs, informs the choice of analysis methods in projects using a similar protocol, and impacts on the interpretation of the results. Several of the ROIs that were assessed here were used in a project comparing f_M and T_1 values in the brain in patients compared with healthy subjects, which we report on in the next chapter. With the multiplication of multi-site studies, data on the inter-scanner reproducibility of various protocols across vendors and scanners in the brain and cord would be valuable.

III.7. Additional information

Boxplots for all T_1, T_2 and f_M values at the three time points are included hereafter in **Figure III.10**, **Figure III.11** and **Figure III.12**.

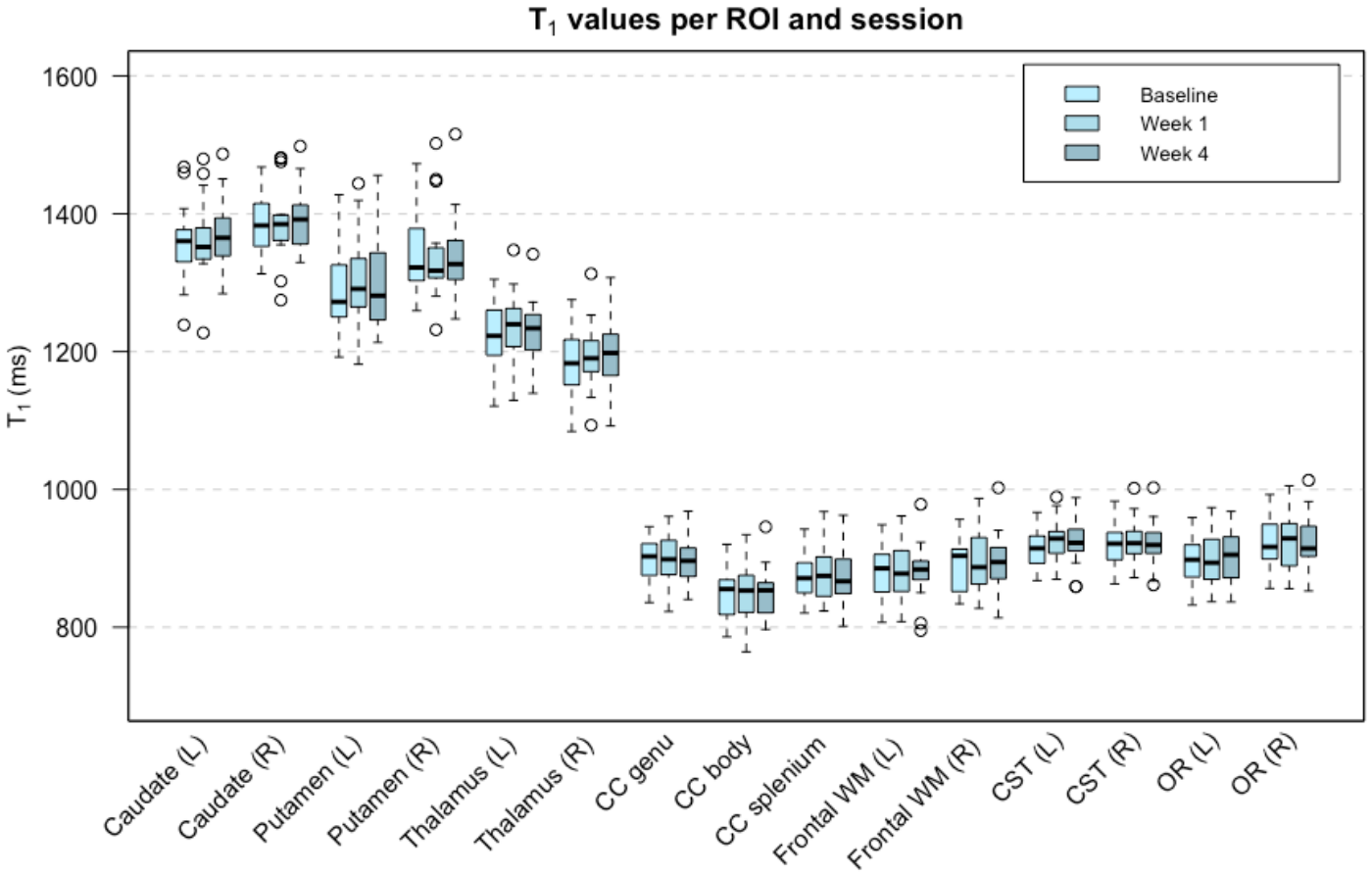

Figure III.10. T_1 values by region of interest across the three sessions. Data points outside of boxplot whiskers are outliers, defined as being beyond 1.5 interquartile range of each quartile. CC: corpus callosum. CST: corticospinal tract. L/R: left/right. ms: milliseconds. OR: optic radiation. ROI: region of interest. WM: white matter.

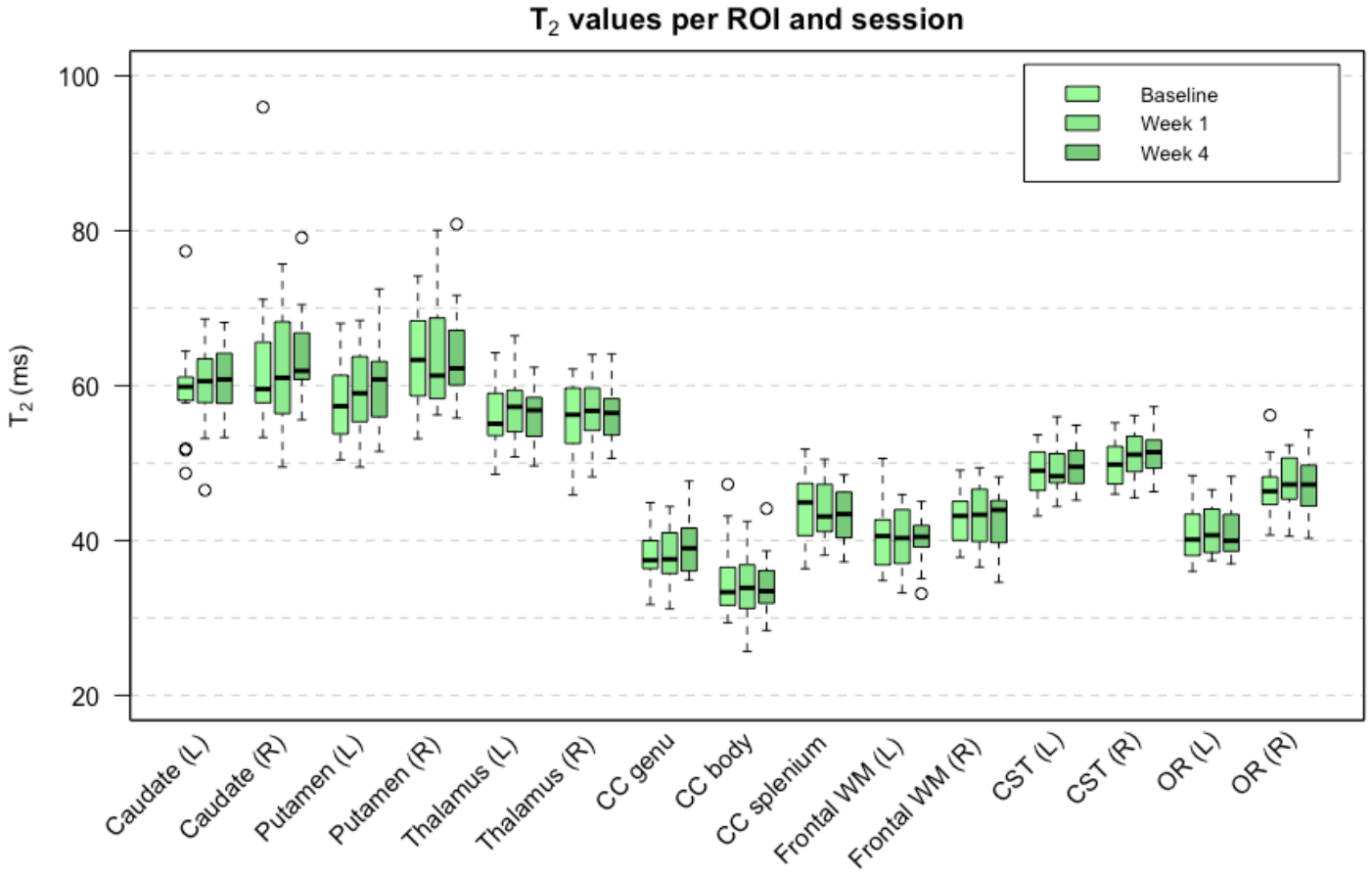

Figure III.11. T_2 values by region of interest across the three sessions. Data points outside of boxplot whiskers are outliers, defined as being beyond 1.5 interquartile range of each quartile. CC: corpus callosum. CST: corticospinal tract. L/R: left/right. ms: milliseconds. OR: optic radiation. ROI: region of interest. WM: white matter.

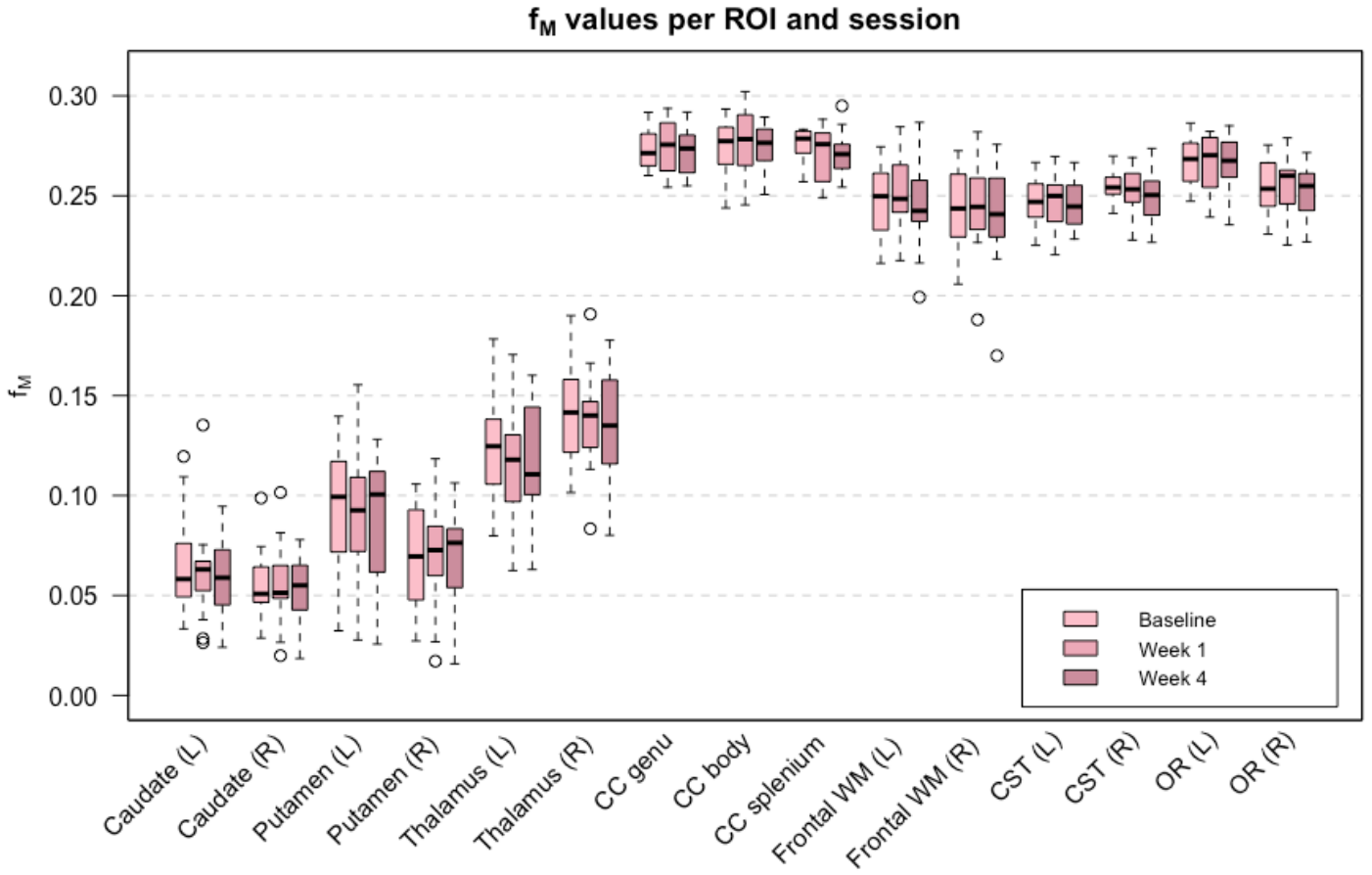

Figure III.12. Myelin water fraction values by region of interest across the three sessions. Data points outside of boxplot whiskers are outliers, defined as being beyond 1.5 interquartile range of each quartile. CC: corpus callosum. CST: corticospinal tract. f_M: myelin water fraction. L/R: left/right. OR: optic radiation. ROI: region of interest. WM: white matter.

Chapter IV. Subcortical pathology and relationship with cognitive performance in neuromyelitis optica spectrum disorder

In this chapter, we investigate subcortical pathology in an NMOSD group compared with healthy controls. We report volumetric measures and quantitative indices in the thalamus and several white matter regions, and assess the relationship of thalamus pathology to a measure of information processing speed in a subset of subjects.

IV.1. Introduction 107

IV.2. Background 108

IV.2.1. Cortical pathology 109

IV.2.2. White matter pathology 110

IV.2.3. Thalamus pathology 112

IV.2.3.1. Neuroanatomy and function 112

IV.2.3.2. Thalamic pathology in NMOSD 113

IV.2.3.3. Functional abnormalities of thalamic networks 114

IV.2.3.4. Differentiating between MS and NMOSD with thalamic volume 115

IV.2.4. Brain substrates of cognitive impairment in NMOSD 115

IV.2.5. Study aims 117

IV.2.5.1. Summary of current evidence 117

IV.2.5.2. Research questions and hypotheses 118

IV.3. Methods 119

IV.3.1. Population characteristics 119

IV.3.2. Data acquisition 120

IV.3.2.1. MRI acquisition 120

IV.3.2.2. Cognitive testing 121

IV.3.3. Image processing 122

IV.3.3.1. Lesion identification 122

IV.3.3.2. Tissue-class volume estimation using SIENAX 123

IV.3.3.3. mcDESPOT analysis 123

IV.3.3.4. Segmentation of white matter regions 124

IV.3.3.5. Thalamic segmentation 124

IV.3.4. Statistical analysis 125

IV.4. Results 126

IV.4.1.1. Sample description 126
IV.4.1.2. Volumes 126
IV.4.1.3. WM regions 127
IV.4.1.4. Thalamus metrics 129
IV.4.1.5. Relationships with SDMT score 131
IV.5. Discussion 132
IV.5.1. Summary of findings 132
IV.5.2. Volumetric measures 132
IV.5.3. NAWM pathology 132
IV.5.3.1. Possible aetiology 132
IV.5.3.2. Corpus callosum 134
IV.5.4. Thalamus findings 134
IV.5.4.1. Structural damage 134
IV.5.4.2. Influence of demographic factors 135
IV.5.4.3. Thalamic segmentation 135
IV.5.4.4. Relationship of thalamic metrics with cognitive performance 136
IV.5.5. General limitations 137
IV.5.5.1. Population 137
IV.5.5.2. Defining cognitive performance 138
IV.5.5.3. Lesion segmentation 139
IV.6. Conclusion 140

IV.1. Introduction

Brain involvement is a recognized and documented feature of neuromyelitis optica spectrum disorder (NMOSD), informed by a growing number of advanced imaging and histopathology studies. However, due in part to the recent redefinition of the currently used diagnostic criteria and the rarity of this clinical population, several questions remain regarding the characterisation of cerebral pathology and its clinical correlates.

Cognitive impairment is found in over half of relapsing-remitting multiple sclerosis (MS) patients (Chiaravalloti and DeLuca, 2008), and has been linked with grey matter (GM) damage, in particular cortical thinning, demyelination, and thalamic

pathology (Messina and Patti, 2014). The prevalence of cognitive impairment is thought to be slightly lower in NMOSD, although select deficits are found in nearly half of patients. As cortical damage is limited in NMOSD, currently available evidence suggests that subcortical pathology may play a greater role; this theory is consistent with the pattern of deficits typically found in this group (Blanc et al., 2012; Hyun et al., 2016).

As a second point of interest, the presence of diffuse brain pathology in NMOSD is a point of contention in the field, and only inconsistently found across advanced magnetic resonance imaging (MRI) studies and methods. Specifically, the presence of diffuse myelin loss outside of lesions, and outside typically involved regions, is debated. Similarly, despite thalamic atrophy being a relatively frequent finding, the underlying tissue damage in this structure has not been well characterised and its origin is unknown. Due to its high number of reciprocal connections with other structures, the thalamus may be particularly vulnerable to downstream damage to focal lesions throughout the brain, and especially within the white matter (WM) (Su et al., 2016). The literature pertaining to these observations will be reviewed herein.

Informed by the MS literature, and by studies suggesting a possible subcortical origin to cognitive impairment in NMOSD, we focus here on damage to NMOSD WM and thalamus. We investigate thalamic atrophy and quantitative parameters as indices of tissue integrity using a multicomponent Driven Equilibrium Single Pulse Observation of T_1 and T_2 (mcDESPOT) protocol, and explore whether diffuse WM changes and thalamus pathology relate to an index of cognitive performance in an NMOSD group.

IV.2. Background

NMOSD predominantly affects the optic nerves and spinal cord, although damage to the brain is becoming recognized as an important and clinically significant feature. Here we review the use of advanced imaging to describe brain involvement in NMOSD and differentiate it from MS. We first describe the nature of pathology in the cerebral GM and WM, before summarising current evidence for the brain substrates of cognition in NMOSD.

IV.2.1. Cortical pathology

Although cortical lesions are rarely found in NMOSD, which has been proposed as a possible differentiating feature from MS (see **II.4.6**), some degree of involvement of the cortical GM has been found with advanced MRI.

There is great discrepancy among findings using both voxel-based morphometry (VBM) and global measures of cortical volume, which are summed up below.

Using VBM, Matthews et al. found no significant reduction in cortical volume in NMOSD compared to healthy controls (HC) (Matthews et al., 2015). Regional reductions in GM density and volume limited to primary sensory, motor, and visual cortices are frequently observed (Cai et al., 2017; Calabrese et al., 2012; Liu et al., 2014; Pichiecchio et al., 2012). Atrophy in the frontal and temporal regions has also been reported (Duan et al., 2012; Wang et al., 2015).

Kim et al. found widespread cortical thinning, but regional atrophy in motor, sensory, and visual areas only when including only patients without brain lesions, or patients with a disease duration < 3 years (Kim et al., 2016b). Consistent with previous studies that only found atrophy of these areas, this results suggests that retrograde degeneration is the main feature responsible for cortical volume loss at early stages of the disease or in the absence of direct brain involvement.

However, von Glehn et al. found widespread cortical atrophy, especially but not limited to the motor, sensory and visual areas, and mention that despite the likely interpretation as Wallerian degeneration and axonal damage, primary tissue damage due to cortical inflammation cannot be ruled out (von Glehn et al., 2014). Pache et al. also found widespread, multifocal atrophy, although there results failed to remain significant when corrected for multiple comparisons (Pache et al., 2016). Another finding challenging the hypothesis of retrograde damage as the only cause of focal GM atrophy is the observation of regional volume loss in the auditory cortex (Cai et al., 2017).

Rocca et al. found abnormalities in the normal-appearing GM (NAGM), using magnetisation transfer ratio (MTR) and diffusion tensor imaging (DTI)-derived mean diffusivity (MD) parameters, that were unrelated to the presence and extent of focal brain and cord abnormalities. They proposed several possible explanations for this observation: the presence of discrete GM lesions not seen on conventional imaging; increased sensitivity to age-related changes or perturbations of global cortical metabolism; and possible retrograde neuronal degeneration due to cord

and optic nerves impairment, despite the lack of correlation between lesional and diffuse pathology detected in their study (Rocca et al., 2004b).

A subsequent study found normal MTR and MD parameters in the NAGM, failing to replicate Rocca et al.'s findings, but instead found reduced fractional anisotropy (FA) in the cortical NAGM (Pichiecchio et al., 2012). Increased MD has been measured in the parietal and occipital cortices (Yu et al., 2006) and frontal and temporal cortices (Qian et al., 2016), possibly attributed to neuronal loss. Neuropathological examinations have indeed shown that cortical neuronal loss is not limited to areas connected with the optic radiations (OR) or corticospinal tract (CST) (Saji et al., 2013), and it has been suggested that the prominent and widespread astrogliosis and neuronal pathology observed in the cortex post-mortem cannot be entirely attributed to retrograde degeneration from axonal transection in the optic nerves and spinal cord, or to downstream WM lesions (Popescu et al., 2010). However, no evidence of widespread cortical demyelination has been found thus far (Popescu et al., 2010). Kim et al. have proposed altered glutamate metabolism as a possible cause for the observed cortical changes in the absence of demyelination, although this remains a hypothesis (Kim et al., 2016b).

Overall, regional atrophy is most often seen in sensory and motor cortices. More widespread changes are only infrequently observed, and the heterogeneity in these findings may be influenced by the impact of disease duration and focal brain involvement. The use of exploratory statistical thresholds in some of these studies must also be noted (Duan et al., 2012; Pache et al., 2016). In addition, the impact of the number and severity of optic neuritis attacks across patients has been shown to be a potential confound, and may explain some discrepancies in the reported results regarding focal volume loss (Sanchez-Catasus et al., 2015).

IV.2.2. White matter pathology

When global tissue compartment volume is considered, WM atrophy is a consistent finding in NMOSD (Blanc et al., 2012; Chanson et al., 2013; Qian et al., 2016). One study suggested that WM atrophy is broadly distributed: focal atrophy was observed using FreeSurfer in several regions connected to the optic nerves and spinal cord (optic chiasm, brainstem, pre- and postcentral gyri which are connected to the CST), as well as in areas that are not (cerebellum, corpus callosum (CC)), and in the frontal, parietal and temporal WM (Calabrese et al., 2012).

Investigations using MR spectroscopy have shown normal ratios of n-acetylaspartate (NAA), choline and myo-inositol, putative markers of axonal loss, inflammation and gliosis respectively (Aboul-Enein et al., 2010; Bichuetti et al., 2008b; Pichiecchio et al., 2012). Only a single study found a mild increase in choline, in the absence of changes in NAA, suggesting the presence of “subtle metabolic changes” (Duan et al., 2017). Another study using MR elastography found reduced ‘tissue softening’ in the WM in the absence of atrophy, which the authors attribute to a non-specific change in tissue integrity possibly linked with astrocyte death or neurodegeneration, favouring the hypothesis of a diffuse disease process independent from focal damage and distinct from ageing (Streitberger et al., 2016).

Using DTI, abnormal MD and FA have been found in regions within the WM connected with the spinal tracts and optic nerves, such as the CST and OR, while parameters in areas not connected to these tracts, such as the cingulum and CC, were normal relative to controls (Yu et al., 2008, 2007, 2006).

Abnormalities in the OR have been confirmed via several observations of reduced FA (Jeantroux et al., 2012; Kimura et al., 2014; Pache et al., 2016; Pichiecchio et al., 2012), increased MD (Zhao et al., 2012), and increased apparent diffusion coefficient (reflecting “cellular size and integrity”) (Jeantroux et al., 2012). Observations of lower FA in the posterior limbs of the internal capsule (Jeantroux et al., 2012), borderline significant reduction in the cerebral peduncle (Pache et al., 2016), and reduced MD in the medulla oblongata and internal capsule (Zhao et al., 2012), often in the absence of abnormalities in other regions, suggests damage restricted to visual and motor pathways. Additionally, significant correlations have been found between diffusion parameters in the CST and OR with the pyramidal and visual functional systems scores, respectively (Yu et al., 2008). DTI abnormalities have been noted in the CC (He et al., 2011b; Kimura et al., 2014; Zhao et al., 2012).

Across studies, FA appears as the parameter most sensitive to the detection of diffuse abnormalities, as it can be reduced even in the absence of MD or MTR abnormalities (Pichiecchio et al., 2012). This suggests that the use of other techniques may bring complementary information.

More recently, a limited number of studies have used myelin water imaging (MWI) to evaluate WM demyelination with increased specificity. Using gradient and spin-echo MWI (GRASE), decreased myelin water fraction has been measured in the

OR (Manogaran et al., 2016b) and CST (Manogaran et al., 2015), consistent with previous DTI investigations. Using a semi-quantitative MWI technique (ViSTa; see **II.1.3.7**), reductions in normal-appearing WM (NAWM) myelin water fraction have been found, as well as local changes in the OR, CST, CC, periventricular WM and centrum semiovale. However, these differences were not apparent when using multi-echo T_2 MWI measures in the same sample (Jeong et al., 2017).

Abnormal structural connectivity in WM networks was shown in one study using DTI data and graph theory analysis, with regional inefficiency being found in the default-mode, sensorimotor and visual systems. The authors hypothesized that these alterations may be due to reorganisation following cord or optic nerves injury, but favoured the idea that these changes may be due to widespread, diffuse pathology (Liu et al., 2012a).

Unsurprisingly, recent studies at higher field strength and with greater sample sizes are those that tend to find more evidence for the presence of occult damage in the NAWM (Zhao et al., 2012), and some authors have argued that the increased sensitivity of techniques like tract-based spatial statistics (TBSS), and increased sample sizes, allow for previously unseen widespread damage beyond the CST and OR to be observed (Liu et al., 2012b). However, even subsequent studies using TBSS have reported the absence of abnormalities across the whole WM skeleton, reporting normal DTI and diffusional kurtosis metrics (Qian et al., 2016), and normal mcDESPOT-derived myelin water fraction (Matthews et al., 2015).

IV.2.3. Thalamus pathology

IV.2.3.1. Neuroanatomy and function

The thalamus is a subcortical deep GM (DGM) structure adjacent to the lateral and third ventricles, and is composed of several nuclei: relay, association, and unspecific (Jacobson and Marcus, 2011). The thalamus receives information from motor structures, sensory input from peripheral receptors (retina, auditory systems), projects onto the corresponding cortical areas, and connects subcortical nuclei within the same hemisphere. Functionally, it serves as a relay for sensory and motor information, and is broadly involved in perception and cognition, as well as higher order and integrative functions (sleep regulation, ocular motility, posture, memory, emotion, consciousness, awareness and attention) (Minagar et al., 2013). Animal, electrophysiological, and lesion studies have shown a role of the thalamus

in memory, executive function, attention, inhibition, and decision-making, planning and response selection, response monitoring, spatial perception and visuo-motor coordination (Mitchell et al., 2014).

In health, there is heterogeneous evidence for age-related MRI-assessed thalamic atrophy (Walhovd et al., 2005). Thalamic volume loss may be linear with age (Walhovd et al., 2005), but gender-independent (Sullivan et al., 2004). Thalamic atrophy may occur earlier, and more severely, than whole brain volume loss; cognitive performance (assessed via measures of the speed of information processing, and executive function) was correlated with thalamic volume, when correcting for intracranial volume and brain size, in subjects under 61 years old (Van Der Werf et al., 2001).

IV.2.3.2. Thalamic pathology in NMOSD

A limited number of studies have reported inconsistent evidence for both the presence and absence of atrophy and microstructural abnormalities in the thalamus in NMOSD, which we summarize below. These studies have used both voxelwise (e.g. voxel-based morphometry (VBM)) and region of interest (ROI)-based approaches (e.g. FreeSurfer, FSL-FIRST).

Some studies have reported the absence of thalamic pathology compared to HC. Normal thalamic volumes have been found using VBM, FSL-FIRST and FreeSurfer (Duan et al., 2012; Finke et al., 2016; Pache et al., 2016), and in one study, no significant change was seen in thalamic volume in NMOSD over one year (Matthews et al., 2015). Normal MD and FA in the thalamus have been observed using DTI (Finke et al., 2016; Yu et al., 2006), as well as normal MTR (Pichiecchio et al., 2012). One study reported no evidence of iron deposition in the DGM in NMOSD brains using susceptibility-weighted angiography, in contrast to what is usually seen in MS (Chen et al., 2012).

On the opposite hand, a number of studies have detected thalamic atrophy in NMOSD compared to HC (Chanson et al., 2013; Liu et al., 2015a). Atrophy has been reported in the absence of thalamic lesions (Calabrese et al., 2012), and in the presence of otherwise normal DGM volumes (Hyun et al., 2016). Some studies have found relationships between brain lesion load and thalamic atrophy, suggesting that atrophy in this region may be secondary to the effect of lesions causing axonal degeneration (Hyun et al., 2016; Wang et al., 2015). In one of these

studies, thalamic volumes were normal compared to HC in the subset of NMOSD subjects with no brain lesions (Hyun et al., 2016). Some studies have found atrophy limited to the right thalamus only (Su et al., 2016; Wang et al., 2015). One study reported a correlation between Expanded Disability Status Scale (EDSS) score and thalamic volume (Hyun et al., 2016).

Investigations using DTI-derived indices have yielded inconsistent findings. Reduced MD was found in the thalamus in patients in period of remission, and higher FA in both stable and remitted patients compared to controls (Zhao et al., 2012). Contrarily, one study reported reduced FA and increased MD, that were not correlated with thalamic volume loss (Liu et al., 2015a). Qian et al. also found increased MD, but normal mean kurtosis in the thalamus, indicating 'tissue heterogeneity' (Qian et al., 2016). Of note, these authors remark on the lower reliability of directional DTI metrics in GM, mentioning that MD may be a more robust measure when applied to a structure with relatively low myelin content like the thalamus – but making the discrepancies in findings with this metric all the more puzzling. Reduced thalamic 'stiffness' has also been found using MR elastography, presumably denoting loss of structural integrity, even in the absence of atrophy (Streitberger et al., 2016).

The two most prevalent explanations for the origins for thalamic pathology in NMOSD that have been proposed are: 1) a primary degenerative process, possibly due to the vicinity of this structure to the ventricles, where aquaporin-4 (AQP4) protein expression is high; 2) a secondary process due to axonal transection in the rest of the brain, especially in the WM (Hyun et al., 2016; Su et al., 2016).

IV.2.3.3. Functional abnormalities of thalamic networks

Abnormal functional activity at rest was found in one patient group using measures of regional homogeneity (Liang et al., 2011) and amplitude of low frequency fluctuation (Liu et al., 2011). Changes were observed in networks supporting cognition, visual and motor systems, for which the thalamus acts as a 'relay point'. These may reflect compensatory mechanisms to support the visual and motor systems following structural damage, which may in turn be a potential cause for the neuropsychological deficits reported in this population (Liu et al., 2011). Hyperactivation of the thalamus at rest has been reported, possibly to preserve visual and motor function in injured systems (Liu et al., 2011). However, another

study found no resting-state abnormalities involving the thalamus, purportedly denoting “intact thalamic function” even in the presence of atrophy and microstructural damage assessed with DTI (Liu et al., 2015a).

IV.2.3.4. Differentiating between MS and NMOSD with thalamic volume

The thalamus, along with the basal ganglia, is extensively involved in MS, and has been recognized as an “early sensor” of brain pathology in the disease (Absinta et al., 2016). Thalamic pathology, and in particular volume loss, is a known predictor of disease progression even in the relapsing stage (Rocca et al., 2010), and linked to cognitive impairment. Thalamic pathology accumulates on “a background of” the age-related atrophy described above, and has been described as a “barometer of diffuse neuropathological damage in MS”, due to numerous connections with cortical and subcortical GM structures (Minagar et al., 2013).

Studies comparing MS and NMOSD cohorts often find atrophy in relapsing-remitting MS (RRMS), but absent or milder atrophy in NMOSD, following the typical ‘MS > NMOSD > HC’ pattern seen in most studies regarding the severity of observed abnormalities. Thus, thalamic atrophy has been proposed as a differentiating feature between these patient groups with potential clinical diagnostic usefulness (Duan et al., 2012; Liu et al., 2015a; Matthews et al., 2015). Matthews et al. devised a discriminant function based on thalamic and normalized brain volume, which successfully separated RRMS and NMOSD subjects with 89.5% sensitivity and 92.9% specificity (Matthews et al., 2015). Using machine learning, Eshaghi et al. found that thalamic atrophy was the most discriminating measure, and the best predictor of disease status among other GM volumetric variables, and along with WM lesion volume, could be used to classify MS and NMOSD patients with 74% accuracy (Eshaghi et al., 2016).

IV.2.4. Brain substrates of cognitive impairment in NMOSD

Neuropsychological deficits in several domains can generally be found in over half of NMOSD patients (Blanc et al., 2008; Saji et al., 2013; N. Zhang et al., 2015). ‘Core deficits’ in attention and information processing speed (IPS) have consistently been found across Chinese, Japanese, French, Brazilian and Argentinian cohorts; deficits in verbal fluency, working and long-term memory, and emotional face

processing have also been reported (Blanc et al., 2008; Cardona et al., 2014; Kim et al., 2016c; Liu et al., 2015b; Saji et al., 2013). Studies comparing NMOSD and matched MS subjects have suggested an overall similar pattern of cognitive impairment, and no relationships have been found with disease duration, EDSS, or the presence of abnormalities on conventional MRI (Blanc et al., 2008; He et al., 2011b; Saji et al., 2013; Vanotti et al., 2013). Because most studies evaluate patients during remission, the effects of acute, attack-related inflammation and oedema are unlikely to account entirely for the observed deficits (N. Zhang et al., 2015). Therefore, a number of studies have aimed to investigate the substrates of cognitive impairment in NMOSD.

In MS, cortical thinning, focal lesions and demyelination have been linked with abnormal cognitive function (Calabrese et al., 2009; Filippi et al., 2010; Kutzelnigg and Lassmann, 2006). In NMOSD, cortical lesions are more rare, and atrophy findings are generally limited to visual and motor cortices (see **IV.2.1**). Moreover, the absence of cortical demyelination suggests a different aetiology to cognitive impairment in NMOSD (Popescu et al., 2010).

There is limited evidence for relationships between cortical MRI measures and cognition in NMOSD. He et al. linked impaired IPS and executive control with DTI metrics (MD and FA) in the anterior cingulate cortex and adjacent medial prefrontal cortex (He et al., 2011b). A relationship between GM volume reduction in the medial prefrontal cortex and working memory was also reported by another group (Wang et al., 2015). Conversely, Liu et al. reported cortical thinning limited to the visual cortex, and found no relationship between scores on the Paced Auditory Serial Addition Test (PASAT) and cortical thickness (Liu et al., 2014). In another study, regional atrophy was not linked with any cognitive scores, despite widespread cortical thinning. The authors postulate that deficits in IPS and working memory, functions which require wider cortical involvement and rely on cortico-cortical connections via long WM tracts, may be due to WM involvement, which they did not evaluate. They also suggest that the lack of focal cortical involvement may explain the relative preservation of function in a measure of delayed memory observed in their sample (Kim et al., 2016b).

It has been proposed that the pattern of cognitive deficits observed in NMOSD is consistent with a ‘subcortical’ pattern of neurocognitive impairment (Blanc et al., 2012), typical of inflammatory disorders and characterised by a relative sparing of the cortex, greater WM involvement, and causing deficits in the aforementioned

domains: slowing of IPS, executive dysfunction, and attentional deficits, while language ability and visuoperceptual deficits are relatively preserved[13] (Filley, 2012). Consistent with this hypothesis, the presence of WM atrophy is well-documented (see **IV.2.2**). In one study, WM volume loss was more severe in NMOSD subjects with vs. without cognitive impairment compared to HC. Patients with cognitive impairment showed greater global and focal WM atrophy (in the frontal and parietal lobes, CC, cerebellum, brainstem, optic chiasm and CST), while no global or focal GM atrophy was observed (Blanc et al., 2012). One study found abnormal MD and FA in the CC, linked with several cognitive measures (He et al., 2011b).

In the absence of widespread cortical pathology, and consistently with the above described theory, the question has been raised as to whether thalamic atrophy may contribute to cognitive impairment, as is seen in MS (Ciccarelli, 2012). Memory performance has been linked with GM volume reduction in the right thalamus (Wang et al., 2015), and WM volume adjacent to the thalamus has been linked with phonemic fluency (Blanc et al., 2012). Liu et al. found a correlation between reduced FA in the thalamus and PASAT-2 scores (Liu et al., 2015a). In one study, thalamic atrophy was only found in cognitively impaired NMOSD subjects, and not in a cognitively preserved group; moreover, thalamic volume was positively correlated with a global index of cognitive function (Hyun et al., 2016).

IV.2.5. Study aims

IV.2.5.1. Summary of current evidence

- Cortical pathology is less extensive in NMODS than in MS. Regional atrophy seems mostly related to retrograde degeneration from optic nerves and spinal cord lesions, although there may be some degree of NAGM damage not confined to these areas.
- WM atrophy is a frequent finding. Most studies looking at the NAWM have used DTI, and investigations using quantitative metrics of myelin content are few. The body of literature suggests secondary damage related to focal optic and spinal

[13] Interestingly, in a separate project involving a wider group of NMOSD patients, only a subset of whom also underwent MRI for research purposes and are included in this study, subjects showed overall slowed cognitive processing but relative sparing of verbal fluency [data not shown].

pathology, as in the cortex, rather than inflammatory or degenerative processes in the brain. The existence of “chronic and diffuse neurodegeneration” remains unproven (Kawachi and Lassmann, 2017).

- In the thalamus, assessments of atrophy and microstructural parameters provide conflicting findings regarding the prevalence, severity, and nature of abnormalities. Thalamic atrophy is found more frequently than in other DGM structures, and is generally less severe than in MS. Its sensitivity to the secondary effects of focal brain pathology, and preliminary evidence regarding relationships with clinical measures (EDSS, cognitive tests), suggests that even subtle thalamic pathology may have functional relevance.

- Cognitive impairment in NMOSD may follow a typically ‘subcortical’ pattern, with deficits in IPS and attention being most frequently observed. Cortical atrophy appears unrelated to cognitive performance, and the absence of cortical demyelination suggests a different aetiology than in MS. There is some evidence for the involvement of both WM and thalamic abnormalities in cognitive impairment in NMOSD.

IV.2.5.2. Research questions and hypotheses

Here we aimed to investigate subcortical pathology in the NMOSD brain using MWI, in order to answer the following questions.

1) Are MWI-derived parameters sensitive to abnormalities in the cerebral NAWM of NMOSD subjects compared to HC?
2) Can abnormalities of the thalamus be detected using these parameters, and are they related to focal WM pathology?
3) Are either of these features related to cognitive performance?

We used measures of volume, myelin content, and quantitative relaxation time T_1, acquired with a mcDESPOT protocol, in the NAWM and thalamus, in an NMOSD group compared to matched HC. First, we report tissue-compartment volumes to assess the presence of atrophy. We report measures of thalamic volume, as well as multicomponent relaxometry parameters relating to tissue microstructure, to investigate the presence and characteristics of thalamic pathology. We also correlate these measures to determine whether thalamic pathology can be related to the extent of focal and/or diffuse WM damage. Finally, we aim to explore (in a

subset of patients) whether these parameters are related to cognitive performance, by assessing relationships between quantitative MRI metrics and a measure of IPS. We used the Symbol Digit Modalities Test (SDMT), a highly sensitive task that is widely used in MS research, as well as nearly all of the studies on cognition in NMOSD cited above.

We hypothesized that WM atrophy and NAWM abnormalities would be present; that thalamic atrophy and abnormal parameters would be found in the NMOSD group compared to controls; that thalamus pathology would be related to WM pathology, in the form of either focal abnormalities (lesion load) or more subtle damage to the NAWM; and that these indices would be related with cognitive performance.

IV.3. Methods

IV.3.1. Population characteristics

NMOSD participants were recruited from the MS and NMO clinic at the University of British Columbia in Vancouver, Canada. Patients were diagnosed according to the 2015 criteria[14] (Wingerchuk et al., 2015). A HC group was selected based on age and gender from an available database. Two NMOSD subjects were excluded at the time of analysis: one for being significantly older than the rest of the sample (70 years old), and one who displayed an unusually large lesion in the right temporal WM, rendering most measures biased and potentially meaningless. In total, 19 NMOSD subjects and 21 HC were included (see **Table IV.1**).

Nearly all patients were receiving immunosuppressant or immunomodulatory treatment. Seven were on mycophenolate mofetil, six on azathioprine, one on rituximab, one on mitoxantrone, one on prednisone, and two were receiving combinations thereof (one on prednisone and azathioprine, one on mycophenolate mofetil and rituximab). One was unmedicated.

[14] Of note, two of the subjects originally included in this cohort had their diagnosis revoked: one was subsequently diagnosed as RRMS, and one as brain inflammation of unknown aetiology, which speaks of the difficulty in differentiating and diagnosing this condition in the clinical setting. These subjects' data were not used in this project.

Table IV.1. Population characteristics for healthy controls and NMOSD subjects.

	HC	NMOSD
N	21	19
Age, years (mean ± SD, range)	42 ± 7 (28-56)	43 ± 10 (24-60)
Sex, M:F	6:15	6:13
Disease duration, years (mean ± SD, range)	N/A	6.2 ± 4.1 (0.5-14)
EDSS (median ± IQR, range)	N/A	3.5 ± 2.25 (1-6)
Aquaporin-4 antibody seropositivity (n, %)	N/A	9 (47%)

EDSS: Expanded Disability Status Scale. HC: healthy controls. IQR: inter-quartile range. NMOSD: neuromyelitis optica spectrum disorder. N/A: not applicable. SD: standard deviation.

IV.3.2. Data acquisition

IV.3.2.1. MRI acquisition

All participants were scanned on a 3.0T Philips Achieva MRI scanner (Best, the Netherlands) using an 8-channel head coil. Acquired scans included three-dimensional (3D) T_1-, T_2-weighted, and fluid-attenuated inversion recovery (FLAIR) scans, and a mcDESPOT protocol (Deoni et al., 2008a) that consisted in seven spoiled gradient recalled (SPGR) scans, one inversion recovery SPGR (IRSPGR) scan, and seven balanced steady-state free precession (bSSFP) scans with phase-cycling at 0° and 180° for correction of B_0 inhomogeneity. All were acquired in sagittal orientation. Repetition (TR), echo (TE), and inversion times (TI) below are in milliseconds, voxel sizes in millimetres (mm).

3D T_1-weighted fast field echo: TR/TE = 6.2/3; matrix size = 256 x 256 x 200; voxel size = 1 x 1 x 1.6 mm; reconstructed to 320 x 320 x 200, 0.8 mm^3 isotropic.

3D T_2-weighted spin echo: TR/TE = 2500/363; matrix size = 256 x 256 x 200; voxel size = 1 x 1 x 1.6 mm; reconstructed to 320 x 320 x 200, 0.8 mm^3 isotropic.

3D FLAIR: TR/TE = 8000/337; TI = 2400; matrix size = 256 x 256 x 200; voxel size = 1 x 1 x 1.6 mm; reconstructed to 320 x 320 x 200, 0.8 mm^3 isotropic.

SPGR: TR/TE = 6.5/3.6; α = [2, 3, 4, 6, 9, 13, 18]°; matrix size = 128 x 128 x 92 mm; voxel size = 1.7 mm^3 isotropic.

IR-SPGR: TR/TE = 6.5/3.2; TI = 450; α = 5°; matrix size = 128 x 128 x 92; voxel size = voxel size = 1.7 x 1.7 x 3.4 mm, reconstructed to 1.7 mm^3 isotropic.

bSSFP: TR/TE = 5.8/2.9; α = [7, 11, 15, 19, 24, 30, 47]°; matrix size = 128 x 128 x 92; voxel size = 1.7 mm^3 isotropic.

IV.3.2.2. Cognitive testing

A subset of NMOSD subjects (n = 12) received the SDMT, a timed pen-and-paper test. It is a quickly administered substitution task where participants are required to match numbers to symbols using a reference key, completing as many symbol-digit matches as possible, without skipping one, within 90 seconds. An example of the task sheet is shown in **Figure IV.1**. The score is calculated as the number of correct matches, and therefore better performance is reflected by a higher score. This test measures IPS, and is widely used as a screening tool with high sensitivity to cognitive impairment that has been shown to be independent of education level in adults (Sheridan et al., 2006). The test was administered by a trained instructor.

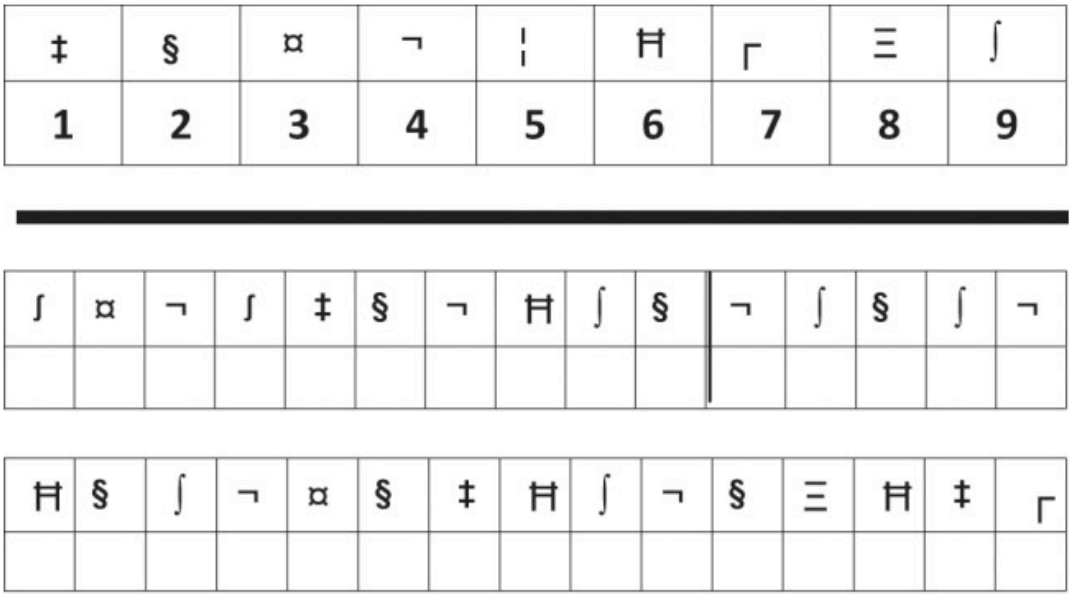

Figure IV.1. Example task sheet for the Symbol Digit Modalities Test. The top row is the 'key' of corresponding symbol and digits. The bottom two rows are the task stimuli to be 'decoded' by the participant, with a training set of 10 items delimited by the vertical line in the middle row. (Actual test is under copyright; image shows an equivalent setup for illustrative purposes.) Source: (Langdon et al., 2012).

IV.3.3. Image processing

All structural processing was performed on the SPGR 13° scan using tools from FMRIB's Software Library (FSL) version 4.8 (Smith et al., 2004).

IV.3.3.1. Lesion identification

Lesions were identified using T_1-weighted and FLAIR^2 images and in-house software.

FLAIR^2 ('FLAIR-squared') refers to the process of multiplying a T_2-weighted scan by a FLAIR scan to obtain a hybrid image with T_2 contrast where cerebrospinal fluid (CSF) appears dark, and lesion brightness is increased (Wiggerman et al., 2016). This serves to increase conspicuity of lesions. NMOSD subjects' T_2-weighted and FLAIR scans were linearly co-registered, when necessary, to create FLAIR^2 images. Examples of scans from one subject can be seen in **Figure IV.2**.

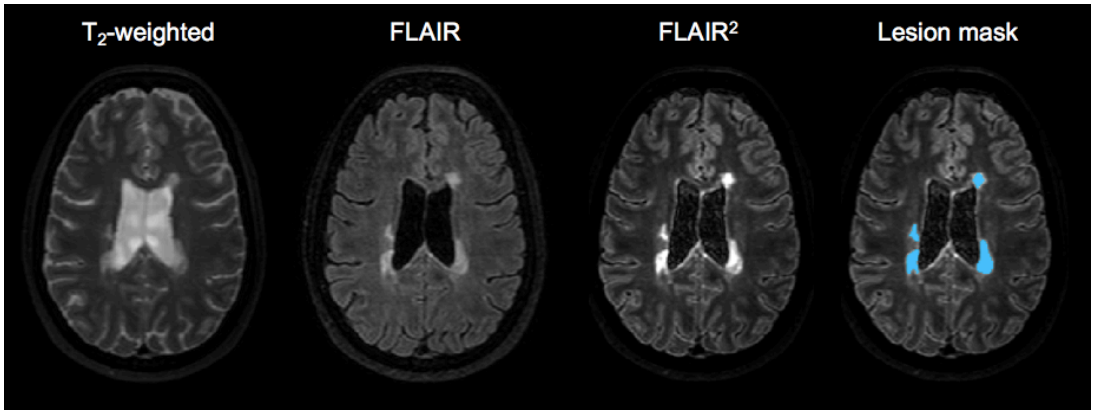

Figure IV.2. Example of FLAIR^2 image for lesion segmentation for a subject with periventricular lesions. From left to right: T_2-weighted, FLAIR, FLAIR^2 image, and overlaid lesion mask in blue. This subject (52 years old, female, aquaporin-4 antibody negative, disease duration 6 years, EDSS 2.5) presents with several T_2-hyperintense periventricular lesions and has a lesion load of 4104.19 mm^3 (4.10 millilitres).

The software used to segment lesions is a semi-automated region-growing tool; a point in each lesion is manually identified, and the lesioned area is expanded to the surrounding voxels using a specified intensity threshold, which can be adjusted interactively so that the mask can be 'grown' or 'shrunk' to fill the lesioned area. Lesions were drawn on the FLAIR^2 image, with concurrent information gleaned from the T_1-weighted image, referring back to the individual FLAIR and T_2-weighted

scans when required. Two subjects had missing data: one was missing the FLAIR scan, and one only had the T_1-weighted scan. For these subjects, lesions were assessed based on the available scans. The lesion masks obtained were reviewed by an experienced neurologist.

Lesions masks drawn in FLAIR[2] space were transferred to mcDESPOT space using the SPGR 13° as a reference. FSL's Linear Image Registration Tool (FLIRT) (Jenkinson et al., 2002) was used with 6 degrees of freedom (DOF) from the T_2- to the T_1-weighted scans, and the T_1-weighted scan to the SPGR, and the two transforms concatenated to obtain a final unique transform to transpose the lesion masks into SPGR space.

IV.3.3.2. Tissue-class volume estimation using SIENAX

Tissue class volumes were estimated using the FSL tool for cross-sectional Structural Image Evaluation, using Normalization, of Atrophy (SIENAX) (Smith et al., 2002) on the SPGR 13° scan. After initialization with robust brain extraction (Smith, 2002), SIENAX uses linear registration to register to MNI152 space, in order to derive a scaling factor used to correct the obtained raw volumes for head size. The tissue compartment classification is based on the FAST algorithm (Zhang et al., 2001), including bias field correction and partial volume estimation. Lesion masks were included in the pipeline. The following volume measures were obtained: GM, WM, ventricular CSF, cortical GM, and lesion. We calculated subcortical GM volume by subtracting the cortical from the total GM volume.

IV.3.3.3. mcDESPOT analysis

In order to ensure compatibility with other datasets as part of a larger study, mcDESPOT preprocessing was performed according to a predetermined pipeline in which all images are registered to the SPGR 13° scan using FLIRT, with 6 DOF, using a correlation ratio cost function and trilinear interpolation.

Voxelwise mcDESPOT analysis was performed to create single-component T_1 relaxation time and f_M maps, using a three-pool model and with the version of the algorithm described in **II.2.4.2** as per Deoni et al. (Deoni et al., 2013).

IV.3.3.4. Segmentation of white matter regions

FAST segmentation (Zhang et al., 2001) was carried out on the SPGR 13° to obtain WM masks. These were eroded by two voxels using a 3D kernel to avoid voxels with partial volume effects, and lesion masks were subtracted to create conservative NAWM masks. All masks were visually checked for quality assurance.

Mean f_M and T_1 were calculated within whole NAWM. We also compared f_M and T_1 in specific tracts: OR, CST, CC, and frontal WM. Regions were obtained by warping standard space masks, including hand-drawn regions and regions derived from the Jülich histological atlas (OR, CST) and John Hopkins WM atlas (CC), in the same procedure as described in **Chapter III**. Example ROIs can be seen in **Figure III.2**.

WM lesion load was obtained by calculating the volume of the overlapping lesion and WM masks, and normalized using the SIENAX-derived scaling factor.

IV.3.3.5. Thalamic segmentation

Thalamic segmentation was performed on the SPGR 13° scan using FIRST (Patenaude et al., 2011), and the obtained volumes were normalized for intracranial volume using a scaling factor derived using SIENAX, as noted above. FIRST uses shape deformation from a-priori models made from a library of manually segmented healthy and pathological brains. Boundary correction is performed to classify voxels overlapping between adjacent structures (e.g. left and right thalami) depending on probability. Presence or absence of thalamic lesions was assessed systematically by looking at overlap of lesion masks with the thalamic masks.

ROIs were created in the left and right thalamus by eroding the segmented masks by two, voxels in order to avoid partial volume effects. Thalamic segmentation and ROI masks are shown in **Figure IV.3**.

Exploratory comparison between left and right thalamic volumes in the HC group revealed a significant difference, with the right thalamus being on average 2.13% smaller than the left (paired t-test, $p < 0.001$). To assess whether this effect was consistent across both groups, an asymmetry index was calculated as the ratio of the difference between left and right, to the average volume. Because this ratio did not significantly differ between the groups ($p = 0.1$), volumetric and quantitative values between left and right thalamus were averaged for each subject.

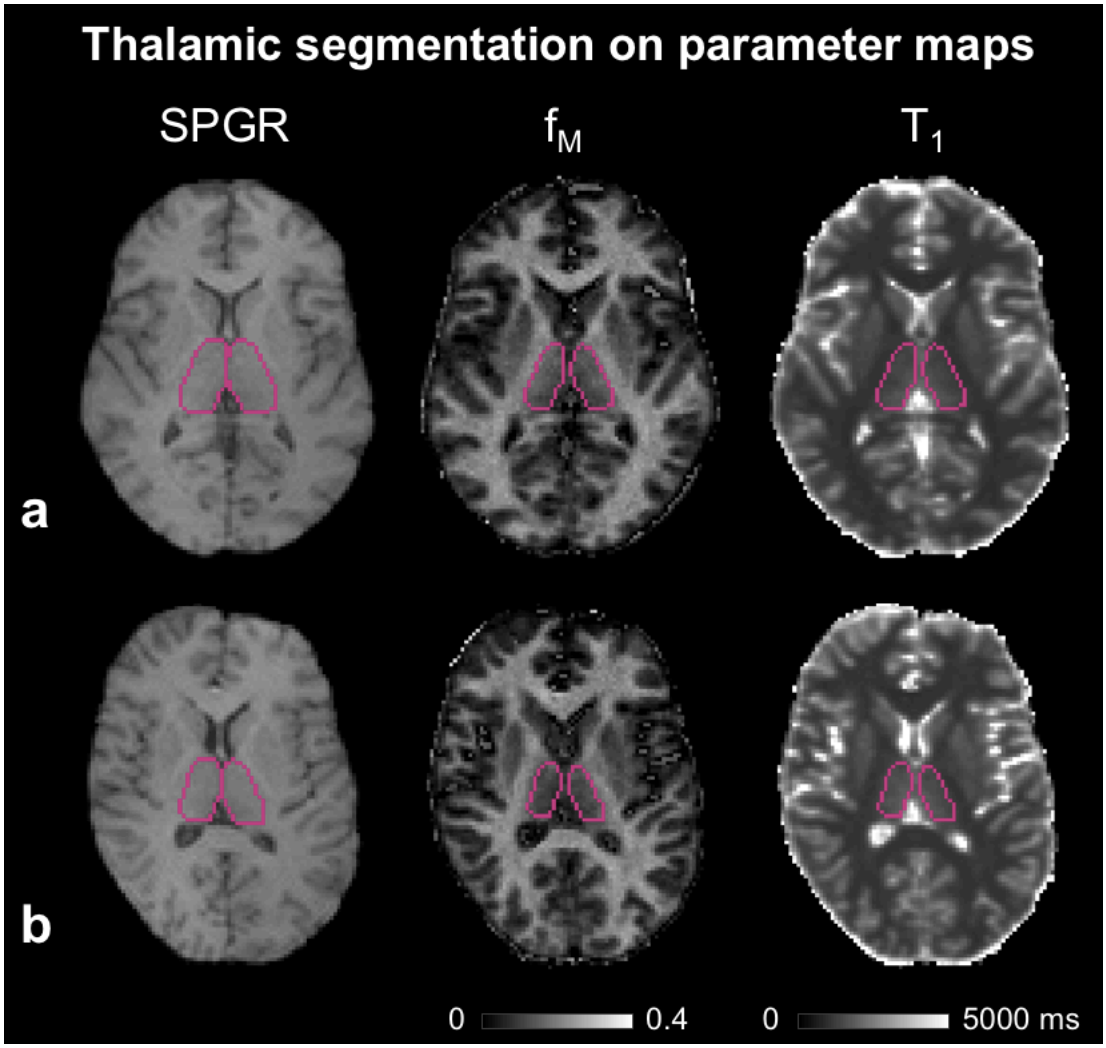

Figure IV.3. Example thalamic masks and quantitative maps with overlaid regions of interest for: **a)** a healthy control, 46 years old, female; **b)** a neuromyelitis optica spectrum disorder subject, 48 years old, female, disease duration 7 years, EDSS 1. The masks used to collect quantitative metrics are slightly eroded compared to the volume mask to avoid partial volume effects. f_M: myelin water fraction. ms: milliseconds. SPGR: (T_1-weighted) spoiled gradient recalled.

IV.3.4. Statistical analysis

Statistical analysis was conducted in R version 3.3.3 (R Core Team, 2017). Group comparisons were performed using Student's t-test. As lesion load was found to have a non-normal distribution, the relationships between this measure and thalamic metrics were assessed using Spearman's rank correlation coefficient. Multiple regression analysis was used to test whether thalamic metrics could predict SDMT score in the NMOSD subgroup, with age as a covariate. All tests were considered significant at $\alpha = 0.05$.

IV.4. Results

IV.4.1.1. Sample description

The NMOSD and HC groups did not significantly differ in age (p = 0.8). In the NMOSD group, all but two subjects had detectable brain lesions. Among those with lesions, all had lesions in the WM, apart from one subject whose focal abnormalities were restricted to the right thalamus.

IV.4.1.2. Volumes

Tissue-compartment-specific volumes for NMOSD and HC, and results from group comparisons performed using Student's t-test are presented in **Table IV.2**, and shown in **Figure IV.4**.

Table IV.2. Tissue compartment volumes.

Volumes (cm^3)	HC	NMOSD	% diff.	p
Whole-brain	1715.42 ± 77.18	1578.68 ± 116.27	-7.97%	**< 0.001*** **
Cortical GM	563.08 ± 39.9	568.98 ± 69.16	+1.05%	0.747
Subcortical GM	131.04 ± 13.32	133 ± 17.10	+1.68%	0.655
WM	1021.230 ± 64.87	876.45 ± 45.10	-14.18%	**< 0.001*** **
vCSF	26.76 ± 13.43	41.27 ± 21.18	+54.21%	**0.016***
Lesions	N/A	2.55 ± 3.44	N/A	N/A
Lesions in WM	N/A	1.97 ± 2.60	N/A	N/A

All volumetric measures, including white matter (WM) lesion volume, are normalized with respect to intracranial volume. cm: centimetre. f_M: myelin water fraction. GM: grey matter. HC: healthy controls. ms: milliseconds. NMOSD: neuromyelitis optica spectrum disorder. N/A: not applicable. vCSF: ventricular cerebrospinal fluid. WM: white matter. % diff.: percent difference of NMOSD relative to HC. *Significant at p < 0.05; ***at p < 0.001.

There were highly significant reductions in whole-brain and WM volume (both p < 0.001), as well as an increase in ventricular CSF volume (p = 0.016) in NMOSD compared to HC. There were no significant differences between the groups in cortical or subcortical GM volumes.

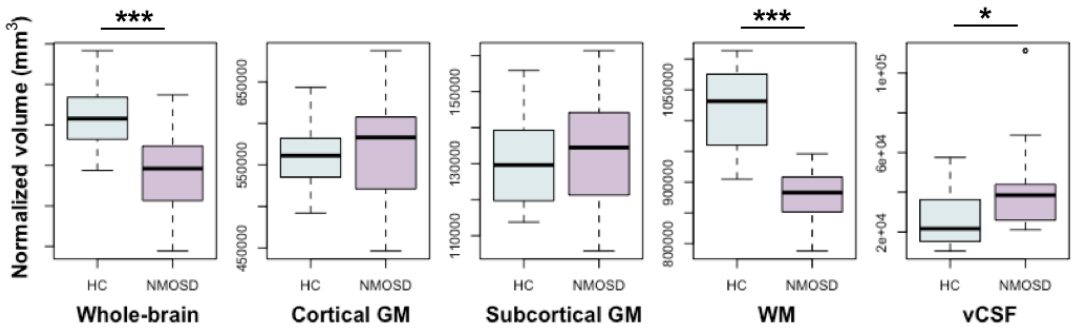

Figure IV.4. Group comparison between SIENAX-derived normalized volumes. Data points outside of boxplot whiskers are outliers, defined as being beyond 1.5 interquartile range of each quartile. GM: grey matter. HC: healthy controls. mm: millimetres. NMOSD: neuromyelitis optica spectrum disorder. vCSF: ventricular cerebrospinal fluid. WM: white matter. *Significant at $p < 0.05$; ***at $p < 0.001$.

IV.4.1.3. WM regions

Group averages and differences in f_M and T_1 between WM ROIs are reported in **Table IV.3**, and shown in **Figure IV.5**.

Across all NAWM, f_M was reduced by 2.96% in the NMOSD group compared to HC, although this did not reach statistical significance ($p = 0.068$). There was a significant increase of 2.15% in T_1 ($p = 0.02$).

T_1 was increased in NMOSD in the frontal, CST, OR and total NAWM, while f_M was only reduced in NMOSD in the frontal WM and OR. Metrics in the CC differed only at a trend level of significance for both parameters (both $p < 0.1$).

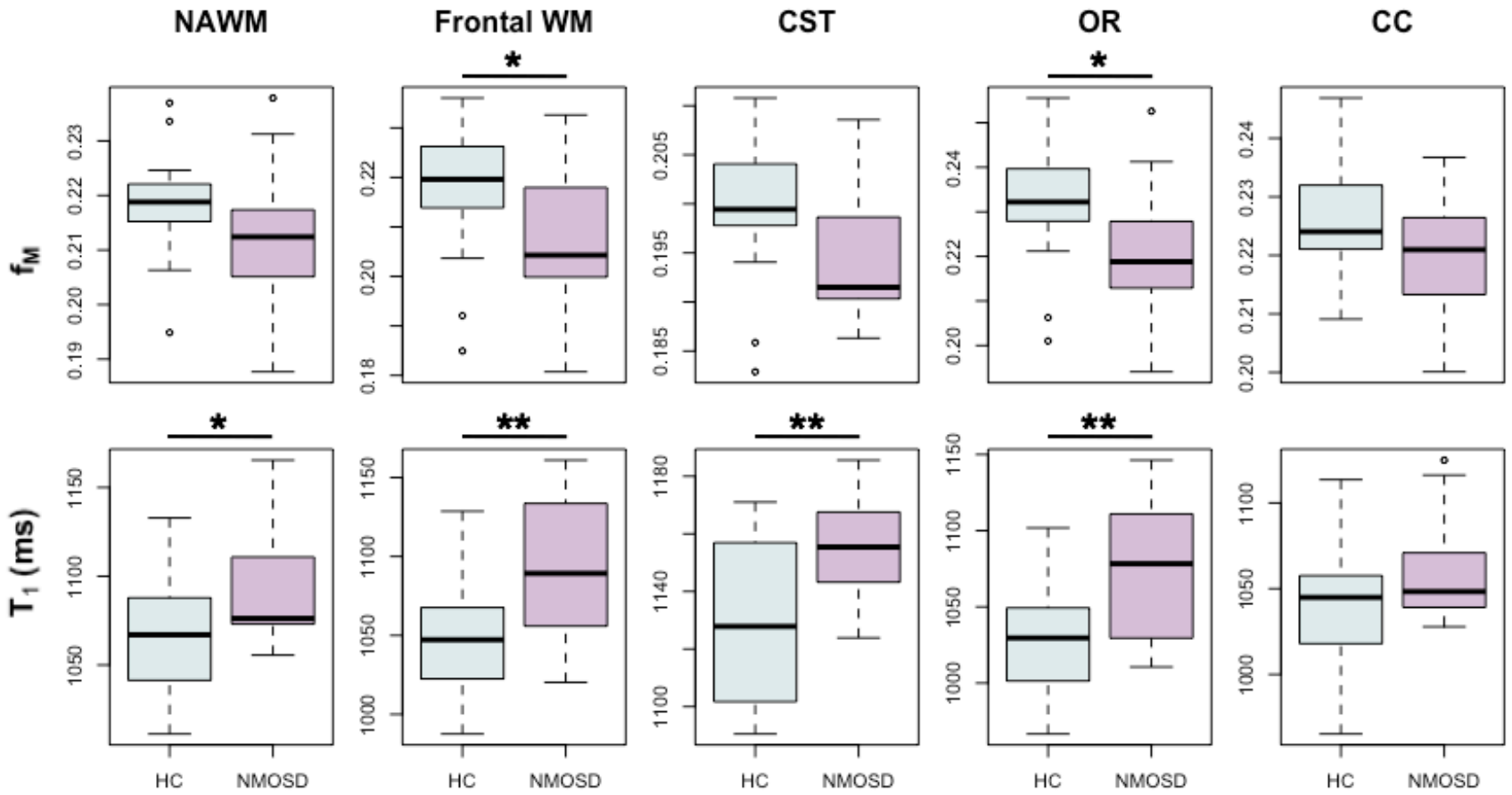

Figure IV.5. Myelin water fraction and T_1 across white matter regions of interest. Data points outside of boxplot whiskers are outliers, defined as being beyond 1.5 interquartile range of each quartile. CC: corpus callosum. CST: corticospinal tract. f_M: myelin water fraction. HC: healthy controls. ms: milliseconds. NAWM: normal-appearing white matter. NMOSD: neuromyelitis optica spectrum disorder. OR: optic radiation. WM: white matter. *Significant at $p < 0.05$; **at $p < 0.01$.

Table IV.3. f_M and T_1 values for white matter regions of interest.

	HC	NMOSD	% diff.	p
f_M				
Frontal WM	0.218 ± 0.013	0.208 ± 0.16	-5.06%	**0.047***
CST	0.200 ± 0.007	0.195 ± 0.007	-2.52%	0.077
OR	0.233 ± 0.013	0.221 ± 0.017	-5.17%	**0.037***
CC	0.226 ± 0.009	0.220 ± 0.010	-2.63%	0.070
Total NAWM	0.218 ± 0.009	0.212 ± 0.012	-2.96%	0.068
T_1 (ms)				
Frontal WM	1051.87 ± 36.26	1089.72 ± 42.90	+3.94%	**0.005****
CST	1131.31 ± 27.57	1155.09 ± 20.06	+2.10%	**0.010****
OR	1028.66 ± 37.79	1074.44 ± 47.38	+4.45%	**0.008****
CC	1040.08 ± 36.98	1058.17 ± 28.55	+1.73%	0.098
Total NAWM	1067.71 ± 31.53	1090.69 ± 30.31	+2.15%	**0.024***

Subjects with lesions in specific regions were excluded on a region of interest basis. Three NMOSD subjects had lesions in the frontal white matter; two in the corpus callosum; six in the optic radiations; eight in the corticospinal tract. CC: corpus callosum. CST: corticospinal tract. f_M: myelin water fraction. HC: healthy controls. ms: milliseconds. NAWM: normal-appearing white matter. NMOSD: neuromyelitis optica spectrum disorder. OR; optic radiations. WM: white matter. % diff.: percent difference of NMOSD relative to HC. *Significant at $p < 0.05$; **at $p < 0.01$.

IV.4.1.4. Thalamus metrics

Four NMOSD subjects had small unilateral thalamic lesions (one left, three right). Thalamic volumes and quantitative parameters are reported in **Table IV.4**, and shown in **Figure IV.6**.

The NMOSD group had on average lower thalamic volumes compared to HC, although this did not reach significance (-5.35%, $p = 0.08$). There were no significant differences in either f_M or T_1 within the thalamus between the groups (both $p > 0.05$).

Scatter plots showing relationships with WM lesion load are shown in **Figure IV.7**. There were no significant correlations between WM lesion load and thalamic volume (Spearman's rho = -0.29, $p = 0.2$), nor between WM lesion load and thalamic f_M (rho = 0.2, $p = 0.5$) or T_1 (rho = -0.44, $p = 0.06$).

Table IV.4. Thalamic quantitative metrics.

Thalamic parameters	HC	NMOSD	% diff.	p
Volume (cm^3)	11.77 ± 0.95	11.14 ± 1.24	-5.35%	0.084
f_M	0.126 ± 0.007	0.124 ± 0.012	-1.86%	0.457
T_1 (ms)	1505.86 ± 47.96	1514.57 ± 65.14	+0.58%	0.636

Thalamic volume is normalized with respect to intracranial volume. Metrics are shown averaged between left and right. cm: centimetre. f_M: myelin water fraction. HC: healthy controls. ms: milliseconds. NMOSD: neuromyelitis optica spectrum disorder. % diff.: percent difference of NMOSD relative to HC.

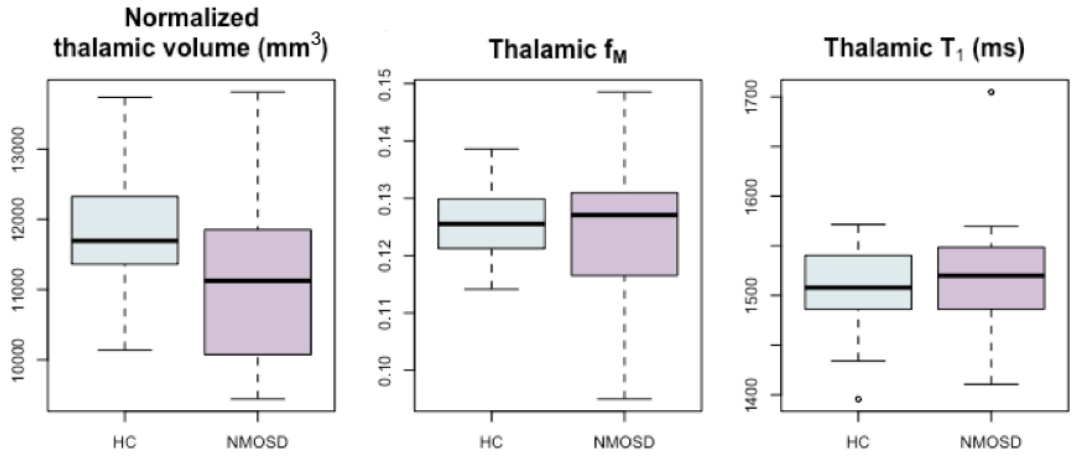

Figure IV.6. Group differences in normalized thalamic volume, thalamic f_M and T_1 between healthy controls (HC) and neuromyelitis optica spectrum disorder (NMOSD) subjects. Data points outside of boxplot whiskers are outliers, defined as being beyond 1.5 interquartile range of each quartile. f_M: myelin water fraction. mm: millimetres. ms: milliseconds.

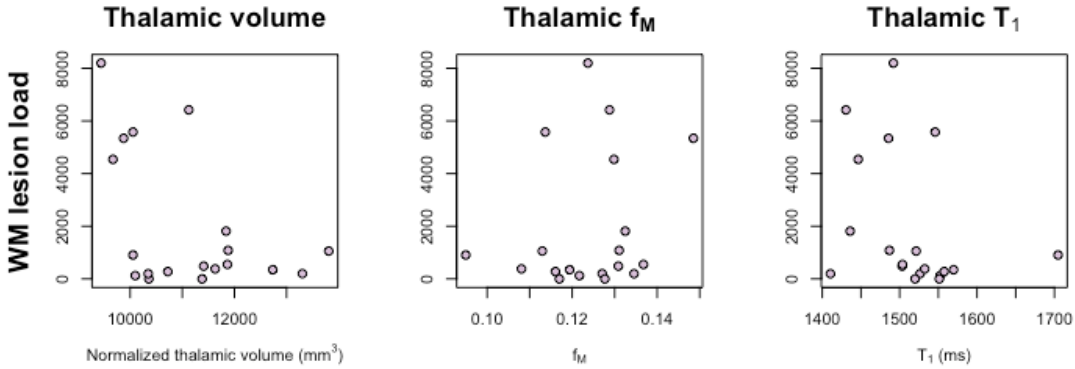

Figure IV.7. Scatter plots between white matter lesion volume and thalamic metrics in the neuromyelitis optica spectrum disorder group, all scaled to intracranial volume. None of the correlations assessed were significant (all $p > 0.05$). f_M: myelin water fraction. mm: millimetre. ms: milliseconds. WM: white matter.

IV.4.1.5. Relationships with SDMT score

Relationships between SDMT and thalamic quantitative parameters (volume, f_M and T_1) are shown in **Figure IV.8**.

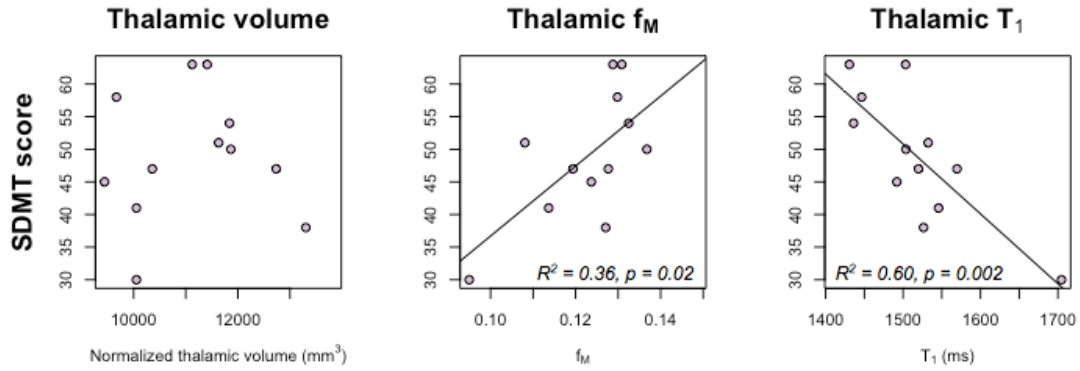

Figure IV.8. Scatter plots between SDMT score and thalamic metrics: normalized thalamic volume, average thalamic f_M and T_1 in a subset of neuromyelitis optica spectrum disorder subjects (n = 12). A higher SDMT score reflects better performance. Significant results from univariate linear regressions are shown. f_M: myelin water fraction. SDMT: symbol digit modalities test.

Exploration of variables while setting up the multiple regression analysis revealed that f_M and T_1 were highly related (Pearson's r = -0.77, p < 0.001), violating the assumption of non-collinearity between independent variables. Univariate linear regressions showed that T_1 significantly explained a higher amount of variance in SDMT score (R^2 = 0.60, p = 0.002) than f_M (R^2 = 0.36, p = 0.02), therefore f_M was not included in the regression model. Thalamic volume was not related to either f_M (r = -0.07, p = 0.8) or T_1 (r = 0.01, p = 0.9).

Multiple regression analysis showed a significant overall effect of thalamic metrics on SDMT score when controlling for age (adjusted R^2 = 0.51, p = 0.04). However, neither age (p = 0.6) nor thalamic volume (p = 0.8) significantly contributed to the model, and therefore T_1 was retained as the sole predictor of SDMT score.

IV.5. Discussion

IV.5.1. Summary of findings

We used MWI to investigate abnormalities in the NAWM and the thalamus in an NMOSD group compared to HC. Regional analysis of quantitative parameters revealed abnormal f_M, and elevated T_1 in several selected ROIs: f_M was reduced in the frontal WM and OR, and T_1 was increased in the frontal WM, OR, CST and total NAWM in NMOSD compared to controls. Indices in the CC were normal. Thalamic volume, f_M and T_1 did not differ between NMOSD and HC, and in the NMOSD group, these metrics were unrelated to WM lesion load. Assessing relationships between thalamic variables and SDMT score while controlling for age, T_1 emerged as a strong predictor of performance.

IV.5.2. Volumetric measures

Volumetric analysis showed a similar pattern to that seen in the literature, with significant WM atrophy and preserved GM volumes. The absence of cortical atrophy is expected and in line with most previous studies, that only find distributed regional volume loss in select areas. Of note, the large difference in ventricular CSF volumes reflects a high variance in the NMOSD group (i.e. some subjects having severe ventricular enlargement). One study using VBM of the ventricular CSF compartment found that enlargement of the third ventricle was especially severe compared to controls. Tissue loss due to periependymal inflammation has been brought up as a possible explanation for this observation (Schneider et al., 2016).

IV.5.3. NAWM pathology

IV.5.3.1. Possible aetiology

There is mounting, if inconclusive, evidence for the presence of diffuse demyelination in NAWM; its detection appears to depend in part on the technique used. Jeong et al. used ViSTa and GRASE MWI to compare a range of ROIs between seropositive NMOSD and HC subjects (Jeong et al., 2017). They found that ViSTa was more sensitive than ‘conventional’ MWI in detecting group differences; this however raises the question of the specificity of this more recent, non-quantitative technique to demyelination as opposed to other pathological

substrates. Preliminary work comparing mcDESPOT with GRASE in MS and NMOSD has suggested that the latter may be more sensitive to group differences (Kolind et al., 2015a), which requires further investigation.

Using a quantitative, myelin-specific technique, we bring further evidence that demyelination can be observed outside of lesions. We observed abnormal parameters in areas where secondary damage is expected (OR, CST), however, the presence of abnormalities in areas where other influences may be at play (CC, frontal WM) remains unclear. Alterations in T_1 were observed in more regions than f_M; when considering the whole NAWM as an ROI, only T_1 was abnormal. We confirm some robust findings in the literature showing relative preservation of CC integrity, and abnormalities in the OR and CST. Significant demyelination in the OR has been shown before, including with two different MWI techniques (Jeong et al., 2017; Manogaran et al., 2016a).

The greater sensitivity of T_1 to detect group differences in these regions suggests that, when present, demyelination is unlikely to be the main pathological process, and that changes in water content and/or axonal pathology may underlie the diffuse abnormalities seen in the brain. In support of this, Liu et al. found abnormal MD and radial diffusivity parameters, but normal FA in the NAWM, and raised the possibility of the presence of 'low-grade' damage, possibly due to an increase in intracellular water content, astrocytic pathology, or antibody-mediated cellular injury (Liu et al., 2012b).

Disruption of AQP4 channels may lead to disturbances in cerebral water homeostasis, but the relationship between this process and MRI metrics is unknown, and the influence of water content changes in brain tissue specific to NMOSD pathology on MRI parameters remains to be examined. Therefore, techniques such as absolute water content measurement, and markers of axonal damage and loss (e.g. g-ratio, neurite orientation dispersion measures) used in combination may hold promise for the assessment of diffuse WM damage, and to determine whether a primary pathological process can explain the abnormalities observed in regions putatively less susceptible to secondary damage (CC, frontal WM). Using multi-echo T_2 relaxometry data to obtain absolute measures of water content, preliminary work has shown increases in water content in the NAWM (Vavasour et al., 2016), which would be an interesting measure to explore in conjunction with MWI.

IV.5.3.2. Corpus callosum

A number of the studies cited above report abnormalities of the CC (He et al., 2011b; Zhao et al., 2012), which in MS has known susceptibility to axonal damage following lesions throughout the WM, via secondary degeneration of commissural fibres (Evangelou, 2000). Despite inconsistent findings, it has been proposed that DTI indices in the CC could help differentiate between RRMS and NMO (Yu et al., 2007). While we did not assess callosal atrophy, we found normal f_M and T_1 values in this structure (although both of these results could be considered borderline significant at $p < 0.1$). The severity of pathology in the CC has been proposed as a differentiating feature between MS and NMOSD, which is supported by the present observation.

IV.5.4. Thalamus findings

IV.5.4.1. Structural damage

The absence of significant thalamic atrophy is in line with other studies using FIRST (see **IV.2.3**). The present results provide complementary evidence that tissue integrity in this structure may be preserved, or only subject to subtle alterations, in NMOSD.

One study found increased FA and decreased MD in the thalamus of NMOSD subjects, which the authors suggest may be consistent with "increased myelination and axonal packing" (Zhao et al., 2012). They raise the hypothesis of a possible compensatory effect from damage to other regions, or to the surrounding white matter; however, this has not been consistently replicated (Finke et al., 2016; Liu et al., 2015a). We found normal myelin content in the thalamus, and no relationship of f_M to WM lesion load. Although not yet extensively studied, in MS, demyelination of DGM structures has been found to be related to cortical, but not WM demyelination (Minagar et al., 2013); therefore, normal f_M would be consistent with the lack of cortical demyelination found in NMOSD. Normal microstructural parameters suggest that thalamic demyelination may not be the main feature underlying the abnormalities reported in the DTI literature. Further multimodal investigations into the type of tissue damage driving the loss of thalamic volume observed in some studies would shed light on this.

The vicinity of the thalamus to the ventricles, a region of high AQP4 expression, has been invoked as reason it may be vulnerable to AQP4-antibody attacks (Hyun

et al., 2016; Su et al., 2016), suggesting that abnormalities may be due to a direct pathological process, and not just secondary damage. However, previous investigations have shown a relationship with lesion volume (excluding subjects with thalamic lesions), which is evidence towards a secondary origin of thalamic pathology as it would result from distal lesions in thalamic tracts. In MS, it has been proposed that lesions in the thalamocortical WM could cause retrograde damage to the thalamic nuclei (Henry et al., 2009), and thalamus volume has been linked with T_2 lesion volume in RRMS (Duan et al., 2012; Shiee et al., 2012). In this study, we found thalamic parameters to be unrelated to WM lesion load. However, the lack of spread in lesion load in the current sample may be a limiting factor.

IV.5.4.2. Influence of demographic factors

Thalamic atrophy has been an inconsistent finding in previous studies. The present investigation used a Canadian group of mixed ethnicity and AQP4 antibody status. Some authors have remarked that studies in Asian populations tend to find thalamic atrophy, while those in Caucasian groups do so less often (Hyun et al., 2016). Although the distinction regarding a distinct 'Asian optic-spinal MS' and NMOSD is generally regarded as outdated, and the differences are as likely to be due to differences in analysis methods, centre-dependent therapeutic options, and genuine heterogeneity in cohorts as they are attributable to race, the differing prevalence of NMOSD based on ethnicity suggests these discrepancies may be grounded in real phenotypic differences, although this remains to be examined (Finke et al., 2016).

Fan et al. found reduced thalamic volumes in seronegative, but not in seropositive subjects compared to HC, and suggested that AQP4-antibody-negative NMOSD could represent a 'halfway phenotype' between MS and NMO (Fan et al., 2017).

IV.5.4.3. Thalamic segmentation

Regarding volume measurements, segmentation of the thalamus can be complicated by its mixed grey and white matter content, which gives it a 'blurry' delineation on T_1-weighted images and may lessen the precision of volume estimates. When it came to ROI measurements, conservative masks were used in order to prevent contamination by ventricular CSF.

Only one study has looked at regional variations in thalamic parameters, segmenting the structure into functionally distinct subregions; all subregions were consistently affected with respect to volume loss, reduced FA and increased MD (Liu et al., 2015a). However, Pache et al. found reduced FA in the posterior thalamic radiations but normal thalamic volumes, using an ROI approach (Pache et al., 2016). Using TBSS, Pichiecchio et al. found reduced FA in the OR extending into the thalamic lateral geniculate nuclei, part of the optic pathways, in patients with a history of optic neuritis (Pichiecchio et al., 2012).

Therefore, it is possible that subregional differences may exist; thalamus parcellation may afford additional information, as would voxelwise assessment of volume and quantitative parameters, which may reveal localized changes not detectable with whole-ROI measures. The use of T_1 maps has been proposed to improve segmentation of thalamic nuclei, based on an a priori atlas (Traynor et al., 2011), which may be an interesting extension to the current study, although this would require images with higher resolution than were available here. Other advanced methods for segmenting the thalamus have been proposed, based on structural connectivity assessed with diffusion tensor imaging (Behrens et al., 2003).

IV.5.4.4. Relationship of thalamic metrics with cognitive performance

We found relationships between both f_M and T_1 with SDMT score in an NMOSD group. T_1 and f_M are intrinsically correlated (De Santis et al., 2014), due to the influence of macromolecules on longitudinal relaxation; however, T_1 emerged as the strongest predictor of performance, even in the absence of significant differences with a control group. Associations between indices of thalamic pathology and cognitive scores have previously been reported (Blanc et al., 2012; Wang et al., 2015), and the present finding provides further evidence that this structure may be linked with cognitive impairment in NMOSD.

It is likely, as is frequent in neurological populations, that other causes or mediating factors contribute to cognitive slowing than a purely organic aetiology. No studies have so far found links between cognitive impairment and depression in NMOSD (Blanc et al., 2008; He et al., 2011a; Saji et al., 2013). A link with sleep abnormalities is possible; thalamic neurons are involved in sleep regulation, and thalamic atrophy (right-lateralized only) has also been linked with disturbances in

slow wave sleep (Su et al., 2016). The interaction of sleep, depression, and their impact on cognitive disturbances are unknown, and further studies are needed to address this in the context of NMOSD.

IV.5.5. General limitations

IV.5.5.1. Population

Kim et al. remarked that the heterogeneity of results obtained in investigations of the brain in NMOSD may be attributable to the following causes: discrepancy in diagnostic criteria employed; proportion of seropositive subjects, and presence of brain lesions (Kim et al., 2016b).

All but two subjects included in this study had detectable brain lesions. Despite the presence of some subjects with short disease durations, all NMOSD subjects had an EDSS ≥ 1, ensuring at least some degree of disease evolution. Moreover, the group included a balance of AQP4 antibody-positive and negative subjects. While reflecting the broad spectrum of NMOSD disease in a real-world setting is interesting, it could be argued that research should focus on seropositive cases in order to better identify the pathological features of the disease. We did not assess the influence of serostatus on results, although exploration of the results did not show differences between these subgroups [data not shown]. (This negative result should of course be viewed in the context of the small group sizes, as well as the resulting differences in other clinical characteristics in the subgroups, after subdividing by seropositivity.)

Myelin oligodendrocyte glycoprotein (MOG) antibodies are found in 21-33% of AQP4-IgG-negative NMOSD cases, although MOG-immunoglobulin (MOG-IgG) seropositivity is not specific to NMOSD (Sato et al., 2014; van Pelt et al., 2016). Of particular relevance to the present study, one group noted the higher prevalence of deep grey matter lesions in a MOG-IgG-positive sample compared with AQP4-IgG-positive NMOSD subjects (Kitley et al., 2014b). Here, the presence of MOG antibodies was not assessed, and thus we could not ascertain the proportion of these patients in our sample nor compare and contrast their characteristics to HC and AQP4-IgG-positive subjects.

Sample size is an evident issue common to research in rare disorders, and especially for the cognitive data presented here. Another general limitation, as noted by Pache et al., is that chronically ill patients on polypharmacotherapies are

likely to show various structural changes when compared to matched “super-controls” in research studies (Pache et al., 2016).

IV.5.5.2. Defining cognitive performance

Defining individual patients as cognitively impaired vs. preserved requires normative data, or ranking performance compared to a control population. This can be done by determining cut-off values based on deviation from normalized performance on one or an assortment of cognitive tests, in comparison with a control group assessed concurrently, or using literature-derived normative values. However, in MS research, the separation of patients in two groups (impaired vs. non-impaired) based on cut-off values on one or several tests, or on the number of tests within a battery meeting a certain cut-off point, has been criticized as disregarding which domains cognitive impairment manifests in (Levin et al., 2017). The definition of “cognitive phenotypes”, and the potential of such classification in improving detection of cognitive impairment and therefore the efficacy of treatment and remediation strategies, has been highlighted as a priority in the field of cognitive rehabilitation (Sumowski et al., 2018).

The SDMT, considered the most sensitive method of measuring information processing speed (IPS), is itself related to broader cognitive functioning, which has a high impact on activities of daily living in MS (Benedict et al., 2017). IPS is thought to be the main domain underlying impaired performance in other domains, such as executive function and working memory (Leavitt et al., 2014), and plays a greater role than working memory impairment in explaining general information processing deficits in MS patients (DeLuca et al., 2004). Slowed IPS also underlies difficulties in planning ability in a problem-solving context (Tower of London task) (Owens et al., 2013), and SDMT score has been linked with automobile driving performance in MS patients (Schultheis et al., 2010).

This score can therefore be regarded as a measure of cognitive performance rather than impairment. In MS, it is strongly associated with brain atrophy, T_2 lesion volume (Rao et al., 2014) and thalamic atrophy (Batista et al., 2012). There is strong support for its use above other tests in clinical practice (Benedict et al., 2002; Langdon et al., 2012), and it has recently been suggested as a replacement for the PASAT in MS clinical trials (Benedict et al., 2017), due to its ease of administration and rating, and its strong psychometric profile in terms of sensitivity

and construct validity (Sonder et al., 2014). Here, we were interested not in defining cognitive impairment, or even impaired IPS, as a discrete category, but in probing subtle changes in performance. We therefore employed the SDMT as a measure of cognitive slowing.

Additional information on performance in other cognitive domains, such as attention, memory or visuospatial perception, would without a doubt be valuable. A self-contained battery designed for use in MS, such as the Brief International Cognitive Assessment for MS (BICAMS; (Langdon et al., 2012)), would offer the advantage of providing normative values based on demographic characteristics. Other available batteries designed for use with MS populations include the Brief Repeatable Battery of Neuropsychological tests (BRB-N) and the Minimal Assessment of Cognitive Function in MS (MACFIMS), which take 45 and 90 minutes respectively (Langdon, 2011). A range of neuropsychological tests have been used in previous studies of NMOSD (see IV.2.4), with the BRB-N battery appearing most frequently (Eizaguirre et al., 2017). However, these tools have not yet been validated for use in NMOSD. The SDMT forms part of these three batteries, and the BICAMS panel echoed previous recommendations that when time or other constraints should limit assessment to a single test, the SDMT should be used, which motivated the choice of this measure in the present study (Sepulcre et al., 2006).

Other limitations of the cognitive assessment performed here include the lack of cognitive data for HC. Cognitive testing for some subjects was not done at the time of scanning, a major limitation to the precision of this analysis. In addition, longitudinal studies tracking the evolution of cognitive performance over time, in relation to attacks and MRI activity, would be useful.

IV.5.5.3. Lesion segmentation

It should be noted that the FLAIR^2 method is experimental, and has only been fully evaluated for the assessment of MS lesions. The different characteristics of NMOSD lesions may lead to different contrast and thus appearance on FLAIR^2, and this would require validation. In this project, it was meant to be an aid to lesion identification, in conjunction with other images.

Moreover, lesion assessment was performed by trained, but not expert, assessors, the aim being to isolate gross areas of focal pathology. While masks were reviewed

by an expert neurologist, the focus was on preventing false positives, and it is a possibility that some smaller, or less conspicuous lesions were missed. However, the purpose of lesion identification here was to measure WM lesion load, to mask out lesions from NAWM, and to identify lesions within specific ROIs. Therefore, we do not anticipate great impact of false positive or negatives in lesion detection to be a major factor in any of the results (i.e. lesions small enough to be missed would not have a major impact on the measurements performed here).

IV.6. Conclusion

We investigated quantitative indices of myelin content and T_1 relaxation time in NMOSD compared to HC. We found abnormal metrics in the OR and CST, consistently with previous literature findings, as well as in the frontal MW, a region where secondary demyelination would not typically be observed. Metrics in the CC were normal. The borderline significance of some results raises the question of the sensitivity of the metrics used to the tissue abnormalities in NMOSD in these regions. Because T_1 revealed a greater number of significant differences relative to the HC group, we hypothesize that changes in water content, rather than severe demyelination, are responsible for the differences observed. We also observed relationships between quantitative metrics of tissue integrity in the thalamus and a measure of IPS, even when those parameters were normal compared to controls and in the absence of atrophy. This result provides encouraging evidence for the association of thalamic pathology and cognitive performance in NMOSD.

Chapter V. Longitudinal cervical cord myelin water imaging in multiple sclerosis and neuromyelitis optica spectrum disorder

In this chapter, we present a longitudinal study of the cervical spinal cord in multiple sclerosis and neuromyelitis optica spectrum disorder using myelin water imaging. We collected mcDESPOT at baseline and one-year follow-up in matched controls and patients, in the absence of clinical relapses. We aimed to compare measures of cord volume and myelin water fraction at both time points, to assess the presence of abnormalities in normal-appearing and lesioned areas of the cord, as well as atrophy and changes in myelin content over time.

V.1. Introduction 142
V.2. Background 143
V.2.1. Disease progression in MS and NMOSD 143
V.2.2. Imaging the cervical cord 144
V.2.3. Cervical cord pathology in MS and NMOSD 146
V.2.4. Rationale for this study 147
V.2.4.1. Previous work 147
V.2.4.2. Study aims 147
V.3. Methods 148
V.3.1. Study design and population characteristics 148
V.3.2. MRI acquisition 148
V.3.3. Image analysis 149
V.3.3.1. Cord segmentation 149
V.3.3.2. Lesion identification 150
V.3.3.3. Volume measurements 151
V.3.3.4. Myelin water fraction measurements 151
V.3.4. Statistical analysis 152
V.4. Results 153
V.4.1. Cross-sectional 153
V.4.1.1. Lesion identification 153
V.4.1.2. Cord volume 154
V.4.1.3. Myelin measurements 155

V.4.2. Longitudinal 158
V.4.2.1. Changes in EDSS 158
V.4.2.2. Lesions 158
V.4.2.3. Volume changes 158
V.4.2.4. Changes in myelin water fraction 159
V.5. Discussion 159
V.5.1. Summary of findings 159
V.5.2. Volume differences and atrophy 160
V.5.3. Myelin water fraction measurements 161
V.5.3.1. f_M is reduced in lesioned areas in MS and NMOSD 161
V.5.3.2. f_M is reduced in NASCT in MS and NMOSD 161
V.5.3.3. f_M decreases over time in MS NASCT only 162
V.5.4. Methodological considerations 164
V.5.4.1. Influence of motion 164
V.5.4.2. Methods for cord volume measurement 164
V.5.4.3. Segmentation of lesions 166
V.5.4.4. Variations in myelin content along the cord 166
V.5.4.5. Treatment effects 167
V.5.4.6. Sample size 167
V.6. Conclusion 167
V.7. Additional information 169

V.1. Introduction

Spinal cord pathology is a feature of both neuromyelitis optica spectrum disorder (NMOSD) and relapsing-remitting multiple sclerosis (MS). While subclinical disease activity has been described in MS using quantitative magnetic resonance imaging (MRI) measures, current evidence suggests that neurodegeneration is absent between relapses in NMOSD. However, most of the evidence comes from brain studies, and only a limited number of studies have investigated cord pathology in NMOSD using advanced MRI.

A previous longitudinal study using a range of quantitative MRI metrics in the brain showed a lack of nonfocal damage in an NMOSD group at baseline, as well as stability over one year, but evidence of widespread abnormalities and ongoing neurodegeneration in a relapsing-remitting MS group (Matthews et al., 2015). Following up on this project, we investigated cervical cord atrophy and myelin integrity in clinically stable NMOSD and MS subjects compared to healthy controls. All participants were scanned using a multicomponent Driven Equilibrium Single Pulse Observation of T_1 and T_2 (mcDESPOT) protocol at baseline, and after one year in the absence of relapses. We collected measures of cervical cord volume, as well as myelin water fraction (f_M) within lesioned and non-lesioned areas. We aimed to assess myelin content in the cord outside of lesions in the patient groups, as well as the presence of detectable changes in these metrics over time.

V.2. Background

V.2.1. Disease progression in MS and NMOSD

NMOSD is a relapsing autoimmune disease of the central nervous system that, due to similar clinical and neurological features, was long thought to be a rare variant of MS (Wingerchuk et al., 2015). Since the discovery of a highly specific antibody (Jarius and Wildemann, 2010), and the advent of serum testing to aid differential diagnosis, it is now considered a separate entity (Weinshenker, 2007). Serum antibodies to the aquaporin-4 water channel protein (AQP4-Ab), found on astrocytic foot processes, are detectable in a high proportion of patients (Pandit et al., 2015). AQP4 is expressed throughout the brain, and is found in particularly high concentration in the optic nerve and spinal cord, in line with the observed frequency of pathology in these regions in NMOSD (Pittock et al., 2006b).

Unlike in MS, which can present as a relapsing-remitting disease with secondary conversion to a progressive phase, or as progressive from onset (Compston and Coles, 2008), conversion to a progressive phase is extremely rare in NMOSD (Aboul-Enein et al., 2013; Cabre et al., 2009; Collongues et al., 2014, 2010). Clinical disability is accrued as a consequence of damage sustained during relapses, whereas clinical disability scores in MS increase more steadily during the progressive phase (Collongues et al., 2011; Wingerchuk et al., 2007a). Current clinical and neuroimaging evidence suggests that subclinical disease activity does not occur between attacks in NMOSD (Wingerchuk et al., 2007b), contrary to what is observed in MS (Filippi and Agosta, 2010; Matthews et al., 2015). However, it

has been suggested that NMOSD attacks are so severe that the resulting sequelae hide the subtler changes that may accrue over time as a result of progressive axonal deterioration following relapse-related inflammation (Wingerchuk et al., 1999).

V.2.2. Imaging the cervical cord

The cervical cord is the portion of the spinal cord at the neck level. Anatomical locations of the cord can be labelled relative to the vertebral bones; the cervical cord corresponds to vertebral levels C1 to C7. It is 10-12 centimetres (cm) long, around 1 cm in diameter, and occupies about two thirds of the space in the spinal canal (Jacobson and Marcus, 2011). Morphological measures of the cord include volume and cross-sectional area (CSA) measurements, grey and white matter (GM, WM) areas and their ratio. These measurements vary across segments, although the cervical cord is relatively homogeneous in the rostro-caudal direction compared to the lower cord sections (Fradet et al., 2014).

There are several challenges to imaging the cervical cord, due to its small size, its high sensitivity to motion artefacts from the cardiac and respiratory cycles, and magnetic susceptibility effects due to the interface of air, tissue, and bone; however, recent technical efforts have endeavoured to translate the wide array of techniques available for brain imaging to the cord (Stroman et al., 2014), including myelin water imaging (MWI).

Wu et al. first implemented multi-echo T_2 (MET_2)-based MWI in the cervical cord *in vivo*, and showed good reproducibility (Wu et al., 2006). A similar protocol was subsequently applied to the cervical and thoracic portions of the cord (Minty et al., 2009), and used in primary progressive MS subjects to demonstrate reduced myelin water fraction at the C2/C3 level, and continued decrease over two years (Laule et al., 2010). MacMillan et al. found differences in MET_2-derived myelin water fraction at the C5 level between younger and older healthy adults (MacMillan et al., 2011).

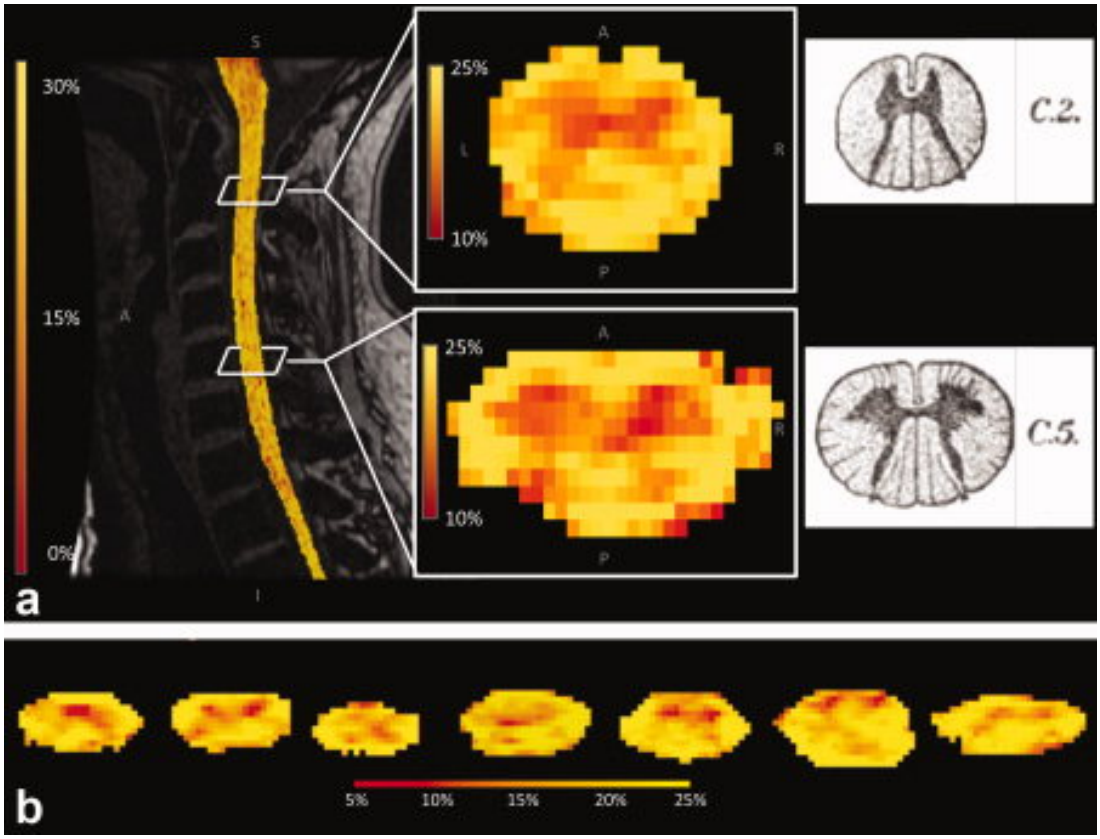

Figure V.1. mcDESPOT protocol in the cervical spinal cord. **a)** Cervical cord myelin water fraction (f_M) map for a healthy volunteer, with axial cross-sections at the C2 and C5 levels where the characteristic grey matter 'butterfly' is visible. **b)** Axial sections of f_M maps from seven healthy volunteers at the C2 level. Source: (Kolind and Deoni, 2011); inset from Gray's Anatomy (Mancall and Brock, 2011).

mcDESPOT is a quantitative MWI method with high sensitivity for the estimation of myelin content (Deoni et al., 2008a). Kolind and Deoni first implemented the protocol in the cervical cord (Kolind and Deoni, 2011). They showed good reliability for f_M estimates with the whole cervical cord taken as a region of interest, with an average coefficient of variation of 2.6% (range 0.6-5.7% across five healthy volunteers, scanned twice within 3 months), which compared favourably to the scan-rescan repeatability of other MWI methods. The axial resolution of 1 mm^2 also allowed for the visualization of GM and WM, with good contrast (**Figure V.1**). Only one study so far has used mcDESPOT in the cord in clinical research, to show that f_M in primary progressive MS patients was reduced by 11% compared to controls, and correlated with ambulatory and manual dexterity scores (Kolind et al., 2015b).

V.2.3. Cervical cord pathology in MS and NMOSD

Cord pathology is present in 80-90% of relapsing-remitting MS cases, with the cervical cord being a preferential site of involvement; demyelinating cord lesions are most often seen in the lateral and dorsal WM columns (Gass et al., 2015). In NMOSD, the main feature of cord pathology is the presence of longitudinally extensive lesions, spanning three or more vertebral segments, that favour the GM (Nakamura et al., 2008).

Cord lesions in NMOSD are characterised by abnormal diffusion metrics, reflecting greater tissue injury compared with MS lesions (Klawiter et al., 2012; Rivero et al., 2014). Abnormally low myo-inositol (normalized to creatine) levels have been measured in the upper cervical cord, proposed to reflect astrocytic dysfunction within lesions, a process thought to play a major role in the pathogenesis of the disease by contributing to oligodendrocyte dysfunction and eventually secondary demyelination (Ciccarelli et al., 2013). Abnormal magnetization transfer (Benedetti et al., 2006; Filippi et al., 1999; Rocca et al., 2004a) and diffusion parameters (Jeantroux et al., 2012; Pessôa et al., 2012; Qian et al., 2011; Rivero et al., 2014) have been observed in the cervical cord, suggesting the presence of inflammatory processes, demyelination and axonal pathology.

However, very few studies have differentiated between lesional and normal-appearing spinal cord tissue (NASCT). Abnormal mean diffusivity and perpendicular diffusivity parameters in the NASCT have been attributed to inflammation and demyelination, respectively (Qian et al., 2011). In another study, altered diffusion parameters were found in WM tracts in regions up- or down-stream of focal lesions in both diseases, while tracts not directly adjoining lesions were affected in MS, but not in NMOSD (Klawiter et al., 2012). Diffuse damage in unaffected tracts can be attributed to MS lesions not visible on standard imaging (e.g. those below the imaging resolution), diffuse damage, or distal effects of regions outside the cervical cord. Moreover, some of the abnormalities observed in brain may be secondary to cord pathology (Calabrese et al., 2012; Rocca et al., 2004b; Saji et al., 2013).

Overall, focal cord pathology in NMOSD is considered more aggressive; secondary degenerative processes in WM tracts may be common to both diseases (Klawiter et al., 2012). To date, no longitudinal advanced imaging study has assessed whether changes in NASCT occur in NMOSD outside of clinical relapses.

V.2.4. Rationale for this study

V.2.4.1. Previous work

In a recent multimodal investigation, Matthews et al. built upon the theory that occult damage in relapsing-remitting MS results from subclinical disease progression, rather than being merely secondary to focal pathology. They hypothesized that in NMOSD, evidence of disease activity between relapses would be absent, despite more severe relapse-related damage (Matthews et al., 2015). Advanced MRI surrogate markers of neurodegeneration, including regional atrophy measures, diffusion and MWI metrics in the brain were investigated over one year in clinically stable MS and aquaporin-4 antibody-positive NMOSD patients.

Their results showed evidence of widespread non-lesional abnormalities in the MS group only, using several MRI parameters including volumetric measures, MWI and diffusion tensor imaging. NMOSD non-lesional cerebral tissue was found to be similar to controls, except for abnormalities in the optic radiations, in relation with the high prevalence of previous optic neuritis in this group. No evidence of disease progression was seen in the NMOSD group, while several measures in the MS group showed changes over one year suggestive of subclinical disease activity, including the mcDESPOT-derived f_M in major WM tracts.

V.2.4.2. Study aims

In this study, we extend this work to the cervical spinal cord in a subset of the same cohort, including aquaporin-4 antibody-positive NMOSD, relapsing-remitting MS subjects, and matched healthy controls. Participants were scanned at baseline and one-year follow-up using mcDESPOT. We obtained measures of cervical cord volume and f_M, a surrogate marker of myelin content, differentiating between lesional and normal-appearing portions of the cord, to investigate cross-sectional differences and changes over time in patients and controls. We aimed to characterise normal-appearing and lesional cervical cord pathology at baseline, and to assess whether evidence of degenerative changes could be detected over one year in either patient group.

V.3. Methods

V.3.1. Study design and population characteristics

This study was approved by the South East Hampshire NHS Research Ethics Committee. 15 antibody-positive NMOSD patients, 15 relapsing-remitting MS patients, and 17 sex and age-matched healthy controls were recruited from the NHS Neuromyelitis Optica Highly Specialized Service in Oxford, UK. All participants gave written informed consent before taking part.

All NMOSD subjects were receiving immunosuppressant medication: 7 were on azathioprine, 2 on methotrexate, 1 on prednisone, and 5 on combinations thereof. The majority of MS subjects were on disease-modifying therapies (DMTs): 6 on Copaxone, 3 on beta-interferons, and 1 on low-dose naltrexone; 5 were not receiving treatment.

A subset of 8 NMOSD, 11 MS and 14 controls completed a follow-up scan after one year. All patients had been relapse-free for at least 6 months prior to the baseline scan, and none experienced a relapse between baseline and follow-up.

EDSS assessments were performed at both time points by a neurologist. There are varying definitions of what constitutes significant clinical deterioration using this scale. A commonly agreed upon definition in MS clinical trials is a change of 1 point if baseline score is ≤ 5.5, and 0.5 if baseline is ≥ 5.5, although a cut-off of 6 has also been recommended (Healy et al., 2013; Meyer-Moock et al., 2014).

V.3.2. MRI acquisition

Participants were scanned on a 3T MRI scanner (Siemens MAGNETOM Verio, Erlangen, Germany) using a custom-built neck coil.

The mcDESPOT protocol was acquired sagittally, and covered the whole cervical cord with 0.9 x 0.9 x 1.8 mm voxels, reconstructed to 0.9 mm^3 isotropic (Kolind and Deoni, 2011). Acquisition time was 22 minutes. Data consisted in a series of eight spoiled gradient echo (SPGR) scans over a range of flip angles (α), an inversion recovery-prepared SPGR scan for correction of B_1 inhomogeneity (Deoni, 2011), and eight balanced steady-state free precession scans (bSSFP). Repetition (TR), echo (TE), and inversion times (TI) below are in milliseconds.

SPGR: TE/TR = 2.7/6.1 ms; α = [2.25, 4.5, 6.75, 9, 11.25, 13.5, 15.75, 18]°.

IR-SPGR: TE/TR = 2.7/6.3 ms; TI = 450 ms; α = 5°.

bSSFP: TE/TR = 2.3/4.6 ms; α = [5.625, 11.25, 16.875, 22.5, 28.125, 33.75, 39.375, 45]°, acquired over two phase-cycling patterns (0° and 180°) to correct for off-resonance effects (Deoni, 2009a).

An axial T_2-weighted multi-echo gradient echo sequence (voxel size: 0.7 x 0.7 x 3 mm, TE/TR = 17/470 ms, 30 slices with the uppermost slice at the superior border of C2), a sagittal T_1-weighted magnetization-prepared rapid gradient echo (voxel size: 1 x 1 x 0.9 mm, TE/TR = 3.59/2300 ms, α = 9°), and a sagittal T_2-weighted turbo spin echo sequence (voxel size: 0.6 x 0.6 x 3 mm, 15 slices, TE/TR = 67/4590 ms) were acquired for lesion identification.

V.3.3. Image analysis

V.3.3.1. Cord segmentation

For each subject, an SPGR image from the mcDESPOT protocol with good contrast between tissue and cerebrospinal fluid (α = 9°) was used for preprocessing. The spinal cord was segmented using *PropSeg* (De Leener et al., 2014), a semi-automated propagation-based method from the Spinal Cord Toolbox[15] (SCT) (De Leener et al., 2017). Each subject's SPGR was warped to the MNI-Poly-AMU template (Fonov et al., 2014). The inverse transform was then applied to the template in order to obtain vertebral level segmentation in subject space (see **Figure V.2**).

[15] Details on the software can be found at: http://sourceforge.net/projects/spinalcordtoolbox

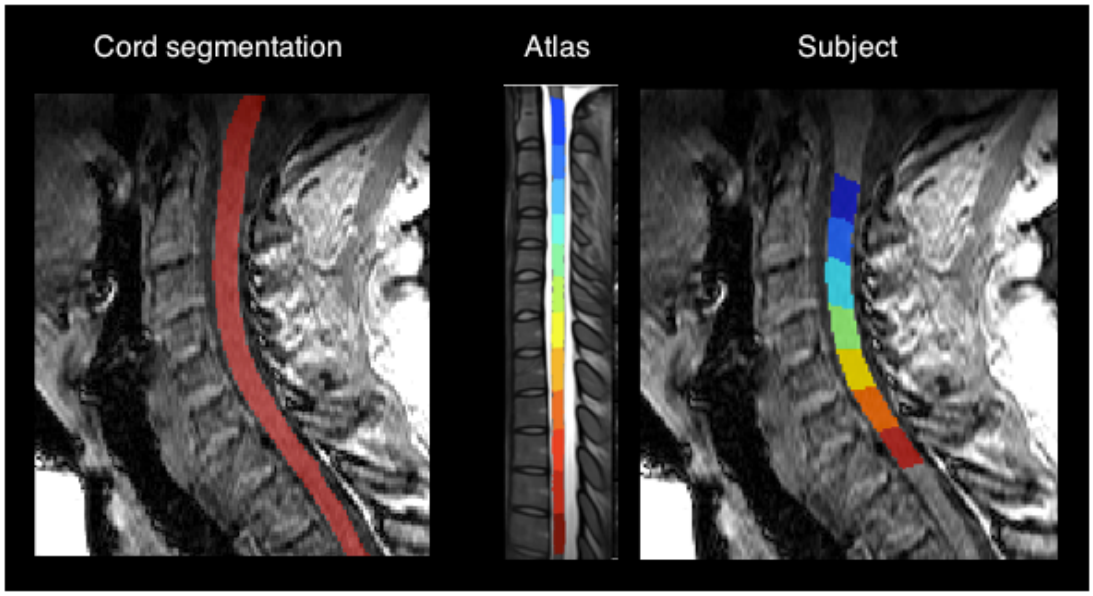

Figure V.2. Cord segmentation and vertebral level identification using the Spinal Cord Toolbox. A semi-automated binary segmentation method (*PropSeg*) is first applied to a structural T_1-weighted scan. A nonlinear transform from atlas to subject space is then applied to the MNI-Poly_AMU atlas. The labelling of vertebral segments, from C1 to C7, enables isolation of normal-appearing and lesioned areas of the cord.

V.3.3.2. Lesion identification

Lesions were identified on the patients' anatomical scans by an experienced radiologist blinded to diagnosis, primarily based on the sagittal T_2-weighted scan with additional information gleaned from the sagittal T_1 and axial T_2-weighted scans. The assessment was done for both baseline and follow-up concurrently. Spinal levels were identified as normal-appearing or lesioned. For small lesions located at a disc level, both adjoining segments were considered lesioned.

Using the segmentation and labelling procedure described above, separate masks were created including only segments marked as either normal-appearing or lesioned. An example of a lesioned tissue mask is shown in **Figure V.3**.

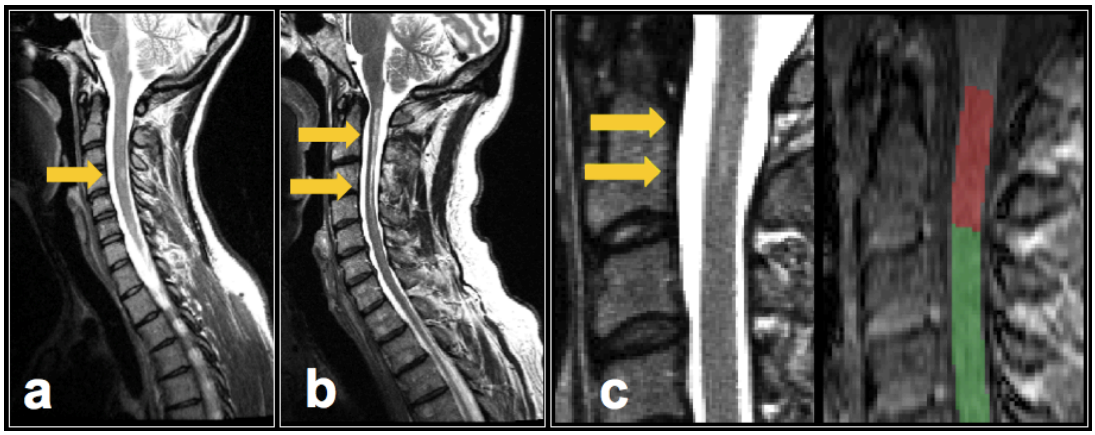

Figure V.3. Procedure for segmentation of lesioned areas. **a)** Example of a T_2-hyperintense lesion at the C4 level in a multiple sclerosis subject (female, 28 years old, EDSS 2), and **b**) an extensive lesion from C1 to C4 in a neuromyelitis optica spectrum disorder (NMOSD) subject (female, 39 years old, EDSS 3.5). **c)** Example of a T_2-hyperintense lesion in a (different) NMOSD subject at the C1/C2 level (left), and corresponding cord segmentation on an SPGR image from the mcDESPOT protocol (right). The area at the C1/C2 level was categorized as lesioned (in red), and the remaining portion of the cord as preserved tissue (in green).

V.3.3.3. Volume measurements

Cord length from the top of C1 to the bottom of C7 was calculated using the SCT, which determines the centerline of the segmented volume and corrects it for cord orientation. Cord volume, normalized by length, was measured on the SPGR scan. Volumes were collected in cubic millimetres, and cervical cord length in millimetres, therefore normalized volumes are reported in square millimetres (mm^2). This corresponds to the average cross-sectional area (CSA) of the cord, despite not being a direct measurement of this metric.

V.3.3.4. Myelin water fraction measurements

Visual quality control of individual images from mcDESPOT acquisition showed no significant nonlinear deformations between scans (see **V.5.4.1** for discussion of motion). Images were linearly registered within-subject to the reference SPGR scan with FSL-FLIRT (Jenkinson et al., 2002), using trilinear interpolation. Individual linear registration strategies were employed to ensure optimal co-registration for each volume when necessary (e.g. masking/weighting of relevant portions of the

region of interest; two-step registration using an intermediate image for bSSFP images with banding artefacts, etc.).

f_M maps were calculated with a three-pool model (Deoni et al., 2013), and manually edited by an observer blinded to group and time point to exclude voxels where partial volume effects in the acquired images led to artificially very low computed values. Visual inspection was performed on all images to ensure the quality of co-registration. Median f_M values were collected within the whole cervical cord for controls, and within NASCT and lesioned tissue separately for patients, using the masks described above.

V.3.4. Statistical analysis

Non-parametric tests were chosen due to small sample sizes, the presence of outliers, and after visual inspection showed that MRI variables were not normally distributed.

Percent changes between baseline and follow-up metrics were calculated for each subject. Differences between patient groups were evaluated using the Mann-Whitney U test, and between the three groups using the Kruskal-Wallis test. Post hoc comparisons following a significant omnibus test ($\alpha = 0.05$) were conducted with the Mann-Whitney U test.

Within-group differences were assessed using paired Wilcoxon's signed rank tests. We tested cross-sectional differences between NASCT and lesional segments within each patient group, and changes over time within each group and tissue type.

Results were not corrected for multiple comparisons, due to the exploratory nature of this study. Statistical analysis was conducted in R version 3.3.3 (R Core Team, 2017).

V.4. Results

Subject characteristics are summarized in **Table V.1**. There was no significant difference in age between the three groups (p = 0.6). Both patient groups had equivalent disease duration (p = 0.6). The NMOSD group had a higher median Expanded Disability Status Score (EDSS) (p = 0.03).

Summary baseline and longitudinal MRI metrics, and group comparisons are displayed in **Table V.2**.

Table V.1. Population characteristics for the cross-sectional sample.

	Controls	MS	NMOSD	p
N (sex)	17 (4M)	15 (4M)	15 (3M)	-
Age (years)	54 (19-76)	41 (22-68)	45 (20-76)	0.586
Disease duration (months)	-	72 (24-254)	60 (12-186)	0.589
Baseline EDSS	-	2 (0-5)	4 (2-7.5)	0.033*
Lesioned segments per subject	-	5 (0-7)	3 (0-7)	0.098
Number of subjects with NASCT	-	11	13	-
Number of subjects with ≥ 1 lesion	-	14	13	-

Values are reported as median (range) unless specified otherwise. Group comparisons are performed with the Kruskal-Wallis test. Where only pairwise MS vs. NMOSD comparisons are appropriate, results from the Mann-Whitney U test are reported. *Significant at p ≤ 0.05. EDSS: Expanded Disability Status Scale. M: male. MS: multiple sclerosis. NASCT: normal-appearing spinal cord tissue. NMOSD: neuromyelitis optica spectrum disorder.

V.4.1. Cross-sectional

V.4.1.1. Lesion identification

At baseline, in the MS group, a total of 67/105 segments (65%) were identified as containing lesioned tissue. Four MS subjects had lesions spanning the whole cervical cord, and one had no detectable lesions. In the NMOSD group, a total of 47/105 segments (45%) contained lesions. Two NMOSD subjects had lesions spanning the whole cord, and two had none. The number of lesional segments per subject did not differ significantly between groups (p = 0.1) (see **Table V.1**). The distribution of lesions along the cord is shown in **Figure V.8**.

V.4.1.2. Cord volume

Normalized cord volumes for each group can be seen in **Figure V.4**.

Compared to controls, both the MS (on average -6.5%, p = 0.1; not significant) and NMOSD (-12.5%, p = 0.009) groups had smaller volumes. The difference between MS and NMOSD was not significant, despite NMOSD having smaller volumes on average (-6.4%, p = 0.2).

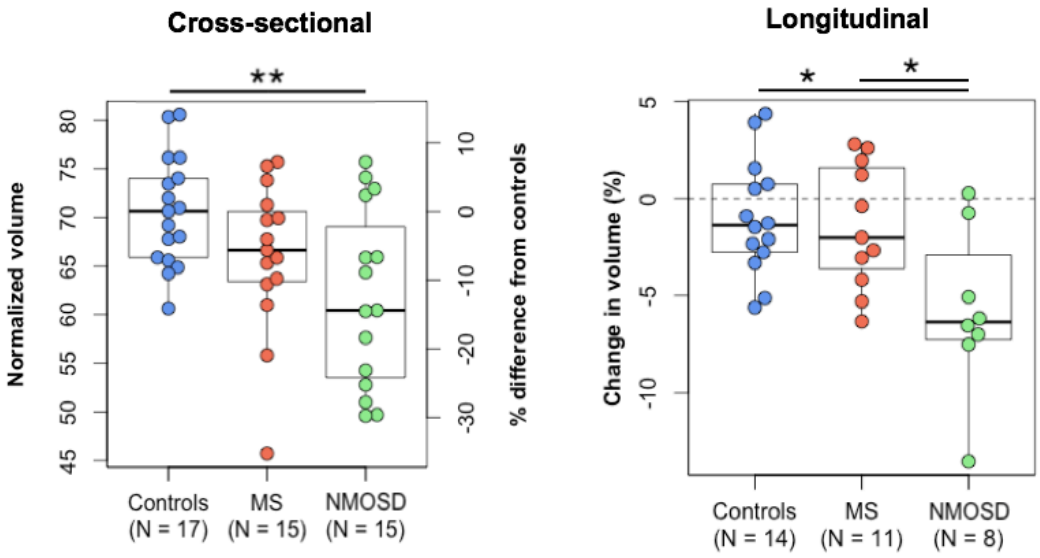

Figure V.4. Cervical cord volumes at baseline and over time. **Cross-sectional:** normalized cord volume at baseline. Right-hand axis shows percent difference of each data point from the control group average. **Longitudinal:** percent change over one year. Dotted line represents 0% change from baseline. Data points outside of boxplot whiskers are outliers, defined as being beyond 1.5 interquartile range of each quartile. *Significant at p ≤ 0.05, **p ≤ 0.01. MS: multiple sclerosis. NMOSD: neuromyelitis optica spectrum disorder.

V.4.1.3. Myelin measurements

Example maps are shown in **Figure V.5**, and f_M measurements at baseline in **Figure V.6**.

f_M was significantly reduced in the NASCT for both MS (on average -9.66%, p = 0.03) and NMOSD (-9.8%, p = 0.002) compared to controls. f_M in lesioned areas was also reduced in both MS (-14.9%, p = 0.002) and NMOSD (-16.4%, p < 0.001). Neither NASCT nor lesioned tissue f_M differed between MS and NMOSD. There were no significant differences between NASCT and lesional areas within either patient group.

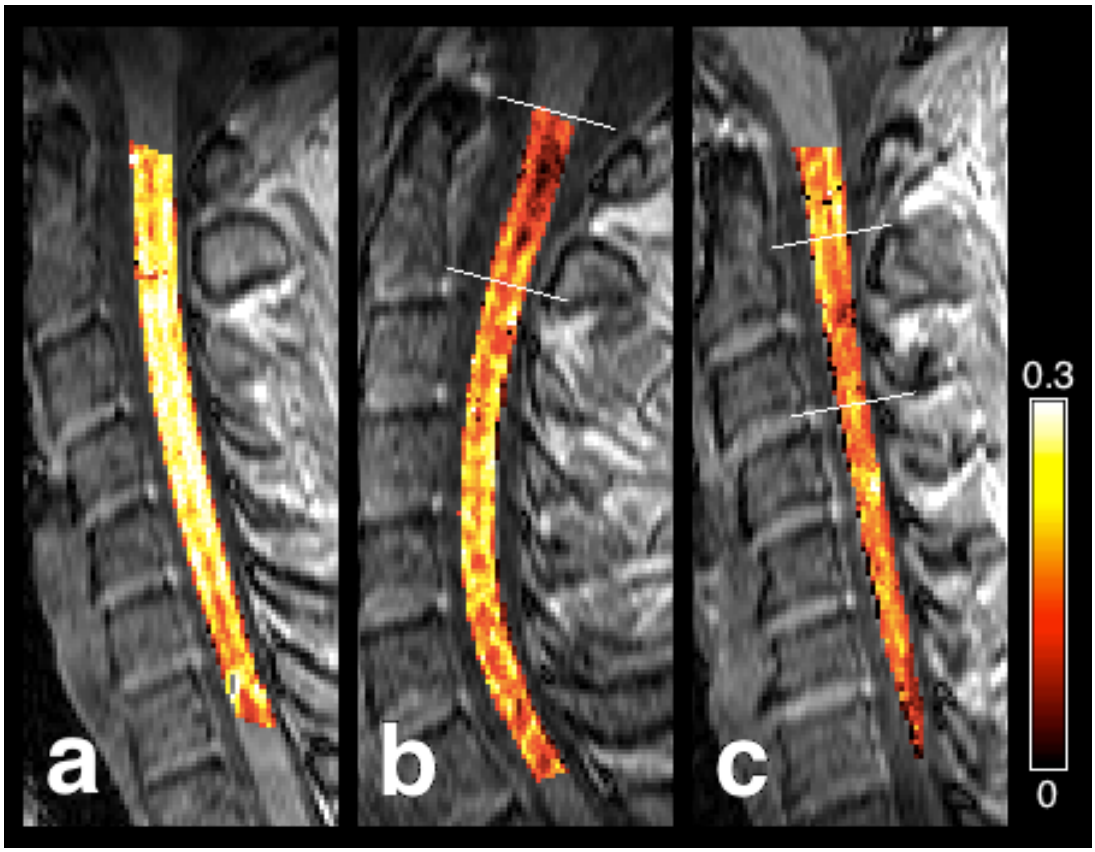

Figure V.5. Example myelin water fraction (f_M) maps for three subjects, overlaid on a T_1-weighted SPGR scan. **a)** Healthy control: female, 26 years old. **b)** Multiple sclerosis subject: male, 35 years old, Expanded Disability Status Scale (EDSS) 2, disease duration of 4 years, with lesions at the C1 and C2 levels. **c)** Neuromyelitis optica spectrum disorder subject: female, 41 years old, EDSS 3.5, disease duration of 2 years, with a lesion at the C2/C3 level. White lines represent upper and lower limits for cord segments identified as lesioned. Reduced f_M is visible in lesions and along the length of the cord for both patients.

Table V.2. Baseline and longitudinal spinal cord MRI measures.

		Within-group			Between groups			
		Controls	**MS**	**NMOSD**	**Kruskal-Wallis**	**MS vs. controls**	**NMOSD vs. controls**	**NMOSD vs. MS**
Cross-sectional								
Normalized volume (mm^2)		70.6 ± 8.1	66.6 ± 7.2	60.4 ± 15.6	0.023*	0.105	0.009**	0.202
NASCT f_M		0.159 ± 0.017	0.148 ± 0.016	0.149 ± 0.015	0.006**	0.025*	0.002**	0.820
Lesioned tissue f_M		-	0.140 ± 0.023	0.138 ± 0.035	< 0.001***	0.002**	< 0.001***	0.706
NASCT vs. lesioned tissue f_M†		-	.846	.322	-	-	-	-
Longitudinal								
Change in volume	**% diff.**	-1.4 ± 3.4%	-2.0 ± 5.2%	-6.4 ± 3.1%	0.026*	0.809	0.013*	0.020*
	p	0.194	0.206	0.016*				
Change in NASCT f_M	**% diff.**	-0.9% ± 7.0%	-7.3 ± 5.2%	+5.8 ± 10.2%	0.005**	0.020*	0.095	0.002**
	p	0.626	0.016*	0.109				
Change in lesioned tissue f_M	**% diff.**	-	-1.4% ± 7.6	+3.1% ± 10.5	0.201	-	-	-
	p		0.322	0.297				

Values reported are median ± interquartile range. Baseline values and percent change in magnetic resonance imaging (MRI) metrics over time, and group differences are presented. *Significant at $p \leq 0.05$, **$p \leq 0.01$, ***$p \leq 0.001$. †Within-group paired Wilcoxon signed-rank test. f_M: myelin water fraction. MS: multiple sclerosis. NASCT: normal-appearing spinal cord tissue. NMOSD: neuromyelitis optica spectrum disorder. NS: non-significant. mm: millimetres. % diff.: percent difference.

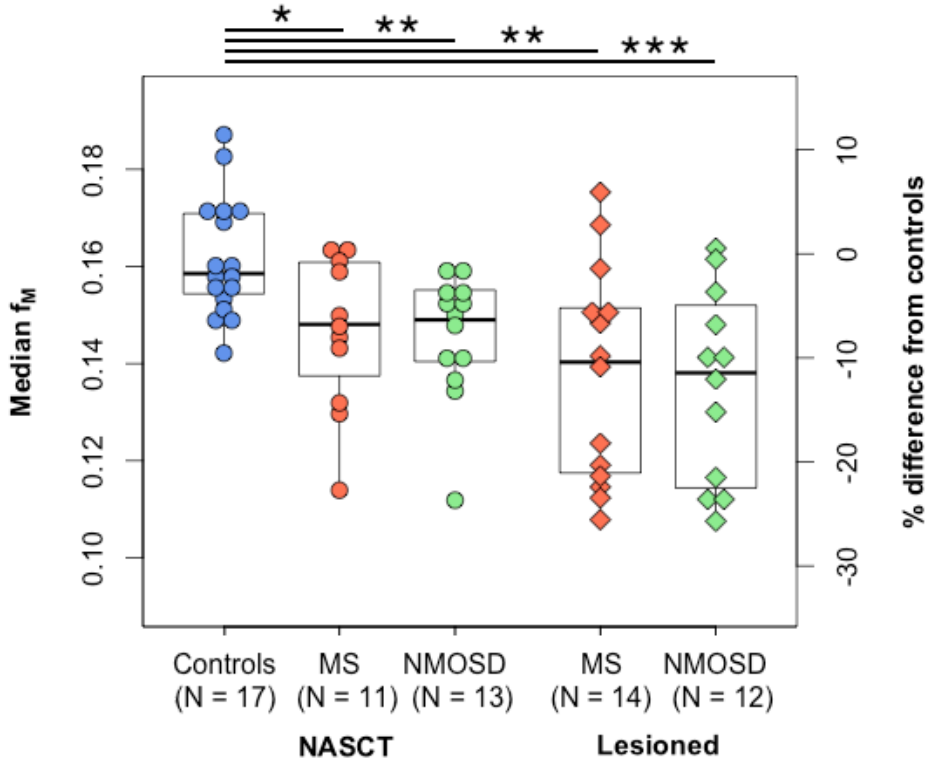

Figure V.6. Myelin water fraction for the cross-sectional sample, by group and tissue type. Right-hand axis shows percent difference of each data point from the control group average.

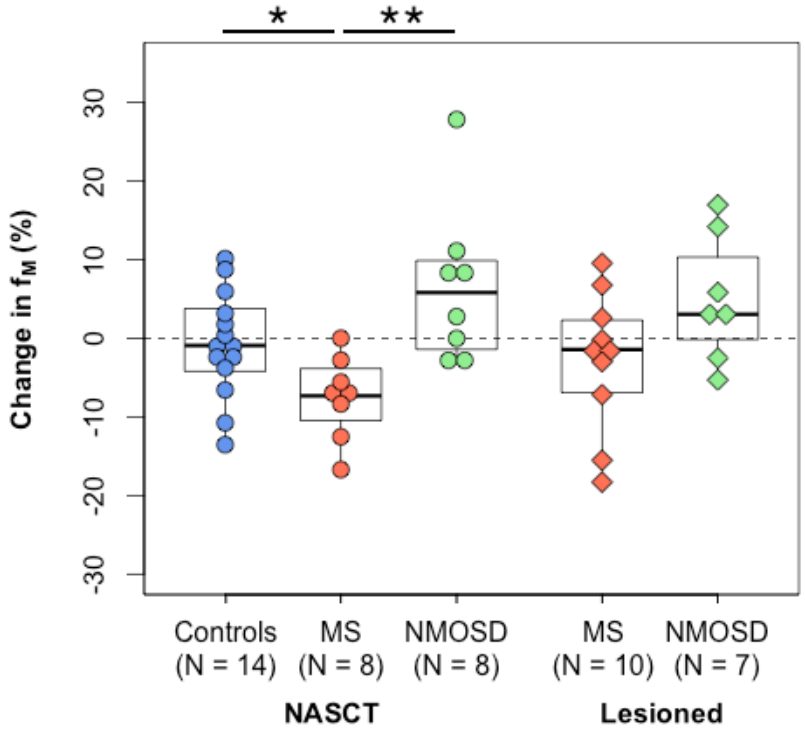

Figure V.7. Percent changes in median myelin water fraction by group and tissue type over one year. Dotted line represents 0% change from baseline.

Data points outside of boxplot whiskers are outliers, defined as being beyond 1.5 interquartile range of each quartile. *Significant at $p \leq 0.05$, **$p \leq 0.01$, ***$p \leq 0.001$. MS: multiple sclerosis. NASCT: within normal-appearing spinal cord tissue. NMOSD: neuromyelitis optica spectrum disorder. f_M: myelin water fraction.

V.4.2. Longitudinal

Because only a subset of participants had data available at follow-up, additional information regarding baseline metrics for the longitudinal subset can be found in **Table V.3** at the end of this chapter. Reasons for drop-out included geographical and scheduling conflicts, technical difficulties during scanning, as well as a few of the patients feeling unwell at the time of appointment. The results observed at baseline overall held true for the subset of subjects who took part in the longitudinal part of the study.

V.4.2.1. Changes in EDSS

In the MS group, three subjects had an increase of 0.5 points on the EDSS, and two subjects a decrease of 0.5 points; all of them had a baseline score ≤ 4.5. In the NMOSD group, one subject had a one-point decrease from 7.5 to 6.5, and one had an 0.5-point increase from 5.5 to 6. Depending on the criteria chosen for the definition of significant clinical deterioration outlined above in **V.3.1**, this last subject is the only one that showed a significant increase in disability at follow-up, although this person did not experience a clinical relapse.

V.4.2.2. Lesions

None of the subjects developed any new lesions between baseline and follow-up.

Within the longitudinal MS sample (n = 11), a total of 47/77 segments (61%) contained lesions. One subject had no lesions, therefore lesional analysis included 10 patients; 3 had entirely lesioned cords, therefore NASCT analysis only included 8 patients. Within the NMOSD group, 23/56 segments (41%) were counted as lesioned. All 8 subjects had some degree of NASCT tissue, and one had no lesions, therefore 7 patients were included in lesional analysis. Details are shown in **Figure V.8**. The number of lesioned segments did not differ between groups (p = 0.2).

V.4.2.3. Volume changes

Changes in cord volume are shown in **Figure V.4**. Median volume change did not differ between controls (-1.4%) and MS (-2.0%) (p = 0.8). Volume loss in NMOSD

was -6.4%, significantly greater than in either controls (p = 0.01) or MS (p = 0.02). Volume change was significant within the NMOSD group over time (p = 0.02).

V.4.2.4. Changes in myelin water fraction

Changes in f_M in NASCT and lesioned tissue are shown in **Figure V.7**.

We report, for NASCT and lesioned tissue separately, change within-group (i.e. baseline vs. follow-up values within each sample) as well as comparisons between groups.

In NASCT f_M, only the decrease in the MS group was significant (p = 0.02). f_M in the control and NMOSD groups remained stable over time. Between groups, there was a greater reduction in the MS group (-7.3%) compared to controls (-0.9%, p = 0.02) and NMOSD (+5.8%, p = 0.002). There was no difference between controls and NMOSD.

In lesioned tissue, the MS group showed a median decrease of -1.42%, and the NMOSD group increased by +3.05%, although neither of these within-group changes was significant. A Kruskal-Wallis test revealed that there was no significant difference between change in NASCT in controls and change in lesioned tissue for either patient group.

V.5. Discussion

V.5.1. Summary of findings

Cross-sectionally, NMOSD subjects had significantly lower cervical cord volume than controls. f_M in lesioned and non-lesioned segments was significantly reduced in MS and NMOSD compared to controls, to a similar extent in both groups.

Longitudinally, volume loss was only significant in the NMOSD group. f_M decreased within NASCT in the MS group, but remained stable in NMOSD. There was no significant change in myelin content in lesioned segments over time in either group.

These observations, their implications and limitations are discussed below.

V.5.2. Volume differences and atrophy

Using normalized cervical cord volume, we observed (non-significantly) smaller values in MS compared to controls; no change occurred in this group over time. This result is likely due to a lack of statistical power with the present sample size. As a potential confounding factor, the presence of inflammation and oedema are known to influence cord volume in relapsing-remitting MS, and have been observed to cause cord expansion, potentially offsetting pathological changes (Klein et al., 2011). However, although non-significant, the observed median volume loss of 2% in the MS group is well within the expected range, which has been estimated at 1-5% per year using CSA measurements (Gass et al., 2015).

The NMOSD group had smaller cord volume at baseline, and showed significant volume loss (median -6.4%) over one year. In Matthews et al.'s investigation, including many of the same subjects, no difference was found between NMOSD and controls when looking at normal-appearing cord volume at the C1/C2 level, excluding slices that contained a lesion. By choosing a measure that would reflect the extent of damage to the entire cervical cord, including lesioned tissue, we were able to detect volume loss in NMOSD compared to controls both cross-sectionally and over time. This suggests that the group differences observed here may be driven by volume loss at lesion sites, and delayed focal atrophy. In contrast, while a significant difference was found by Matthews et al. between MS and controls when looking at normal-appearing upper cord volume, the difference in whole cervical cord volume was not significant here, suggesting that focal volume loss plays a lesser role than in NMOSD.

These results are consistent with previous literature findings that volume loss is more severe in NMOSD than in relapsing MS (Liu et al., 2015c; Weier et al., 2015), and suggest that atrophy occurs over time in a process driven by tissue loss at lesion sites. Global and focal atrophy is in fact known to occur in NMOSD in relation with the extent and intensity of lesions (Cassinotto et al., 2009; Krampla et al., 2009). In contrast, focal atrophy is unrelated to cervical cord lesion load in relapsing-remitting MS (Evangelou et al., 2005; Lukas et al., 2013).

V.5.3. Myelin water fraction measurements

V.5.3.1. f_M is reduced in lesioned areas in MS and NMOSD

In this study, we segmented the cervical cord into spinal levels and isolated segments identified as containing a lesion on standard clinical T_2-weighted scans. Lesioned segments had lower f_M compared to controls in both MS and NMOSD, but there was no difference between patient groups, and no longitudinal changes in these areas.

There were no within-group differences between NASCT and lesional areas for either MS or NMOSD, which may be explained by the observed extent of damage to NASCT in both groups, as well as the varying proportion of NASCT tissue within segments counted as lesioned.

While observing comparably lower f_M in MS and NMOSD lesions may indicate similar degrees of demyelination in the affected segments, it is likely that the identified lesions may be of different sizes, types, and at different stages, especially given the heterogeneity of lesion types in NMOSD (Misu et al., 2013). The large spread of values within each group would corroborate this; moreover, the proportion of lesioned tissue included in any segment may vary (see **V.5.4.1**).

Further exploration of quantitative differences in metrics within segmented lesions would be of interest, as would tract- or tissue compartment-specific assessments. Recent advancements are making high-resolution MWI in the cervical cord feasible in acceptable times; gradient-echo and spin-echo (GRASE) MWI has been demonstrated (Ljungberg et al., 2016), and preliminary results have been presented with an alternative mcDESPOT protocol providing high-resolution axial slices (Ljungberg et al., 2017).

V.5.3.2. f_M is reduced in NASCT in MS and NMOSD

We observed lower f_M in the NASCT in both MS and NMOSD groups compared to controls. The presence of diffuse abnormalities in the MS cervical cord is well-documented (Gass et al., 2015); these may be attributed to lesions not visible on conventional MRI (e.g. below the imaging resolution), distal effects of damage to regions outside the cervical cord, or a more diffuse disease process.

A similar finding in NMOSD is more surprising, given that diffuse damage is only seldom observed in the brain in NMOSD (for further discussion, refer back to

Chapter IV), although the presence of NASCT damage has been noted previously (Klawiter et al., 2012; Qian et al., 2011). As in MS, the influence of secondary degeneration processes due to focal damage is likely, given the extent and prevalence of cervical cord lesions in this sample. Alternatively, the abnormalities observed in NASCT may be the consequence of previous focal abnormalities, resolved at the time of scanning. Complete or partial resolution of lesions is possible, and lesions may break up during periods of remission, leading to a marbled appearance (Asgari et al., 2013b; Krampla et al., 2009; Lalan et al., 2012). In this case, it would therefore be possible that previous lesion sites may have a normal appearance on conventional imaging, but with residual reduction in myelin content, to which MWI is sensitive. These findings bring further evidence for the presence of demyelination outside of areas of focal damage in NMOSD.

V.5.3.3. f_M decreases over time in MS NASCT only

After one year, we measured a decrease in f_M in non-lesional areas in the MS group. Interestingly, this phenomenon was not seen in NMOSD. Given comparable degrees of demyelination in the cord at baseline, the differences observed between MS and NMOSD groups over time seem to reflect distinct inflammatory and neurodegenerative processes (Kawachi and Lassmann, 2017).

One possible explanation for this observation in MS would be the formation of new demyelinating lesions, undetected on the clinical scans available. However, patients in this cohort were relapse-free over the course of the study, and while new spinal cord lesions in MS can be silent (Barkhof, 2002), this is thought to be a rare occurrence (Filippi et al., 2016). Notwithstanding, recent work has shown improved lesion detection at 7T compared to 3T in the MS cord (Dula et al., 2016), and thus the development of small, undetected lesions cannot be ruled out.

Alternatively, a significant loss of myelin content in the MS cord, in clinically stable patients and without the appearance of new lesions, may reflect ongoing demyelination due to secondary degeneration, especially given the extent of focal pathology in this sample. However, since subjects in the present study were relapse-free for a minimum of 6 months before enrolment, any lesion-related secondary changes would have in all probability already occurred at the time of baseline scan, and would not show further worsening over the subsequent year. Moreover, if demyelination secondary to focal lesions were the main process at

play, it is likely that similar changes would have been observed in the NMOSD group, which was not the case.

While chronic inflammatory demyelination is characteristic of progressive disease (Zeis et al., 2007), our findings are consistent with the hypothesis of a primary neurodegenerative process in MS, which has been proposed before (Stys et al., 2012), as well as with the results of the preceding investigation in brain in the same sample.

Additionally, the relatively high change in f_M observed (median -7.3%) is likely influenced by several factors such as time to last relapse, treatment effects, distance to and extent of focal pathology (including outside of the imaged area), etc. The heterogeneity of these factors in the current sample is reflected in the variance seen in this variable. Laule et al. observed a decrease of 10% over two years in the cord in primary progressive subjects (Laule et al., 2010). Although in relapsing-remitting MS, the same neurodegenerative processes are not expected, changes of this magnitude are possible, especially considering the already reduced f_M in NASCT at baseline. Moreover, even for those subjects who experience a greater decrease during the observation period, this process is not expected to be linear over time.

The observed increase in NASCT f_M in NMOSD warrants discussion, despite not being a statistically significant result. Remyelination in diffusely abnormal areas is a possibility, although unlikely. This would be corroborated by the fact that f_M in lesions also tends to increase (non-significant; to be interpreted with caution), and some lesions are known to heal at least partly, indicating that some degree of repair is possible (Asgari et al., 2011; Benedetti et al., 2006).

This observation could also be a by-product of volume loss in lesions, and by extension in normal-appearing areas: where necrotic tissue is lost, a greater relative amount of healthy tissue remains, producing the observed increase in f_M. Volume loss in the cord, driven by shrinkage of lesioned areas, may lead to changes in f_M in preserved areas, presuming a constant amount of myelin.

Alternatively, f_M being the ratio of myelin water to total water content, elevated water content at baseline (possibly due to cystic change or oedema in relation to the disruption of water homeostasis characteristic of NMOSD) could, when returning to normal during a period of quiescence, lead to increased f_M at follow-up. However, given that all subjects in this study were relapse-free for 6 months before baseline, and the likely variation in time to last relapse within the NMOSD group, delayed

ongoing atrophy is a more likely explanation for the observed increase in $f_{M.}$ All of these hypotheses imply that myelin content does not decrease over one year in NMOSD, in stark contrast to MS.

Interestingly, a recent study observed smaller cord volumes in NMOSD subjects with no history of transverse myelitis or detectable cord lesions, albeit to a lesser degree than subjects with cord pathology, but comparably to MS subjects (Ventura et al., 2016). While the authors raise the possibility of a diffuse pathological process occurring in the cord, our results do not appear to support this hypothesis. Another possibility is that of the occurrence of a transient inflammatory episode culminating neither in clinically detected myelitis nor in overt focal pathology, that would be responsible for tissue damage and loss, in parallel or in addition to shrinkage of lesions in NMOSD.

V.5.4. Methodological considerations

V.5.4.1. Influence of motion

The mcDESPOT protocol is composed of steady-state scans, which are intrinsically relatively insensitive to motion (Chavhan et al., 2008). Cervical cord movement is greatest in the 'up-and-down' direction, affected by cardiac pulsation; therefore, acquisition was done with read-out in the superior-inferior direction so as to minimize motion artefacts in the direction in which they are most severe. Natural motion in the anterior-posterior direction has previously been assessed at 0.25-0.5 mm (Figley et al., 2008). At the current voxel size (0.9 x 0.9 mm in-plane), any blurring in the data would be at an acceptable level. mcDESPOT acquisition results in 25 separate collected scans; thus, individual acquisition time is relatively short which serves to limit noise from intrascan motion.

V.5.4.2. Methods for cord volume measurement

A number of metrics and normalization approaches have been proposed for the assessment of cervical cord atrophy. The most widely used measure is CSA at the C2/C3 level, due its relative robustness to motion artefacts, and because it has been found to be representative of overall spinal cord atrophy; however, it requires appropriate axial resolution (Tench et al., 2005b). Another proposed metric, the mean upper cervical cord area (MUCCA; (Daams et al., 2014)), consists in

measuring volume in the uppermost portion of the cord (i.e. usually at the C1-C2 or C2-C3 level) and normalizing by length, similar to the approach used here. Whole cervical cord volume, employed in the present work, has been found similarly effective to C2/C3 volume in terms of revealing group differences in MS, and has the added benefit of taking into account tissue loss due to focal damage along the extent of the cord (Zivadinov et al., 2008).

Possible normalization factors have been investigated before and include, but are not limited to, height, body-mass index, intracranial volume, number of acquired slices, and length of individual segments or portions of the cord (Oh et al., 2014). We chose here to normalize by cord length. While the choice of one approach over the other is still a matter of debate, these metrics have been found to be highly correlated (Healy et al., 2012), and both studies cited above mention normalization by cord length as the recommended approach.

To ensure the validity of this measure in the present sample, average CSA at the C2/C3 level was also collected using the SCT, which measures the area of the segmented cord on each slice over the chosen volume, and corrects it for cord orientation. Using the larger baseline dataset, normalized volume showed excellent correlation with average CSA at the C2/C3 level, within each of the HC, MS, and NMOSD groups (Pearson's correlation coefficient: all $r > 0.93$, $p < 0.001$). The group differences reported above were also preserved [data not shown]. This contributes to guaranteeing high confidence in the presented results, regardless of methodological approach to atrophy measurement.

We obtained a median normalized cord volume (equivalent to average CSA across C1-C7) of 70 mm^2 in the control group. Cord area decreases at the C5-C7 levels compared to higher segments, thus averaged across the whole cord, this result is naturally slightly smaller compared to most reported estimates of CSA at C2/C3 (Tench et al., 2005a). The choice of including or excluding edge voxels is also known to affect volume estimation; the *PropSeg* method only provides a binary segmentation, and does not provide estimates of partial volume effects. The choice of performing manual editing, in order to create conservative masks for f_M measurement, may also have had an impact. Nevertheless, this result is in line with measurements obtained in other studies that used the same method in healthy subjects (De Leener et al., 2014; Ventura et al., 2016).

When used for longitudinal assessment of cord atrophy, all the methods mentioned above rely on using cord segmentation to collect measures of area or volume at

each time point, and comparing the obtained metrics. In the brain, methods have been developed that rely on within-subject registration between two time points, such as FSL-SIENA (Smith et al., 2002) or the brain boundary shift integral (BBSI; (Freeborough and Fox, 1997)). These methods use registered data from two time points to compute either distance or difference in intensity between voxels at the tissue interface, and afford greater reproducibility and power to detect group differences compared to segmentation-based approaches (Moccia et al., 2017). An implementation of the BBSI technique has recently been developed for use in the cord (Prados Carrasco et al., 2016), and may lead to more precise estimates of atrophy for use with longitudinal data; further work is expected in this area.

V.5.4.3. Segmentation of lesions

An important limitation of the current approach lies in the segmentation of lesioned areas, which include varying proportions of NASCT, and are therefore lesioned areas and not purely lesioned tissue. While this approach enables isolation of NASCT, it does not constitute lesion segmentation per se, and thus limits the specificity of this measure to lesional pathology. This may contribute to explain the lack of significant baseline differences between NASCT and lesioned areas in each patient group, as would be expected, although the observed extent of damage to NASCT areas is another contributing factor.

It is worth also noting that despite the fact that NMOSD cord pathology is usually more severe than in MS, in this study, the MS group had on average more affected segments than the NMOSD group, although this difference was not significant in the smaller follow-up subset (see **Table V.3**). While possible that the extent of cord pathology may by chance be greater in this particular MS sample, this is compounded by the fact that the number of segments considered lesioned does not represent the extent of lesions in itself, as well as the fact that some subjects from both disease group had lesions in the brainstem and thoracic portion of the spine that may have had up- and downstream effects (which we did not assess systematically).

V.5.4.4. Variations in myelin content along the cord

The ratio of white and grey matter, and consequently myelin concentration and thus f_M, are known to vary along the length of the cord (Fradet et al., 2014; Kolind and Deoni, 2011; Minty et al., 2009). In order to exclude lesions from normal-appearing

tissue analysis, we excluded cord segments identified as lesioned on T_2-weighted scans, and compared preserved areas of the cord at different spinal levels. However, the distribution of lesions across cord levels was relatively uniform within and between each disease group (see **Figure V.8**), thus mitigating possible bias in comparing unmatched regions that are expected to vary in myelin content. Distance of normal-appearing segments from lesion sites, as well as lesion type, length and age are all parameters that would warrant attention in further investigations of secondary degeneration processes in both diseases.

V.5.4.5. Treatment effects

Half of the MS and all of the NMOSD subjects were on immunomodulatory and immunosuppressant treatments, respectively. While all patients were in remission for the duration of the study, DMTs are likely to mediate background inflammatory activity, and thus may affect volume and changes in myelin content compared to patients not currently on treatment. However, discussions on the effects of DMTs on spinal cord pathology in the current context remain speculative. Characterisation of the influence of volume changes (i.e. atrophy) on the f_M measurements would also be of interest to allow description of the relationship between possible volume loss and changes in myelin content.

V.5.4.6. Sample size

Limitations to this study also include the small sample size, especially for the longitudinal sample, and the resulting heterogeneity in age and clinical profiles within the patient groups, including in DMTs. Results should therefore be regarded as preliminary, and warrant replication in larger samples.

V.6. Conclusion

In this study, we aimed to ascertain whether evidence of cervical cord atrophy and demyelination could be seen in stable relapsing-remitting MS and NMOSD subjects. Using MWI, we found that measures of myelin content are similarly reduced in MS and NMOSD compared to controls in cervical spinal cord lesions and in normal-appearing tissue.

At one-year follow-up, there was a significant decrease in NASCT f_M in the MS group. This observation suggests that chronic changes occur in the absence of new detectable lesions, bringing further evidence that occult activity occurs in MS tissue, either due to secondary degeneration following lesions, or to lesions appearing below the imaging resolution of clinical scans. Detection of a significant change over a short period supports the use of cervical cord f_M as a potential imaging marker of ongoing neurodegeneration in MS. Particularly, this measure may constitute a valuable imaging outcome in clinical trials in progressive disease.

In contrast, despite ongoing loss of volume in the NMOSD cervical cord, likely driven by lesions, and diffuse damage at baseline comparable to that seen in MS, no significant change in myelin content was seen in NMOSD. Instead, f_M showed a (non-significant) tendency to increase in normal-appearing areas, which could result from the observed reduction in volume while actual myelin content remained stable. This observation suggest that the NASCT is not subject to further degeneration, lending new evidence to the idea that subclinical disease activity is not a feature of NMOSD, and supporting the observation that disease progression is absent clinically.

Evaluations of the effects of the location and extent of focal cord pathology in both disease groups are required before making assumptions about the pathological substrates of these observations. Recent technical developments will allow collection of mcDESPOT in the cervical cord with reduced coverage, but higher resolution in the axial plane, which will enable tract-specific assessments and differentiation between the up- vs. downstream effects of focal damage, as well as enhance the precision of lesional measurements.

Finally, these results support the use of longitudinal MWI for the assessment of pathological changes in the cervical cord in demyelinating diseases. Further longitudinal investigations should address the link between such changes and progression of disability in order to establish its potential use as a clinically relevant marker of pathology.

V.7. Additional information

Included here are a diagram showing the distribution of lesioned cervical cord segments cervical cord level for each patient group in **Figure V.8**, and summary statistics for the subset of subjects who took part in the follow-up study in **Table V.3**.

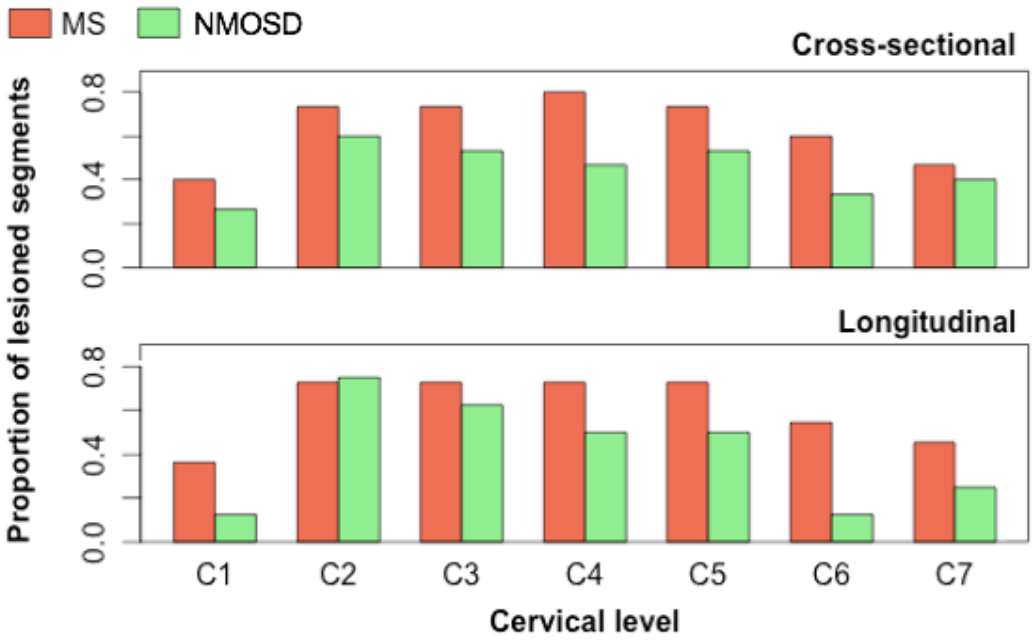

Figure V.8. Repartition of lesions by cervical segment for the cross-sectional and longitudinal sub-samples. The proportion of subjects out of each group for whom each segment was considered as lesional is shown. In the follow-up subset, three MS subjects had lesions covering the whole cervical cord, and one had none. In the NMOSD group, one subject had no lesions. The number of lesioned segments by subject did not differ between groups (p = 0.2). MS: multiple sclerosis. NMOSD: neuromyelitis optica spectrum disorder.

Table V.3. Population characteristics and MRI metrics at baseline for the longitudinal sub-sample.

	Within-group			Between groups			
	Controls	**MS**	**NMOSD**	**Kruskal-Wallis**	**MS vs. controls**	**NMOSD vs. controls**	**NMOSD vs. MS**
Demographics							
N (sex)	14 (3M)	11 (3M)	8 (0M)	-	-	-	-
Age (years)	51 (26-76)	41 (28-62)	46 (27-76)	0.613	-	-	-
Disease duration (months)	-	54 (26-156)	65 (24-186)	-	-	-	.934
Baseline EDSS	-	2 (1-5)	5 (2-7.5)	-	-	-	.045*
Lesioned segments per subject	-	4 (0-7)	3 (0-5)	-	-	-	.196
Number of subjects with NASCT	-	8	8	-	-	-	-
Number of subjects with ≥ 1 lesion	-	10	7	-	-	-	-
Time between scans (months)	12 (10-14)	12 (11-14)	12 (11-15)	.342	-	-	-
MRI measures							
Normalized volume	70.8 ± 7.6	66.6 ± 6.4	63.1 ± 13.0	0.076	-	-	-
NASCT f_M	0.159 ± 0.016	0.148 ± 0.018	0.150 ± 0.008	0.020*	0.042*	0.010*	0.959
Lesioned tissue f_M	-	0.143 ± 0.033	0.149 ± 0.018	0.017*	0.007**	0.098	0.847

Values are reported as median ± interquartile range (range). *Significant at $p \leq 0.05$, **$p \leq 0.01$. EDSS: Expanded Disability Status Scale. f_M: myelin water fraction. M: male. MRI: magnetic resonance imaging. MS: multiple sclerosis. NASCT: normal-appearing spinal cord tissue. NMOSD: neuromyelitis optica spectrum disorder. NS: non-significant. mm: millimetres. % diff.: percent difference.

Chapter VI. Conclusion

Summary of presented work

In this work, I focused on the application of myelin water imaging (MWI) to the study of neuromyelitis optica spectrum disorder (NMOSD). Due to the rapid evolution of the nosology of NMOSD in the last twelve years, as well as it being a rare disease, the body of literature is limited. This is in contrast to the study of multiple sclerosis (MS) in which, as a large, active field, a vast range of techniques have been applied. Overall, the use of advanced imaging is relatively recent in NMOSD, and the field suffers from lack of replication, and the potential of various available techniques to inform on the particular pathology of this disease is still being assessed. The central thesis of this work is that MWI, and especially mcDESPOT, can provide valuable information and inform current research questions in NMSOD research.

In **Chapter III**, I reported results from a single-scanner reliability study of mcDESPOT in healthy older adults. I showed good scan-rescan reliability of T_1, T_2, and myelin water fraction indices in the brain. In the following chapter I then applied the method in the brain and cervical cord to investigate NMOSD pathology.

In **Chapter IV**, I presented the results of an investigation of subcortical pathology using a mcDESPOT protocol. I investigated abnormalities in the normal-appearing white matter (WM) and the thalamus in an NMOSD group compared to healthy controls. Regional analysis of quantitative parameters revealed reduced myelin water fraction and elevated T_1 in several regions. The sensitivity of the T_1 relaxation time to abnormalities in the brain suggests changes in water content as the likely substrate behind these observations, which would warrant further investigation. In contrast, thalamic indices were normal. Thalamic T_1 emerged as a strong predictor of performance on a cognitive measure of the speed of information processing, supporting further exploration of thalamic involvement in relation to the known pattern of neuropsychological deficits in NMOSD.

In **Chapter V**, I presented results from a longitudinal study into cervical spinal cord pathology in NMOSD and MS subjects and healthy controls over one year. Evidence of abnormal myelin content outside of lesioned areas of the cord was apparent in both patient groups. Significant cord atrophy occurred over time in the NMOSD group only. Despite similar levels of nonfocal pathology at baseline,

changes in myelin content over time were only visible in the MS group, in the absence of clinical and radiological activity. These results attest to the ability of mcDESPOT to show evidence of degenerative processes in the MS cord over a relatively short follow-up duration.

Each chapter being a different, independent project on a different cohort, the methodological limitations of each presented study have been detailed in each section. Here, I further expand on the limitations inherent to all three studies, as well as those routinely encountered in the NMOSD literature, and provide general discussion points regarding the use of cord and brain MWI in NMOSD and MS research.

Translational potential of MWI

In this work, I provide evidence for the utility of mcDESPOT as a research tool in the study of demyelinating disease. Regarding its translational value, however, several factors limit its potential, including absence of histological validation, lack of standardisation of protocols and analysis methods, and high post-processing requirements both in terms of expertise and computational demands. For instance, MR spectroscopy, diffusion tensor imaging (DTI), and magnetisation transfer ratio (MTR) measures have shown promise in determining prognosis in clinically isolated syndrome cases (Rovira et al., 2015). Research into MWI is also a smaller field than the larger bodies of work behind the aforementioned methods, which make more likely candidates for acceptance and use in the clinic in the near future.

For instance, MWI has been recommended as a more appropriate tool to assess myelin integrity in vivo than blood/CSF markers or other MRI methods in the study of mild traumatic brain injury, due to its high specificity and sensitivity (Weber et al., 2018; Wright et al., 2016). However, diffusion-weighted and diffusion tensor imaging can already be used clinically in the characterisation of ischemia or traumatic brain injury (TBI), and tractography also has potential in the study of stroke and perioperative planning (Sundgren et al., 2004). DTI has been suggested as the most “mature” in terms of development and validation, and to thus be the first contender for broader use in clinical trials and translational applications (Martin et al., 2016).

On the individual level, MWI has been used to assess WM changes with higher specificity than traditional imaging can afford in a case study of a patient suffering

from post-radiation necrosis (Lapointe et al., 2017), and to evaluate the long-term effects of stem cell transplantation in a Krabbe disease patient (Laule et al., 2016). Current investigations using MWI are also looking at lowering necessary sample sizes in clinical trials using advanced methods that yield higher statistical power than conventional metrics (i.e. cerebral atrophy), which may lead to lowered costs and therefore increased speed in clinical trials and thus drug evaluation and deployment, and increased treatment options.

Defining clinical utility as the capacity of a technique to generate information about individual cases – diagnostic, prognostic, and as a biomarker having a relationship with clinical measures (Martin et al., 2016) – it is clear that making such use of MWI will require further extensive work, including: validation using animal models, histology, or other established techniques; assessments of cross-platform and test-retest reliability; development of consensus methods for analysis; and determination of clinical correlations in various samples. The assessment of precision, i.e. repeatability and reproducibility, is paramount in a technique meeting the standards required for a potential translation to clinical practice (Jackson, 2018), which I contribute to in **Chapter III** of the present work.

Limitations and future directions

I discuss below some of the general limitations to the work presented in this thesis and, following up on this, how a number of interesting avenues of investigation can be proposed going forward into a new, “exciting” decade of research (Kister and Paul, 2015).

Throughout this work, note is often made of discrepancies between advanced MRI studies, especially when it comes to brain investigations. As summarised by Pache et al., advanced MRI studies into nonfocal damage in the NMOSD brain have yielded results “ranging from: 1) widespread brain damage, 2) damage only in visual and sensorimotor systems, or 3) no substantial damage at all” (Pache et al., 2016). Several reasons can be invoked for this. First, in a relatively young field of research, diagnostic criteria have undergone several reappraisals; the potential differences in phenotypes across various ethnic groups were also evoked earlier (see **IV.5.4.2**). The difficulty of obtaining homogeneous populations, reflecting the plurality of disease presentations in the real world, may be improved in the future as larger samples become available, and with better categorisation of existing patient

groups due to advances in defining the different 'branches' of the NMO spectrum. These points will be discussed below.

With new and improved serological assays, detection rates of AQP4-IgG-positivity increase. Comparison between assays in two multi-centre studies showed that sensitivity and specificity can be improved with the use of a new generation of tests, with cell-based assays yielding the best results overall (Waters et al., 2016, 2012). MOG-IgG and AQP4-IgG seropositivity were found to be mutually exclusive in nearly all studies; rare evidence to the contrary has been suggested to hinge on the sensitivity of the assays used for testing (Sato et al., 2014; Zamvil and Slavin, 2015). MOG-IgG seropositivity is also only rarely observed in adult MS (Reindl et al., 2013). Therefore, as assay methods improve and MOG antibody testing becomes more widely conducted, the nosology of NMOSD is likely to require re-evaluation in the future (Zabad et al., 2017). Several studies have found that MOG-IgG-positive NMOSD patients present with different demographic, clinical, and conventional imaging characteristics, and that different pathogenic mechanisms may be at play (Jarius et al., 2016a, 2016b; Sato et al., 2014; van Pelt et al., 2016); thus, further exploration of these different profiles may be of interest. To facilitate this, studies with larger sample sizes and better-defined patient samples will be necessary.

Inherent to the study of a rare disease, most studies in the field have very small sample sizes, and the high prevalence of borderline significant results (many examples being cited in **Chapter IV**, and as evidenced by the results presented in the current work) suggests a lack of statistical power. This is a limitation from which the two NMOSD studies presented here suffer (with sample sizes of $n < 20$ for patient groups in both **Chapter IV** and **V**). This is, however, representative of the number of research subjects that can be expected to be recruited from a single NMO clinic over a period of approximately one year, which was the case for both projects presented here.

Multi-centre studies are therefore crucial in the study of rare populations, to enable stricter inclusion criteria and maximise sample sizes. Recent national and international initiatives have seen the implementation of large-scale databases for demographic, clinical and biological information in NMOSD, such as the CIRCLES study in North America, the NEMOS project in Germany, and the NOMADMUS

cohort in France[16]. All three examples are registry and repositories that aim to collect demographic, clinical, and biological data, offering researchers the means to conduct investigations with adequate data samples. Imaging data is expected to follow soon, which will enable moving past the stage of exploratory, hypothesis-generating, pilot or replication studies (often with conflicting, or hard to compare results, due to differences in populations and techniques) and enable precisely addressing research questions. The deployment of such initiatives is a strong argument for the validation and use of quantitative imaging techniques with known reliability. I contribute to those efforts in this work by providing supporting evidence for the use of the technique of interest, mcDESPOT, in a test-rest design. With this in mind, multi-centre assessments of reproducibility would also be valuable. For instance, a group of healthy controls, and ideally a sample of patients, could be scanned across several sites and, pending harmonization of sequences between vendors and scanner models. Inter-site reproducibility may be assessed using a scheme similar to that used in **Chapter III**, by registering data within-subject and comparing metrics across regions and voxelwise using statistical measures (e.g. intraclass correlation coefficients taking into account the effect of scanner, within-subject coefficients of variation, correlation measures) to investigate the influence of site and potential bias. Another obvious extension to the work presented here would be assessing the reliability of mcDESPOT-derived measures in the cervical cord longitudinally, as a first step to permitting multi-centre and/or longitudinal designs in clinical populations.

Applied to the study of NMOSD, advanced imaging of the brain is important for several reasons. As recounted here, brain involvement is greater than previously thought, and especially relevant in the understanding of cognitive impairment and therefore quality of life. Advanced brain MRI has the potential to feature changes brought on by both optic nerves and spinal cord pathology, and therefore reflect disease progression comprehensively; the time-course of brain involvement with regards to the evolution of opticospinal pathology remains to be explored through longitudinal studies involving eye, cord and brain imaging.

---

[16] CIRCLES: Collaborative International Research in Clinical Longitudinal Experience in NMO Studies (Cook et al., 2016).
NEMOS: NMO Study Group; https://nemos-net.de/english-summary.html
NOMADMUS: French Cohort and Biobank of Devic's NMO and Related Neurological Disorders; https://clinicaltrials.gov/ct2/show/NCT02850705

Considering the fact that each advanced MRI method comes with its own set of technical limitations and susceptibility to different biological phenomena, the simultaneous use of several, complementary methods has been recommended for a more comprehensive characterization of tissue (Groeschel et al., 2016). Earlier mention was made of the advantages of concurrent MWI and absolute water content mapping. With regards to mcDESPOT itself, it should be possible to make use of the other quantitative parameters that the technique affords. In particular, the myelin residence time holds promise as a potential marker of myelin sheath thickness and integrity (see **Chapter II**). Recent preliminary work has shown that residence time reflects the expected regional variations in the corpus callosum of healthy subjects, and may show promise in helping characterise the pathological substrates of callosal pathology in NMOSD (Abel et al., 2017). Investigation of this parameter in the cervical cord would also be of interest, for instance starting with comparing its information potential compared to other metrics of WM integrity in healthy controls.

In regard to **Chapter V**, a similar longitudinal investigation with a longer follow-up duration would be interesting – two or even three years being a feasible duration, to balance between power to detect significant pathological changes, while keeping the drop-out rate to a minimum due to practical considerations. Increasing the number of time points as well as the follow-up duration may also contribute to increasing sensitivity, although the latter may have a greater impact (Moccia et al., 2017).

A central limitation to this work taken as a whole is the use of different cohorts for the brain and cervical cord studies; collecting both datasets from the same sample, followed over time, and analysing the two concurrently is an obvious continuation and expansion of this work. In the spinal cord, development and deployment of advanced techniques is naturally lagging behind that of brain methods; however, the field of advanced cord MRI is growing rapidly. In a similar vein to the insights that multimodal imaging and longitudinal designs can bring, one particularly interesting advance is the development of simultaneous brain and spine imaging protocols. Focusing on the possibilities afforded by MWI, investigating the time-course and relationships between WM alterations in the brain and cord over time, and the downstream/upstream effects of each, would be of interest (Lycklama et al., 2003). Improvements in image resolution, and segmentation methods for the identification of regions and tracts may allow the study of functionally relevant

networks, and to explore whether any changes in the cord are mirrored in the brain (e.g. brainstem, corticospinal tract, motor cortical areas).

Methodological work has focused on ways of merging brain and cord datasets, for instance the recent creation of a spinal cord atlas compatible with the widely-used MNI152 brain template and using the same coordinate system, and of methods enabling nonlinear registration and merging of scans (Leener et al., 2017). Other advancements include the possibility of acquiring upper cervical cord area measures from high-resolution T_1-weighted scans of the brain (Liu et al., 2016), with appropriate correction for the impact of gradient-induced distortions (Papinutto et al., 2018), as well as previously mentioned technical developments enabling mcDESPOT in the cord at higher resolution (Ljungberg et al., 2017) (see **Chapter V**). These techniques hold great promise to better capture the extent of pathology in the central nervous system.

In this work, I have shown that mcDESPOT can be a useful, reliable tool for the assessment of quantitative parameters in the brain and cervical cord. Although complex questions remain that need to be addressed further, the current work helps address outstanding questions in NMOSD research. It brings additional evidence to characterise the nature and extent of brain involvement, the correlates of cognitive impairment, and the existence of subclinical disease progression between clinical relapses. It supports the use of mcDESPOT as an informative technique in the study of this rare disease in particular, and neurological disorders involving WM in general.

References

Abel, S., Vavasour, I., Lee, L., Carruthers, R., Traboulsee, T., Combes, A., Kolind, S., 2017. Advanced imaging detects variations in myelin content and thickness in the corpus callosum of neuromyelitis optica patients and healthy controls, in: ECTRIMS 33rd Meeting. Paris, France.

Aboul-Enein, F., Krssak, M., Hoftberger, R., Prayer, D., Kristoferitsch, W., 2010. Diffuse White Matter Damage Is Absent in Neuromyelitis Optica. Am. J. Neuroradiol. 31, 76–79. doi:10.3174/ajnr.A1791

Aboul-Enein, F., Seifert-Held, T., Mader, S., Kuenz, B., Lutterotti, A., Rauschka, H., Rommer, P., Leutmezer, F., Vass, K., Flamm-Horak, A., Stepansky, R., Lang, W., Fertl, E., Schlager, T., Heller, T., Eggers, C., Safoschnik, G., Fuchs, S., Kraus, J., Assar, H., Guggenberger, S., Reisz, M., Schnabl, P., Komposch, M., Simschitz, P., Skrobal, A., Moser, A., Jeschow, M., Stadlbauer, D., Freimüller, M., Guger, M., Schmidegg, S., Franta, C., Weiser, V., Koppi, S., Niederkorn-Duft, M., Raber, B., Schmeissner, I., Jecel, J., Tinchon, A., Storch, M.K., Reindl, M., Berger, T., Kristoferitsch, W., 2013. Neuromyelitis Optica in Austria in 2011: To Bridge the Gap between Neuroepidemiological Research and Practice in a Study Population of 8.4 Million People. PLoS One 8, e79649. doi:10.1371/journal.pone.0079649

Absinta, M., Reich, D.S., Filippi, M., 2016. Spring cleaning: time to rethink imaging research lines in MS? J. Neurol. 263, 1893–1902. doi:10.1007/s00415-016-8060-0

Alonso-Ortiz, E., Levesque, I.R., Pike, G.B., 2015. MRI-based myelin water imaging: A technical review. Magn. Reson. Med. 73, 70–81. doi:10.1002/mrm.25198

Andersson, J.L.R., Jenkinson, M., Smith, S., 2007. Non-linear registration aka Spatial normalisation - FMRIB Technical Report (TR07JA2). In Pract. 22.

Antel, J., Antel, S., Caramanos, Z., Arnold, D.L., Kuhlmann, T., 2012. Primary progressive multiple sclerosis: part of the MS disease spectrum or separate disease entity? Acta Neuropathol. 123, 627–638. doi:10.1007/s00401-012-0953-0

Arshad, M., Stanley, J.A., Raz, N., 2017. Test-retest reliability and concurrent validity of in vivo myelin content indices: Myelin water fraction and calibrated T 1 w/T 2 w image ratio. Hum. Brain Mapp. 38, 1780–1790. doi:10.1002/hbm.23481

Asgari, N., Owens, T., Frøkiaer, J., Stenager, E., Lillevang, S.T., Kyvik, K.O., 2011. Neuromyelitis optica (NMO)--an autoimmune disease of the central nervous system (CNS). Acta Neurol. Scand. 123, 369–384. doi:10.1111/j.1600-0404.2010.01416.x

Asgari, N., Skejoe, H.P.B., Lennon, V.A., 2013a. Evolution of longitudinally extensive transverse myelitis in an aquaporin-4 IgG-positive patient. Neurology 81, 95–96. doi:10.1212/WNL.0b013e318297ef07

Asgari, N., Skejoe, H.P.B., Lillevang, S.T., Steenstrup, T., Stenager, E., Kyvik, K.O., 2013b. Modifications of longitudinally extensive transverse myelitis and brainstem lesions in the course of neuromyelitis optica (NMO): a population-based, descriptive study. BMC Neurol. 13, 33. doi:10.1186/1471-2377-13-33

Ashburner, J., Friston, K.J., 2000. Voxel-Based Morphometry — The Methods. Neuroimage 11, 805–821. doi:10.1006/nimg.2000.0582

Barkhof, F., 2002. The clinico-radiological paradox in multiple sclerosis revisited. Curr. Opin. Neurol. 15, 239–245. doi:10.1097/00019052-200206000-00003

Barkhof, F., Brück, W., De Groot, C.J.A., Bergers, E., Hulshof, S., Geurts, J., Polman, C.H., van der Valk, P., 2003. Remyelinated Lesions in Multiple Sclerosis: Magnetic Resonance Image Appearance. Arch. Neurol. 60, 1073. doi:10.1001/archneur.60.8.1073

Barnett, Y., Sutton, I.J., Ghadiri, M., Masters, L., Zivadinov, R., Barnett, M.H., 2014. Conventional and Advanced Imaging in Neuromyelitis Optica. Am. J. Neuroradiol. 35, 1458–1466. doi:10.3174/ajnr.A3592

Behrens, T.E.J., Johansen-Berg, H., Woolrich, M.W., Smith, S.M., Wheeler-Kingshott, C.A.M., Boulby, P.A., Barker, G.J., Sillery, E.L., Sheehan, K., Ciccarelli, O., Thompson, A.J., Brady, J.M., Matthews, P.M., 2003. Non-invasive mapping of connections between human thalamus and cortex using diffusion imaging. Nat. Neurosci. 6, 750–757. doi:10.1038/nn1075

Benedetti, B., Valsasina, P., Judica, E., Martinelli, V., Ghezzi, A., Capra, R., Bergamaschi, R., Comi, G., Filippi, M., 2006. Grading cervical cord damage in neuromyelitis optica and MS by diffusion tensor MRI. Neurology 67, 161–163. doi:10.1212/01.wnl.0000223637.65208.7c

Berger, M.F., Silverman, H.F., 1991. Microphone array optimization by stochastic region contraction. IEEE Trans. Signal Process. 39, 2377–2386. doi:10.1109/78.97993

Bichuetti, D.B., Rivero, R.L., Oliveira, D.M., Souza, N.A., Abdala, N., Oliveira, E.M., Gabbai, A.A., 2008a. Neuromyelitis optica: brain abnormalities in a Brazilian cohort. Arq. Neuropsiquiatr. 66, 1–4. doi:10.1590/S0004-282X2008000100001

Bichuetti, D.B., Rivero, R.L.M., de Oliveira, E.M.L., Oliveira, D.M., de Souza, N.A., Nogueira, R.G., Abdala, N., Gabbai, A., 2008b. White matter spectroscopy in neuromyelitis optica: a case control study. J. Neurol. 255, 1895–1899. doi:10.1007/s00415-009-0940-0

Bielekova, B., Martin, R., 2004. Development of biomarkers in multiple sclerosis. Brain 127, 1463–1478. doi:10.1093/brain/awh176

Blanc, F., Noblet, V., Jung, B., Rousseau, F., Renard, F., Bourre, B., Longato, N., Cremel, N., Di Bitonto, L., Kleitz, C., Collongues, N., Foucher, J., Kremer, S., Armspach, J.-P., de Seze, J., 2012. White Matter Atrophy and Cognitive Dysfunctions in Neuromyelitis Optica. PLoS One 7, e33878. doi:10.1371/journal.pone.0033878

Blanc, F., Zéphir, H., Lebrun, C., Labauge, P., Castelnovo, G., Fleury, M., Sellal, F., Tranchant, C., Dujardin, K., Vermersch, P., de Seze, J., 2008. Cognitive functions in neuromyelitis optica. Arch. Neurol. 65, 84–8. doi:10.1001/archneurol.2007.16

Blystad, I., Warntjes, J.B.M., Smedby, O., L, a-M., Tblom, Lundberg, P., Larsson, E.-M.E.-M., Landtblom, a-M. a.-M., Lundberg, P., Larsson, E.-M.E.-M., 2012. Synthetic MRI of the brain in a clinical setting. Acta Radiol. 53, 1158–63. doi:10.1258/ar.2012.120195

Bodini, B., Stankoff, B., 2016. Imaging Central Nervous System Demyelination and Remyelination by Positron-Emission Tomography. Brain Plast. 1–6. doi:10.3233/BPL-160042

Bonnan, M., Cabre, P., 2011. Plasma Exchange in Severe Attacks of Neuromyelitis Optica. Mult. Scler. Int. 2012, 1155–1164. doi:10.1155/2012/787630

Boulby, P.A., Rugg-Gunn, F.J., 2003. T2: the Transverse Relaxation Time, in: Tofts, P. (Ed.), Quantitative MRI of the Brain: Measuring Changes Caused by Disease. John Wiley & Sons, pp. 143–201.

Bradl, M., Misu, T., Takahashi, T., Watanabe, M., Mader, S., Reindl, M., Adzemovic, M., Bauer, J., Berger, T., Fujihara, K., Itoyama, Y., Lassmann, H., 2009. Neuromyelitis optica: pathogenicity of patient immunoglobulin in vivo. Ann. Neurol. 66, 630–43. doi:10.1002/ana.21837

Braksick, S. a., Cutsforth-Gregory, J.K., Black, D.F., Weinshenker, B.G., Pittock, S.J., Kantarci, O.H., 2014. Teaching neuroimages: MRI in advanced neuromyelitis optica. Neurology 82, e101-2. doi:10.1212/WNL.0000000000000246

Brass, S.D., Chen, N.K., Mulkern, R. V, Bakshi, R., 2006. Magnetic resonance imaging of iron deposition in neurological disorders. Top. Magn. Reson. Imaging.

doi:10.1097/01.rmr.0000245459.82782.e4\r00002142-200602000-00004 [pii]

Bydder, G.M., Fullerton, G.D., Young, I.R., 2012. MRI of Tissues with Short T2s or T2*s, EMR. Wiley. doi:10.1002/nbm.2941

Cabre, P., González-Quevedo, A., Bonnan, M., Saiz, A., Olindo, S., Graus, F., Smadja, D., Merle, H., Thomas, L., Cabrera-Gomez, J.A., 2009. Relapsing neuromyelitis optica: long term history and clinical predictors of death. J. Neurol. Neurosurg. Psychiatry 80, 1162–4. doi:10.1136/jnnp.2007.143529

Cabrera-Gomez, J.A., Kister, I., 2012. Conventional brain MRI in neuromyelitis optica. Eur. J. Neurol. 19, 812–9. doi:10.1111/j.1468-1331.2011.03565.x

Cai, H., Zhu, J., Zhang, N., Wang, Q., Zhang, C., Yang, C., Sun, J., Sun, X., Yang, L., Yu, C., 2017. Subregional structural and connectivity damage in the visual cortex in neuromyelitis optica. Sci. Rep. 7, 41914. doi:10.1038/srep41914

Calabrese, M., Agosta, F., Rinaldi, F., Mattisi, I., Grossi, P., Favaretto, A., Atzori, M., Bernardi, V., Barachino, L., Rinaldi, L., Perini, P., Gallo, P., Filippi, M., 2009. Cortical Lesions and Atrophy Associated With Cognitive Impairment in Relapsing-Remitting Multiple Sclerosis. Arch. Neurol. 66. doi:10.1001/archneurol.2009.174

Calabrese, M., Oh, M.S., Favaretto, A., Rinaldi, F., Poretto, V., Alessio, S., Lee, B.-C., Yu, K.-H., Ma, H.-I., Perini, P., Gallo, P., 2012. No MRI evidence of cortical lesions in neuromyelitis optica. Neurology 79, 1671–6. doi:10.1212/WNL.0b013e31826e9a96

Cardona, J.F., Sinay, V., Amoruso, L., Hesse, E., Manes, F., Ib??ez, A., 2014. The impact of neuromyelitis optica on the recognition of emotional facial expressions: A preliminary report. Soc. Neurosci. 1–6. doi:10.1080/17470919.2014.935474

Cassinotto, C., Deramond, H., Olindo, S., Aveillan, M., Smadja, D., Cabre, P., 2009. MRI of the spinal cord in neuromyelitis optica and recurrent longitudinal extensive myelitis. J. Neuroradiol. 36, 199–205. doi:10.1016/j.neurad.2008.12.008

Chan, K.H., Tse, C.T., Chung, C.P., Lee, R.L.C., Kwan, J.S.C., Ho, P.W.L., Ho, J.W.M., 2011. Brain Involvement in Neuromyelitis Optica Spectrum Disorders. Arch. Neurol. 68, 1432–1439. doi:10.1001/archneurol.2011.249

Chang, L.C., Cheng, G.K., Basser, P.J., Pierpaoli, C., 2008. Linear least-squares method for unbiased estimation of T1 from SPGR signals. Magn. Reson. Med. 60, 496–501. doi:10.1002/mrm.21669

Chanson, J.-B.J.-B., Lamy, J., Rousseau, F., Blanc, F., Collongues, N., Fleury, M., Armspach, J.-P.J.-P., Kremer, S., de Seze, J., 2013. White matter volume is decreased in the brain of patients with neuromyelitis optica. Eur. J. Neurol. 20, 361–367. doi:10.1111/j.1468-1331.2012.03867.x

Chavhan, G.B., Babyn, P.S., Jankharia, B.G., Cheng, H.-L.M., Shroff, M.M., 2008. Steady-State MR Imaging Sequences: Physics, Classification, and Clinical Applications. RadioGraphics 28, 1147–1160. doi:10.1148/rg.284075031

Chavhan, G.B., Babyn, P.S., Thomas, B., Shroff, M.M., Haacke, E.M., 2009. Principles, Techniques, and Applications of T2*-based MR Imaging and Its Special Applications. RadioGraphics 29, 1433–1449. doi:10.1148/rg.295095034

Chen, X., Zeng, C., Luo, T., Ouyang, Y., Lv, F., Rumzan, R., Wang, Z., Li, Q., Wang, J., Hou, H., Huang, F., Li, Y., 2012. Iron deposition of the deep grey matter in patients with multiple sclerosis and neuromyelitis optica: a control quantitative study by 3D-enhanced susceptibility-weighted angiography (ESWAN). Eur. J. Radiol. 81, e633-9. doi:10.1016/j.ejrad.2012.01.003

Cheng, H.-L.M., Stikov, N., Ghugre, N.R., Wright, G. a, 2012. Practical medical applications of quantitative MR relaxometry. J. Magn. Reson. Imaging 36, 805–24. doi:10.1002/jmri.23718

Chiaravalloti, N.D., DeLuca, J., 2008. Cognitive impairment in multiple sclerosis. Lancet Neurol. 7, 1139–1151. doi:10.1016/S1474-4422(08)70259-X

Ciccarelli, O., 2012. Do cortical lesions help us to distinguish MS from NMO? Neurology 79, 1630–1. doi:10.1212/WNL.0b013e31826e9bbf

Ciccarelli, O., Thomas, D.L., De Vita, E., Wheeler-Kingshott, C.A.M., Kachramanoglou, C., Kapoor, R., Leary, S., Matthews, L., Palace, J., Chard, D., Miller, D.H., Toosy, A.T., Thompson, A.J., 2013. Low Myo-inositol indicating astrocytic damage in a case series of neuromyelitis optica. Ann. Neurol. 74, 301–305. doi:10.1002/ana.23909

Cohen-Adad, J., Wheeler-Kingshott, C.A.M., 2014. Quantitative MRI of the Spinal Cord.

Cohen, J.A., Reingold, S.C., Polman, C.H., Wolinsky, J.S., 2012. Disability outcome measures in multiple sclerosis clinical trials: current status and future prospects. Lancet Neurol. 11, 467–476. doi:10.1016/S1474-4422(12)70059-5

Collongues, N., Cabre, P., Marignier, R., Zéphir, H., Papeix, C., Audoin, B., Lebrun-Frenay, C., Pelletier, J., Fontaine, B., Vermersch, P., Confavreux, C., de Seze, J., Group Members for NOMADMUS and CF-SEP, 2011. A benign form of neuromyelitis optica: does it exist? Arch. Neurol. 68, 918–24. doi:10.1001/archneurol.2011.127

Collongues, N., Marignier, R., Jacob, A., Leite, M.I., Siva, A., Paul, F., Zephir, H., Akman-Demir, G., Elsone, L., Jarius, S., Papeix, C., Mutch, K., Saip, S., Wildemann, B., Kitley, J., Karabudak, R., Aktas, O., Kuscu, D., Altintas, A., Palace, J., Confavreux, C., De Seze, J., 2014. Characterization of neuromyelitis optica and neuromyelitis optica spectrum disorder patients with a late onset. Mult. Scler. J. 20, 1086–1094. doi:10.1177/1352458513515085

Collongues, N., Marignier, R., Zéphir, H., Papeix, C., Blanc, F., Ritleng, C., Tchikviladzé, M., Outteryck, O., Vukusic, S., Fleury, M., Fontaine, B., Brassat, D., Clanet, M., Milh, M., Pelletier, J., Audoin, B., Ruet, A., Lebrun-Frenay, C., Thouvenot, E., Camu, W., Debouverie, M., Créange, A., Moreau, T., Labauge, P., Castelnovo, G., Edan, G., Le Page, E., Defer, G., Barroso, B., Heinzlef, O., Gout, O., Rodriguez, D., Wiertlewski, S., Laplaud, D., Borgel, F., Tourniaire, P., Grimaud, J., Brochet, B., Vermersch, P., Confavreux, C., De Seze, J., 2010. Neuromyelitis optica in France: A multicenter study of 125 patients. Neurology 74, 736–742. doi:10.1212/WNL.0b013e3181d31e35

Compston, A., Coles, A., 2008. Multiple sclerosis. Lancet 372, 1502–1517. doi:10.1016/S0140-6736(08)61620-7

Compston, A., McDonald, I., Noseworthy, J., Lassmann, H., Miller, D., Smith, K., Wekerle, H., Confavreux, C., 2005. McAlpine's Multiple Sclerosis, 4th ed. Elsevier, London. doi:10.1016/B978-0-443-07271-0.50004-5

Cook, L.., Rose, J.., Jolley, A.., Alvey, J., Kuhn, R., Pederson, M., Han, M., Levy, M., Mealy, M., Bennett, J., Carruthers, R., Traboulsee, A., Kenneally, M., Behne, D., Rodriguez, R., Blackway, D., Coords, B., Blaschke, T., Smith, T.., Yeaman, M.., Behne, J., the Guthy-Jackson Charitable Foundation International Clinical Consortium (GJCF-ICC), 2016. The CIRCLES program: accelerating solutions to neuromyelitis optica spectrum disorder, in: ECTRIMS 31st Meeting. London, UK.

Cree, B.A.C., Gourraud, P.-A., Oksenberg, J.R., Bevan, C., Crabtree-Hartman, E., Gelfand, J.M., Goodin, D.S., Graves, J., Green, A.J., Mowry, E., Okuda, D.T., Pelletier, D., von Büdingen, H.-C., Zamvil, S.S., Agrawal, A., Caillier, S., Ciocca, C., Gomez, R., Kanner, R., Lincoln, R., Lizee, A., Qualley, P., Santaniello, A., Suleiman, L., Bucci, M., Panara, V., Papinutto, N., Stern, W.A., Zhu, A.H., Cutter, G.R., Baranzini, S., Henry, R.G., Hauser, S.L., 2016. Long-term evolution of multiple sclerosis disability in the treatment era. Ann. Neurol. 80, 499–510. doi:10.1002/ana.24747

Crooijmans, H.J.A., Scheffler, K., Bieri, O., 2011. Finite RF pulse correction on DESPOT2. Magn. Reson. Med. 65, 858–862. doi:10.1002/mrm.22661

Croteau-Chonka, E.C., Dean, D.C., Remer, J., Dirks, H., O'Muircheartaigh, J., Deoni,

S.C.L., 2016. Examining the relationships between cortical maturation and white matter myelination throughout early childhood. Neuroimage 125, 413–421. doi:10.1016/j.neuroimage.2015.10.038

Daams, M., Weiler, F., Steenwijk, M.D., Hahn, H.K., Geurts, J.J., Vrenken, H., van Schijndel, R.A., Balk, L.J., Tewarie, P.K., Tillema, J.-M., Killestein, J., Uitdehaag, B.M., Barkhof, F., 2014. Mean upper cervical cord area (MUCCA) measurement in long-standing multiple sclerosis: Relation to brain findings and clinical disability. Mult. Scler. J. 20, 1860–1865. doi:10.1177/1352458514533399

Davis, M., Auh, S., Riva, M., Richert, N.D., Frank, J.A., McFarland, H.F., Bagnato, F., 2010. Ring and nodular multiple sclerosis lesions: A retrospective natural history study. Neurology 74, 851–856. doi:10.1212/WNL.0b013e3181d31df5

De Leener, B., Kadoury, S., Cohen-Adad, J., 2014. Robust, accurate and fast automatic segmentation of the spinal cord. Neuroimage 98, 528–536. doi:10.1016/j.neuroimage.2014.04.051

De Leener, B., Lévy, S., Dupont, S.M., Fonov, V.S., Stikov, N., Louis Collins, D., Callot, V., Cohen-Adad, J., 2017. SCT: Spinal Cord Toolbox, an open-source software for processing spinal cord MRI data. Neuroimage 145, 24–43. doi:10.1016/j.neuroimage.2016.10.009

Dean, D.C., Sojkova, J., Hurley, S., Kecskemeti, S., Okonkwo, O., Bendlin, B.B., Theisen, F., Johnson, S.C., Alexander, A.L., Gallagher, C.L., 2016. Alterations of myelin content in Parkinson's disease:a cross-sectional neuroimaging study. PLoS One 11, 1–20. doi:10.1371/journal.pone.0163774

De Santis, S., Drakesmith, M., Bells, S., Assaf, Y., Jones, D.K., 2014. Why diffusion tensor MRI does well only some of the time: Variance and covariance of white matter tissue microstructure attributes in the living human brain. Neuroimage 89, 35–44. doi:10.1016/j.neuroimage.2013.12.003

DeLuca, J., Chelune, G.J., Tulsky, D.S., Lengenfelder, J., Chiaravalloti, N.D., 2004. Is Speed of Processing or Working Memory the Primary Information Processing Deficit in Multiple Sclerosis? J. Clin. Exp. Neuropsychol. 26, 550–562. doi:10.1080/13803390490496641

Deoni, S., 2009a. Transverse relaxation time (T2) mapping in the brain with off-resonance correction using phase-cycled steady-state free precession imaging. J. Magn. Reson. Imaging 30, 411–7. doi:10.1002/jmri.21849

Deoni, S., 2009b. Intra and inter-site reproducibility of myelin water volume fraction values derived using mcDESPOT. 17th Annu. Meet. … 17, 4530.

Deoni, S.C., Rutt, B.K., Arun, T., Pierpaoli, C., Jones, D.K., 2008a. Gleaning multicomponent T1 and T2 information from steady-state imaging data. Magn. Reson. Med. 60, 1372–1387. doi:10.1002/mrm.21704

Deoni, S.C., Williams, S., Jezzard, P., Suckling, J., Murphy, D., Jones, D., 2008b. Standardized structural magnetic resonance imaging in multicentre studies using quantitative T 1 and T 2 imaging at 1.5 T. Neuroimage 40, 662–71. doi:10.1016/j.neuroimage.2007.11.052

Deoni, S.C.L., 2011. Correction of main and transmit magnetic field (B0 and B1) inhomogeneity effects in multicomponent-driven equilibrium single-pulse observation of T1 and T2. Magn. Reson. Med. 65, 1021–1035. doi:10.1002/mrm.22685

Deoni, S.C.L., 2010. Quantitative Relaxometry of the Brain. Top. Magn. Reson. Imaging 21, 101–113. doi:10.1097/RMR.0b013e31821e56d8

Deoni, S.C.L., 2007. High-Resolution T1 Mapping of the Brain at 3T with Driven Equilibrium Single Pulse Observation of T1 with High-Speed Incorporation of RF Field Inhomogeneities (DESPOT1-HIFI). J. Magn. Reson. Imaging 26, 1106–11.

doi:10.1002/jmri.21130

Deoni, S.C.L., Catani, M., 2007. Visualization of the deep cerebellar nuclei using quantitative T1 and rho magnetic resonance imaging at 3 Tesla. Neuroimage 37, 1260–6. doi:10.1016/j.neuroimage.2007.06.036

Deoni, S.C.L., Dean, D.C., O'Muircheartaigh, J., Dirks, H., Jerskey, B. a, 2012. Investigating white matter development in infancy and early childhood using myelin water faction and relaxation time mapping. Neuroimage 63, 1038–1053. doi:10.1016/j.neuroimage.2012.07.037

Deoni, S.C.L., Kolind, S.H., 2015. Investigating the stability of mcDESPOT myelin water fraction values derived using a stochastic region contraction approach. Magn. Reson. Med. 73, 161–169. doi:10.1002/mrm.25108

Deoni, S.C.L., Matthews, L., Kolind, S.H., 2013. One component? Two components? Three? The effect of including a nonexchanging "free" water component in multicomponent driven equilibrium single pulse observation of T1 and T2. Magn. Reson. Med. 70, 147–154. doi:10.1002/mrm.24429

Deoni, S.C.L., Mercure, E., Blasi, A., Gasston, D., Thomson, A., Johnson, M., Williams, S.C.R., Murphy, D.G.M., 2011. Mapping infant brain myelination with magnetic resonance imaging. J. Neurosci. 31, 784–91. doi:10.1523/JNEUROSCI.2106-10.2011

Deoni, S.C.L., O'Muircheartaigh, J., Elison, J.T., Walker, L., Doernberg, E., Waskiewicz, N., Dirks, H., Piryatinsky, I., Dean, D.C., Jumbe, N.L., 2016. White matter maturation profiles through early childhood predict general cognitive ability. Brain Struct. Funct. 221, 1189–1203. doi:10.1007/s00429-014-0947-x

Deoni, S.C.L., Rutt, B.K., Parrent, A.G., Peters, T.M., 2007. Segmentation of thalamic nuclei using a modified k-means clustering algorithm and high-resolution quantitative magnetic resonance imaging at 1.5 T. Neuroimage 34, 117–126. doi:10.1016/j.neuroimage.2006.09.016

Deoni, S.C.L., Rutt, B.K., Peters, T.M., 2006. Synthetic T1-weighted brain image generation with incorporated coil intensity correction using DESPOT1. Magn. Reson. Imaging 24, 1241–1248. doi:10.1016/j.mri.2006.03.015

Deoni, S.C.L., Ward, H.A., Peters, T.M., Rutt, B.K., 2004. Rapid T2 estimation with phase-cycled variable nutation steady-state free precession. Magn. Reson. Med. 52, 435–439. doi:10.1002/mrm.20159

Deoni, S.C.L., Zinkstok, J.R., Daly, E., Ecker, C., Williams, S.C.R., Murphy, D.G.M., 2015. White-matter relaxation time and myelin water fraction differences in young adults with autism. Psychol. Med. 45, 795–805. doi:10.1017/S0033291714001858

Deoni, S.C.L.S., Rutt, B.B.K., Peters, T.M.T., 2003. Rapid combined T1 and T2 mapping using gradient recalled acquisition in the steady state. Magn. Reson. … 49, 515–26. doi:10.1002/mrm.10407

Dortch, R.D., Harkins, K.D., Juttukonda, M.R., Gore, J.C., Does, M.D., 2013. Characterizing inter-compartmental water exchange in myelinated tissue using relaxation exchange spectroscopy. Magn. Reson. Med. 70, 1450–1459. doi:10.1002/mrm.24571

Duan, Y., Liu, Y., Liang, P., Jia, X., Yu, C., Qin, W., Sun, H., Liao, Z., Ye, J., Li, K., 2012. Comparison of grey matter atrophy between patients with neuromyelitis optica and multiple sclerosis: A voxel-based morphometry study. Eur. J. Radiol. 81, e110–e114. doi:10.1016/j.ejrad.2011.01.065

Duan, Y., Liu, Z., Liu, Y., Huang, J., Ren, Z., Sun, Z., Chen, H., Dong, H., Ye, J., Li, K., 2017. Metabolic changes in normal-appearing white matter in patients with neuromyelitis optica and multiple sclerosis: a comparative magnetic resonance spectroscopy study. Acta radiol. 0, 28418511668357. doi:10.1177/0284185116683575

Dula, A.N., Gochberg, D.F., Valentine, H.L., Valentine, W.M., Does, M.D., 2010.

Multiexponential T2, magnetization transfer, and Quantitative histology in white matter tracts of rat spinal cord. Magn. Reson. Med. 63, 902–909. doi:10.1002/mrm.22267

Dula, A.N., Pawate, S., Dortch, R.D., Barry, R.L., George-Durrett, K.M., Lyttle, B.D., Dethrage, L.M., Gore, J.C., Smith, S.A., 2016. Magnetic resonance imaging of the cervical spinal cord in multiple sclerosis at 7T. Mult. Scler. J. 22, 320–328. doi:10.1177/1352458515591070

Duncan, I.D., Radcliff, A.B., 2016. Inherited and acquired disorders of myelin: The underlying myelin pathology. Exp. Neurol. 283, 452–475. doi:10.1016/j.expneurol.2016.04.002

Duval, T., 2016. Modeling white matter microstructure. Funct. Neurol. 31, 217–228. doi:10.11138/FNeur/2016.31.4.217

Eickhoff, S.B., Paus, T., Caspers, S., Grosbras, M.H., Evans, A.C., Zilles, K., Amunts, K., 2007. Assignment of functional activations to probabilistic cytoarchitectonic areas revisited. Neuroimage 36, 511–521. doi:10.1016/j.neuroimage.2007.03.060

Eizaguirre, M.B., Alonso, R., Vanotti, S., Garcea, O., 2017. Cognitive impairment in neuromyelitis optica spectrum disorders: What do we know? Mult. Scler. Relat. Disord. 18, 225–229. doi:10.1016/j.msard.2017.10.003

Eshaghi, A., Wottschel, V., Cortese, R., Calabrese, M., Sahraian, M.A., Thompson, A.J., Alexander, D.C., Ciccarelli, O., 2016. Gray matter MRI differentiates neuromyelitis optica from multiple sclerosis using random forest. Neurology 87, 2463–2470. doi:10.1212/WNL.0000000000003395

Etemadifar, M., Nasr, Z., Khalili, B., Taherioun, M., Vosoughi, R., 2015. Epidemiology of Neuromyelitis Optica in the World: A Systematic Review and Meta-Analysis. Mult. Scler. Int. 2015, 1–8. doi:10.1155/2015/174720

Evangelou, N., 2000. Regional axonal loss in the corpus callosum correlates with cerebral white matter lesion volume and distribution in multiple sclerosis. Brain. doi:10.1093/brain/123.9.1845

Evangelou, N., DeLuca, G.C., Owens, T., Esiri, M.M., 2005. Pathological study of spinal cord atrophy in multiple sclerosis suggests limited role of local lesions. Brain 128, 29–34. doi:10.1093/brain/awh323

Evans, A., Collins, L., Holmes, C., Paus, T., MacDonald, D., Zijdenbos, A., Toga, A., Fox, P., Lancaster, J., Mazziota, J., 1997. A 3D probabilistic atlas of normal human neuroanatomy, in: Third International Conference on Functional Mapping of the Human Brain. p. 349.

Fan, M., Fu, Y., Su, L., Shen, Y., Wood, K., Yang, L., Liu, Y., Shi, F.-D., 2017. Comparison of brain and spinal cord magnetic resonance imaging features in neuromyelitis optica spectrum disorders patients with or without aquaporin-4 antibody. Mult. Scler. Relat. Disord. 13, 58–66. doi:10.1016/j.msard.2017.02.003

Fields, R.D., 2008. White matter in learning, cognition and psychiatric disorders. Trends Neurosci. 31, 361–370. doi:10.1016/j.tins.2008.04.001

Figley, C.R., Yau, D., Stroman, P.W., 2008. Attenuation of Lower-Thoracic, Lumbar, and Sacral Spinal Cord Motion: Implications for Imaging Human Spinal Cord Structure and Function. Am. J. Neuroradiol. 29, 1450–1454. doi:10.3174/ajnr.A1154

Filippi, M., Agosta, F., 2010. Imaging biomarkers in multiple sclerosis. J. Magn. Reson. Imaging 31, 770–788. doi:10.1002/jmri.22102

Filippi, M., Rocca, M.A., Barkhof, F., Brück, W., Chen, J.T., Comi, G., DeLuca, G., De Stefano, N., Erickson, B.J., Evangelou, N., Fazekas, F., Geurts, J.J.G., Lucchinetti, C., Miller, D.H., Pelletier, D., Popescu, B.F.G., Lassmann, H., 2012. Association between pathological and MRI findings in multiple sclerosis. Lancet Neurol. 11, 349–360. doi:10.1016/S1474-4422(12)70003-0

Filippi, M., Rocca, M.A., Benedict, R.H.B., DeLuca, J., Geurts, J.J.G., Rombouts, S.A.R.B., Ron, M., Comi, G., 2010. The contribution of MRI in assessing cognitive impairment in multiple sclerosis. Neurology 75, 2121–8. doi:10.1212/WNL.0b013e318200d768

Filippi, M., Rocca, M.A., Ciccarelli, O., De Stefano, N., Evangelou, N., Kappos, L., Rovira, A., Sastre-Garriga, J., Tintor??, M., Frederiksen, J.L., Gasperini, C., Palace, J., Reich, D.S., Banwell, B., Montalban, X., Barkhof, F., 2016. MRI criteria for the diagnosis of multiple sclerosis: MAGNIMS consensus guidelines. Lancet Neurol. 15, 292–303. doi:10.1016/S1474-4422(15)00393-2

Filippi, M., Rocca, M., Moiola, L., Martinelli, V., Ghezzi, A., Capra, R., Salvi, F., Comi, G., 1999. MRI and magnetization transfer imaging changes in the brain and cervical cord of patients with Devic's neuromyelitis optica. Neurology 53, 1705–1710.

Filley, C.M., 2012. White matter dementia. Ther. Adv. Neurol. Disord. 5, 267–77. doi:10.1177/1756285612454323

Filley, C.M., 2010. White matter: Organization and functional relevance. Neuropsychol. Rev. 20, 158–173. doi:10.1007/s11065-010-9127-9

Filley, C.M., Fields, R.D., 2016. White Matter and Cognition: Making the Connection. J. Neurophysiol. jn.00221.2016. doi:10.1152/jn.00221.2016

Finke, C., Heine, J., Pache, F., Lacheta, A., Borisow, N., Kuchling, J., Bellmann-Strobl, J., Ruprecht, K., Brandt, A.U., Paul, F., 2016. Normal volumes and microstructural integrity of deep gray matter structures in AQP4+ NMOSD. Neurol. Neuroimmunol. Neuroinflammation 3, e229–e229. doi:10.1212/NXI.0000000000000229

Flanagan, E.P., Weinshenker, B.G., Krecke, K.N., Lennon, V.A., Lucchinetti, C.F., McKeon, A., Wingerchuk, D.M., Shuster, E.A., Jiao, Y., Horta, E.S., Pittock, S.J., 2015. Short Myelitis Lesions in Aquaporin-4-IgG–Positive Neuromyelitis Optica Spectrum Disorders. JAMA Neurol. 72, 81. doi:10.1001/jamaneurol.2014.2137

Fleiss, J.L., 1999. The design and analysis of clinical experiments, A Wiley-Interscience Publication. doi:10.1016/0898-1221(87)90245-8

Flynn, S.W., Lang, D.J., Mackay, A.L., Goghari, V., Vavasour, I.M., Whittall, K.P., Smith, G.N., Arango, V., Mann, J.J., Dwork, A.J., Falkai, P., Honer, W.G., 2003. Abnormalities of myelination in schizophrenia detected in vivo with MRI, and post-mortem with analysis of oligodendrocyte proteins. Mol. Psychiatry 8, 811–820. doi:10.1038/sj.mp.4001337

Fonov, V.S., Le Troter, A., Taso, M., De Leener, B., Lévêque, G., Benhamou, M., Sdika, M., Benali, H., Pradat, P.F., Collins, D.L., Callot, V., Cohen-Adad, J., 2014. Framework for integrated MRI average of the spinal cord white and gray matter: The MNI-Poly-AMU template. Neuroimage 102, 817–827. doi:10.1016/j.neuroimage.2014.08.057

Fox, R., 2008. Picturing Multiple Sclerosis: Conventional and Diffusion Tensor Imaging. Semin. Neurol. 28, 453–466. doi:10.1055/s-0028-1083689

Fradet, L., Arnoux, P.-J., Ranjeva, J.-P., Petit, Y., Callot, V., 2014. Morphometrics of the Entire Human Spinal Cord and Spinal Canal Measured From In Vivo High-Resolution Anatomical Magnetic Resonance Imaging. Spine (Phila. Pa. 1976). 39, E262–E269. doi:10.1097/BRS.0000000000000125

Freeborough, P.A., Fox, N.C., 1997. The boundary shift integral: an accurate and robust measure of cerebral volume changes from registered repeat MRI. IEEE Trans. Med. Imaging 16, 623–629. doi:10.1109/42.640753

Frischer, J.M., Bramow, S., Dal-Bianco, A., Lucchinetti, C.F., Rauschka, H., Schmidbauer, M., Laursen, H., Sorensen, P.S., Lassmann, H., 2009. The relation between inflammation and neurodegeneration in multiple sclerosis brains. Brain 132, 1175–1189. doi:10.1093/brain/awp070

Frohman, E.M., Filippi, M., Stuve, O., Waxman, S.G., Corboy, J., Phillips, J.T., Lucchinetti,

C., Wilken, J., Karandikar, N., Hemmer, B., Monson, N., De Keyser, J., Hartung, H., Steinman, L., Oksenberg, J.R., Cree, B.A.C., Hauser, S., Racke, M.K., 2005. Characterizing the Mechanisms of Progression in Multiple Sclerosis. Arch. Neurol. 62, 1345. doi:10.1001/archneur.62.9.1345

Gareau, P.J., Rutt, B.K., Karlik, S.J., Mitchell, J.R., 2000. Magnetization transfer and multicomponent T2 relaxation measurements with histopathologic correlation in an experimental model of MS. J. Magn. Reson. Imaging 11, 586–595. doi:10.1002/1522-2586(200006)11:6<586::AID-JMRI3>3.0.CO;2-V

Gass, A., Rocca, M.A., Agosta, F., Ciccarelli, O., Chard, D., Valsasina, P., Brooks, J.C.W., Bischof, A., Eisele, P., Kappos, L., Barkhof, F., Filippi, M., 2015. MRI monitoring of pathological changes in the spinal cord in patients with multiple sclerosis. Lancet Neurol. doi:10.1016/S1474-4422(14)70294-7

Giovannoni, G., Butzkueven, H., Dhib-Jalbut, S., Hobart, J., Kobelt, G., Pepper, G., Sormani, M.P., Thalheim, C., Traboulsee, A., Vollmer, T., 2016. Brain health: time matters in multiple sclerosis. Mult. Scler. Relat. Disord. 9, S5–S48. doi:10.1016/j.msard.2016.07.003

Glasser, M.F., Van Essen, D.C., 2011. Mapping human cortical areas in vivo based on myelin content as revealed by T1- and T2-weighted MRI. J. Neurosci. 31, 11597–616. doi:10.1523/JNEUROSCI.2180-11.2011

Groeschel, S., Hagberg, G.E., Schultz, T., Balla, D.Z., Klose, U., Hauser, T.-K., Nägele, T., Bieri, O., Prasloski, T., MacKay, A.L., Krägeloh-Mann, I., Scheffler, K., 2016. Assessing White Matter Microstructure in Brain Regions with Different Myelin Architecture Using MRI. PLoS One 11, e0167274. doi:10.1371/journal.pone.0167274

Gunning-Dixon, F.M., Brickman, A.M., Cheng, J.C., Alexopoulos, G.S., 2009. Aging of cerebral white matter: a review of MRI findings. Int. J. Geriatr. Psychiatry 24, 109–117. doi:10.1002/gps.2087

Harkins, K.D., Dula, A.N., Does, M.D., 2012. Effect of intercompartmental water exchange on the apparent myelin water fraction in multiexponential T2 measurements of rat spinal cord. Magn. Reson. Med. 67, 793–800. doi:10.1002/mrm.23053

He, D., Chen, X., Zhao, D., Zhou, H., 2011a. Cognitive Function, Depression, Fatigue, and Activities of Daily Living in Patients With Neuromyelitis Optica After Acute Relapse. Int. J. Neurosci. 121, 677–683. doi:10.3109/00207454.2011.608456

He, D., Wu, Q., Chen, X., Zhao, D., Gong, Q., Zhou, H., 2011b. Cognitive impairment and whole brain diffusion in patients with neuromyelitis optica after acute relapse. Brain Cogn. 77, 80–8. doi:10.1016/j.bandc.2011.05.007

Healy, B.C., Arora, A., Hayden, D.L., Ceccarelli, A., Tauhid, S.S., Neema, M., Bakshi, R., 2012. Approaches to normalization of spinal cord volume: Application to multiple sclerosis. J. Neuroimaging 22, 12–19. doi:10.1111/j.1552-6569.2011.00629.x

Healy, B.C., Engler, D., Glanz, B., Musallam, A., Chitnis, T., 2013. Assessment of Definitions of Sustained Disease Progression in Relapsing-Remitting Multiple Sclerosis. Mult. Scler. Int. 2013, 1–9. doi:10.1155/2013/189624

Henry, R.G., Shieh, M., Amirbekian, B., Chung, S., Okuda, D.T., Pelletier, D., 2009. Connecting white matter injury and thalamic atrophy in clinically isolated syndromes. J. Neurol. Sci. 282, 61–66. doi:10.1016/j.jns.2009.02.379

Hinson, S.R., Romero, M.F., Popescu, B.F.G., Lucchinetti, C.F., Fryer, J.P., Wolburg, H., Fallier-Becker, P., Noell, S., Lennon, V.A., 2012. Molecular outcomes of neuromyelitis optica (NMO)-IgG binding to aquaporin-4 in astrocytes. Proc. Natl. Acad. Sci. U. S. A. 109, 1245–50. doi:10.1073/pnas.1109980108

Homer, J., Beevers, M.S., 1985. Driven-equilibrium single-pulse observation of T1 relaxation. A reevaluation of a rapid “new” method for determining NMR spin-lattice

relaxation times. J. Magn. Reson. 63, 287–297. doi:10.1016/0022-2364(85)90318-X

Hua, K., Zhang, J., Wakana, S., Jiang, H., Li, X., Reich, D.S., Calabresi, P.A., Pekar, J.J., van Zijl, P.C.M., Mori, S., 2008. Tract probability maps in stereotaxic spaces: Analyses of white matter anatomy and tract-specific quantification. Neuroimage 39, 336–347. doi:10.1016/j.neuroimage.2007.07.053

Huh, S.-Y., Kim, S.-H., Hyun, J., Jeong, I.H., Park, M.S., Lee, S., Kim, H.J., 2017. Short segment myelitis as a first manifestation of neuromyelitis optica spectrum disorders. Mult. Scler. J. 23, 413–419. doi:10.1177/1352458516687043

Hurley, S., Mossahebi, P., Samsonov, A., Alexander, A., Deoni, S., Fisher, R., Duncan, I., Field, A., 2010. Multicomponent relaxometry (mcDESPOT) in the shaking pup model of dysmyelination. Proc Intl Soc Magn Reson Med 18, 4516.

Hwang, D., Kim, D., Du, Y.P., 2010. In vivo multi-slice mapping of myelin water content using T2* decay. Neuroimage 52, 198–204. doi:10.1016/j.neuroimage.2010.04.023

Hyun, J.-W., Park, G., Kwak, K., Jo, H.-J., Joung, A., Kim, J.-H., Lee, S.H., Kim, S., Lee, J.-M., Kim, S.-H., Kim, H.J., 2016. Deep gray matter atrophy in neuromyelitis optica spectrum disorder and multiple sclerosis. Eur. J. Neurol. 1–9. doi:10.1111/ene.13224

Ikeda, K., Ito, H., Hidaka, T., Takazawa, T., Sekine, T., Yoshii, Y., Hirayama, T., Kawabe, K., Kano, O., Iwasaki, Y., 2011. Repeated Non-enhancing Tumefactive Lesions in a Patient with a Neuromyelitis Optica Spectrum Disorder. Intern. Med. 50, 1061–1064. doi:10.2169/internalmedicine.50.4295

Ito, S., Mori, M., Makino, T., Hayakawa, S., Kuwabara, S., 2009. “Cloud-like enhancement” is a magnetic resonance imaging abnormality specific to neuromyelitis optica. Ann. Neurol. 66, 425–8. doi:10.1002/ana.21753

Jackson, E.F., 2018. Quantitative Imaging: The Translation from Research Tool to Clinical Practice. Radiology 286, 499–501. doi:10.1148/radiol.2017172258

Jacob, A., McKeon, A., Nakashima, I., Sato, D.K., Elsone, L., Fujihara, K., de Seze, J., 2013. Current concept of neuromyelitis optica (NMO) and NMO spectrum disorders. J. Neurol. Neurosurg. Psychiatry 84, 922–30. doi:10.1136/jnnp-2012-302310

Jacobson, S., Marcus, E.M., 2011. Neuroanatomy for the Neuroscientist, 2nd ed, Neuroanatomy for the Neuroscientist. Springer, New York. doi:10.1007/978-1-4419-9653-4

Jarius, S., Aboul-Enein, F., Waters, P., Kuenz, B., Hauser, A., Berger, T., Lang, W., Reindl, M., Vincent, A., Kristoferitsch, W., 2008a. Antibody to aquaporin-4 in the long-term course of neuromyelitis optica. Brain 131, 3072–3080. doi:10.1093/brain/awn240

Jarius, S., Franciotta, D., Bergamaschi, R., Wright, H., Littleton, E., Palace, J., Hohlfeld, R., Vincent, A., 2007. NMO-IgG in the diagnosis of neuromyelitis optica. Neurology 68, 1076–7. doi:10.1212/01.wnl.0000256822.01222.bd

Jarius, S., Paul, F., Franciotta, D., Waters, P., Zipp, F., Hohlfeld, R., Vincent, A., Wildemann, B., 2008b. Mechanisms of disease: aquaporin-4 antibodies in neuromyelitis optica. Nat. Clin. Pract. Neurol. 4, 202–14. doi:10.1038/ncpneuro0764

Jarius, S., Ruprecht, K., Kleiter, I., Borisow, N., Asgari, N., Pitarokoili, K., Pache, F., Stich, O., Beume, L.-A., Hümmert, M.W., Ringelstein, M., Trebst, C., Winkelmann, A., Schwarz, A., Buttmann, M., Zimmermann, H., Kuchling, J., Franciotta, D., Capobianco, M., Siebert, E., Lukas, C., Korporal-Kuhnke, M., Haas, J., Fechner, K., Brandt, A.U., Schanda, K., Aktas, O., Paul, F., Reindl, M., Wildemann, B., 2016a. MOG-IgG in NMO and related disorders: a multicenter study of 50 patients. Part 2: Epidemiology, clinical presentation, radiological and laboratory features, treatment responses, and long-term outcome. J. Neuroinflammation 13, 280. doi:10.1186/s12974-016-0718-0

Jarius, S., Ruprecht, K., Kleiter, I., Borisow, N., Asgari, N., Pitarokoili, K., Pache, F., Stich, O., Beume, L.-A., Hümmert, M.W., Trebst, C., Ringelstein, M., Aktas, O., Winkelmann,

A., Buttmann, M., Schwarz, A., Zimmermann, H., Brandt, A.U., Franciotta, D., Capobianco, M., Kuchling, J., Haas, J., Korporal-Kuhnke, M., Lillevang, S.T., Fechner, K., Schanda, K., Paul, F., Wildemann, B., Reindl, M., 2016b. MOG-IgG in NMO and related disorders: a multicenter study of 50 patients. Part 1: Frequency, syndrome specificity, influence of disease activity, long-term course, association with AQP4-IgG, and origin. J. Neuroinflammation 13, 279. doi:10.1186/s12974-016-0717-1

Jarius, S., Wildemann, B., 2010. AQP4 antibodies in neuromyelitis optica: diagnostic and pathogenetic relevance. Nat. Rev. Neurol. 6, 383–392. doi:10.1038/nrneurol.2010.72

Jeantroux, J., Kremer, S., Lin, X.Z., Collongues, N., Chanson, J.-B., Bourre, B., Fleury, M., Blanc, F., Dietemann, J.-L., de Seze, J., 2012. Diffusion tensor imaging of normal-appearing white matter in neuromyelitis optica. J. Neuroradiol. 39, 295–300. doi:10.1016/j.neurad.2011.10.003

Jenkinson, M., Bannister, P., Brady, M., Smith, S., 2002. Improved Optimization for the Robust and Accurate Linear Registration and Motion Correction of Brain Images. Neuroimage 17, 825–841. doi:10.1006/nimg.2002.1132

Jenkinson, M., Smith, S., 2001. A global optimisation method for robust affine registration of brain images. Med. Image Anal. 5, 143–156. doi:10.1016/S1361-8415(01)00036-6

Jeong, I.H., Choi, J.Y., Kim, S.-H., Hyun, J.-W., Joung, A., Lee, J., Kim, H.J., 2017. Normal-appearing white matter demyelination in neuromyelitis optica spectrum disorder. Eur. J. Neurol. 24, 5–7. doi:10.1111/ene.13266

Jiao, Y., Fryer, J.P., Lennon, V.A., Jenkins, S.M., Quek, A.M.L., Smith, C.Y., McKeon, A., Costanzi, C., Iorio, R., Weinshenker, B.G., Wingerchuk, D.M., Shuster, E.A., Lucchinetti, C.F., Pittock, S.J., 2013. Updated estimate of AQP4-IgG serostatus and disability outcome in neuromyelitis optica. Neurology 81, 1197–204. doi:10.1212/WNL.0b013e3182a6cb5c

Jones, D.K., Knösche, T.R., Turner, R., 2013. White matter integrity, fiber count, and other fallacies: The do's and don'ts of diffusion MRI. Neuroimage. doi:10.1016/j.neuroimage.2012.06.081

Jurick, S.M., Bangen, K.J., Evangelista, N.D., Sanderson-Cimino, M., Delano-Wood, L., Jak, A.J., 2016. Advanced neuroimaging to quantify myelin *in vivo* : Application to mild TBI. Brain Inj. 30, 1452–1457. doi:10.1080/02699052.2016.1219064

Juryńczyk, M., Tackley, G., Kong, Y., Geraldes, R., Matthews, L., Woodhall, M., Waters, P., Kuker, W., Craner, M., Weir, A., DeLuca, G.C., Kremer, S., Leite, M.I., Vincent, A., Jacob, A., de Sèze, J., Palace, J., 2016. Brain lesion distribution criteria distinguish MS from AQP4-antibody NMOSD and MOG-antibody disease. J. Neurol. Neurosurg. Psychiatry jnnp-2016-314005. doi:10.1136/jnnp-2016-314005

Kandel, E.R., Schwartz, J.H., Jessell, T.M., 2000. Principles of Neural Science, Neurology.

Kawachi, I., Lassmann, H., 2017. Neurodegeneration in multiple sclerosis and neuromyelitis optica. J. Neurol. Neurosurg. Psychiatry 88, 137–145. doi:10.1136/jnnp-2016-313300

Ketelslegers, I.A., Modderman, P.W., Vennegoor, A., Killestein, J., Hamann, D., Hintzen, R.Q., 2011. Antibodies against aquaporin-4 in neuromyelitis optica: distinction between recurrent and monophasic patients. Mult. Scler. 17, 1527–30. doi:10.1177/1352458511412995

Kim, H.J., Paul, F., Lana-Peixoto, M.A., Tenembaum, S., Asgari, N., Palace, J., Klawiter, E.C., Sato, D.K., De Seze, J., Wuerfel, J., Banwell, B.L., Villoslada, P., Saiz, A., Fujihara, K., Kim, S.H., 2015. MRI characteristics of neuromyelitis optica spectrum disorder: An international update. Neurology 84, 1165–1173. doi:10.1212/WNL.0000000000001367

Kim, S.-H., Hyun, J.-W., Joung, A., Lee, S.H., Kim, H.J., 2016a. Occurrence of Asymptomatic Acute Neuromyelitis Optica Spectrum Disorder-Typical Brain Lesions

during an Attack of Optic Neuritis or Myelitis. PLoS One 11, e0167783. doi:10.1371/journal.pone.0167783

Kim, S.-H., Kwak, K., Hyun, J.W., Jeong, I.H., Jo, H.J., Joung, A., Kim, J.H., Lee, S.H., Yun, S., Joo, J., Lee, J.M., Kim, H.J., 2016b. Widespread cortical thinning in patients with neuromyelitis optica spectrum disorder. Eur. J. Neurol. 23, 1165–1173. doi:10.1111/ene.13011

Kim, S.-H., Kwak, K., Jeong, I.H., Hyun, J.-W., Jo, H.-J., Joung, A., Yu, E.-S., Kim, J.-H., Lee, S.H., Yun, S., Joo, J., Lee, D. -k., Lee, J.-M., Kim, H.J., 2016c. Cognitive impairment differs between neuromyelitis optica spectrum disorder and multiple sclerosis. Mult. Scler. J. 1–9. doi:10.1177/1352458516636246

Kim, W., Kim, S.-H., Huh, S.-Y., Kim, H.J., 2012. Brain abnormalities in neuromyelitis optica spectrum disorder. Mult. Scler. Int. 2012, 735486. doi:10.1155/2012/735486

Kim, W., Min Su Park, Sang Hyun Lee, Kim, S.-H., In Ja Jung, Takahashi, T., Misu, T., Fujihara, K., Ho Jin Kim, 2010. Characteristic brain magnetic resonance imaging abnormalities in central nervous system aquaporin-4 autoimmunity. Mult. Scler. J. 16, 1229–1236. doi:10.1177/1352458510376640

Kimura, M.C.G., Doring, T.M., Rueda, F.C., Tukamoto, G., Gasparetto, E.L., 2014. In vivo assessment of white matter damage in neuromyelitis optica: A diffusion tensor and diffusion kurtosis MR imaging study. J. Neurol. Sci. 345, 172–175. doi:10.1016/j.jns.2014.07.035

Kister, I., Ge, Y., Herbert, J., Sinnecker, T., Wuerfel, J., Paul, F., 2013a. Distinction of seropositive NMO spectrum disorder and MS brain lesion distribution. Neurology 81, 1966–1966. doi:10.1212/01.wnl.0000436079.95856.1f

Kister, I., Herbert, J., Zhou, Y., Ge, Y., 2013b. Ultrahigh-Field MR (7 T) Imaging of Brain Lesions in Neuromyelitis Optica. Mult. Scler. Int. 2013, 398259. doi:10.1155/2013/398259

Kister, I., Paul, F., 2015. Pushing the boundaries of neuromyelitis optica. Neurology 85, 118–119. doi:10.1212/WNL.0000000000001749

Kitley, J., Evangelou, N., Küker, W., Jacob, A., Leite, M.I., Palace, J., 2014a. Catastrophic brain relapse in seronegative NMO after a single dose of natalizumab. J. Neurol. Sci. 339, 223–5. doi:10.1016/j.jns.2014.01.035

Kitley, J., Leite, M.I., Nakashima, I., Waters, P., McNeillis, B., Brown, R., Takai, Y., Takahashi, T., Misu, T., Elsone, L., Woodhall, M., George, J., Boggild, M., Vincent, A., Jacob, A., Fujihara, K., Palace, J., 2012. Prognostic factors and disease course in aquaporin-4 antibody-positive patients with neuromyelitis optica spectrum disorder from the United Kingdom and Japan. Brain 135, 1834–49. doi:10.1093/brain/aws109

Kitley, J., Waters, P., Woodhall, M., Leite, M.I., Murchison, A., George, J., Küker, W., Chandratre, S., Vincent, A., Palace, J., 2014b. Neuromyelitis Optica Spectrum Disorders With Aquaporin-4 and Myelin-Oligodendrocyte Glycoprotein Antibodies. JAMA Neurol. 71, 276. doi:10.1001/jamaneurol.2013.5857

Kitzler, H.H., Su, J., Zeineh, M., Harper-Little, C., Leung, A., Kremenchutzky, M., Deoni, S.C., Rutt, B.K., 2012. Deficient MWF mapping in multiple sclerosis using 3D whole-brain multi-component relaxation MRI. Neuroimage 59, 2670–2677. doi:10.1016/j.neuroimage.2011.08.052

Klawiter, E.C., Xu, J., Naismith, R.T., Benzinger, T.L., Shimony, J.S., Lancia, S., Snyder, A.Z., Trinkaus, K., Song, S.-K., Cross, A.H., 2012. Increased radial diffusivity in spinal cord lesions in neuromyelitis optica compared with multiple sclerosis. Mult. Scler. J. 18, 1259–1268. doi:10.1177/1352458512436593

Klein, J.P., Arora, A., Neema, M., Healy, B.C., Tauhid, S., Goldberg-Zimring, D., Chavarro-Nieto, C., Stankiewicz, J.M., Cohen, A.B., Buckle, G.J., Houtchens, M.K., Ceccarelli,

A., Dell'Oglio, E., Guttmann, C.R.G., Alsop, D.C., Hackney, D.B., Bakshi, R., 2011. A 3T MR Imaging Investigation of the Topography of Whole Spinal Cord Atrophy in Multiple Sclerosis. Am. J. Neuroradiol. 32, 1138–1142. doi:10.3174/ajnr.A2459

Kolind, S., Manogaran, P., Vavasour, I., Russell-Schulz, B., Mcmullen, K., Zhang, J., Laule, C., Mackay, A., Rauscher, A., Li, D., Traboulsee, A., 2015a. Pathological Differences in Neuromyelitis Optica Reflected Differently by Two Myelin Water Imaging Techniques, in: 23rd Annual Meeting of the International Society of Magnetic Resonance in Medicine. Toronto, Canada. p. 2014.

Kolind, S., Matthews, L., Johansen-Berg, H., Leite, M.I., Williams, S.C.R., Deoni, S., Palace, J., 2012. Myelin water imaging reflects clinical variability in multiple sclerosis. Neuroimage 60, 263–270. doi:10.1016/j.neuroimage.2011.11.070.Myelin

Kolind, S., Seddigh, A., Combes, A., Russell-Schulz, B., Tam, R., Yogendrakumar, V., Deoni, S., Sibtain, N.A., Traboulsee, A., Williams, S.C.R., Barker, G.J., Brex, P.A., 2015b. Brain and cord myelin water imaging: a progressive multiple sclerosis biomarker. NeuroImage. Clin. 9, 574–80. doi:10.1016/j.nicl.2015.10.002

Kolind, S., Sharma, R., Knight, S., Johansen-Berg, H., Talbot, K., Turner, M.R., 2013. Myelin imaging in amyotrophic and primary lateral sclerosis. Amyotroph. Lateral Scler. Frontotemporal Degener. 14, 562–73. doi:10.3109/21678421.2013.794843

Kolind, S.H., Deoni, S.C., 2011. Rapid three-dimensional multicomponent relaxation imaging of the cervical spinal cord. Magn. Reson. Med. 65, 551–6. doi:10.1002/mrm.22634

Kolind, S.H., Mädler, B., Fischer, S., Li, D.K.B., MacKay, A.L., 2009a. Myelin water imaging: Implementation and development at 3.0T and comparison to 1.5T measurements. Magn. Reson. Med. 62, 106–115. doi:10.1002/mrm.21966

Kolind, S.H., Seixas, D., Palace, J., Deoni, S., Johansen-Berg, H., Weir, A., Tracey, I., 2009b. MS patients with chronic pain have more myelin water and less heterogeneous T1 values in normal-appearing white matter than matched MS patients without pain, in: Multiple Sclerosis. p. S209.

Kozlowski, P., Liu, J., Yung, A.C., Tetzlaff, W., 2008. High-resolution myelin water measurements in rat spinal cord. Magn. Reson. Med. 59, 796–802. doi:10.1002/mrm.21527

Krampla, W., Aboul-Enein, F., Jecel, J., Lang, W., Fertl, E., Hruby, W., Kristoferitsch, W., 2009. Spinal cord lesions in patients with neuromyelitis optica: a retrospective long-term MRI follow-up study. Eur Radiol 19, 2535–43. doi:10.1007/s00330-009-1425-3

Kurtzke, J.F., 1983. Rating neurologic impairment in multiple sclerosis: An expanded disability status scale (EDSS). Neurology 33, 1444–1444. doi:10.1212/WNL.33.11.1444

Kutzelnigg, A., Lassmann, H., 2006. Cortical demyelination in multiple sclerosis: A substrate for cognitive deficits? J. Neurol. Sci. 245, 123–126. doi:10.1016/j.jns.2005.09.021

Lalan, S., Khan, M., Schlakman, B., Penman, A., Gatlin, J., Herndon, R., 2012. Differentiation of neuromyelitis optica from multiple sclerosis on spinal magnetic resonance imaging. Int. J. MS Care 14, 209–214. doi:10.7224/1537-2073-14.4.209

Langdon, D., Amato, M., Boringa, J., Brochet, B., Foley, F., Fredrikson, S., Hämäläinen, P., Hartung, H.-P., Krupp, L., Penner, I., Reder, A., Benedict, R., 2012. Recommendations for a Brief International Cognitive Assessment for Multiple Sclerosis (BICAMS). Mult. Scler. J. 18, 891–898. doi:10.1177/1352458511431076

Langdon, D.W., 2011. Cognition in multiple sclerosis. Curr. Opin. Neurol. 24, 244–249. doi:10.1097/WCO.0b013e328346a43b

Lankford, C.L., Does, M.D., 2013. On the inherent precision of mcDESPOT. Magn. Reson. Med. 69, 127–36. doi:10.1002/mrm.24241

Lapointe, E., Litvin, L., Kolind, S., Vasavour, I., Wiggermann, V., Li, D., Traboulsee, A., 2017. Assessment of radiation-induced white matter changes using myelin water imaging, in: AAN 69th Meeting. Boston.

Lassmann, H., 2014. Mechanisms of white matter damage in multiple sclerosis. Glia 62, 1816–1830. doi:10.1002/glia.22597

Laule, C., Kozlowski, P., Leung, E., Li, D.K.B., MacKay, A.L., Moore, G.R.W., 2008. Myelin water imaging of multiple sclerosis at 7 T: Correlations with histopathology. Neuroimage 40, 1575–1580. doi:10.1016/j.neuroimage.2007.12.008

Laule, C., Leung, E., Li, D.K.K.B., Traboulsee, A.L., Paty, D.W., MacKay, A.L., Moore, G.R.R.W., Kozlowski, P., Leung, E., Li, D.K.K.B., MacKay, A.L., Moore, G.R.R.W., Traboulsee, A.L., Paty, D.W., MacKay, A.L., Moore, G.R.R.W., 2006. Myelin water imaging in multiple sclerosis: quantitative correlations with histopathology. Mult. Scler. J. 12, 747–753. doi:10.1177/1352458506070928

Laule, C., Shahinfard, E., Maedler, B., Zhang, J., Vavasour, I., Aul, R., Li, D.K.B., MacKay, A.L., Sirrs, S., 2016. Hematopoietic stem cell transplantation in late-onset Krabbe disease halts demyelination and axonal loss: A 4 year longitudinal case study, in: ISMRM 24th Meeting. Singapore.

Laule, C., Vavasour, I.M., Kolind, S.H., Li, D.K.B., Traboulsee, T.L., Moore, G.R.W., MacKay, A.L., 2007a. Magnetic Resonance Imaging of Myelin. Neurotherapeutics 4, 460–484. doi:10.1016/j.nurt.2007.05.004

Laule, C., Vavasour, I.M., Leung, E., Li, D.K.B., Kozlowski, P., Traboulsee, A.L., Oger, J., Mackay, A.L., Moore, G.R.W., 2011. Pathological basis of diffusely abnormal white matter: insights from magnetic resonance imaging and histology. Mult. Scler. 17, 144–50. doi:10.1177/1352458510384008

Laule, C., Vavasour, I.M., Mädler, B., Kolind, S.H., Sirrs, S.M., Brief, E.E., Traboulsee, A.L., Moore, G.R.W., Li, D.K.B., MacKay, A.L., 2007b. MR evidence of long T2 water in pathological white matter. J. Magn. Reson. Imaging 26, 1117–1121. doi:10.1002/jmri.21132

Laule, C., Vavasour, I.M., Moore, G.R.W., Oger, J., Li, D.K.B., Paty, D.W., MacKay, a L., 2004. Water content and myelin water fraction in multiple sclerosis. J. Neurol. 251, 284–293. doi:10.1007/s00415-004-0306-6

Laule, C., Vavasour, I.M., Zhao, Y., Traboulsee, a L., Oger, J., Vavasour, J.D., Mackay, a L., Li, D.K.B., 2010. Two-year study of cervical cord volume and myelin water in primary progressive multiple sclerosis. Mult. Scler. 16, 670–7. doi:10.1177/1352458510365586

Leavitt, V.M., Wylie, G., Krch, D., Chiaravalloti, N., DeLuca, J., Sumowski, J.F., 2014. Does slowed processing speed account for executive deficits in multiple sclerosis? Evidence from neuropsychological performance and structural neuroimaging. Rehabil. Psychol. 59, 422–428. doi:10.1037/a0037517

Lee, L.E., Combes, A.J.E., Chan, J., Carruthers, R., Palace, J., Matthews, L., Traboulsee, A., Kolind, S., 2017. mcDESPOT-derived tissue parameters in the brainstem and corpus callosum of MS and NMOSD patients with cervical cord lesions, in: Proceedings of the ISMRM 25th Annual Meeting.

Leener, B. De, Fonov, V., Collins, D.L., Callot, V., Stikov, N., Cohen-Adad, J., 2017. PAM50: Multimodal template of the brainstem and spinal cord compatible with the ICBM152 space, in: Proc Intl Soc Magn Reson Med. Honolulu, Hawaii.

Lennon, V.A., Kryzer, T.J., Pittock, S.J., Verkman, A.S., Hinson, S.R., 2005. IgG marker of optic-spinal multiple sclerosis binds to the aquaporin-4 water channel. J. Exp. Med. 202, 473–7. doi:10.1084/jem.20050304

Lennon, V.A., Wingerchuk, D.M., Kryzer, T.J., Pittock, S.J., Lucchinetti, C.F., Fujihara, K.,

Nakashima, I., Weinshenker, B.G., 2004. A serum autoantibody marker of neuromyelitis optica: distinction from multiple sclerosis. Lancet 364.

Levin, S.N., Habec, C., Riley, C.S., Sumowski, J.F., Li, P., Tsapanou, A., Leavitt, V.M., 2017. Neural correlates of cognitive phenotypes in multiple sclerosis, in: ECTRIMS 32nd Meeting. Paris, France.

Lewis-Beck, M.S., Bryman, A., Liao, T.F., 2004. The SAGE Encyclopedia of Social Science Research Methods, Social Science Research.

Liang, P., Liu, Y., Jia, X., Duan, Y., Yu, C., Qin, W., Dong, H., Ye, J., Li, K., 2011. Regional homogeneity changes in patients with neuromyelitis optica revealed by resting-state functional MRI. Clin. Neurophysiol. 122, 121–7. doi:10.1016/j.clinph.2010.05.026

Liu, Y., Duan, Y., He, Y., Wang, J., Xia, M., Yu, C., Dong, H., Ye, J., Butzkueven, H., Li, K., Shu, N., 2012a. Altered topological organization of white matter structural networks in patients with neuromyelitis optica. PLoS One 7, e48846. doi:10.1371/journal.pone.0048846

Liu, Y., Duan, Y., He, Y., Yu, C., Wang, J., Huang, J., Ye, J., Butzkueven, H., Li, K., Shu, N., 2012b. A tract-based diffusion study of cerebral white matter in neuromyelitis optica reveals widespread pathological alterations. Mult. Scler. 18, 1013–21. doi:10.1177/1352458511431731

Liu, Y., Duan, Y., Huang, J., Ren, Z., Ye, J., Dong, H., Shi, F.-D., Barkhof, F., Vrenken, H., Wattjes, M.P., Wang, J., Li, K., 2015a. Multimodal Quantitative MR Imaging of the Thalamus in Multiple Sclerosis and Neuromyelitis Optica. Radiology 277, 784–792. doi:10.1148/radiol.2015142786

Liu, Y., Fu, Y., Schoonheim, M.M., Zhang, N., Fan, M., Su, L., Shen, Y., Yan, Y., Yang, L., Wang, Q., Zhang, N., Yu, C., Barkhof, F., Shi, F.D., 2015b. Structural MRI substrates of cognitive impairment in neuromyelitis optica. Neurology 85, 1491–1499. doi:10.1212/WNL.0000000000002067

Liu, Y., Liang, P., Duan, Y., Jia, X., Wang, F., Yu, C., Qin, W., Dong, H., Ye, J., Li, K., 2011. Abnormal baseline brain activity in patients with neuromyelitis optica: a resting-state fMRI study. Eur. J. Radiol. 80, 407–11. doi:10.1016/j.ejrad.2010.05.002

Liu, Y., Lukas, C., Steenwijk, M.D., Daams, M., Versteeg, A., Duan, Y., Li, K., Weiler, F., Hahn, H.K., Wattjes, M.P., Barkhof, F., Vrenken, H., 2016. Multicenter Validation of Mean Upper Cervical Cord Area Measurements from Head 3D T1-Weighted MR Imaging in Patients with Multiple Sclerosis. Am. J. Neuroradiol. 37, 749–754. doi:10.3174/ajnr.A4635

Liu, Y., Wang, J., Daams, M., Weiler, F., Hahn, H.K., Duan, Y., Huang, J., Ren, Z., Ye, J., Dong, H., Vrenken, H., Wattjes, M.P., Shi, F.D., Li, K., Barkhof, F., 2015c. Differential patterns of spinal cord and brain atrophy in NMO and MS. Neurology 84, 1465–1472. doi:10.1212/WNL.0000000000001441

Liu, Y., Xie, T., He, Y., Duan, Y., Huang, J., Ren, Z., Gong, G., Wang, J., Ye, J., Dong, H., Butzkueven, H., Shi, F.-D., Shu, N., Li, K., 2014. Cortical Thinning Correlates with Cognitive Change in Multiple Sclerosis but not in Neuromyelitis Optica. Eur. Radiol. 24, 2334–43. doi:10.1007/s00330-014-3239-1

Ljungberg, E., Vavasour, I., Rauscher, A., Traboulsee, A., MacKay, A., Kolind, S., 2017. Myelin Water Imaging Using T2-Relaxation in the Spinal Cord; Comparison of Multi-echo GRASE and mcDESPOT, in: Proc Intl Soc Magn Reson Med. Honolulu, Hawaii.

Ljungberg, E., Vavasour, I., Tam, R., Yoo, Y., Rauscher, A., Li, D., Traboulsee, A., MacKay, A., Kolind, S., 2016. Rapid Myelin Water Imaging in Human Cervical Spinal Cord, in: Magnetic Resonance in Medicine. p. 282. doi:10.1002/mrm.26551

Lublin, F.D., Reingold, S.C., 1996. Defining the clinical course of multiple sclerosis: results of an international survey. National Multiple Sclerosis Society (USA) Advisory

Committee on Clinical Trials of New Agents in Multiple Sclerosis. Neurology 46, 907–911. doi:10.1212/WNL.46.4.907

Lublin, F.D., Reingold, S.C., Cohen, J.A., Cutter, G.R., S??rensen, P.S., Thompson, A.J., Wolinsky, J.S., Balcer, L.J., Banwell, B., Barkhof, F., Bebo, B., Calabresi, P.A., Clanet, M., Comi, G., Fox, R.J., Freedman, M.S., Goodman, A.D., Inglese, M., Kappos, L., Kieseier, B.C., Lincoln, J.A., Lubetzki, C., Miller, A.E., Montalban, X., O'Connor, P.W., Petkau, J., Pozzilli, C., Rudick, R.A., Sormani, M.P., St??ve, O., Waubant, E., Polman, C.H., Connor, P.W.O., Sormani, M.P., 2014. Defining the clinical course of multiple sclerosis: The 2013 revisions. Neurology. doi:10.1212/WNL.0000000000000560

Lucchinetti, C., Brück, W., Parisi, J., Scheithauer, B., Rodriguez, M., Lassmann, H., 2000. Heterogeneity of multiple sclerosis lesions: implications for the pathogenesis of demyelination. Ann. Neurol. 47, 707–17.

Lucchinetti, C.F., Brück, W., Rodriguez, M., Lassmann, H., 1996. Distinct Patterns of Multiple Sclerosis Pathology Indicates Heterogeneity in Pathogenesis. Brain Pathol. 6, 259–274. doi:10.1111/j.1750-3639.1996.tb00854.x

Lucchinetti, C.F., Guo, Y., Popescu, B.F.G., Fujihara, K., Itoyama, Y., Misu, T., 2014. The Pathology of an Autoimmune Astrocytopathy: Lessons Learned from Neuromyelitis Optica. Brain Pathol. 24, 83–97. doi:10.1111/bpa.12099

Lukas, C., Sombekke, M.H., Bellenberg, B., Hahn, H.K., Popescu, V., Bendfeldt, K., Radue, E.W., Gass, A., Borgwardt, S.J., Kappos, L., Naegelin, Y., Knol, D.L., Polman, C.H., Geurts, J.J.G., Barkhof, F., Vrenken, H., 2013. Relevance of spinal cord abnormalities to clinical disability in multiple sclerosis: MR imaging findings in a large cohort of patients. Radiology 269, 542–52. doi:10.1148/radiol.13122566

Lutti, A., Dick, F., Sereno, M.I., Weiskopf, N., 2014. Using high-resolution quantitative mapping of R1 as an index of cortical myelination. Neuroimage 93, 176–188. doi:10.1016/j.neuroimage.2013.06.005

Lycklama, G., Thompson, A., Filippi, M., Miller, D., Polman, C., Fazekas, F., Barkhof, F., 2003. Spinal-cord MRI in multiple sclerosis. Lancet Neurol. 2, 555–562. doi:10.1016/S1474-4422(03)00504-0

Ma, D., Gulani, V., Seiberlich, N., Liu, K., Sunshine, J.L., Duerk, J.L., Griswold, M.A., 2013. Magnetic resonance fingerprinting. Nature 495, 187–92. doi:10.1038/nature11971

MacKay, A., Laule, C., Vavasour, I., Bjarnason, T., Kolind, S., M??dler, B., 2006. Insights into brain microstructure from the T2 distribution. Magn. Reson. Imaging 24, 515–525. doi:10.1016/j.mri.2005.12.037

MacKay, A.L., Laule, C., 2016. Magnetic Resonance of Myelin Water: An in vivo Marker for Myelin. Brain Plast. 2, 71–91. doi:10.3233/BPL-160033

MacKay, a, Whittall, K., Adler, J., Li, D., Paty, D., Graeb, D., 1994. In vivo visualization of myelin water in brain by magnetic resonance. Magn. Reson. Med. 31, 673–7.

MacMillan, E.L., Mädler, B., Fichtner, N., Dvorak, M.F., Li, D.K.B., Curt, A., MacKay, A.L., 2011. Myelin water and T2 relaxation measurements in the healthy cervical spinal cord at 3.0T: Repeatability and changes with age. Neuroimage 54, 1083–1090. doi:10.1016/j.neuroimage.2010.08.076

Mädler, B., Drabycz, S.A., Kolind, S.H., Whittall, K.P., MacKay, A.L., 2008. Is diffusion anisotropy an accurate monitor of myelination?. Correlation of multicomponent T2 relaxation and diffusion tensor anisotropy in human brain. Magn. Reson. Imaging 26, 874–888. doi:10.1016/j.mri.2008.01.047

Mallik, S., Samson, R.S., M Wheeler-Kingshott, C.A., Miller, D.H., Wheeler-Kingshott, C.A.M., Miller, D.H., 2014. Imaging outcomes for trials of remyelination in multiple sclerosis. J. Neurol. Neurosurg. Psychiatry 85, 1396–1404. doi:10.1136/jnnp-2014-307650

Mancall, E.L., Brock, D.G., 2011. Gray's Clinical Neuroanatomy: The Anatomic Basis for Clinical Neuroscience, 1st ed. Elsevier, Philadelphia.

Manogaran, P., Hanson, J., Olbert, E., Egger, C., Wicki, C., Gerth-Kahlert, C., Landau, K., Schippling, S., 2016a. Optical Coherence Tomography and Magnetic Resonance Imaging in Multiple Sclerosis and Neuromyelitis Optica Spectrum Disorder. Int. J. Mol. Sci. 17, 1894. doi:10.3390/ijms17111894

Manogaran, P., Vavasour, I., Borich, M., Kolind, S.H., Lange, A.P., Rauscher, A., Boyd, L., Li, D.K., Traboulsee, A., 2015. Corticospinal tract integrity measured using transcranial magnetic stimulation and magnetic resonance imaging in neuromyelitis optica and multiple sclerosis. Mult. Scler. 22, 1–8. doi:10.1177/1352458515579441

Manogaran, P., Vavasour, I.M., Lange, A.P., Zhao, Y., McMullen, K., Rauscher, A., Carruthers, R., Li, D.K.B., Traboulsee, A.L., Kolind, S.H., 2016b. Quantifying visual pathway axonal and myelin loss in multiple sclerosis and neuromyelitis optica. NeuroImage Clin. 11, 743–750. doi:10.1016/j.nicl.2016.05.014

Marignier, R., De Sèze, J., Vukusic, S., Durand-Dubief, F., Zéphir, H., Vermersch, P., Cabre, P., Cavillon, G., Honnorat, J., Confavreux, C., 2008. NMO-IgG and Devic's neuromyelitis optica: a French experience. Mult. Scler. 14, 440–5. doi:10.1177/1352458507084595

Marignier, R., Nicolle, A., Watrin, C., Touret, M., Cavagna, S., Varrin-Doyer, M., Cavillon, G., Rogemond, V., Confavreux, C., Honnorat, J., Giraudon, P., 2010. Oligodendrocytes are damaged by neuromyelitis optica immunoglobulin G via astrocyte injury. Brain 133, 2578–91. doi:10.1093/brain/awq177

Martin, A.R., Aleksanderek, I., Cohen-Adad, J., Tarmohamed, Z., Tetreault, L., Smith, N., Cadotte, D.W., Crawley, A., Ginsberg, H., Mikulis, D.J., Fehlings, M.G., 2016. Translating state-of-the-art spinal cord MRI techniques to clinical use: A systematic review of clinical studies utilizing DTI, MT, MWF, MRS, and fMRI. NeuroImage Clin. 10, 192–238. doi:10.1016/j.nicl.2015.11.019

Martino, G., Adorini, L., Rieckmann, P., Hillert, J., Kallmann, B., Comi, G., Filippi, M., 2002. Inflammation in multiple sclerosis: The good, the bad, and the complex. Lancet Neurol. 1, 499–509. doi:10.1016/S1474-4422(02)00223-5

Matthews, L., Kolind, S., Brazier, A., Leite, M.I., Brooks, J., Traboulsee, A., Jenkinson, M., Johansen-Berg, H., Palace, J., 2015. Imaging Surrogates of Disease Activity in Neuromyelitis Optica Allow Distinction from Multiple Sclerosis. PLoS One 10, e0137715. doi:10.1371/journal.pone.0137715

Matthews, L., Marasco, R., Jenkinson, M., Kuker, W., Luppe, S., Leite, M.I., Giorgio, A., De Stefano, N., Robertson, N., Johansen-Berg, H., Evangelou, N., Palace, J., 2013. Distinction of seropositive NMO spectrum disorder and MS brain lesion distribution. Neurology 80, 1330–1337. doi:10.1212/WNL.0b013e3182887957

McDonald, W.I., Compston, A., Edan, G., Goodkin, D., Hartung, H.-P., Lublin, F.D., McFarland, H.F., Paty, D.W., Polman, C.H., Reingold, S.C., Sandberg-Wollheim, M., Sibley, W., Thompson, A., Van Den Noort, S., Weinshenker, B.Y., Wolinsky, J.S., 2001. Recommended diagnostic criteria for multiple sclerosis: Guidelines from the international panel on the diagnosis of multiple sclerosis. Ann. Neurol. 50, 121–127. doi:10.1002/ana.1032

McGraw, K.O., Wong, S.P., 1996. Forming inferences about some intraclass correlation coefficients. Psychol. Methods 1, 30–46. doi:10.1037//1082-989X.1.1.30

McRobbie, D.W., Moore, E.A., Graves, M.J., Prince, M.R., 2006. MRI: From Picture to Proton, 2nd ed. Cambridge University Press, Cambridge. doi:10.1097/00004032-200310000-00020

Mealy, M.A., Wingerchuk, D.M., Palace, J., Greenberg, B.M., Levy, M., 2014. Comparison of relapse and treatment failure rates among patients with neuromyelitis optica:

multicenter study of treatment efficacy. JAMA Neurol. 71, 324–30. doi:10.1001/jamaneurol.2013.5699

Messina, S., Patti, F., 2014. Gray Matters in Multiple Sclerosis: Cognitive Impairment and Structural MRI. Mult. Scler. Int. 2014, 1–9. doi:10.1155/2014/609694

Meyer-Moock, S., Feng, Y.-S., Maeurer, M., Dippel, F.-W., Kohlmann, T., 2014. Systematic literature review and validity evaluation of the Expanded Disability Status Scale (EDSS) and the Multiple Sclerosis Functional Composite (MSFC) in patients with multiple sclerosis. BMC Neurol. 14, 58. doi:10.1186/1471-2377-14-58

Meyers, S.M., Kolind, S.H., MacKay, A.L., 2017. Simultaneous measurement of total water content and myelin water fraction in brain at 3 T using a T 2 relaxation based method. Magn. Reson. Imaging 37, 187–194. doi:10.1016/j.mri.2016.12.001

Meyers, S.M., Tam, R., Lee, J.S., Kolind, S.H., Vavasour, I.M., Mackie, E., Zhao, Y., Laule, C., Mädler, B., Li, D.K.B., MacKay, A.L., Traboulsee, A.L., 2016. Does hydration status affect MRI measures of brain volume or water content? J. Magn. Reson. Imaging 44, 296–304. doi:10.1002/jmri.25168

Meyers, S.M., Vavasour, I.M., Mädler, B., Harris, T., Fu, E., Li, D.K.B., Traboulsee, A.L., Mackay, A.L., Laule, C., 2013. Multicenter measurements of myelin water fraction and geometric mean T2 : Intra- and intersite reproducibility. J. Magn. Reson. Imaging 0. doi:10.1002/jmri.24106

Mezer, A., Yeatman, J.D., Stikov, N., Kay, K.N., Cho, N.-J., Dougherty, R.F., Perry, M.L., Parvizi, J., Hua, L.H., Butts-Pauly, K., Wandell, B.A., 2013. Quantifying the local tissue volume and composition in individual brains with magnetic resonance imaging. Nat. Med. 19, 1667–72. doi:10.1038/nm.3390

Miller, D.H., 2002. Measurement of atrophy in multiple sclerosis: pathological basis, methodological aspects and clinical relevance. Brain 125, 1676–1695. doi:10.1093/brain/awf177

Minagar, A., Barnett, M.H., Benedict, R.H.B., Pelletier, D., Pirko, I., Sahraian, M.A., Frohman, E., Zivadinov, R., 2013. The thalamus and multiple sclerosis: Modern views on pathologic, imaging, and clinical aspects. Neurology 80, 210–219. doi:10.1212/WNL.0b013e31827b910b

Minty, E.P., Bjarnason, T.A., Laule, C., Mackay, A.L., 2009. Myelin water measurement in the spinal cord. Magn. Reson. Med. 61, 883–892. doi:10.1002/mrm.21936

Misu, T., Höftberger, R., Fujihara, K., Wimmer, I., Takai, Y., Nishiyama, S., Nakashima, I., Konno, H., Bradl, M., Garzuly, F., Itoyama, Y., Aoki, M., Lassmann, H., 2013. Presence of six different lesion types suggests diverse mechanisms of tissue injury in neuromyelitis optica. Acta Neuropathol. 125, 815–827. doi:10.1007/s00401-013-1116-7

Mitchell, A.S., Sherman, S.M., Sommer, M.A., Mair, R.G., Vertes, R.P., Chudasama, Y., 2014. Advances in Understanding Mechanisms of Thalamic Relays in Cognition and Behavior. J. Neurosci. 34, 15340–15346. doi:10.1523/JNEUROSCI.3289-14.2014

Moccia, M., de Stefano, N., Barkhof, F., 2017. Imaging outcome measures for progressive multiple sclerosis trials. Mult. Scler. J. 23, 1614–1626. doi:10.1177/1352458517729456

Moore, G.R., Leung, E., MacKay, a L., Vavasour, I.M., Whittall, K.P., Cover, K.S., Li, D.K., Hashimoto, S. a, Oger, J., Sprinkle, T.J., Paty, D.W., 2000. A pathology-MRI study of the short-T2 component in formalin-fixed multiple sclerosis brain. Neurology 55, 1506–10. doi:10.1212/WNL.55.10.1506

Morell, P., Quarles, R.H., 1999. Myelin Formation, Structure and Biochemistry, in: Siegel, G.J., Agranoff, B.W., Albers, R.W., Fisher, S.K., Uhler, M.D. (Eds.), Basic Neurochemistry, 6th Edition. Molecular, Cellular and Medical Aspects. Lippincott-

Raven, Philadelphia.

Mutch, K., Methley, A., Moore, P., Jacob, A., 2014. Life on hold: the experience of living with neuromyelitis optica. Disabil. Rehabil. 36, 1100–7. doi:10.3109/09638288.2013.833301

Nakamura, M., Misu, T., Fujihara, K., Miyazawa, I., Nakashima, I., Takahashi, T., Watanabe, S., Itoyama, Y., 2009. Occurrence of acute large and edematous callosal lesions in neuromyelitis optica. Mult. Scler. 15, 695–700. doi:10.1177/1352458509103301

Nakamura, M., Miyazawa, I., Fujihara, K., Nakashima, I., Misu, T., Watanabe, S., Takahashi, T., Itoyama, Y., 2008. Preferential spinal central gray matter involvement in neuromyelitis optica. An MRI study. J. Neurol. 255, 163–70. doi:10.1007/s00415-008-0545-z

Nave, K.-A., 2010. Myelination and support of axonal integrity by glia. Nature 468, 244–252. doi:10.1038/nature09614

Neema, M., Stankiewicz, J., Arora, A., Dandamudi, V.S.R., Batt, C.E., Guss, Z.D., Al-Sabbagh, A., Bakshi, R., 2007. T1- and T2-Based MRI Measures of Diffuse Gray Matter and White Matter Damage in Patients with Multiple Sclerosis. J. Neuroimaging 17, 16S–21S. doi:10.1111/j.1552-6569.2007.00131.x

Nguyen, T.D., Deh, K., Monohan, E., Pandya, S., Spincemaille, P., Raj, A., Wang, Y., Gauthier, S.A., 2016. Feasibility and reproducibility of whole brain myelin water mapping in 4 minutes using fast acquisition with spiral trajectory and adiabatic T2prep (FAST-T2) at 3T. Magn. Reson. Med. 76, 456–465. doi:10.1002/mrm.25877

Noseworthy, J.H., Lucchinetti, C., Rodriguez, M., Weinshenker, B.G., 2000. Multiple Sclerosis. N. Engl. J. Med. 343, 938–952. doi:10.1056/NEJM200009283431307

O'Muircheartaigh, J., Dean, D.C., Ginestet, C.E., Walker, L., Waskiewicz, N., Lehman, K., Dirks, H., Piryatinsky, I., Deoni, S.C.L., 2014. White matter development and early cognition in babies and toddlers. Hum. Brain Mapp. 35, 4475–4487. doi:10.1002/hbm.22488

Odrobina, E.E., Lam, T.Y.J., Pun, T., Midha, R., Stanisz, G.J., 2005. MR properties of excised neural tissue following experimentally induced demyelination. NMR Biomed. 18, 277–284. doi:10.1002/nbm.951

Oh, J., Seigo, M., Saidha, S., Sotirchos, E., Zackowski, K., Chen, M., Prince, J., Diener-West, M., Calabresi, P. a., Reich, D.S., 2014. Spinal cord normalization in multiple sclerosis. J. Neuroimaging 5–7. doi:10.1111/jon.12097

Oh, S.-H., Bilello, M., Schindler, M., Markowitz, C.E., Detre, J. a, Lee, J., 2013. Direct visualization of short transverse relaxation time component (ViSTa). Neuroimage 83, 485–92. doi:10.1016/j.neuroimage.2013.06.047

Okuda, D.T., Siva, A., Kantarci, O., Inglese, M., Katz, I., Tutuncu, M., Keegan, B.M., Donlon, S., Hua, L.H., Vidal-Jordana, A., Montalban, X., Rovira, A., Tintoré, M., Amato, M.P., Brochet, B., de Seze, J., Brassat, D., Vermersch, P., De Stefano, N., Sormani, M.P., Pelletier, D., Lebrun, C., 2014. Radiologically Isolated Syndrome: 5-Year Risk for an Initial Clinical Event. PLoS One 9, e90509. doi:10.1371/journal.pone.0090509

Owens, E.M., Denney, D.R., Lynch, S.G., 2013. Difficulties in Planning Among Patients with Multiple Sclerosis: A Relative Consequence of Deficits in Information Processing Speed. J. Int. Neuropsychol. Soc. 19, 613–620. doi:10.1017/S1355617713000155

Pache, F., Zimmermann, H., Finke, C., Lacheta, A., Papazoglou, S., Kuchling, J., Wuerfel, J., Hamm, B., Ruprecht, K., Paul, F., Brandt, A.U., Scheel, M., 2016. Brain parenchymal damage in neuromyelitis optica spectrum disorder – A multimodal MRI study. Eur. Radiol. 1–10. doi:10.1007/s00330-016-4282-x

Pandit, L., Asgari, N., Apiwattanakul, M., Palace, J., Paul, F., Leite, M., Kleiter, I., Chitnis, T., 2015. Demographic and clinical features of neuromyelitis optica: A review. Mult. Scler. J. 21, 845–853. doi:10.1177/1352458515572406

Papinutto, N., Bakshi, R., Bischof, A., Calabresi, P.A., Caverzasi, E., Constable, R.T., Datta, E., Kirkish, G., Nair, G., Oh, J., Pelletier, D., Pham, D.L., Reich, D.S., Rooney, W., Roy, S., Schwartz, D., Shinohara, R.T., Sicotte, N.L., Stern, W.A., Tagge, I., Tauhid, S., Tummala, S., Henry, R.G., 2018. Gradient nonlinearity effects on upper cervical spinal cord area measurement from 3D T 1 -weighted brain MRI acquisitions. Magn. Reson. Med. 79, 1595–1601. doi:10.1002/mrm.26776

Patenaude, B., Smith, S.M., Kennedy, D.N., Jenkinson, M., 2011. A Bayesian model of shape and appearance for subcortical brain segmentation. Neuroimage 56, 907–922. doi:10.1016/j.neuroimage.2011.02.046

Pessôa, F.M.C., Lopes, F.C.R., Costa, J.V.A., Leon, S.V.A., Domingues, R.C., Gasparetto, E.L., 2012. The cervical spinal cord in neuromyelitis optica patients: A comparative study with multiple sclerosis using diffusion tensor imaging. Eur. J. Radiol. 81, 2697–2701. doi:10.1016/j.ejrad.2011.11.026

Pichiecchio, A., Tavazzi, E., Poloni, G., Ponzio, M., Palesi, F., Pasin, M., Piccolo, L., Tosello, D., Romani, A., Bergamaschi, R., Piccolo, G., Bastianello, S., 2012. Advanced magnetic resonance imaging of neuromyelitis optica: a multiparametric approach. Mult. Scler. J. 18, 817–824. doi:10.1177/1352458511431072

Pittock, S., Lennon, V., Krecke, K., Wingerchuk, D., Lucchinetti, C., Weinshenker, B., 2006a. Brain abnormalities in neuromyelitis optica. Arch. Neurol. 302, 43–8. doi:10.1016/j.jns.2010.12.001

Pittock, S., Lucchinetti, C.F., 2016. Neuromyelitis optica and the evolving spectrum of autoimmune aquaporin-4 channelopathies: A decade later. Ann. N. Y. Acad. Sci. 1366, 20–39. doi:10.1111/nyas.12794

Pittock, S., Weinshenker, B.G., Lucchinetti, C.F., Wingerchuk, D.M., Corboy, J.R., Lennon, V.A., 2006b. Neuromyelitis optica brain lesions localized at sites of high aquaporin 4 expression. Arch. Neurol. 63, 964–968. doi:10.1016/S0513-5117(08)70130-3

Polman, C.H., Reingold, S.C., Banwell, B., Clanet, M., Cohen, J. a, Filippi, M., Fujihara, K., Havrdova, E., Hutchinson, M., Kappos, L., Lublin, F.D., Montalban, X., O'Connor, P., Sandberg-Wollheim, M., Thompson, A.J., Waubant, E., Weinshenker, B., Wolinsky, J.S., 2011. Diagnostic criteria for multiple sclerosis: 2010 Revisions to the McDonald criteria. Ann. Neurol. 69, 292–302. doi:10.1002/ana.22366

Popescu, B.F.G., Parisi, J.E., Cabrera-Gomez, J.A., Newell, K., Mandler, R.N., Pittock, S.J., Lennon, V.A., Weinshenker, B.G., Lucchinetti, C.F., 2010. Absence of cortical demyelination in neuromyelitis optica. Neurology 75, 2103–2109. doi:10.1212/WNL.0b013e318200d80c

Poppe, A.Y., Lapierre, Y., Melançon, D., Lowden, D., Wardell, L., Fullerton, L.M., Bar-Or, A., 2005. Neuromyelitis optica with hypothalamic involvement. Mult. Scler. 11, 617–621. doi:10.1191/1352458505ms1200cr

Portney, L.G., Watkins, M.P., 2009. Foundations of Clinical Research.

Prados Carrasco, F., Yiannakas, M., Cardoso, M., Grussu, F., De Angelis, F., Plantone, D., Miller, D., Ciccarelli, O., Wheeler-Kingshott, C., Ourselin, S., 2016. Computing spinal cord atrophy using the Boundary Shift Integral: a more powerful outcome measure for clinical trials?, in: ECTRIMS. London, UK.

Prasloski, T., Mädler, B., Xiang, Q.S., MacKay, A., Jones, C., 2012a. Applications of stimulated echo correction to multicomponent T2 analysis. Magn. Reson. Med. 67, 1803–1814. doi:10.1002/mrm.23157

Prasloski, T., Rauscher, A., MacKay, A.L., Hodgson, M., Vavasour, I.M., Laule, C., Mädler,

B., 2012b. Rapid whole cerebrum myelin water imaging using a 3D GRASE sequence. Neuroimage 63, 533–539. doi:10.1016/j.neuroimage.2012.06.064

Pun, T.W.C., Odrobina, E., Xu, Q.G., Lam, T.Y.J., Munro, C.A., Midha, R., Stanisz, G.J., 2005. Histological and magnetic resonance analysis of sciatic nerves in the tellurium model of neuropathy. J. Peripher. Nerv. Syst. 10, 38–46. doi:10.1111/j.1085-9489.2005.10107.x

Qian, W., Chan, K.H., Hui, E.S., Lee, C.Y., Hu, Y., Mak, H.K.-F., 2016. Application of diffusional kurtosis imaging to detect occult brain damage in multiple sclerosis and neuromyelitis optica. NMR Biomed. 1536–1545. doi:10.1002/nbm.3607

Qian, W., Chan, Q., Mak, H., Zhang, Z., Anthony, M.-P., Yau, K.K.-W., Khong, P.-L., Chan, K.H., Kim, M., 2011. Quantitative assessment of the cervical spinal cord damage in neuromyelitis optica using diffusion tensor imaging at 3 Tesla. J. Magn. Reson. Imaging 33, 1312–1320. doi:10.1002/jmri.22575

R Core Team, 2017. R: A language and environment for statistical computing. R Found. Stat. Comput. Vienna, Austria. URL https//www.r-project.org/.

Ramagopalan, S. V., Dobson, R., Meier, U.C., Giovannoni, G., 2010. Multiple sclerosis: risk factors, prodromes, and potential causal pathways. Lancet Neurol. 9, 727–739. doi:10.1016/S1474-4422(10)70094-6

Ransohoff, R.M., 2012. Illuminating neuromyelitis optica pathogenesis. Proc. Natl. Acad. Sci. U. S. A. 109, 1001–2. doi:10.1073/pnas.1119288109

Ransohoff, R.M., Hafler, D.A., Lucchinetti, C.F., 2015. Multiple sclerosis—a quiet revolution. Nat. Rev. Neurol. 11, 134–142. doi:10.1038/nrneurol.2015.14

Reindl, M., Di Pauli, F., Rostásy, K., Berger, T., 2013. The spectrum of MOG autoantibody-associated demyelinating diseases. Nat. Rev. Neurol. 9, 455–461. doi:10.1038/nrneurol.2013.118

Rivero, R.L.M., Oliveira, E.M.L., Bichuetti, D.B., Gabbai, A.A., Nogueira, R.G., Abdala, N., 2014. Diffusion tensor imaging of the cervical spinal cord of patients with Neuromyelitis Optica. Magn. Reson. Imaging 32, 457–63. doi:10.1016/j.mri.2014.01.023

Rocca, M.A., Agosta, F., Mezzapesa, D.M., Falini, A., Martinelli, V., Salvi, F., Bergamaschi, R., Scotti, G., Comi, G., Filippi, M., 2004a. A functional MRI study of movement-associated cortical changes in patients with Devic's neuromyelitis optica. Neuroimage 21, 1061–8. doi:10.1016/j.neuroimage.2003.10.013

Rocca, M.A., Agosta, F., Mezzapesa, D.M., Martinelli, V., Salvi, F., Ghezzi, A., Bergamaschi, R., Comi, G., Filippi, M., 2004b. Magnetization transfer and diffusion tensor MRI show gray matter damage in neuromyelitis optica. Neurology 62, 476–478. doi:10.1212/01.WNL.0000106946.08741.41

Rocca, M.A., Mesaros, S., Pagani, E., Sormani, M.P., Comi, G., Filippi, M., 2010. Thalamic Damage and Long-term Progression of Disability in Multiple Sclerosis. Radiology 257, 463–469. doi:10.1148/radiol.10100326

Rovira, À., Wattjes, M.P., Tintoré, M., Tur, C., Yousry, T.A., Sormani, M.P., De Stefano, N., Filippi, M., Auger, C., Rocca, M.A., Barkhof, F., Fazekas, F., Kappos, L., Polman, C., Miller, D., Montalban, X., 2015. Evidence-based guidelines: MAGNIMS consensus guidelines on the use of MRI in multiple sclerosis—clinical implementation in the diagnostic process. Nat. Rev. Neurol. 11, 471–482. doi:10.1038/nrneurol.2015.106

Saadoun, S., Waters, P., Bell, B.A., Vincent, A., Verkman, a S., Papadopoulos, M.C., 2010. Intra-cerebral injection of neuromyelitis optica immunoglobulin G and human complement produces neuromyelitis optica lesions in mice. Brain 133, 349–61. doi:10.1093/brain/awp309

Saji, E., Arakawa, M., Yanagawa, K., Toyoshima, Y., Yokoseki, A., Okamoto, K., Otsuki, M., Akazawa, K., Kakita, A., Takahashi, H., Nishizawa, M., Kawachi, I., 2013. Cognitive

impairment and cortical degeneration in neuromyelitis optica. Ann. Neurol. 73, 65–76. doi:10.1002/ana.23721

Sanchez-Catasus, C.A., Cabrera-Gomez, J., Almaguer Melian, W., Bosch Bayard, J., Rodriguez Rojas, R., Valdes-Sosa, P., 2015. The number of optic neuritis attacks is a potential confounder when comparing patients with NMO vs. controls by voxel-based neuroimaging analysis. Acta radiol. 0, 1–7. doi:10.1177/0284185115610935

Sato, D., Callegaro, D., Lana-Peixoto, M.A., Fujihara, K., 2012. Treatment of neuromyelitis optica: an evidence based review. Arq. Neuropsiquiatr. 70, 59–66.

Sato, D.K., Callegaro, D., Lana-Peixoto, M.A., Waters, P.J., Jorge, F.M. d. H., Takahashi, T., Nakashima, I., Apostolos-Pereira, S.L., Talim, N., Simm, R.F., Lino, A.M.M., Misu, T., Leite, M.I., Aoki, M., Fujihara, K., 2014. Distinction between MOG antibody-positive and AQP4 antibody-positive NMO spectrum disorders. Neurology 82, 474–481. doi:10.1212/WNL.0000000000000101

Schneider, R., Bellenberg, B., Kleiter, I., Gold, R., K??ster, O., Weiler, F., Hahn, H., Lukas, C., 2016. Cervical cord and ventricle affection in neuromyelitis optica. Acta Neurol. Scand. 1–8. doi:10.1111/ane.12601

Schultheis, M.T., Weisser, V., Ang, J., Elovic, E., Nead, R., Sestito, N., Fleksher, C., Millis, S.R., 2010. Examining the Relationship Between Cognition and Driving Performance in Multiple Sclerosis. Arch. Phys. Med. Rehabil. 91, 465–473. doi:10.1016/j.apmr.2009.09.026

Seewann, A., Vrenken, H., van der Valk, P., Blezer, E.L. a, Knol, D.L., Castelijns, J. a, Polman, C.H., Pouwels, P.J.W., Barkhof, F., Geurts, J.J.G., 2009. Diffusely Abnormal White Matter in Chronic Multiple Sclerosis. Arch. Neurol. 66, 601–609. doi:10.1001/archneurol.2009.57

Sepulcre, J., Vanotti, S., Hernández, R., Sandoval, G., Cáceres, F., Garcea, O., Villoslada, P., 2006. Cognitive impairment in patients with multiple sclerosis using the Brief Repeatable Battery-Neuropsychology test. Mult. Scler. J. 12, 187–195. doi:10.1191/1352458506ms1258oa

Sheridan, L.K., Fitzgerald, H.E., Adams, K.M., Nigg, J.T., Martel, M.M., Puttler, L.I., Wong, M.M., Zucker, R.A., 2006. Normative Symbol Digit Modalities Test performance in a community-based sample. Arch. Clin. Neuropsychol. 21, 23–28. doi:10.1016/j.acn.2005.07.003

Shiee, N., Bazin, P.-L., Zackowski, K.M., Farrell, S.K., Harrison, D.M., Newsome, S.D., Ratchford, J.N., Caffo, B.S., Calabresi, P.A., Pham, D.L., Reich, D.S., 2012. Revisiting Brain Atrophy and Its Relationship to Disability in Multiple Sclerosis. PLoS One 7, e37049. doi:10.1371/journal.pone.0037049

Shrout, P., Fleiss, J., 1979. Intraclass correlations: uses in assessing rater reliability. Psychol. Bull.

Siegel, G.J., Agranoff, B.W., 1999. Basic Neurochemistry: Molecular, Cellular, and Medical Aspects, 7th Editio. ed. doi:10.1212/WNL.39.3.460-b

Siffrin, V., Vogt, J., Radbruch, H., Nitsch, R., Zipp, F., 2010. Multiple sclerosis – candidate mechanisms underlying CNS atrophy. Trends Neurosci. 33, 202–210. doi:10.1016/j.tins.2010.01.002

Sinnecker, T., Dörr, J., Pfueller, C.F., Harms, L., Ruprecht, K., Jarius, S., Brück, W., Niendorf, T., Wuerfel, J., Paul, F., 2012. Distinct lesion morphology at 7-T MRI differentiates neuromyelitis optica from multiple sclerosis. Neurology 79, 708–14. doi:10.1212/WNL.0b013e3182648bc8

Smith, S.M., Jenkinson, M., Woolrich, M.W., Beckmann, C.F., Behrens, T.E.J., Johansen-Berg, H., Bannister, P.R., Luca, M. De, Drobnjak, I., Flitney, D.E., Niazy, R.K., Saunders, J., Vickers, J., Zhang, Y., Stefano, N. De, Brady, J.M., Matthews, P.M., De

Luca, M., Drobnjak, I., Flitney, D.E., Niazy, R.K., Saunders, J., Vickers, J., Zhang, Y., De Stefano, N., Brady, J.M., Matthews, P.M., 2004. Advances in functional and structural MR image analysis and implementation as FSL. Neuroimage 23 Suppl 1, S208-19. doi:10.1016/j.neuroimage.2004.07.051

Smith, S.M., Zhang, Y., Jenkinson, M., Chen, J., Matthews, P.M., Federico, A., De Stefano, N., 2002. Accurate, Robust, and Automated Longitudinal and Cross-Sectional Brain Change Analysis. Neuroimage 17, 479–489. doi:10.1006/nimg.2002.1040

Smith, S.S.M., 2002. Fast robust automated brain extraction. Hum. Brain Mapp. 17, 143–155. doi:10.1002/hbm.10062

Solomon, A., Klein, E., Bourdette, D., 2012. “Undiagnosing” multiple sclerosis The challenge of misdiagnosis in MS. Neurology.

Stanisz, G.J., Webb, S., Munro, C.A., Pun, T., Midha, R., 2004. MR properties of excised neural tissue following experimentally induced inflammation. Magn. Reson. Med. 51, 473–479. doi:10.1002/mrm.20008

Stewart, W.A., MacKay, A.L., Whittall, K.P., Moore, G.R.W., Paty, D.W., 1993. Spin-Spin Relaxation in Experimental Allergic Encephalomyelitis. Analysis of CPMG Data Using a Non-Linear Least Squares Method and Linear Inverse Theory. Magn Reson Med 29, 767–75. doi:10.1002/mrm.1910290608

Stikov, N., Boudreau, M., Levesque, I.R., Tardif, C.L., Barral, J.K., Pike, G.B., 2015. On the accuracy of T1 mapping: Searching for common ground. Magn. Reson. Med. 73, 514–522. doi:10.1002/mrm.25135

Streiner, D.L., Norman, G.R., 2006. “Precision” and “accuracy”: Two terms that are neither. J. Clin. Epidemiol. 59, 327–330. doi:10.1016/j.jclinepi.2005.09.005

Streiner, D.L., Norman, G.R., Cairney, J., 2015. Health Measurement Scales: A practical guide to their development and use.

Streitberger, K.J., Fehlner, A., Pache, F., Lacheta, A., Papazoglou, S., Bellmann-Strobl, J., Ruprecht, K., Brandt, A., Braun, J., Sack, I., Paul, F., Wuerfel, J., 2016. Multifrequency magnetic resonance elastography of the brain reveals tissue degeneration in neuromyelitis optica spectrum disorder. Eur. Radiol. 1–10. doi:10.1007/s00330-016-4561-6

Stroman, P.W., Wheeler-Kingshott, C., Bacon, M., Schwab, J.M., Bosma, R., Brooks, J., Cadotte, D., Carlstedt, T., Ciccarelli, O., Cohen-Adad, J., Curt, A., Evangelou, N., Fehlings, M.G., Filippi, M., Kelley, B.J., Kollias, S., Mackay, A., Porro, C.A., Smith, S., Strittmatter, S.M., Summers, P., Tracey, I., 2014. The current state-of-the-art of spinal cord imaging: Methods. Neuroimage 84, 1070–1081. doi:10.1016/j.neuroimage.2013.04.124

Stys, P.K., Zamponi, G.W., van Minnen, J., Geurts, J.J.G., 2012. Will the real multiple sclerosis please stand up? Nat. Rev. Neurosci. 13, 507–514. doi:10.1038/nrn3275

Su, L., Han, Y., Xue, R., Wood, K., Shi, F., Liu, Y., Fu, Y., 2016. Thalamic Atrophy Contributes to Low Slow Wave Sleep in Neuromyelitis Optica Spectrum Disorder. Aging Dis. 7, 691. doi:10.14336/AD.2016.0419

Sullivan, E. V., Rosenbloom, M., Serventi, K.L., Pfefferbaum, A., 2004. Effects of age and sex on volumes of the thalamus, pons, and cortex. Neurobiol. Aging 25, 185–192. doi:10.1016/S0197-4580(03)00044-7

Sumowski, J.F., Benedict, R., Enzinger, C., Filippi, M., Geurts, J.J., Hamalainen, P., Hulst, H., Inglese, M., Leavitt, V.M., Rocca, M.A., Rosti-Otajarvi, E.M., Rao, S., 2018. Cognition in multiple sclerosis. Neurology 10.1212/WNL.0000000000004977. doi:10.1212/WNL.0000000000004977

Sundgren, P.C., Dong, Q., Gomez-Hassan, D., Mukherji, S.K., Maly, P., Welsh, R., 2004. Diffusion tensor imaging of the brain: review of clinical applications. Neuroradiology

46, 339–350. doi:10.1007/s00234-003-1114-x

Takano, R., Misu, T., Takahashi, T., Sato, S., Fujihara, K., Itoyama, Y., 2010. Astrocytic damage is far more severe than demyelination in NMO: A clinical CSF biomarker study. Neurology 75, 208–216. doi:10.1212/WNL.0b013e3181e2414b

Tench, C.R., Morgan, P.S., Constantinescu, C.S., 2005a. Measurement of cervical spinal cord cross-sectional area by MRI using edge detection and partial volume correction. J. Magn. Reson. Imaging 21, 197–203. doi:10.1002/jmri.20253

Tench, C.R., Morgan, P.S., Jaspan, T., Auer, D.P., Constantinescu, C.S., 2005b. Spinal Cord Imaging in Multiple Sclerosis. J. Neuroimaging 15, 94S–102S. doi:10.1177/1051228405283292

Tofts, P.S., 2003a. Quantitative MRI of the Brain: Measuring Changes Caused by Disease, Quantitative MRI of the Brain Measuring Changes Caused by Disease. Wiley.

Tofts, P.S., 2003b. QA: Quality Assurance, Accuracy, Precision and Phantoms, in: Tofts, P.S. (Ed.), Quantitative MRI of the Brain. pp. 55–81. doi:10.1002/0470869526.ch3

Tozer, D., Ramani, A., Barker, G.J., Davies, G.R., Miller, D.H., Tofts, P.S., 2003. Quantitative magnetization transfer mapping of bound protons in multiple sclerosis. Magn. Reson. Med. 50, 83–91. doi:10.1002/mrm.10514

Traboulsee, A., Li, D.K.B., Zhao, G., Paty, D.W., 2005. Conventional MRI Techniques in Multiple Sclerosis, in: Filippi, M., De Stefano, N., Dousset, V., McGowan, J. (Eds.), MR Imaging in White Matter Diseases of the Brain and Spinal Cord. Springer-Verlag, Berlin/Heidelberg, pp. 211–223. doi:10.1007/3-540-27644-0_14

Trapp, B.D., Nave, K.-A., 2008. Multiple Sclerosis: An Immune or Neurodegenerative Disorder? Annu. Rev. Neurosci. 31, 247–269. doi:10.1146/annurev.neuro.30.051606.094313

Traynor, C., Barker, G., Crum, W., 2011. Segmentation of the thalamus in MRI based on T1 and T2. Neuroimage 56, 939–50. doi:10.1016/j.neuroimage.2011.01.083

Uzawa, A., Mori, M., Kuwabara, S., 2014. Neuromyelitis optica: concept, immunology and treatment. J. Clin. Neurosci. 21, 12–21. doi:10.1016/j.jocn.2012.12.022

Van Der Werf, Y.D., Tisserand, D.J., Visser, P.J., Hofman, P.A.M., Vuurman, E., Uylings, H.B.M., Jolles, J., 2001. Thalamic volume predicts performance on tests of cognitive speed and decreases in healthy aging: A magnetic resonance imaging-based volumetric analysis. Cogn. Brain Res. 11, 377–385. doi:10.1016/S0926-6410(01)00010-6

van Munster, C.E.P., Uitdehaag, B.M.J., 2017. Outcome Measures in Clinical Trials for Multiple Sclerosis. CNS Drugs 31, 217–236. doi:10.1007/s40263-017-0412-5

van Pelt, E.D., Wong, Y.Y.M., Ketelslegers, I.A., Hamann, D., Hintzen, R.Q., 2016. Neuromyelitis optica spectrum disorders: comparison of clinical and magnetic resonance imaging characteristics of AQP4-IgG versus MOG-IgG seropositive cases in the Netherlands. Eur. J. Neurol. 23, 580–587. doi:10.1111/ene.12898

Vanotti, S., Cores, E.V., Eizaguirre, B., Melamud, L., Rey, R., Villa, A., 2013. Cognitive performance of neuromyelitis optica patients: comparison with multiple sclerosis. Arq. Neuropsiquiatr. 71, 357–61. doi:10.1590/0004-282X20130038

Vargas, W.S., Monohan, E., Pandya, S., Raj, A., Vartanian, T., Nguyen, T.D., Hurtado Rúa, S.M., Gauthier, S.A., 2015. Measuring longitudinal myelin water fraction in new multiple sclerosis lesions. NeuroImage Clin. 9, 369–375. doi:10.1016/j.nicl.2015.09.003

Vavasour, I., Meyers, S., Manogaran, P., Xiao, S., Wurl, A., McMullen, K., Li, D., Traboulsee, A., Kolind, S., 2016. White Matter Water Content in Multiple Sclerosis and Neuromyelitis Optica, in: Proc Intl Soc Magn Reson Med.

Vavasour, I.M., Clark, C.M., Li, D.K.B., MacKay, A.L., 2006. Reproducibility and reliability of MR measurements in white matter: Clinical implications. Neuroimage 32, 637–642. doi:10.1016/j.neuroimage.2006.03.036

Vavasour, I.M., Laule, C., Li, D.K.B., Oger, J., Moore, G.R.W., Traboulsee, A., MacKay, A.L., 2009. Longitudinal changes in myelin water fraction in two MS patients with active disease. J. Neurol. Sci. 276, 49–53. doi:10.1016/j.jns.2008.08.022

Vavasour, I.M., Laule, C., Li, D.K.B., Traboulsee, A.L., MacKay, A.L., 2011. Is the magnetization transfer ratio a marker for myelin in multiple sclerosis? J. Magn. Reson. Imaging 33, 713–718. doi:10.1002/jmri.22441

Ventura, R.E., Kister, I., Chung, S., Babb, J.S., Shepherd, T.M., 2016. Cervical Spinal Cord Atrophy in NMOSD Without a History of Myelitis or MRI-Visible Lesions. Neurol Neuroimmunol Neuroinflamm 3, 1–4. doi:10.1212/

Viegas, S., Weir, a, Esiri, M., Kuker, W., Waters, P., Leite, M.I., Vincent, a, Palace, J., 2009. Symptomatic, radiological and pathological involvement of the hypothalamus in neuromyelitis optica. J. Neurol. Neurosurg. Psychiatry 80, 679–82. doi:10.1136/jnnp.2008.157693

von Glehn, F., Jarius, S., Cavalcanti Lira, R.P., Alves Ferreira, M.C., von Glehn, F.H.R., Costa e Castro, S.M., Beltramini, G.C., Bergo, F.P., Farias, A.S., Brandão, C.O., Wildemann, B., Damasceno, B.P., Cendes, F., Santos, L.M.B., Yasuda, C.L., 2014. Structural brain abnormalities are related to retinal nerve fiber layer thinning and disease duration in neuromyelitis optica spectrum disorders. Mult. Scler. J. 20, 1189–1197. doi:10.1177/1352458513519838

Walhovd, K.B., Fjell, A.M., Reinvang, I., Lundervold, A., Dale, A.M., Eilertsen, D.E., Quinn, B.T., Salat, D., Makris, N., Fischl, B., 2005. Effects of age on volumes of cortex, white matter and subcortical structures. Neurobiol. Aging 26, 1261–1270. doi:10.1016/j.neurobiolaging.2005.05.020

Wang, Q., Zhang, N., Qin, W., Li, Y., Fu, Y., Li, T., Shao, J., Yang, L., Shi, F.D., Yu, C., 2015. Gray Matter Volume Reduction Is Associated with Cognitive Impairment in Neuromyelitis Optica. Am. J. Neuroradiol. 36, 1822–1829. doi:10.3174/ajnr.A4403

Wansapura, J.P., Holland, S.K., Dunn, R.S., Ball, W.S., 1999. NMR relaxation times in the human brain at 3.0 tesla. J. Magn. Reson. Imaging 9, 531–8.

Waters, P., Reindl, M., Saiz, A., Schanda, K., Tuller, F., Kral, V., Nytrova, P., Sobek, O., Nielsen, H.H., Barington, T., Lillevang, S.T., Illes, Z., Rentzsch, K., Berthele, A., Berki, T., Granieri, L., Bertolotto, A., Giometto, B., Zuliani, L., Hamann, D., van Pelt, E.D., Hintzen, R., H?ftberger, R., Costa, C., Comabella, M., Montalban, X., Tintor?, M., Siva, A., Altintas, A., Deniz, G., Woodhall, M., Palace, J., Paul, F., Hartung, H.-P., Aktas, O., Jarius, S., Wildemann, B., Vedeler, C., Ruiz, A., Leite, M.I., Trillenberg, P., Probst, M., Saschenbrecker, S., Vincent, A., Marignier, R., 2016. Multicentre comparison of a diagnostic assay: aquaporin-4 antibodies in neuromyelitis optica. J. Neurol. Neurosurg. Psychiatry 87, 1005–1015. doi:10.1136/jnnp-2015-312601

Waters, P., Vincent, A., 2008. Detection of anti-aquaporin-4 antibodies in neuromyelitis optica: current status of the assays. Int Ms J 15, 99–105.

Waters, P.J., McKeon, A., Leite, M.I., Rajasekharan, S., Lennon, V.A., Villalobos, A., Palace, J., Mandrekar, J.N., Vincent, A., Bar-Or, A., Pittock, S.J., 2012. Serologic diagnosis of NMO: A multicenter comparison of aquaporin-4-IgG assays. Neurology 78, 665–671. doi:10.1212/WNL.0b013e318248dec1

Webb, S., Munro, C.A., Midha, R., Stanisz, G.J., 2003. Is multicomponent T2 a good measure of myelin content in peripheral nerve? Magn. Reson. Med. 49, 638–645. doi:10.1002/mrm.10411

Weber, A.M., Torres, C., Rauscher, A., 2018. Imaging the Role of Myelin in Concussion. Neuroimaging Clin. N. Am. 28, 83–90. doi:doi.org/10.1016/j.nic.2017.09.005

Weier, K., Eshaghi, A., Magon, S., Andelova, M., Radue, E.-W., Kappos, L., Azimi, A.R., Sahraian, M.A., Sprenger, T., 2015. The role of cerebellar abnormalities in neuromyelitis optica – a comparison with multiple sclerosis and healthy controls. Mult. Scler. J. 21, 757–766. doi:10.1177/1352458514554051

Weinshenker, B., 2007. Neuromyelitis optica is distinct from multiple sclerosis. Arch. Neurol. 64, 899–901. doi:10.1001/archneur.64.6.899

Weinshenker, B., 2003. Neuromyelitis optica: what it is and what it might be. Lancet 361, 889–890.

Weinshenker, B.G., 2008. Neuromyelitis optica in western countries: Establishing diagnostic criteria and characterization of the spectrum. Neurol. Asia 13, 161–166.

Weinshenker, B.G., Wingerchuk, D.M., 2014. The two faces of neuromyelitis optica. Neurology 82, 466–467. doi:10.1212/WNL.0000000000000114

Whittall, K.P., MacKay, A.L., Graeb, D. a., Nugent, R. a., Li, D.K.B., Paty, D.W., 1997. In vivo measurement of T2 distributions and water contents in normal human brain. Magn. Reson. Med. 37, 34–43. doi:10.1002/mrm.1910370107

Whittall, K.P., MacKay, A.L., Li, D.K.B., 1999. Are mono-exponential fits to a few echoes sufficient to determine T2 relaxation for in vivo human brain? Magn. Reson. Med. 41, 1255–1257. doi:10.1002/(SICI)1522-2594(199906)41:6<1255::AID-MRM23>3.0.CO;2-I

Wiggerman, V., Hernandez-Torres, E., Traboulsee, A., Li, D., Rauscher, A., 2016. FLAIR2 : A Combination of FLAIR and T2 for Improved MS Lesion Detection. Am J Neuroradiol 37, 259–65. doi:http://dx.doi.org/10.3174/ajnr.A4514

Wingerchuk, D.M., 2009. Neuromyelitis optica: effect of gender. J. Neurol. Sci. 286, 18–23. doi:10.1016/j.jns.2009.08.045

Wingerchuk, D.M., 2004. Neuromyelitis optica: Current concepts. Front. Biosci.

Wingerchuk, D.M., Banwell, B., Bennett, J.L., Cabre, P., Carroll, W., Chitnis, T., de Seze, J., Fujihara, K., Greenberg, B., Jacob, A., Jarius, S., Lana-Peixoto, M., Levy, M., Simon, J.H., Tenembaum, S., Traboulsee, A.L., Waters, P., Wellik, K.E., Weinshenker, B.G., 2015. International consensus diagnostic criteria for neuromyelitis optica spectrum disorders. Neurology 85, 177–189. doi:10.1212/WNL.0000000000001729

Wingerchuk, D.M., Hogancamp, W.F., O'Brien, P.C., Weinshenker, B.G., 1999. The clinical course of neuromyelitis optica (Devic's syndrome). Neurology 53, 1107–14.

Wingerchuk, D.M., Lennon, V.A., Lucchinetti, C.F., Pittock, S.J., Weinshenker, B.G., 2007a. The spectrum of neuromyelitis optica. Lancet Neurol. 6, 805–815. doi:10.1016/S1474-4422(07)70216-8

Wingerchuk, D.M., Lennon, V.A., Pittock, S.J., Lucchinetti, C.F., Weinshenker, B.G., 2006. Revised diagnostic criteria for neuromyelitis optica. Neurology 66, 1485–9. doi:10.1212/01.wnl.0000216139.44259.74

Wingerchuk, D.M., Pittock, S.J., Lucchinetti, C.F., Lennon, V.A., Weinshenker, B.G., 2007b. A secondary progressive clinical course is uncommon in neuromyelitis optica. Neurology 68, 603–5. doi:10.1212/01.wnl.0000254502.87233.9a

Wingerchuk, D.M., Weinshenker, B.G., 2017. Neuromyelitis optica spectrum disorder diagnostic criteria: Sensitivity and specificity are both important. MSJ 1–3. doi:10.1177/1352458516688352

Wingerchuk, D.M., Weinshenker, B.G., 2003. Neuromyelitis optica: clinical predictors of a relapsing course and survival. Neurology 60, 848–53. doi:10.1212/01.WNL.0000049912.02954.2C

Wolinsky, J.S., Narayana, P.A., O'Connor, P., Coyle, P.K., Ford, C., Johnson, K., Miller, A.,

Pardo, L., Kadosh, S., Ladkani, D., the PROMiSe Trial Study Group, 2007. Glatiramer acetate in primary progressive multiple sclerosis: Results of a multinational, multicenter, double-blind, placebo-controlled trial. Ann. Neurol. 61, 14–24. doi:10.1002/ana.21079

Wolinsky, J.S., the PROMiSe Study Group, 2003. The diagnosis of primary progressive multiple sclerosis. J. Neurol. Sci. 206, 145–152. doi:10.1016/S0022-510X(02)00346-5

Wolinsky, J.S., the PROMiSe Trial Study Group, 2004. The PROMiSe trial: baseline data review and progress report. Mult. Scler. J. 10, S65–S72. doi:10.1191/1352458504ms1034oa

Wood, T., Hurley, S., Vernon, a, Williams, S., 2013. High Resolution Quantitative Imaging of Rodent Brains at 7T. Submissions.Miracd.Com 21, 2465.

Wood, T.C., Simmons, C., Hurley, S.A., Vernon, A.C., Torres, J., Dell'Acqua, F., Williams, S.C.R., Cash, D., 2016. Whole-brain ex-vivo quantitative MRI of the cuprizone mouse model. PeerJ 4, e2632. doi:10.7717/peerj.2632

Wright, A.D., Jarrett, M., Vavasour, I., Shahinfard, E., Kolind, S., Van Donkelaar, P., Taunton, J., Li, D., Rauscher, A., 2016. Myelin Water Fraction Is Transiently Reduced after a Single Mild Traumatic Brain Injury – A Prospective Cohort Study in Collegiate Hockey Players. PLoS One 11, e0150215. doi:10.1371/journal.pone.0150215

Wu, Y., Alexander, A.L., Fleming, J.O., Duncan, I.D., Field, A.S., 2006. Myelin water fraction in human cervical spinal cord in vivo. J. Comput. Assist. Tomogr. 30, 304–306. doi:10.1097/00004728-200603000-00026

Yoo, Y., Tam, R., 2013. Non-local spatial regularization of MRI T2 relaxation images for myelin water quantification. Lect. Notes Comput. Sci. (including Subser. Lect. Notes Artif. Intell. Lect. Notes Bioinformatics) 8149 LNCS, 614–621. doi:10.1007/978-3-642-40811-3_77

Yu, C., Lin, F., Li, K., Jiang, T., Qin, W., Sun, H., Chan, P., 2008. Pathogenesis of Normal-appearing White Matter Damage in Neuromyelitis Optica: Diffusion-Tensor MR Imaging. Radiology 246, 222–228. doi:10.1148/radiol.2461062075

Yu, C., Zhu, C., Li, K., Xuan, Y., Qin, W., Sun, H., Chan, P., 2007. Relapsing Neuromyelitis Optica and Relapsing-Remitting Multiple Sclerosis: Differentiation at Diffusion-Tensor MR Imaging of Corpus Callosum. Radiology 244, 249–256.

Yu, C.S., Lin, F.C., Li, K.C., Jiang, T.Z., Zhu, C.Z., Qin, W., Sun, H., Chan, P., 2006. Diffusion tensor imaging in the assessment of normal-appearing brain tissue damage in relapsing neuromyelitis optica. AJNR Am. J. Neuroradiol. 27, 1009–1015. doi:27/5/1009 [pii]

Zabad, R., Stewart, R., Healey, K., 2017. Pattern Recognition of the Multiple Sclerosis Syndrome. Brain Sci. 7, 138. doi:10.3390/brainsci7100138

Zalewski, N.L., Morris, P.P., Weinshenker, B.G., Lucchinetti, C.F., Guo, Y., Pittock, S.J., Krecke, K.N., Kaufmann, T.J., Wingerchuk, D.M., Kumar, N., Flanagan, E.P., 2016. Ring-enhancing spinal cord lesions in neuromyelitis optica spectrum disorders. J. Neurol. Neurosurg. Psychiatry jnnp-2016-314738. doi:10.1136/jnnp-2016-314738

Zamvil, S.S., Slavin, A.J., 2015. Does MOG Ig-positive AQP4-seronegative opticospinal inflammatory disease justify a diagnosis of NMO spectrum disorder? Neurol. - Neuroimmunol. Neuroinflammation 2, e62. doi:10.1212/NXI.0000000000000062

Zeis, T., Graumann, U., Reynolds, R., Schaeren-Wiemers, N., 2007. Normal-appearing white matter in multiple sclerosis is in a subtle balance between inflammation and neuroprotection. Brain 131, 288–303. doi:10.1093/brain/awm291

Zhang, J., Kolind, S.H., Laule, C., MacKay, A.L., 2015. How does magnetization transfer influence mcDESPOT results? Magn. Reson. Med. 74, 1327–1335. doi:10.1002/mrm.25520

Zhang, N., Li, Y., Fu, Y., Shao, J., Luo, L., Yang, L., Shi, F., Liu, Y., 2015. Cognitive impairment in Chinese neuromyelitis optica. Mult. Scler. J. 21, 1839–1846. doi:10.1177/1352458515576982

Zhang, Y., Brady, M., Smith, S., 2001. Segmentation of brain MR images through a hidden Markov random field model and the expectation-maximization algorithm. IEEE Trans. Med. Imaging 20, 45–57. doi:10.1109/42.906424

Zhao, D. Di, Zhou, H.Y., Wu, Q.Z., Liu, J., Chen, X.Y., He, D., He, X.F., Han, W.J., Gong, Q.Y., 2012. Diffusion tensor imaging characterization of occult brain damage in relapsing neuromyelitis optica using 3.0T magnetic resonance imaging techniques. Neuroimage 59, 3173–3177. doi:10.1016/j.neuroimage.2011.11.022

Zivadinov, R., Banas, a C., Yella, V., Abdelrahman, N., Weinstock-Guttman, B., Dwyer, M.G., 2008. Comparison of three different methods for measurement of cervical cord atrophy in multiple sclerosis. AJNR. Am. J. Neuroradiol. 29, 319–325. doi:10.3174/ajnr.A0813